Genome-wide CRISPR-Cas9 knockout screens decipher genetic dependencies and chemogenetic interactors in sonic hedgehog subgroup of medulloblastoma

Dissertation

zur Erlangung des Grades eines

Doktors der Naturwissenschaften

der Mathematisch-Naturwissenschaftlichen Fakultät

und

der Medizinischen Fakultät

der Eberhard-Karls-Universität Tübingen

vorgelegt

von

Foteini Tsiami

aus Serres, Griechenland

2025

Tag der mündlichen Prüfung: 10 November 2025

Dekan der Math.-Nat. Fakultät: Prof. Dr. Thilo Stehle

Dekan der Medizinischen Fakultät: Prof. Dr. Bernd Pichler

1. Berichterstatter: Prof. Dr. Ghazaleh Tabatabai
2. Berichterstatter: Assoc. Prof. Dr. Pratiti Bandopadhayay
3. Dritter Berichterstatter: PD Dr. Dr. Tobias Weiss

Prüfungskommission: Prof. Dr. Ghazaleh Tabatabai

Asst. Prof. Dr. Pratiti Bandopadhayay

Prof. Dr. Simone Mayer

Prof. Dr. Lisa Sevenich

Erklärung / Declaration:

Ich erkläre, dass ich die zur Promotion eingereichte Arbeit mit dem Titel:

„Genome-wide CRISPR-Cas9 knockout screens decipher genetic dependencies and chemogenetic interactors in sonic hedgehog subgroup of medulloblastoma“

selbständig verfasst, nur die angegebenen Quellen und Hilfsmittel benutzt und wörtlich oder inhaltlich übernommene Stellen als solche gekennzeichnet habe. Ich versichere an Eides statt, dass diese Angaben wahr sind und dass ich nichts verschwiegen habe. Mir ist bekannt, dass die falsche Abgabe einer Versicherung an Eides statt mit Freiheitsstrafe bis zu drei Jahren oder mit Geldstrafe bestraft wird.

I hereby declare that I have produced the work entitled "Genome-wide CRISPR-Cas9 knockout screens decipher genetic dependencies and chemogenetic interactors in sonic hedgehog subgroup of medulloblastoma", submitted for the award of a doctorate, on my own (without external help), have used only the sources and aids indicated and have marked passages included from other works, whether verbatim or in content, as such. I swear upon oath that these statements are true and that I have not concealed anything. I am aware that making a false declaration under oath is punishable by a term of imprisonment of up to three years or by a fine.

Tübingen, den ....

Datum / Date Unterschrift /Signature

Contents

List of figures

List of tables

List of abbreviations

^{o}C	Centigrade
3D	Three dimensional
5-AzaC	5-Azacytidine
aa	Amino acids
AKT	Serine-threonine protein kinase
APC	Adenomatous polyposis coli
AT/RT	Atypical teratoid/rhabdoid tumors
BAGEL2	Bayesian analysis of gene essentiality
BCC	Basal cell carcinoma
BCOR	BCL6 (B-cell lymphoma 6) interacting corepressor
BP	Biological process
BRCA2	Breast cancer gene 2
BRPF1	Bromodomain and PHD (plant homeodomain) finger containing 1
BMP	Bone morphogenetic protein
Bp	Base pair
BSA	Bovine serum albumin
CC	Cellular component
CC3	Cleaved caspase 3
CCND1	Cyclin D1
CDKs	Cyclin-dependent kinases
CDKN2A/B	Cyclin-dependent kinase inhibitor 2A/B
cm	Centimeter
CNS	Central nervous system

CpG	5´-C-phosphate-G-3´
CREBBP	CREB (cAMP-response element) binding protein
CRISPR	Clustered regularly interspaced short palindromic repeats
CSI	Craniospinal irradiation
CTDNEP1	CTD nuclear envelope phosphatase 1
CTNNB1	Catenin beta 1
Ctr	Control
DGIdb	Drug-gene interaction database
DEG	Differentially expressed gene
DNA	Deoxyribonucleic acid
DNMT1	DNA methyltransferase 1
DMEM	Dulbecco´s modified eagle medium
DMSO	Dimethyl sulfoxide
DSB	Double-strand breaks
E	Embryonal day
EGL	External granule layer
FDA	Food and Drug Administration
FDR	False discovery rate
FSC	Forward scatter
GDC-0449	Vismodegib
GCNP	Granule cell neuron precursor
GLI	Glioma-associated oncogene family zinc finger
GO	Gene ontology
GOF	Gain-of-function
GRi	Growth rate inhibition

GS	Gorlin syndrome
GSEA	Gene set enrichment analysis
HDAC	Histone deacetylase
H&E	Haematoxylin & eosin
IGL	Internal granule layer
i.p.	Intraperitoneally
KBTBD4	Kelch Repeat and BTB Domain Containing 4
KMT2D (MLL2)	Lysine methyltransferase 2D
KO	Knockout
LC/A	Large cell/anaplastic
LDE-225	Sonidegib
LFC (log_2FC)	Log_2 fold change
LFS	Li-Fraumeni syndrome
LOF	Loss-of-function
MAGeCK	Model-based analysis of genome-wide CRISPR-Cas9 knockout screen
MATH1 (ATOH1)	Atonal bHLH (basic helix-loop-helix) transcription factor 1
MB	Medulloblastoma
MBEN	Medulloblastoma with extensive nodularity
Meis	Myeloid ectopic viral integration site 1 homolog
MEK	Mitogen-activated protein kinase
µg	Microgram
ML	Molecular layer
MLE	Maximum likelihood estimation

µl	Microliter
µm	Micrometer
µM	Micromolar
MOI	Multiplicity of infection
mRNA	Messenger RNA
mTOR	Mechanistic target of rapamycin kinase
MYC	MYC proto-oncogene
MYCN	MYCN proto-oncogene
NES	Normalized enrichment score
NeuN	Neuronal nuclei
NGS	Next generation sequencing
ng	Nanogram
nM	Nanomolar
o.g.	Oral gavage
P	Postnatal day
P_{adj}	P adjusted value
PALB2	Partner and localizer of BRCA2
Pax6	Paired box 6
PBS	Phosphate-buffered saline
PCA	Principal component analysis
PCL	Purkinje cell layer
PCNA	Proliferating cell nuclear antigen
PCR	Polymerase chain reaction
PDO	Patient-derived organoids
PDXO	Patient-derived xenograft organoid

PFA	Paraformaldehyde
PI3K	Phosphoinositide 3-kinase
PRDM6	PR/SET domain 6
PTCH1	Patched 1
PTEN	Phosphatase and tensin homolog
RNA	Ribonucleic acid
RNAi	RNA interference pathway
Rpm	Revolutions per minute
RRA	Robust rank aggregation
RT	Room temperature
SD	Standard deviation
sem	Standard error of mean
sgRNA	Single guide RNA
SHH	Sonic hedgehog
shRNA	Short hairpin RNA
SMARCA4/5/6	SWI/SNF-related, matrix associated, actin dependent regulator of chromatin, subfamily A, member 4/5/6
SMB	SHH-MB cell lines
SMO	Smoothened
SSC	Side scatter
STRING	Search tool for the retrieval of interacting genes/proteins
SWI/SNF	Switch/sucrose non-fermentable
SUFU	Suppressor of fused homolog
ISWI	Initiation Switch
TAM	Tamoxifen

TBS	Tris-buffered saline
TBS-T	Tris-buffered saline-Tween-20
TERT	Telomerase reverse transcriptase
TP53	Tumor protein 53
uRL	Upper rhombic lip
USA	United States of America
V	Volt
Vs	Versus
VZ	Ventricular zone
WHO	World Health Organization
Wt	Wildtype
WNT	Wingless
ZIP	Zero interaction potency

Abstract

Medulloblastomas (MB) are the most common malignant embryonal tumors of the Central Nervous System (CNS), primarily diagnosed during childhood. This highly heterogeneous tumor entity encompasses four molecular consensus subgroups: wingless (WNT), sonic hedgehog (SHH), Group 3 and Group 4, which exhibit differential transcriptomic, epigenetic and proteomic signatures. SHH subgroup of MB (SHH-MB), which belongs to the scope of this thesis, accounts for approximately 30% of all MBs and displays a bimodal age distribution, as it more frequently affects infants and adults. As the name suggests, SHH-MB is characterized by constitutive activation of SHH signaling cascade, induced by genetic alterations in critical components of the SHH pathway. Inhibition of Smoothened (SMO), an upstream member of the SHH pathway, is a targeted therapy approach applied in several SHH-driven cancers, including MB, displaying promising anti-tumor results. However, due to primary or secondary resistance mechanisms, its clinical efficacy is limited. Hence, there is an urgent need for novel therapeutic interventions that will be able to inhibit SHH-MB growth regardless of the genetic mutations within the SHH pathway.

In light of limited targeted therapies for SHH-MB, the primary aim of this thesis is to identify genetic vulnerabilities in SHH-MB potentially beyond the SHH pathway that could potentially serve as novel therapeutic targets. To this end, CRISPR-Cas9 genome-wide knockout screens were carried out in this study, in order to unravel genetic vulnerabilities in SHH-MB. Two distinct models murine SMB21 and human DAOY cells were screened and their suitability as SHH-representative model systems was addressed. Our functional genomics data provide evidence that SMB21 cells recapitulate SHH-associated hallmark features, while DAOY cells do not, emphasizing the potential of SMB21 cells to serve as a faithful *in vitro* model for SHH-MB.

Among the top scored hits, members of the epigenetic machinery including DNA methyltransferase 1 *Dnmt1* and chromatin remodeler *Smarca5* showed robust depletion in SMB21-screened cells, indicating that they represent genetic dependencies for SHH-MB. Genetic and pharmacological inhibition experiments showed that DNMT1 inhibition suppresses SHH-MB proliferation *in vitro*, by blocking SHH signaling, as further supported by DNA methylation and RNA sequencing analyses. We also demonstrate that *Dnmt1* plays a crucial role in proper formation of the murine cerebellum, while its genetic ablation prolongs survival outcome of tumor bearing SHH-MB mice. Of note, by conducting an additional CRISPR-Cas9 knockout drug, we unraveled *Smo* knockout as a synergistic partner for DNMT1 inhibitor, 5-Azacytidine. We show that simultaneous combination treatment of 5-Azacytidine and Sonidegib effectively inhibited tumor growth in murine and human SHH-MB cell models. These findings were further evaluated *in vivo* using an

established preclinical model of SHH-MB and we demonstrated that combination therapy of both inhibitors extends survival of SHH-MB mice by reducing tumor cell proliferative activity.

Finally, we assessed the role of SNF2-family member of ATP-dependent chromatin remodeler *Smarca5* in SHH-MB development. By genetically targeting *Smarca5* in SMB cells, we could prove that its loss reduces SMB survival *in vitro*, by inhibiting SHH pathway activation. Furthermore, we present that loss of *Smarca5* in granule cell neuron precursors (GCNPs) affects their viability and migratory activity, resulting in developmental abnormalities in regard to murine cerebellar growth. In parallel, our data indicate that *Smarca5* is required for tumor progression in mouse models of SHH-MB.

Taken together, we provide strong evidence that epigenetic regulators *Dnmt1* and *Smarca5* are essential for normal cerebellar, as well as GCNP-derived SHH-MB development. We unraveled DNMT1 as a novel therapeutic target for SHH-driven MB that acts downstream of the SHH signaling cascade, thus representing an efficacious treatment for this tumor entity irrespective of the genetic alterations within the SHH pathway. Finally, we propose that inhibiting DNMT1 alone or in combination with SMO inhibition could serve as a novel treatment modality for SHH-MB tumors.

1 Introduction

1.1 Medulloblastoma

1.1.1 Epidemiology and therapy

Central nervous system (CNS) tumors are the second most common cancer type after leukemia in children (Steliarova-Foucher et al., 2017). Embryonal brain tumors, which constitute a heterogeneous entity of undifferentiated or poorly differentiated neuroepithelial tumors, account for 9.1% of all CNS tumors in children and adolescents aged 0-19 years (Ostrom et al., 2023). The most common malignant embryonal brain tumors in this age group are medulloblastomas (MB) (Ostrom et al., 2023), which primarily derive from neuronal stem or progenitor cell populations of the developing cerebellum or brainstem (Huang et al., 2016, Grammel et al., 2012, Schüller et al., 2008, Gibson et al., 2010) and are classified as grade IV by the World Health Organization (WHO) (Louis et al., 2007). The median age of diagnosis is approximately 6 years, with MB occurring more frequently in males aged 0-14 years than females of the same age group, while incidence rates decline with increasing age for those aged 0-19 years (Ostrom et al., 2023).

Standard-of-care therapy for MB, consisting of maximal surgical resection, craniospinal irradiation (CSI) in non-infants, and adjuvant platinum-based chemotherapy, has increased 5-year event-free survival up to 70-80% for newly diagnosed MB patients and approximately 60% for metastatic patients (Packer et al., 2006, Gajjar et al., 2006, von Bueren et al., 2016, Michalski et al., 2021). However, such intensive treatment modalities may cause long-term side effects, including neuro-cognitive deficits, which have a significant impact on survivors´ quality of life (Ribi et al., 2005, Mulhern et al., 2005, King et al., 2017) and therefore, novel, less toxic therapeutic strategies are urgently needed.

1.1.2 Molecular classification

Based predominantly on histopathology, long-established histological variants, including classic, desmoplastic/nodular, large cell/anaplastic (LC/A) and MB with extensive nodularity (MBEN) laid the basis for the diagnosis and classification schemes of MB (Louis et al., 2007). Transcriptional profiling of MB cohorts performed by several research groups deciphered its molecular heterogeneity, resulting in tumor classification into four distinct subgroups, as proposed in 2012: wingless (WNT), sonic hedgehog (SHH), Group 3 and Group 4 (Taylor et al., 2012). The designated subgroups present distinct epidemiological, clinical, and genetic features, as summarized on **Figure 1**. Deeper transcriptomic, epigenomic and proteomic analyses have further revealed intertumoral heterogeneity within the different subgroups, leading to subtype delineation, thereby contributing to a better understanding of the biology underlying the discrepancies among

MB subgroups (Hovestadt et al., 2014, Cavalli et al., 2017, Northcott et al., 2017, Archer et al., 2018).

In brief, while only approximately 10% of all MBs are classified as WNT tumors, WNT-MB patients carry the best long-term prognosis compared to the rest subgroups (**Supplementary figure 1**) (Taylor et al., 2012). WNT-MB has a median age of diagnosis of 10 years (Ostrom et al., 2023). Approximately 90% of WNT-MB patients carry somatic activating mutations in *CTNNB1*, resulting in nuclear accumulation of β-catenin in the nucleus and therefore, constitutive activation of the WNT signaling (Northcott et al., 2017). In the absence of *CTNNB1* mutations, WNT-MB patients often harbor germline mutations in tumor suppressor *APC*, predisposing them to Turcot´s syndrome (Zurawel et al., 1998).

SHH-MB, which belongs to the scope of the current thesis, is among the best understood subgroups. It accounts approximately for 30% of all MBs and exhibits a bimodal age distribution, as it occurs more often in infants (0-3 years old) and adults (older than 16 years old) but much less frequently children (3-16 years old) (Taylor et al., 2012). SHH-MB is characterized by aberrant activation of the canonical SHH signaling pathway, resulting from germline or somatic mutations in major members of the signaling cascade including loss-of-function (LOF) mutations in *Patched 1* (*PTCH1*) and activating mutations in *Smoothened* (*SMO*). Unlike WNT-MB, SHH-MB exhibits great inter-subgroup heterogeneity from a clinical and biological point of view, as will further be discussed in the subsequent chapter.

Although the transcriptomics of Group 3- and Group 4-MB are more similar to each other, gene expression and DNA methylation profiling have established that these are molecularly distinct entities (Cavalli et al., 2017). Group 3-MB accounts for approximately 25% of all MBs, primarily present in infants and children, and is associated with the worst survival outcome among all MB subgroups (under 60% at 5 years) (Taylor et al., 2012). Together with Group 4-MB, Group 3-MB patients display the highest frequency of metastatic disease at diagnosis (30%) (Kool et al., 2012). These tumors are characterized by genomic instability and have high levels of *MYC* expression, with amplifications of the proto-oncogene *MYC* appearing almost exclusively in Group 3 (17%) (Northcott et al., 2011b). Recurrent somatic mutations are less common in Group 3-MB, with *SMARCA4*, *KBTBD4*, *CTDNEP1* and *KMT2D* being the only genes mutated in more than 5% of Group 3-MB patients (Northcott et al., 2017). Group 4 is the least well understood MB subgroup with regard to its underlying tumor biology. It typically appears in children and adolescents and it accounts for 35-40% of all MBs (Taylor et al., 2012). The most prevalent putative driver event in this subgroup involves enhancer-hijacking-mediated overexpression of *PRDM6*, while other

events include amplifications of *MYCN* (6%) and *CDK6* (6%) (Northcott et al., 2017). Despite the high frequency of metastasis, survival outcomes are intermediate in Group 4-MB (Taylor et al., 2012).

	Subgroup	WNT	SHH	Group 3	Group 4
Clinical Characteristics	% of Cases	10	30	25	35
	Age at Diagnosis				
	Gender Ratio (M:F)	1:1	1:1	2:1	3:1
	Anatomic Location				
	Histology	Classic, Rarely LCA	Desmoplastic, Classic, LCA	Classic, LCA	Classic, LCA
	Metastasis at Diagnosis (%)	5-10	15-20	40-45	35-40
	Recurrence Pattern	Rare; Local or metastatic	Local	Metastatic	Metastatic
	Prognosis	Very good	Infants good, others intermediate	Poor	Intermediate
Molecular Characteristics	Proposed Cell of Origin	Progenitor cells in the lower rhombic lip	Granule precursors of the external granule layer	Neural stem cells	Unipolar brush cells
	Recurrent Gene Amplifications	-	*MYCN* *GLI1* or *GLI2*	*MYC* *MYCN* *OTX2*	*SNCAIP* *MYCN* *OTX2* *CDK6*
	Recurrent SNVs	*CTNNB1* *DDX3X* *SMARCA4* *TP53*	*PTCH1* *TERT* *SUFU* *SMO* *TP53*	*SMARCA4* *KBTBD4* *CTDNEP1* *KMT2D*	*KDM6A* *ZMYM3* *KTM2C* *KBTBD4*
	Cytogenetic Events ■ Gain ■ Loss	6	3q, 9p 9q, 10q, 17p	1q, 7, 18 8, 10q, 11, 16q i17q	7, 18q 8, 11p, X i17q
	Other Recurrent Genetic Events	-	-	*GFI1* and *GFI1B* enhancer hijacking	*PRDM6*, *GFI1*, and *GFI1B* enhancer hijacking

Age: Infant Child Adult

Figure 1. Current consensus on medulloblastoma classification. Clinical and molecular differential characteristics of WNT-, SHH-, Group 3- and Group 4-MB subgroups are described. Source from Juraschka, K., & Taylor, M. D. (2019). Medulloblastoma in the age of molecular subgroups: a review. *J Neurosurg Pediatr*, *24*(4), 353-363. https://doi.org/10.3171/2019.5.Peds18381 (Juraschka and Taylor, 2019).

1.2 Sonic hedgehog subgroup of medulloblastoma

1.2.1 Subclassification of SHH-MB

Regarding SHH subgroup of MB, *WHO Classification of Tumors of the Central Nervous System* in 2016 divided this tumor entity according to *TP53* status into *TP53*-wildtype and *TP53*-mutant tumors, highlighting their markedly different clinicopathological features (Louis et al., 2016). *TP53*-wildtype tumors have an incidence rate of 0.03 per 100,000 population and a median age of diagnosis of 19 years, while *TP53*-mutated tumors of 11 years (Ostrom et al., 2023). *TP53* mutation status has a prognostic role in SHH-MB, as SHH-activated and *TP53*-mutant MBs occur more often in young children, constituting a very high-risk group with worse outcome (< 50% survival) (Zhukova et al., 2013, Ramaswamy et al., 2016).

Recent advances in molecular classification of SHH-MB have proposed various subtypes of SHH-MB, thereby revealing great molecular intertumoral heterogeneity. Gene expression and DNA methylation profiling have defined four distinct SHH subtypes α, β, γ and δ, which differ in terms of demographic, clinical and genetic features (**Supplementary figure 1**) (Cavalli et al., 2017). *TP53* sequencing across all subtypes has shown that *TP53* mutations are enriched in SHH-α tumors (21%), which are prevalent in children and adolescents (> 3 years of age), and are associated with worse outcomes (Zhukova et al., 2013, Cavalli et al., 2017). While SHH-β and SHH-γ tumors correspond to infants (≤ 3 years of age), γ subtype has a better overall survival than β due to the increased rate of metastatic dissemination that the latter possesses. In contrast, SHH-δ tumors mostly affect adults and are associated with a more favorable prognosis. Enrichment analysis also revealed differential pathway activation among the four subtypes, including DNA repair and cell cycle associated pathways being prevalent in SHH-α tumors, while developmental pathways being represented more in γ than β subtype.

Another retrospective cohort study has classified SHH-MB on the basis of age distribution, defining two age-dependent subgroups corresponding to infants (< 4.3 years of age; $MB_{SHH\text{-}Infant}$) and childhood patients (≥ 4.3 years of age; $MB_{SHH\text{-}Child}$) (Schwalbe et al., 2017). Each subgroup exhibits distinct clinical or molecular features, with LC/A pathology, *TP53* mutations and *MYCN* amplifications being significantly prevalent in $MB_{SHH\text{-}Child}$ subgroup. Similarly, based on the methylation profiling of MB cohorts another study designated two infant subtypes among children patients younger than 5 years of age, iSHH-I and iSHH-II, which are associated with 5-year progression-free survivals of 27.8% and 75.4%, respectively (Robinson et al., 2018). Differential genetic events included deleterious *SUFU* alterations enriched in iSHH-I, as well as activating *SMO* mutations and deletions in the long arm of chromosome 9 (9q) prevalent in iSHH-II. The most recent *WHO Classification of CNS Tumors* re-designated SHH-MB into four distinct subtypes

SHH-1, 2, 3 and 4, which correspond to β, γ, α and δ subtypes described by Cavalli *et al.* (Cavalli et al., 2017), thereby leveraging diverse large-scale *omics* studies (**Figure 2**) (Louis et al., 2021).

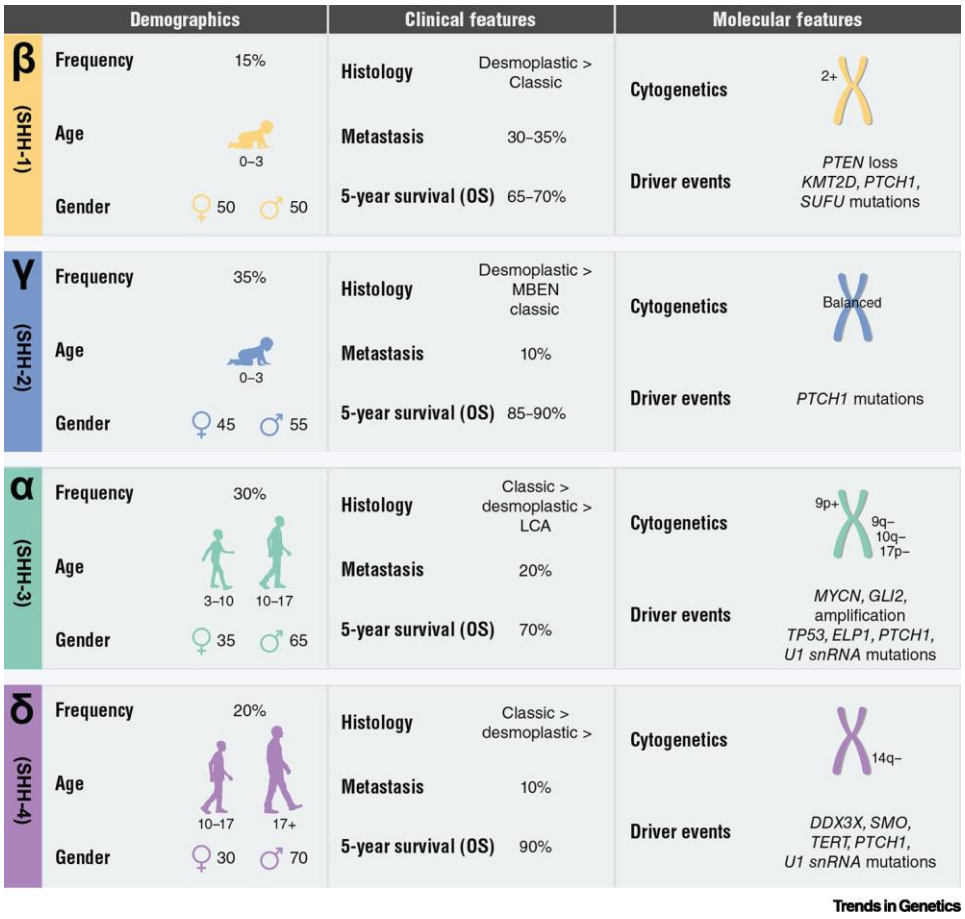

Figure 2. Current subclassification of sonic hedgehog subgroup of medulloblastoma (SHH-MB) according to 2021 *WHO Classification of CNS Tumors*. Summary of designated subtypes of SHH-MB: SHH-1 (β), SHH-2 (γ), SHH-3 (α) and SHH-4 (δ). Demographic, clinical and molecular features per subtype are described. Source from Garcia-Lopez J, Kumar R, Smith KS, Northcott PA. (2021). Deconstructing sonic hedgehog medulloblastoma: Molecular subtypes, drivers, and beyond. *Trends Genet*, *37*(3), 235-250. https://doi.org/10.1016/j.tig.2020.11.001 (Garcia-Lopez et al., 2021).

1.2.2 Genomics

The majority of SHH-MB patients harbor either somatic or germline mutations in critical components of the pathway (**Figure 3**), which include loss-of-function mutations or deletions in tumor suppressor genes *PTCH1* (43%) and *SUFU* (10%), activating mutations of *SMO* (9%) and amplifications in *GLI2* (9%) and *MYCN* (7%) (Kool et al., 2014, Northcott et al., 2017). Physiologically, transmembrane receptor *PTCH1* suppresses G-protein coupled receptor *SMO*,

maintaining the SHH pathway in an inactive state. However, genetic alterations within the pathway can result in downstream aberrant pathway activation, and therefore upregulation of SHH-responsive genes which drive uncontrolled cell proliferation and eventually tumorigenesis. Additionally, profiling MB has revealed age-related clinical and genetic discrepancies between pediatric and adult patients. Overall, adult patients are characterized by higher mutational burden and in regard to SHH pathway, most adults harbor mutations in *PTCH1* or *SMO*, as compared to infants and children, who frequently harbor mutations downstream of *SMO* such as *SUFU* (Northcott et al., 2011a, Kool et al., 2014).

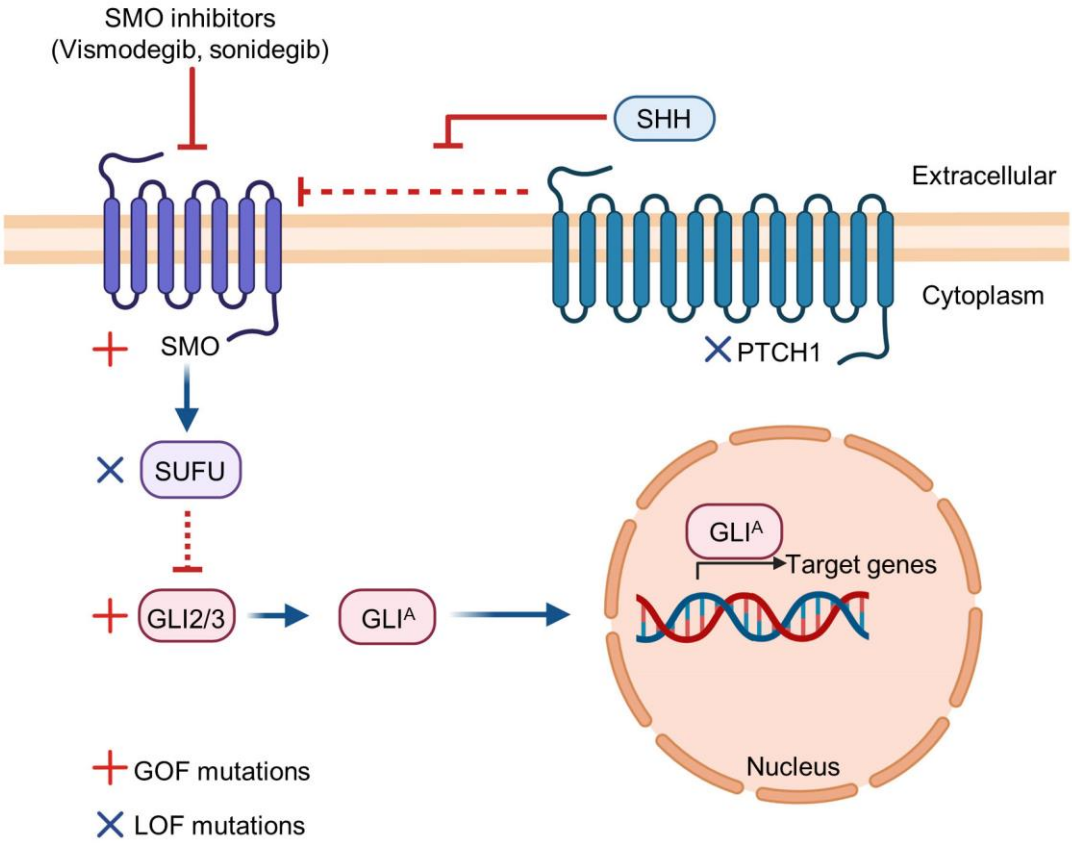

Figure 3. Constitutive activation of sonic hedgehog signaling in SHH-driven medulloblastoma. Genetic alterations in major components of the SHH pathway are denoted. These include inactivating mutations in transmembrane receptor PTCH1 or negative regulator of SHH pathway, SUFU, as well as activating mutations in SMO and amplifications of GLI2 or GLI3. Upon pathway activation, SMO is de-repressed and migrated to the primary cilia, thereby activating GLI transcription factors. Gli2/3 transcription factors accumulate in the primary cilia, which in turn shift GLI into its active form GLI^A, overcoming the negative regulation of SUFU (Garcia-Lopez et al., 2021). After GLI^A is translocated into the nucleus, it allows the

expression of oncogenes such as GLI1 and MYCN, which lead to uncontrolled cell proliferation and eventually SHH-MB growth. Illustration generated with Biorender.com. Figure adapted from Northcott PA., Robinson GW, Kratz CP, Mabbott DJ, Pomeroy SL, Clifford SC, Rutkowski S, Ellison DW, Malkin D, Taylor MD, Gajjar A, Pfister SM. (2019). Medulloblastoma. *Nat Rev Dis Primers*, *5*(1), 11. https://doi.org/10.1038/s41572-019-0063-6 (Northcott et al., 2019).

In addition to SHH signaling-related genetic alterations, cytogenetic events appear often in SHH-MB patients, including losses of the long arm of chromosomes 9 (9q) and 10 (10q), which result in loss of heterozygosity for *PTCH1* and *SUFU*, respectively (Kool et al., 2014). Genetic aberrations in the PI3K/AKT/mTOR signaling including *PTEN*, as well as activating *TERT* promoter mutations, which affect telomerase maintenance, act also as tumor drivers and are identified predominantly in adult SH-MB patients (SHH-4 subtype) (Kool et al., 2014). Childhood SHH-MBs have greater genomic instability and are characterized by catastrophic DNA rearrangements referred to as chromothripsis, attributed to *TP53* mutations (Kool et al., 2014, Rausch et al., 2012). MB profiling has also uncovered the critical role of the epigenetic machinery with somatic mutations in chromatin modifiers (44%) occurring across all SHH subtypes. Among others, these include inactivating mutations in *KMT2D* and *CREBBP*, which are predominantly found in SHH-β (SHH-1) and SHH-δ (SHH-4) MBs, respectively (Skowron et al., 2021).

Approximately 20-25% of SHH-MBs harbor germline variants predisposing them to malignancy (Waszak et al., 2018). Germline mutations in consensus cancer predisposition genes *APC*, *BRCA2*, *PALB2*, *PTCH1*, *SUFU* and *TP53* account for approximately 6% of MB diagnoses (Waszak et al., 2018). Compared to adult SHH-MB, frequency of germline predisposition is much higher in pediatric patients (Waszak et al., 2018). Primary risk factors for the development of SHH-MB include hereditary syndromes such as Gorlin syndrome (GS) and Li-Fraumeni syndrome (LFS), which are associated with mutations in *PTCH1* or *SUFU*, and *TP53*, respectively (Li and Fraumeni, 1969, Taylor et al., 2002, Brugières et al., 2012, Smith et al., 2014, Wolter et al., 1997). Germline mutations in *PTCH1* and *SUFU* are enriched in infant SHH-MBs, while *TP53* in older children (Waszak et al., 2018). In contrast, *BRCA2* and *PALB2* germline mutations related to mutational signatures typical of homologous recombination repair deficiency display no association with age at diagnosis (Waszak et al., 2018).

1.2.3 SMO inhibition as a targeted therapy

When it comes to the current treatment avenues for SHH-MB, besides the standard treatment protocols, targeted therapies have emerged as an alternative treatment approach for SHH-MB. In

particular, vismodegib (GDC-0449) and sonidegib (LDE-225) are Food and Drug Administration (FDA)-approved small molecule inhibitors that target SHH pathway at the level of SMO (**Figure 3**) and have demonstrated anti-tumor activity in SHH-driven cancers including basal cell carcinoma (BCC) (Sekulic et al., 2015, Migden et al., 2015, Collier et al., 2016) and SHH-MB (Rudin et al., 2009, Robinson et al., 2015, Lou et al., 2016, Li et al., 2019). Despite the promising therapeutic results of SMO inhibition in SHH-MB patients, the mutational burden of these tumors in regard to SHH pathway can induce differential response to treatment (Kool et al., 2014). While tumors with mutations in *PTCH1* are found across all age groups and are expected to respond to SMO inhibition, genetic alterations downstream of *PTCH1*, such as LOF mutations in *SUFU* or GLI2/MYCN amplifications, which are prevalent in infants and children, respectively, potentially demonstrate primary resistance to SMO inhibition. These data suggest that most adult patients but only half of the pediatric patients will most likely respond to therapy (Lee et al., 2007, Kool et al., 2014). In addition, even those patients with an initial favorable response to SMO inhibition are prone to develop secondary resistance to treatment due to continuous drug exposure (Rudin et al., 2009, Yauch et al., 2009, Dijkgraaf et al., 2011), thereby limiting the long-term efficacy of SMO inhibitors. Similarly, resistance to SMO inhibition has also been observed in mouse models of SHH-MB despite initial sensitivity to treatment (Yauch et al., 2009, Dijkgraaf et al., 2011). Single-cell RNA sequencing has revealed surviving subsets of cells including $Sox2^{+}$ cells, in which vismodegib treatment failed to suppress SHH-driven activation (Ocasio et al., 2019), thus representing a therapeutic challenge for SMO inhibitors (Garcia-Lopez et al., 2021). Therefore, in light of pre-existing or acquired resistance mechanisms developed against SMO inhibition, it is imperative that novel therapeutic targets are unraveled that will be efficacious in both SMO inhibition-sensitive and resistant SHH-MB patients.

1.2.4 Developmental origin of sonic hedgehog subgroup of medulloblastoma

While MBs are considered predominantly cerebellar tumors, different MB subgroups have distinct cellular origins. Particularly, WNT-MB is suggested to derive from the brainstem (Gibson et al., 2010), while SHH- and Group 3-MB from the cerebellum (Schüller et al., 2008, Pei et al., 2012, Kawauchi et al., 2012, Grammel et al., 2012, Huang et al., 2016). Although the exact developmental origin for Group 4-MB still needs to be elucidated, these tumors appear to transcriptionally resemble unipolar brush cells (Vladoiu et al., 2019).

Located in the dorsal hindbrain, the cerebellar anlage consists of two proliferative niches: the ventricular zone (VZ) and the rhombic lip (RL), which generate distinct cell populations. Starting

from embryonic day 13.5 (E13.5) in mice and after 10 post-conceptional weeks in humans, the upper rhombic lip (uRL) of the developing cerebellum gives rise to many neuronal populations including granule cell neuron precursors GCNPs (Carter et al., 2018, Aldinger et al., 2021), which are the proposed cell origin for SHH-MB (Kim et al., 2003, Yang et al., 2008, Schüller et al., 2008). After GCNPs exit the uRL, they migrate rostrally towards the external granule layer (EGL), where they proliferate upon exposure to SHH ligand, which is secreted by the Purkinje cells (Komuro and Rakic, 1998, Komuro et al., 2001, Wallace, 1999, Wechsler-Reya and Scott, 1999) (**Figure 4**). GCNPs reach their peak proliferative capacity between postnatal days 5 and 7 (P5 and P7) in mice and finally, they migrate inwards, across the Purkinje cell layer, to form the internal granule layer (IGL) as mature, differentiated granule neurons. This process is completed by P15 in mice and around one year in humans (Garcia-Lopez et al., 2021, Abrahám et al., 2001, Borghesani et al., 2002).

Several key transcriptional factors along with SHH signaling activation regulate GCNP activity in the developing cerebellum. These include the proneural basic helix-loop-helix transcription factor Math1, which drives several steps of GCNP development from cell proliferation to differentiation and migration (Klisch et al., 2011) and has been shown to sensitize GCNPs to SHH signaling by maintaining the presence of primary cilia on their surface (Chang et al., 2019). Furthermore, Pax6, another transcription factor known to be involved in granule cell migration and differentiation (Swanson and Goldowitz, 2011), together with Meis regulate GCNP differentiation in the inner EGL by degrading Math1 via the BMP signaling (Owa et al., 2018).

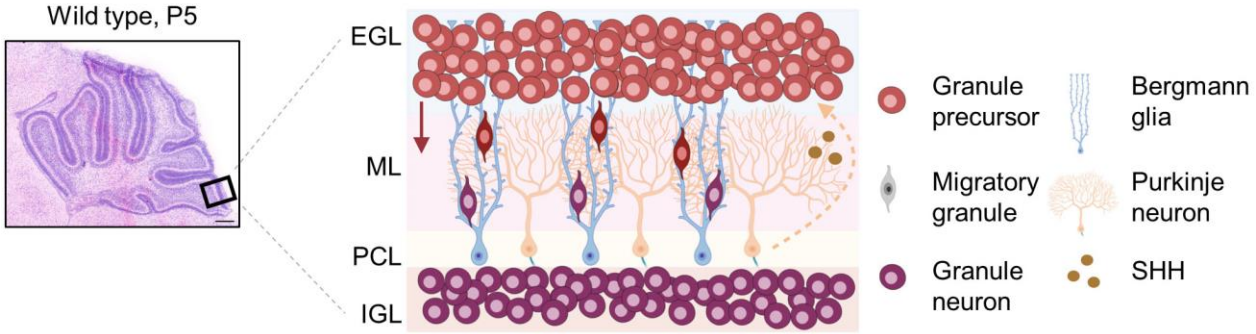

Figure 4. Haematoxylin and eosin staining of a sagittal section from murine cerebellum at postnatal day 5 and illustration of different layers constituting the cerebellar cortex. Highly proliferative granule cell neuron precursors (GCNPs) in the EGL respond to SHH signaling secreted by Purkinje neurons and migrate radially along the Bergmann glia fibers in the molecular layer. After exiting the cell cycle, GCNPs eventually populate the IGL as differentiated granule neurons. H&E staining; 4x magnification, scale bar, 500µm. Red arrow

denotes the direction of GCNP migration. EGL, external granular layer; ML, molecular layer; PCL, Purkinje cell layer; IGL, internal granular layer. Illustration generated with Biorender.com.

1.2.5 Mouse models of sonic hedgehog medulloblastoma

In order to better understand tumorigenesis on a molecular, cellular and histological level, preclinical models with active SHH signaling restricted to GCNPs that recapitulate SHH-MB development have been described, further suggesting GCNPs as the cellular origin of SHH-MB (Goodrich et al., 1997, Schüller et al., 2008, Yang et al., 2008).

While homozygous depletion of *Ptch1* in mice resulted in embryonic lethality, mice of genetic background *Ptch1*$^{+/-}$ represented one of the first genetically engineered models for tumor development in the cerebellum (Goodrich et al., 1997, Hahn et al., 2000, Kim et al., 2003, Oliver et al., 2005) with a tumor 6-month incidence rate of 15-20%. Inactivation of one *Ptch1* allele in combination with *TP53* depletion (*TP53*$^{-/-}$) has further increased MB incidence at > 95% (Wetmore et al., 2001). Constitutive expression of an activating allele of *Smo* (*SmoA1 or SmoM2*) in GCNPs constitutes also a well-established model of SHH pathway activation and subsequent MB formation in mice (Mao et al., 2006, Hatton et al., 2008, Hallahan et al., 2004). Of note, some of these models display leptomeningeal metastasis within the brain and to the spine (Hatton et al., 2008), which often occurs in MB patients as well, rendering such preclinical models useful to mimic SHH-MB progression. In this context, the tamoxifen (TAM) inducible Cre recombinase system is extensively used to generate experimental models including SHH-MB (Mao et al., 2006, Schüller et al., 2008), as it allows tissue- and time- specific gene recombination. Other models with active SHH signaling include *Sufu*$^{+/-}$*/Tp53*$^{-/-}$ double-mutant mice with a longer median survival period (2 months) than *Ptch1*$^{+/-}$*/Tp53*$^{-/-}$ mice, suggesting that *Ptch1* mutations are more potent than *Sufu* in reducing tumor latency (Lee et al., 2007). While pediatric and adult SHH-MBs display distinct clinically and gene expression profiles (Northcott et al., 2011a), many of the established mouse models exhibit a higher resemblance to human adult SHH-MBs than to infant SHH-MBs (Pöschl et al., 2014), suggesting that more mouse models that faithfully reflect human infant SHH-MBs still need to be developed (Lau et al., 2012).

1.3 Genome-wide CRISPR-Cas9 screens applications in cancer research

Forward genetic screens constitute a “phenotype-to-genotype” approach, as they allow mapping genetic perturbations to phenotypes of interest (Joung et al., 2017). Pooled screens begin with the introduction of a library of genetic perturbations into mammalian cell populations, using well-

established genome editing techniques. Such an approach enables identification of genetic perturbations that correspond to distinct phenotypes, thus providing valuable insight into the field of cancer genomics (Doench, 2018).

1.3.1 Genome-editing tools

The RNA interference pathway (RNAi) and specifically its effectors, short hairpin RNAs (shRNAs), have been extensively used to knock down gene function in perturbation screens (Berns et al., 2004, Root et al., 2006, Silva et al., 2005). However, RNAi-mediated gene silencing is impeded by variable knockdown efficiency and confounding off-target effects, resulting in low signal-to-noise ratio, thereby limiting screen data interpretations (Jackson et al., 2003, Jackson and Linsley, 2010, Evers et al., 2016). To eliminate the technical hurdles of RNAi, the bacterial clustered regularly interspaced short palindromic repeats (CRISPR)-Cas9 system has emerged as an efficient genome editing tool in functional genomics (Hsu et al., 2014). In particular, single guide RNAs (sgRNAs) guide endonuclease Cas9 to specific genomic targets, which are complementary to sgRNAs and in turn, Cas9 introduces precise double-strand breaks (DSBs), thus generating insertion or deletion mutations (indels) (Rouet et al., 1994, Hsu et al., 2013, Joung et al., 2017). Frameshifting indels produce a premature stop codon, leading to a LOF mutation in the targeted region (Joung et al., 2017). Using this technology, pooled LOF libraries have been generated to perform both negative and positive selection genome-scale CRISPR-Cas9 knockout screenings (Shalem et al., 2014, Wang et al., 2014). When comparing RNAi- and CRISPR-based screening methods, the latter have fewer off-target effects, higher validation rates, as well as lower false-negative rates, therefore overcoming the limitations of RNAi-mediated screens (Shalem et al., 2014, Evers et al., 2016, Munoz et al., 2016).

Besides LOF mutations, other applications include CRISPR activation (CRISPRa) and interference (CRISPRi), mediated by fusion of catalytically inactive Cas9 (dCas9) to activation and repression domains, respectively (Mali et al., 2013, Gilbert et al., 2014). Human and murine genome-wide CRISPR-based knockout, activation and knockdown libraries with improved on-target activity have been generated, enabling interrogation of gene function in both human and mouse cell models (Sanson et al., 2018, Doench et al., 2016). As described below, genetic screens have different applications and vary in regard to selection pressure applied, abundance of sgRNAs, number of targeted genes, as well as number of sgRNAs per gene (McDade et al., 2016). Depending on the biological question imposed, all these parameters should be taken into consideration for the right CRISPR modality to be selected.

1.3.2 Dependency screens

Genome-scale CRISPR-Cas9 knockout screens offer the opportunity to define gene essentiality, which refers to genes that are required for proliferation and survival of cancer cell lines (Wang et al., 2015a). During negative selection screens, or so-called dropout screens (Doench et al., 2016), cells are transduced with lentiviral libraries which provide thousands of different sgRNAs that target the entire genome (**Figure 5**). After selecting cells with a corresponding selection marker, they are propagating for several weeks. At each passaging a fraction of cells is reseeded to reassure a 500x library coverage, that is, transduced cells receive only one sgRNA and each sgRNA is present on average in 500 different cells (Doench, 2018). At the end of the screening, genomic DNA is extracted from the surviving cells and subjected to Next Generation Sequencing (NGS). The distribution of sgRNAs is analyzed and compared to a reference control plasmid and those sgRNAs which are depleted (dropped out) in the remaining cell population are targeting genes essential for cell viability, thereby revealing context-specific genetic dependencies.

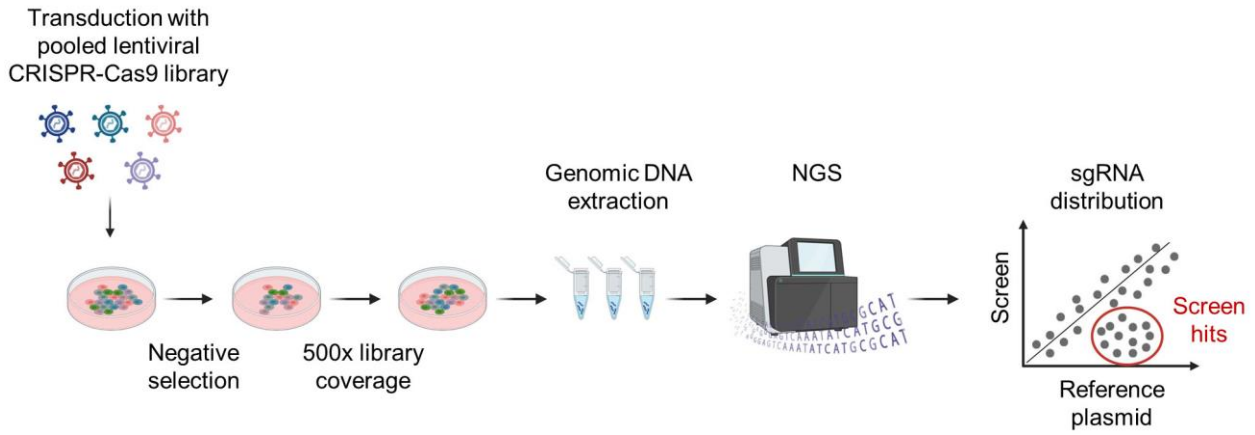

Figure 5. Schematic overview of negative selection screen with CRISPR-Cas9 library. Cells are transduced with a predetermined titer of the pooled lentiviral library at a low multiplicity of infection (MOI) (approximately 0.3-0.5), in order to ensure that each cell has been transduced with one sgRNA. Different sgRNAs delivered by the library are denoted as different colored particles. Unless cells are stably expressing Cas9 prior to the transduction, lentiviral library can additionally deliver Cas9 enzyme to the cells. After a drug-selectable marker has been applied to the cells, transduced cells are allowed to proliferate for several weeks and at each passaging a fraction of cells is reseeded at a density to maintain 500x library representation. At the end of the screening, genomic DNA is extracted from the remaining cells, from which the integrated sgRNA sequences are PCR-amplified and subjected to Next Generation Sequencing. Using advanced bioinformatic tools, sgRNA distribution is analyzed and compared to that of the reference plasmid. Illustration generated with Biorender.com.

Unraveling context-specific genetic vulnerabilities has helped to gain a more profound understanding of signaling pathways and biological processes enriched in cancer cells and therefore, prioritize candidate therapeutic targets for different malignancies (Hart et al., 2015, Behan et al., 2019). A multitude of cancer cell lines have been screened with genome-wide CRISPR-based knockout libraries (e.g. DepMap project), revealing genetic vulnerabilities in different tumor entities (Cheung et al., 2011, Tzelepis et al., 2016, Hart et al., 2015, Wang et al., 2017, Wang et al., 2015a, Doench et al., 2016). Although the majority of genetic screens are performed *in vitro*, CRISPR screens can also be applied *in vivo*. Such screens can be performed either indirectly, enabling study of human rather animal cells, or directly, where perturbations are introduced directly into the living animal, thereby unraveling complex biological processes in physiological conditions (Chen et al., 2015, Cai et al., 2020, Dong et al., 2019, Bajaj et al., 2020, Yau et al., 2017, Chow et al., 2017, Kuhn et al., 2021). Despite the technical challenges, both *in vivo* and *in vitro* screens have similar screening parameters including library representation, and share the same readout, which refers to the relative abundance of sgRNAs, thus offering the opportunity to identify unique genetic dependencies through *in vivo* screens left uncovered by *in vitro* screens (Kuhn et al., 2021).

1.3.3 CRISPR-based chemogenetic screens

In addition to unraveling gene essentialities in cancer cells, other applications of functional genomics include chemogenetic genome-wide CRISPR-Cas9 screens, which allow identification of genetic perturbations that mediate the phenotype of interest under drug treatment. In principle, CRISPR-based knockout libraries are employed to screen for synthetic lethal/synergistic interactors, whose loss-of-function sensitizes cancer cells to known pharmacological inhibitors (Estoppey et al., 2017, Sulahian et al., 2019, Wang et al., 2019b, Walter et al., 2024, Chen et al., 2021), thereby providing new avenues in cancer therapy that involve combination drug treatments (Huang et al., 2020).

On the other hand, positive selection screens are commonly applied to identify mediators of drug resistance. The readout of these screens is the abundance of sgRNAs, which are enriched in the remaining cell population. Both knockout and activation genome-wide CRISPR-Cas9 screens are employed in cancer cells, in order to decipher candidate genes whose loss- or gain-of-function, respectively, confers resistance to drug treatment, thus elucidating underlying molecular

mechanisms driving resistance to known cancer drugs (Wang et al., 2014, Shalem et al., 2014, Konermann et al., 2015, Hou et al., 2017).

1.4 Scientific objectives

SHH pathway inhibition by targeting SMO has emerged as a promising targeted therapy for SHH-MB patients. Despite observed anti-tumor effects, primary or acquired resistance to therapy has limited the clinical efficacy of SMO inhibition. Thus, it is of utmost importance that novel, less toxic treatment strategies are tailored that will be efficacious in SMO inhibition-sensitive, as well as resistant SHH-MB tumors. Unraveling novel therapeutic targets for SHH-MB, potentially beyond the SHH pathway, that will overcome development of therapy resistance belongs to the scope of this research study.

The first aim of this thesis was to characterize two previously described model systems of MB, murine SMB21 and human DAOY cells. To this end, genome-scale CRISPR-Cas9 knockout screens were employed, in order to unravel genetic vulnerabilities of both cell models. By directly comparing screening data from both cell lines, their reliability as SHH-representative MB model systems was thoroughly delineated.

This study further proceeds with the most suitable SHH-MB model, SMB21, as identified at the first part. The next chapter of this thesis deals with investigating members of the epigenetic machinery as SMB21-specific essentialities, as revealed by functional genomics.

In particular, this study focuses on validating DNA methyltrasnferase1 DNMT1 as a novel therapeutic target for SHH-MB, using an FDA-approved hypomethylating drug, 5-Azacyitidine (5-AzaC). By performing large-scale omics analyses, a better understanding of epigenetic and transcriptomic effects of DNMT1 inhibition on SHH pathway output is acquired. Additionally, novel synergistic partners for 5-AzaC were aimed to be deciphered via a CRISPR-Cas9 knockout drug screen. These findings are further translated using preclinical mouse models of SHH-MB, as well as MB patient-derived xenograft organoids (PDXOs).

The final part of this thesis focuses on describing chromatin remodeler *Smarca5* as an SMB21-context specific dependency. By conducting genetic ablation experiments in mouse models, the critical role of *Smarca5* in the development of cerebellum, as well as pathogenesis of GCNP-derived SHH-MB is histologically addressed *in vivo*.

2 Materials & Methods

2.1 *In vitro* studies

2.1.1 Cell lines

SMB21, SMB55 and SMB56 cell lines were derived from spontaneous SHH-MB tumors in *Ptch1*$^{+/-}$ mice, as previously described (Zhao et al., 2015) and specifically, they originate from three individual *Ptch1*$^{+/-}$ mice (Personal communication with Dr. Rosalind Segal, Dana-Farber Cancer Institute, Boston, USA). All three cell lines retain SHH-MB hallmark features, as corroborated by constitutive active SHH signaling, expression of markers such as Math1, as well as transcriptional profiling. Additionally, they are characterized by dysregulated p53 signaling. SMB21 *Sufu* KO and SMB21 Gli2ΔN cells are SMB21 derivatives with loss of *Sufu* and *Gli2* amplifications, respectively, and are both described as SMO-inhibition resistant cell models (Zhao et al., 2015, Zhao et al., 2017). All SMB cell lines were kindly provided by Dr. Rosalind Segal. SMB cells are suspension cells that grow as neurospheres in ultra-low attachment culture flasks (Corning, Glendale, Arizona, United Stated of America, USA) and were cultured in Dulbecco´s Modified Eagle´s Medium/Ham´s F-12 50/50 Mix Medium (DMEM/F12) (15-090-CV, Corning, Glendale, Arizona, USA) supplemented with 2% B27 and vitamin A (Thermo Fisher Scientific Inc., Waltham, Massachusetts, USA), 1% GlutaMAX™ (Thermo Fisher Scientific Inc., Waltham, Massachusetts, USA) and 1% penicillin/streptomycin (Thermo Fisher Scientific Inc., Waltham, Massachusetts, USA).

Human pediatric MB cell line DAOY is adherent and is cultured in Roswell Memorial Institute Medium (RPMI) (Thermo Fisher Scientific Inc., Waltham, Massachusetts, USA) supplemented with 10% fetal calf serum (Thermo Fisher Scientific Inc., Waltham, Massachusetts, USA) and 50µg/ml gentamycin (Thermo Fisher Scientific Inc., Waltham, Massachusetts, USA). DAOY cells were purchased from American Type Culture Collection (ATCC, Manassas, Virginia, USA).

Human embryonic kidney cells HEK-293FT (#R70007, Thermo Fisher Scientific Inc., Waltham, Massachusetts, USA) grow adherent and are cultured in Dulbecco´s Modified Eagle´s Medium (DMEM) (Thermo Fisher Scientific Inc., Waltham, Massachusetts, USA) supplemented with 10% fetal calf serum (Thermo Fisher Scientific Inc., Waltham, Massachusetts, USA) and 50µg/ml gentamycin (Thermo Fisher Scientific Inc., Waltham, Massachusetts, USA).

At each passage, cells were first washed with phosphate-buffered saline (PBS) (Thermo Fisher Scientific Inc., Waltham, Massachusetts, USA), dissociated with accutase® solution (Sigma-Aldrich, Burlington, Massachusetts, USA) for 5 minutes and centrifuged (Eppendorf Centrifuge 5920R, Hamburg, Germany) for 5 minutes. SMBs were centrifuged at 700 revolutions per minute

(rpm), while DAOY and HEK-293FT cells at 1200 rpm. Cells were quantified using an Automated Cell Counter (TC20, Bio-Rad Laboratories, Hercules, California, USA) and finally, seeded back to the culture flask at their optimal density. Cells were renewed after 10-15 passages. All cell lines were kept at 37°C humidity-controlled incubator with 5% CO_2 and were regularly tested for mycoplasma contamination.

2.1.1.1 Patient-derived xenografts organoids

Patient-derived xenografts organoids (PDXOs) representing SHH-MB (MED1712), are *CDKN2A/B* amplified and have a *PTCH1* depletion, while Group 3-MB PDXOs (HT0pGF1) are *MYC* amplified, as previously characterized (Lago et al., 2023). All PDXOs were maintained in patient-derived organoids medium (PDOs medium) containing 1:1 Neurobasal (Thermo Fisher Scientific Inc., Waltham, Massachusetts, USA) and DMEM/F12 (Thermo Fisher Scientific Inc., Waltham, Massachusetts, USA) supplemented with 50X B27 (Thermo Fisher Scientific Inc., Waltham, Massachusetts, USA), 100X GlutaMax (Thermo Fisher Scientific Inc., Waltham, Massachusetts, USA), 100X N2 supplement (Thermo Fisher Scientific Inc., Waltham, Massachusetts, USA), 20 ng/ml FGF2 (PeproTech, Cranbury, New Jersey, USA), 20 ng/ml EGF (PeproTech, Cranbury, New Jersey, USA), penicillin (100 U/ml)/streptomycin (100 µg/ml) (Thermo Fisher Scientific Inc., Waltham, Massachusetts, USA), and 2.5 µg/ml Heparin (Sigma-Aldrich, Burlington, Massachusetts, USA). PDXOs were cultured in 6-cm/10-cm plates in suspension in PDOs medium on an orbital shaker (70 rpm) placed in a 37°C humidity-controlled incubator with 5% CO_2. Twice per week a complete medium change was performed. PDXOs cultures were regularly tested for mycoplasma contamination. All PDXOs were cultured at the Armenise-Harvard Laboratory of Brain Disorders and Cancer in University of Trento in Italy in the group of Dr. Luca Tiberi.

2.1.1.2 Cell optimization studies

Several parameters had to be pre-determined for SMB and DAOY cell lines used for subsequent experimental analyses. First, the optimal seeding density was optimized. Briefly, cells were seeded at different densities in 96-well plates and 20µl of CellTiter-Blue® Reagent (Promega Corporation, Madison, Wisconsin, USA) was added on the cells at 0 and 96 hours, in order to measure viability using GloMax® Discover microplate reader (Promega Corporation, Madison, Wisconsin, USA). The lowest doubling time needed to achieve high cell viability was chosen for each cell line, while for adherent cells an approximately 100% confluence after 96 hours was also

taken into consideration (**Table 1**). Doubling time was calculated using the following formula: LN(2)/(LN(N_{96}/N_0)/96); N_0= cell viability at 0 time point and N_{96}= cell viability after 96 hours.

Cell line	Seeding density	Doubling time (hours)
SMB21	200,000/ml	28.69
SMB55	200,000/ml	36.61
SMB56	200,000/ml	29.77
SMB21 *Sufu* KO	200,000/ml	44.37
SMB21 Gli2ΔN	200,000/ml	37
DAOY	5,000/cm^2	26

Table 1. Optimal seeding density and corresponding doubling time per medulloblastoma cell line.

Additionally, prior to viral transductions conducted in SMB and DAOY cells, the right dose of polybrene and puromycin had to be tested in each cell line (Broad Institute´s protocol modified, Massachusetts Institute of Technology and Harvard, USA). First, 3x10^6 cells were seeded in 2ml medium per well of a 12-well plate supplemented with 0, 4 or 8µg/ml polybrene (Santa Cruz Biotechnology, Dallas, Texas, USA). The plates were centrifuged for 2 hours at 930g. After centrifugation, 2ml of medium was added in each well and cells were incubated overnight. The next day, following cell counting, each well was seeded in triplicate 6-well plates corresponding to 0, 4 and 8µg/ml polybrene at their optimal cell density. After 24 hours, each well was treated with different concentrations of puromycin (Sigma-Aldrich, Burlington, Massachusetts, USA) of 0, 0.5, 1, 1.5, 2 and 4µg/ml, respectively. Cell viability was determined 5 days post puromycin treatment. The highest polybrene concentration that resulted in less than 10% cell toxicity compared to no polybrene was 4µg/ml for SMB cells and 8µg/ml for DAOY. The lowest concentration of puromycin that caused complete death was 0.5µg/ml for SMB and 0.65µg/ml for DAOY.

Last but not least, a range of blasticidin S HCL (Thermo Fisher Scientific Inc., Waltham, Massachusetts, USA) concentrations (2.5, 5, 7.5, 10 and 12.5µg/ml) was tested on SMB21 cells. The lowest blasticidin concentration that induced cell death in SMB21 cells was 10µg/ml.

2.1.2 Genome-wide CRISPR-Cas9 knockout screens

2.1.2.1 Lentivirus titration

Prior to the screens, the optimal lentiviral titers that yield approximately a 30% transduction rate had to be tested. For that, 3x10^6 Cas9-expressing SMB21 cells and 3x10^6 DAOY cells were seeded in 2ml per well supplemented with polybrene in 12-well plates and transduced by

spinfection with different volumes of murine Brie (#73633, Addgene, Watertown, Massachusetts, USA) and human Brunello (#73178, Addgene, Watertown, Massachusetts, USA) libraries, respectively. Viruses were filtered using 0.45μm Millex PVDF syringe filter (Sigma-Aldrich, Burlington, Massachusetts, USA) in advance. Plates were centrifuged at 930g for 2 hours at 30^{o}C and afterwards 2 ml of medium was added to the cells. The next day, cells were seeded at their optimal densities in duplicate 6-well plates and one replicate from each condition was selected with puromycin. Three days post selection, cells were counted and transduction rates were calculated by dividing the cell number from replicate treated with puromycin by cell number from replicate without. 270μl and 125μl of lentiviral libraries resulted in transduction rates close to approximately 30% for SMB21-Cas9 cells and DAOY cells, respectively. These volumes were subsequently selected for the large-scale screenings described below.

2.1.2.2 CRISPR-Cas9 dependency screens methodology

Before SMB21 cells were screened with Brie library, they first had to be transduced with lentiviral lentiCas9-Blast (#52962, Addgene, Watertown, Massachusetts, USA). Cells were transduced by spinfection, as described earlier and selected with 10μg/ml blasticidin. SMB21-Cas9 expressing cells were validated via western blotting analysis (**Supplementary figure 2**). In contrast to SMB21 cells, DAOY cells were transduced with all-in-one Brunello library, which delivers both sgRNAs and Cas9 enzyme to the cells.

SMB21-Cas9 cells were screened with murine CRISPR-Cas9 knockout pooled library, Brie (#73633, Addgene, Watertown, Massachusetts, USA) (Doench et al., 2016), which provides 78,637 different sgRNAs targeting murine 19,674 genes. DAOY cells were screened with corresponding human CRISPR-Cas9 knockout library, Brunello (#73178, Addgene, Watertown, Massachusetts, USA) (Doench et al., 2016), which delivers 76,441 different sgRNAs targeting 19,114 human genes. Both cell lines were transduced by spinfection with pretested volume of filtered lentiviruses and centrifuged at 930g for 2 hours at 30^{o}C. The next day, cells were divided into 3 technical replicates and 48 hours post transduction, cells were selected with puromycin for 5 days. An in-line assay was performed in parallel, in order to approximately calculate the transduction efficiency of the ongoing screening. For that, non-infected cells and cells from all three replicates were seeded in duplicate 6-well plates and one replicate was selected with puromycin. Transduction rate was calculated 5 days post selection. Cells were propagated in culture for 21 days and at each passaging 40x10^6 cells per replicate were seeded, estimated to maintain a 500x library coverage, in order for each sgRNA to be present on average in 500 cells.

At the last day of the screens, 40-60x10^6 cell pellets per replicate collected in 50ml falcon tubes were frozen in liquid nitrogen and stored at -80^{o}C until DNA isolation.

2.1.2.3 Drug sensitivity assay

For the drug screen performed in SMB21 cells, the optimal concentration of 5-AzaC (Selleck Chemicals GmbH, Cologne, Germany) had to be determined, for it to have a cytostatic effect. Therefore, SMB21-Cas9 cells were seeded at their optimized density in T-75 ultra-low attachment flasks and the following day, they were treated with different concentrations of 5-AzaC ranging from 300nM to 1.5μM, as well as corresponding DMSO (dimethyl sulfoxide, AppliChem GmbH, Darmstadt, Germany) control (ctr). Total cell numbers were determined at day 4, 9 and 14 post treatment. At each counting, cells were passaged at their optimized density under the same drug condition. 300nM 5-AzaC was selected for the drug screen.

2.1.2.4 Chemogenetic CRISPR-Cas9 screen methodology

Similar to the dependency screen, 216x10^6 SMB21-Cas9 cells were seeded in 12-well plates and transduced with pre-determined volume of Brie library (#73633, Addgene, Waterdown, Massachusetts, USA). Plates were centrifuged at 930g for 2 hours at 30^{o}C. After centrifugation, 2 ml medium was added to the cells and they were incubated overnight. The next day, following cell counting, all cells were seeded at their optimal density in ultra-low attachment chambers (Corning) and selected with puromycin for 5 days. In parallel, an in-line assay was conducted, in order to ensure efficient transduction rate. After puromycin selection, cells were split into DMSO control and 5-AzaC arms in duplicates and treated the next day with 300nM 5-AzaC and corresponding DMSO. Drug treatment lasted 15 days and 40x10^6 cells per replicate from each condition were passaged every 3-5 days, maintaining a 500x library coverage. At the last day of the screen, all cells from each replicate were collected in 50ml falcon tubes, frozen in liquid nitrogen and stored at -80^{o}C until DNA extraction was performed.

2.1.2.5 DNA sample preparation

Isolation of genomic DNA from cell pellets frozen on the last day of the screen was performed using QIAamp DNA Blood Maxi Kit (Qiagen, Venlo, Netherlands) suitable for samples containing 3x10^7-10^8 cells. The protocol followed was adapted form Broad Institute. Eluted DNA was measured on Thermo Scientific Nanodrop 2000 UV-Vis Spectrophotometer (Thermo Fisher

Scientific Inc., Waltham, Massachusetts, USA) and DNA from each replicate was distributed in DNAase- and RNAase-free 96-well PCR plates (Thermo Fisher Scientific Inc., Waltham, Massachusetts, USA). Approximately 10µg DNA in 50µl volume per well was prepared. All samples were subjected for PCR amplification and Next Generation Sequencing at the Broad Institute at MIT (Cambridge, Massachusetts, USA).

2.1.2.6 CRISPR-Cas9 screens analysis

For the downstream comparative analysis of SMB21 and DAOY dependency screens, murine genes were converted to homologous human gene names. First, both dependency screens were analyzed using *CRISPRcleanR* package. This computational approach detects gene-independent responses to CRISPR-Cas9 targeting in an unsupervised manner by correcting sgRNA $\log_2$ fold changes (LFC), thereby reducing false positive rates in identifying essential genes (Iorio et al., 2018). Then, dependency scores were computed by scaling corrected gene-level LFCs on the basis of pan-species non-essential and pan-essential control genes (Hart et al., 2014).

Additionally, we employed two distinct statistical methods to identify cell-specific essential genes. These included the Model-based Analysis of Genome-wide CRISPR-Cas9 knockout screen using a robust ranking aggregation algorithm (MAGeCK-RRA), which identifies both positively and negatively selected genes (Li et al., 2014), as well as the supervised Bayesian Analysis of Gene Essentiality (BAGEL2) algorithm, which calculates the likelihood for one gene to belong to essential or non-essential class, by computing Bayes Factor (Kim and Hart, 2021). Corrected sgRNA read counts and corrected sgRNA LFCs from *CRISPRcleanR* package were used as input for MAGeCK-RRA and BAGEL2, respectively. Negatively selected and essential genes shared by both methods, respectively, at false discovery rate (FDR) below 5% were considered as context-specific essentialities for each cell line screened.

Venn diagram of overlapping essential genes between the two cell lines were generated using *VennDiagram* package in the R statistical environment (Chen and Boutros, 2011). Enrichment analysis for gene ontology terms of shared essentialities between the two screens was performed on ShinyGO 8.0 (South Dakota State University, South Dakota, USA), while comparative gene enrichment analysis was conducted on R studio using *clusterProfiler* R package (Yu et al., 2012).

For the analysis of the knockout drug screen, the distribution of sgRNAs of 5-AzaC-treated cells was compared to both DMSO control arm, as well as reference plasmid using the Model-based Analysis of Genome-wide CRISPR-Cas9 knockout screen algorithm by a maximum likelihood estimation method (MAGeCK-MLE), which estimates gene essentiality (Li et al., 2015). Raw read

counts from all sgRNAs, as well as a list of negative control sgRNAs targeting non-coding genes were used as an input to MAGeCK-MLE (Python programming language). For each gene per condition a β score indicative of the degree of selection was calculated. To account for inconsistencies in cell cycle among different conditions, β scores were normalized based on known essential genes that are indispensable for cell survival. Screen data were analyzed and visualized using *MAGeCKFlute* R package (Wang et al., 2019a).

2.1.3 *In vitro* drug assays

2.1.3.1 Growth rate inhibition

To evaluate the potency of drugs of interest on cell viability, acute cytotoxic colorimetric assays were performed. Cells were seeded at their optimal density in triplicates in 50µl/well in 96-well plates. The next day, serial dilutions of 14 concentrations of the drug of interest were prepared in corresponding medium (**Figure 6**). An additional 50µl of concentrated drug was instilled into the wells, corresponding to final concentrations ranging from 0.01nM to 50µM. DMSO-treated cells were used as control. 72 hours post drug treatment, cells were stained with 20µl CellTiter-Blue Reagent for 4 hours and were measured on GloMax®. Wells containing only 100µl of corresponding medium were used to subtract background signal.

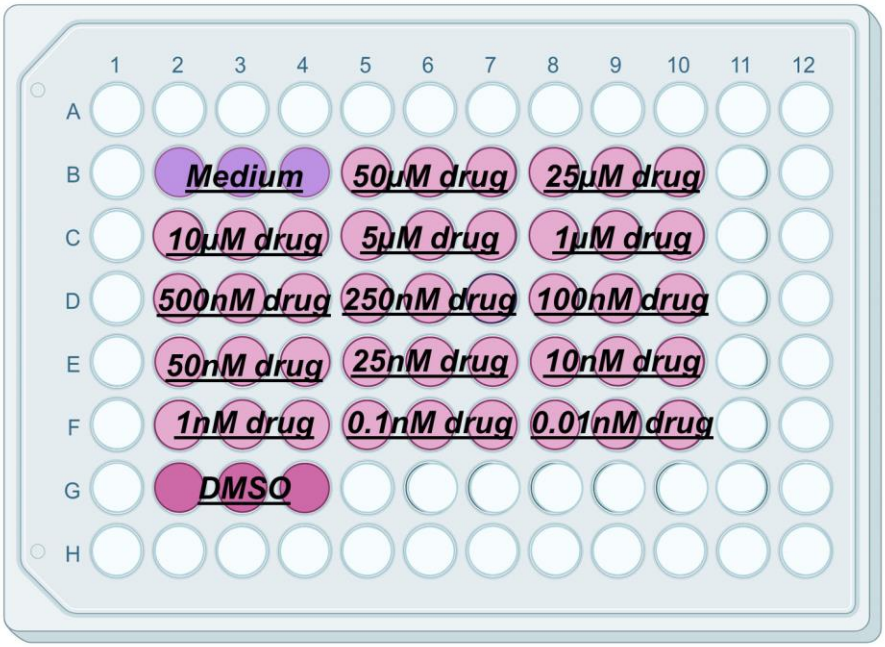

Figure 6. Dose-response assay template. Cells were treated with serial dilutions of 14 different concentrations of drug of interest ranging from 0.01nM to 50µM. 3 wells contained only medium, while DMSO-treated cells were used as controls. The surrounding wells are filled with PBS. Illustration generated with Biorender.com.

To compensate for the confounding effects of different division rates among cell lines on drug response, cell viability was measured as normalized growth rate inhibition (GRi) using *GRmetrics* R package (Hafner et al., 2016). GR values compute the ratio between growth rates under treated and untreated conditions normalized to a single cell division and range from -1 to 1. Values between -1 and 0 indicate cell death, equal to 0 cytotoxic drug effect and between 0 to 1 partial growth inhibition. GR_{50} values indicate the efficacy of the drug, referring to the concentration at which cell viability is half of the control, while GR_{max} is the maximal measured GR value, representing drug potency.

All the compounds tested on cells were purchased from Selleck Chemicals GmbH and dissolved in DMSO according to the manufacturer´s recommendations: 5-AzaC (Batch # S178207), SGI-1027 (Batch # S727601), LDE-225 (Batch # S215102) and GDC-0449 (Batch # S108210).

2.1.3.2 Drug synergy assay

To evaluate potential synergistic effects between 5-AzaC and LDE-225, acute cytotoxic synergy assays were performed. Cells were seeded at their optimal density in triplicates in 50µl/well in 96-

well plates. The next day, cells were treated with 4 different concentrations of each drug, as well as 16 concentration combinations of both drugs. The tested concentrations for 5-Azacytidine were 0.5, 1, 5 and 10μM were tested, while for LDE-225 5, 10, 20 and 100nM. For the monotherapies, 50μl of concentrated drug were added to the wells, while for the combinations, 25μl of each concentrated drug. DMSO-treated wells were used to normalize the data. After 72 hours of treatment, 20μl of CellTiter-Blue Reagent was added to each well for 4 hours and cell viability was measured using GloMax®.

For the analysis of drug combinations, synergy scores were calculated based on the zero interaction potency model (ZIP) and synergy plots were visualized using *Synergyfinder* R package (Zheng et al., 2022).

2.1.3.3 Drug proliferation assay

Cell proliferation assays under drug treatments were performed over the course of 8 days. SMB cells were seeded in their optimal density in triplicates in 2ml per well in ultra-low attachment 6-well plates. 2ml of concentrated drugs or corresponding DMSO control were added into each well. Drug treatments involved 5-AzaC monotherapy, LDE-225 monotherapy and combination of both inhibitors. SMB21 cells were treated with 600nM 5-AzaC and 100nM LDE-225, while SMB21 *Sufu* KO cells were treated with 500nM and 10nM, respectively. Four days post seeding, cells were counted and reseeded back at their optimal density under the same drug conditions and finally counted again after 4 days.

For the proliferation assay assessing sequential treatment of both inhibitors, SMB21 cells were either treated first with 5-AzaC for 4 days and then with LDE-225 monotherapy for another 4 days, or first with LDE-225 followed by 5-AzaC monotherapy. After treated for 48 hours, cells were quantified at day 4 and 8.

2.1.3.4 PDXOs drug treatment assays

All drug assays in PDXOs were conducted in a time period of 7 days. Cells were cultured in PDOs medium and treated with 10μM 5-AzaC, 1μM LDE-225 or combination of both drugs. DMSO-treated cells were used as a control. PDXOs were kept in Ibidi uncoated 96-well black μ-plates (Ibidi, Graefelfing, Germany) and medium supplemented with corresponding drugs was replenished every 48 hours. All experiments were conducted at the Armenise-Harvard Laboratory of Brain Disorders and Cancer in Italy in the group of Dr. Luca Tiberi.

2.1.3.5 Histological preparation of PDXOs

PDXOs were fixed in 4% paraformaldehyde (PFA) in PBS at 4°C overnight, cryoprotected in 30% sucrose in distilled H_2O at 4°C overnight and finally embedded in Frozen Section Compound (Leica, 3801480) and stored at -20°C until processing. Organoids were sectioned at 20 µm thickness using a cryostat (Thermo Scientific HM525 NX) and slides were stored at -20°C until immunohistology.

For immunofluorescence staining of PDXOs, cryosections were treated with a permeabilization solution containing PBS supplemented with 3% BSA (Seqens/H2B, 033IDB1000-70), 0.3% Triton™ X100 (Sigma-Aldrich, Burlington, Massachusetts, USA) and 5% goat serum (Thermo Fisher Scientific Inc., Waltham, Massachusetts, USA) for 1 hour at room temperature (RT). Rabbit polyclonal anti- Ki67 (ab15580, Abcam Limited) was diluted at 1: 500 in PBS supplemented with 3% BSA (Seqens/H2B, 033IDB1000-70), 0.1% Triton™ X100 (Sigma-Aldrich, Burlington, Massachusetts, USA) and 1% goat serum (Thermo Fisher Scientific Inc., Waltham, Massachusetts, USA). Incubation took place overnight at 4°C. The next day, secondary Alexa Fluor 546 goat anti-rabbit IgG antibody (A11035, (Thermo Fisher Scientific Inc., Waltham, Massachusetts, USA) was diluted at 1:500 in the same antibody solution and added on the slides for 1 hour at RT. Nuclei were counterstained with 10 mM DAPI (ab228549, Abcam Limited). All histological experiments were performed at the Armenise-Harvard Laboratory of Brain Disorders and Cancer in Italy in the group of Dr. Luca Tiberi.

2.1.3.6 Flow cytometry

Cell cycle analysis in SMB cells was performed by flow cytometry. For that, SMB21 and SMB55 cells were seeded at their optimal density in 5ml of ultra-low attachment T-25 flasks and the following day they were treated with their corresponding GR_{50} values of 5-AzaC and DMSO control. Following drug treatment for 48 hours, cells were prepared for propidium iodide staining.

After dissociating cells with accutase and centrifuging them, cell pellets were washed twice with sample buffer containing 1g/L glucose (Roth, Karlsruhe, Germany) in PBS and centrifuged at 700g for 5 minutes. Pellets were then resuspended with 1ml sample buffer and 4ml ice-cold absolute ethanol (AppliChem GmbH, Darmstadt, Germany) (-20^{o}C) was carefully added to the cells. Cells were incubated for 15 minutes at -20^{o}C and then centrifuged for 5 minutes. Following another wash with sample buffer for 15 minutes at RT and a last centrifugation, the staining solution was

added to the cells for 15 minutes at RT. Each sample was stained with 300µl solution containing 50 µg/ml propidium iodide (Thermo Fisher Scientific Inc., Waltham, Massachusetts, USA), 0.2% Triton X-100 (Thermo Fisher Scientific Inc., Waltham, Massachusetts, USA) and 100µg RNAase (Thermo Fisher Scientific Inc., Waltham, Massachusetts, USA) diluted in sample buffer.

Samples were subjected to measurement on MACSQuant Analyzer 10 (Miltenyi Biotec GmbH, Bergisch Gladbach, Germany). First, cells were passed through forward and side scatters, in order to identify single cells. DNA-bound propidium iodide was detected using B3-A channel and percentage of cell population in each phase of cell cycle was measured (G_1, S and G2/M transition). Data were analyzed and visualized using FlowJo_V10 software (FlowJo, Ashland Global, Wilmington, Delaware, USA).

2.1.4 Genetic validation experiments

2.1.4.1 Cloning of sgRNAs

In order to generate knockdowns of *Smo*, *Dnmt1* and *Smarca5*, sgRNA target sequences from Brie library (Doench et al., 2016) were used for cloning: GAACTCCAATCGCTACCCTG, ACCTCGGGCCAATCAATCAG and ATGCTTCAAATGATTCGACA, respectively. sgRNA oligonucleotide pairs cloned into lentiviral lentiCRISPRv2 puro vector (#98290, Addgene, Waterdown, Massachusetts, USA) were designed according to manufacturer´s instructions (**Table 2**).

Targeted gene	Forward primer (5´-3´)	Reverse primer (5´-3´)
Smo	CACCGGAACTCCAATCGCTACCCTG	AAACCAGGGTAGCGATTGGAGTTCC
Dnmt1	CACCGACCTCGGGCCAATCAATCAG	AAACCTGATTGATTGGCCCGAGGTC
Smarca5	CACCGATGCTTCAAATGATTCGACA	AAACTGTCGAATCATTTGAAGCATC

Table 2. Sequence of single guide RNA oligonucleotide primer pairs. All oligos were purchased from Sigma-Aldrich (Munich, Germany).

Cloning procedure was adapted from Addgene´s recommended protocol. First, 3µg lentiCRISPRv2 vector was digested with 1µl restriction enzyme BsmBI-v2 (R0739S, New England Biolabs, Ipswich, Massachusetts, USA) in 5µl NEB 3.1 Buffer (New England Biolabs, Ipswich, Massachusetts) and nuclease-free water (Thermo Fisher Scientific Inc., Waltham, Massachusetts, USA) in a total volume of 50µl. Digestion took place overnight at 55ºC on a thermoblock

(ThermoMixer® comfort, Eppendorf, Hamburg, Germany). Digested vector was loaded in 1% agarose gel (Lonza Group AG, Basel, Switzerland) dissolved in 1x TAE buffer (PanReac-AppliChem ITW Reagents GmbH, Darmstadt, Germany) and DNA was purified using QIAquick Gel Extraction Kit (Qiagen, Venlo, Netherlands) according to manufacturer´s instructions. Eluted DNA was measured on Nanodrop. In the meantime, each pair of oligonucleotides (20µM each) was annealed in 20µl total volume containing 2µl of 10X T4 Ligation Buffer (B0202S, New England Biolabs, Ipswich, Massachusetts, USA) and nuclease-free water. Oligos were initially incubated for 4 minutes at 95ºC in a water bath (Phoenix Instrument, Garbsen, Germany) and then slowly cooled down to RT over the period of several hours, after switching off the machine. Afterwards, 50ng of digested plasmid was ligated to 1:200 diluted annealed oligo pairs in a 20µl reaction mix consisting of 0.8µl T4 DNA Ligase (M0202S, New England Biolabs, Ipswich, Massachusetts, USA), 1.2µl 10X T4 DNA Ligase Buffer and nuclease-free water. Ligation reaction was performed overnight at 16ºC.

One Shot Stbl3 Chemically Competent *Escherichia coli* bacteria (Thermo Fisher Scientific Inc., Waltham, Massachusetts, USA) were transformed with 2µl ligation product and incubated on ice for 30 minutes. After heat-shocking the cells for 45 seconds at 42ºC and incubating them for another 2 minutes on ice, 250µl of S.O.C. medium (Thermo Fisher Scientific Inc., Waltham, Massachusetts, USA) was added and bacteria were shaken at 37ºC for 1 hour at 225 rpm at a horizontal position. 90µl of transformed bacteria were spread on LB agar (Sigma-Aldrich, Burlington, Massachusetts, USA) plates containing 100mg/ml ampicillin (AppliChem, Darmstadt, Germany) and incubated overnight at 37ºC. The next day, colonies were selected and cultured overnight at 37ºC in 5ml LB medium with 1:1000 ampicillin. Using the QIAprep Spin Miniprep Kit (Qiagen, Venlo, Netherlands), DNA was extracted and finally was subjected to sequencing at Eurofins Genomics facility (Tuebingen, Germany). Sequencing analysis was performed on BioEdit Sequence Alignment Editor.

2.1.4.2 Virus production

The day before transfection, HEK293FT cells were seeded at approximately 30% confluence in DMEM medium and 10% fetal calf serum. The next afternoon, medium was replaced by Opti-MEM™ I Reduced Serum Medium (Thermo Fisher Scientific Inc., Waltham, Massachusetts, USA) and approximately 2 hours later, cells were transfected using Lipofectamine 3000 Transfection Reagent (Thermo Fisher Scientific Inc., Waltham, Massachusetts, USA). For this procedure, one master mix was prepared consisting of 10µg of lentiCRISPRv2-sgRNA plasmid, equimolar

concentrations of packaging plasmids psPAX2 (#12260, Addgene, Watertown, Massachusetts, USA) and pMD2.G (#12259, Addgene, Watertown, Massachusetts, USA) and 50μl P3000 in 700μl Opti-MEM™ medium. A second mix contained 29μl lipofectamine in 700μl Opti-MEM™ medium. The first reaction was added to the second one, the solution was mixed well and incubated for 5 minutes. Then, transfection reagents were added to HKE293FT cells and cells were incubated overnight.

The next day, the medium was changed to DMEM/F12 medium. After 48 hours, the medium was collected in 15ml falcons, centrifuged for 5 minutes at 1200 rpm and filtered through a 0.45μm Millex PVDF syringe filter. Finally, the produced virus was stored at -80ºC until further use.

2.1.4.3 Cell transduction

SMB cells were transduced with lentiCRISPRv2-sgRNA plasmids by means of spinfection. In particular, $3x10^6$ cells were seeded in 2ml per well supplemented with 4μg/ml polybrene in 12-well plates and approximately 500μl virus was added on the wells. One well with no virus was used as non-infected control. Plates were centrifuged for 2 hours at 930g at 30ºC and afterwards, 2ml medium was added on top. Cells were incubated overnight. The next morning, cells were counted and seeded at their optimal density in flasks under 0.5μl/ml puromycin. Selection ran for 3 to 5 days, until non-infected cells were all dead.

2.1.4.4 Proliferation assay

Following selection with puromycin, SMB21 sgRNA-transduced cells were seeded in triplicates at their optimal density in 100μl/well in 96-well plates. Viability was determined at day 0, 3 and 7, by staining cells with CellTiter-Blue Reagent and conducting cell measurements using GloMax®. SMB21 parental cells were used as a control.

2.1.5 DNA Methylation array

SMB21 and SMB55 cells were seeded at their optimal density in triplicate T-75 flasks. The next day, they were treated with 5-AzaC for 24 hours, as well as with DMSO control. 5-AzaC concentrations were selected based on their GR_{50} values, 3μM and 5μM for SMB21 and SMB55 cells, respectively. Genomic DNA was isolated from cells using QIAamp DNA Blood Mini Kit (Qiagen, Venlo, Netherlands) according to manufacturer´s instructions and eluted DNA concentration was measured on Nanodrop Spectrophotometer. Samples were subjected to

methylation profiling in the Microarray Unit in German Cancer Research Center (DKFZ, Heidelberg, Germany), using Infinium™ Mouse Methylation BeadChip with a > 285K CpGs coverage according to manufacturer´s streamlined workflow. Minimum DNA concentration per sample required for analysis was 12.5ng/µl in 40µl total volume.

Differential methylation analysis was performed using Sensible Step-wise Analysis of DNA Methylation Beadchips (*SeSAMe*) R package (Zhou et al., 2018). Principal component analysis and volcano plots were visualized using *ggplot2* and *factoextra* R packages. For each probe a β-score estimating methylation level was computed. Values below 0 indicated hypomethylation, while values above 0 hypermethylation. Significantly hypo- and hypermethylated probes were defined by setting a threshold of $|\beta \text{ value}| \geq 0.1$ and $p_{adj.} < 0.05$. All gene ontology enrichment analyses of significantly hypomethylated genes were performed in ShinyGO 8.0.

2.1.6 RNA sequencing

SMB21 cells were seeded at their optimal density in triplicate T-75 flasks. The following day, they were treated with 5-AzaC for 2 and 48 hours, as well as DMSO control for 48 hours. Similar to methylation profiling, GR_{50} value of 5-AzaC equal to 3µM was selected. RNA was extracted from cells using RNeasy Plus Mini Kit (Qiagen, Venlo, Netherlands) according to the company´s protocol and measured on Nanodrop Spectrophotometer. Minimum RNA concentration per sample required was 30ng/µl in 25µl total volume. Samples were subjected to RNA sequencing at the c.ATG genomics core facility (University Hospital of Tuebingen, Germany). Messenger RNA (mRNA) fraction was enriched using polyA capture from 200ng of total RNA using NEBNext Poly(A) mRNA Magnetic Isolation Module (New England Biolabs, Ipswich, Massachusetts, USA). Next, mRNA libraries were prepared using the NEB Next Ultra II Directional RNA Library Prep Kit for Illumina (NEB, New England Biolabs, Ipswich, Massachusetts, USA) according to manufacturer´s instructions. The libraries were sequenced as paired-end 50bp reads on Illumina NovaSeq6000 (Illumina) with a sequencing depth of approximately 25 million clusters per sample. RNA raw data quality control and processing were performed using megSAP (version 0.2-135-gd002274) combined with ngs-bits package (version 2019_11-42-gflb98e63). Reads were aligned using Spliced Transcripts Alignment to a Reference (STAR) RNA-seq read mapper (v2.7.3a).

Differential gene expression analysis was performed using *DESeq2* R package (Love et al., 2014). Differentially expressed genes (DEGs) fitting the criteria of $|LFC| \geq 0.58$ and $p_{adj} < 0.05$ were considered significant. Gene Set Enrichment Analysis (GSEA) was conducted on GSEAPreranked tool (Broad Institute, Massachusetts Institute of Technology and Harvard, USA),

for which genes were ranked based on their log_2fold (log2FC) change values. Gene sets with FDR < 25% were significantly enriched in our analysis. Venn diagrams illustrating overlapping up- and downregulated genes were generated using *VennDiagram* R package.

2.1.7 Protein detection and analysis

2.1.7.1 Protein lysates preparation

To harvest protein lysates from either cell pellets or brain tissue, samples were first washed with ice-cold PBS and then resuspended in RIPA Lysis and Extraction buffer (Thermo Fisher Scientific Inc., Waltham, Massachusetts, USA) with phosphatase inhibitors cocktail (1:100) (#5870, Cell Signaling Technology, Danvers, Massachusetts, USA). Approximately 100μl lysis buffer was prepared per $1x10^6$ cells. Samples were incubated on ice for 30 minutes and in the meantime, they were sonicated, in order to ensure DNA shearing and then vortexed every 10 minutes. Afterwards, they were centrifuged at 13,000 rpm for 30 minutes at 4^{o}C and supernatant was collected in 1.5ml eppendorfs and stored at -80^{o}C until future use.

2.1.7.2 Western blotting

First, approximately 40μg of protein lysates were mixed with NuPAGE LDS Sample Buffer (4x, Thermo Fisher Scientific Inc., Waltham, Massachusetts, USA) and incubated at 70^{o}C for 10 minutes. Then, 10-20μl protein samples were separated electrophoretically in NuPAGE Bis-Tris 4-12% gels (Thermo Fisher Scientific Inc., Waltham, Massachusetts, USA) under NuPAGE MOPS SDS Running Buffer (Thermo Fisher Scientific Inc., Waltham, Massachusetts, USA). Spectra Multicolor Broad Range Protein Ladder (Thermo Fihser Scientific, Waltham, Massachusetts, USA) was also loaded on the gel as a reference marker of molecular weights. Electrophoresis took place at 200 Volt for approximately 1.5 hours. Electrophoretic transfer of gels to nitrocellulose membranes (Thermo Fisher Scientific Inc., Waltham, Massachusetts, USA) took place at 25 Volt for 3 hours. Chambers were supplemented with transfer buffer containing 25mM Tris base and 192mM glycine in methanol (AppliChem GmbH, Darmstadt, Germany). In order to prevent non-specific binding of the detection antibodies, membranes were blocked with 5% nonfat dry milk (Carl Roth GmbH + Co KG, Karlsruhe, Germany) in Tris-Buffered Saline- 0.1% Tween-20 detergent buffer (TBS-T, PH = 7.6) for 1 hour at RT. Finally, membranes were incubated overnight with primary antibodies at 4^{o}C.

The next day, membranes were first washed with TBS-T three times for 10 minutes each and then incubated with anti-rabbit or anti-mouse IgG H&L (HRP-conjugated) secondary antibodies for 1

hour. Following more membrane washes with TBS-T for 1 hour, cheluminescence detection of protein bands was performed on ChemiDoc imaging device (Bio-Rad Laboratories, California, USA) using solution kit SuperSignal West Dura (Thermo Fisher Scientific Inc., Waltham, Massachusetts, USA). All primary and secondary antibodies used, and their specific usage properties are summarized on **Table 3**.

Antibody	Species	Dilution buffer	Dilution ratio	Company
β-tubulin	Mouse	5% milk in TBS-T	1:1000	#86298 (Cell Signaling Technology)
Cas9	Mouse	5% milk in TBS-T	1:1000	ab191468 (Abcam Limited)
GLI1	Rabbit	5% BSA in TBS-T	1:1000	#2534 (Cell Signaling Technology)
PCNA	Mouse	5% milk in TBS-T	1:2000	#2586 (Cell Signaling Technology)
SMARCA5	Rabbit	5% milk in TBS-T	1:2000	ab72499 (Abcam Limited)
Anti-rabbit IgG H&L	Goat	5% milk in TBS-T	1:5000	ab97051 (Abcam Limited)
Anti-mouse IgG H&L	Goat	5% milk in TBS-T	1:5000	ab97023 (Abcam Limited)

Table 3. List of all antibodies used for protein detection via western blotting.

Subsequent analysis of all acquired images was conducted on Image Lab software (Bio-Rad Laboratories, California, USA). In order to quantify GLI1 protein levels in SMB cells, ImageJ software (Java, Oracle Corporation, Santa Clara, California, USA) was used. Intensity signal from GLI1 protein bands were measured and divided by signal of corresponding β-tubulin protein bands of each sample. Protein levels were normalized to either parental cells or DMSO control-treated cells.

2.2 Experimental animal studies

2.2.1 Mouse strains

The following transgenic mouse lines were used for the *in vivo* studies (**Table 4**).

International nomenclature	Internal nomenclature	Description	Provided by
B6.Cg-Tg(Atoh1-cre)1Bfri/J	*Math1-Cre (MCre)*	Cre recombinase expression in cerebellar GCNPs under Math1 enhancer element (Matei et al., 2005)	Ulrich Schueller, University Hospital Hamburg, Germany
Tg(Atoh1-cre/Esr1*)14Fsh/J)	*Math1-Cre-ERT (Mert)*	Expression of inducible form of Cre recombinase under the control of Math1 enhancer (Machold and Fishell, 2005)	Ulrich Schueller, University Hospital Hamburg, Germany
Gt(ROSA)26Sor$^{tm1(Smo/EYFP)Amc}$/J	*SmoM2$^{Fl/Fl}$*	Constitutive active form of *Smo* with floxed stop codons (Mao et al., 2006)	Ulrich Schueller, University Hospital Hamburg, Germany
B6.129S4-Dnmt1^{tm2Jae}/Mmucd	*Dnmt1$^{Fl/Fl}$*	Genomic insertion of loxP sites in the locus of Dnmt1, expression of fluorescent-reporter gene dt Tomato (Jackson-Grusby et al., 2001)	Rudolph Jaenisch, Whitehead Institute, Cambridge, USA
Smarca5$^{tm2.1Ais}$	*Smarca5$^{Fl/Fl}$*	Genomic insertion of loxP sites in the locus of Smarca5 (Alvarez-Saavedra et al., 2014)	David Picketts, Ottawa Hospital Research Institute, Canada

Table 4. List of transgenic mouse lines.

All mice were maintained and bred in the animal facility of Hertie Insitute (FORS/HIH, Tuebingen, Germany) under a 12-hour dark/light cycle and regularly monitored for infectious diseases. Food and water were given *ad libitum* and animals of both sexes were used for all experiments.

All experimental procedures were approved by the regional council of Tuebingen and conducted according to animal welfare regulations (license # N10-21G).

2.2.1.1 DNA extraction and genotyping

For genotype verification through PCR, genomic DNA was isolated either from tail in newborn pups (P5) or ear biopsies in older mice (≥ P21). DNA extraction was performed using KAPA Mouse Genotyping Kit (KK7352, KAPA Biosystems Inc., Wilmington, Massachusetts, USA) and for each sample 100µl extraction solution was prepared containing 10µl 10x KAPA Express Extract Buffer, 2µl 10X KAPA Express Extract Enzyme and 88µl nuclease-free water. Biopsies were first lysed at 75ºC for 10 minutes at a thermoblock and enzyme inactivation was achieved at 95ºC for 5 minutes. Extracted DNA was diluted 10-fold prior to use as template in PCR and unless used immediately, it was stored at -20ºC for future use.

Each sample was prepared in 25µl PCR reaction made up of 12.5µl 2x KAPA2G Fast Genotyping Mix with Dye, 1.25µl 10µM forward primer (Sigma-Aldrich, Burlington, Massachusetts, USA), 1.25µl of 10µM reverse primer (Sigma-Aldrich, Burlington, Massachusetts, USA), 1µl of diluted genomic DNA and 6.5µl nuclease-free water. For each primer pair, different PCR cycling parameters were set up (Mastercycler® X50, Eppendorf, Hamburg, Germany). A list of primers used is presented on **Table 5**.

Primers	**Sequence 5´- 3´**	**PCR product length (bp)**
Smo wt- Fw	GGAGCGGGAGAAATGGATATG	410
Smo wt- Rev	CGTGATCTGCAACTCCAGTC	
Smo mutant- Fw	AAGTTCATCTGCACCACCG	490
Smo mutant- Rev	TGCTCAGGTAGTGGTTGTCG	
Cre- Fw	TCCGGGCTGCCACAGACCAA	448

Cre- Rev	GGCGCGGCAACACCATTTT	
Dnmt1- Fw	GGGCCAGTTGTGTGACTTGG	334 (wildtype),
Dnmt1- Rev	CTTGGGCCTGGATCTTGGGGA	368 (mutant)
Smarca5- Fw	GGCCAGCCCTGTCTTATATTT	1000 (wildtype),
Smarca5- Rev	CAAGCAAACAGACCTAAGTGTTG	800 (mutant)
mNtf- Fw	CTGAGTGACAGCACCCCTTT	100
mNtf- Rev	GTTTCCTCCGTGGTGAGGTT	

Table 5. List of primers used for genotyping. Forward (fw) and reverse (Rev) sequences per primer pairs are listed. mNtf primer pair was used as a control.

PCR products were analysed by agarose gel electrophoresis. 1% agarose gels diluted in 1x TAE buffer were prepared and ran at 100 Volt for 1 hour and 30 minutes (PowerEase 90W Power Supply, Thermo Fisher Scientific Inc., Waltham, Massachusetts, USA). Bands were visualized on ChemiDoc imaging machine (Bio-Rad Laboratories, California, USA).

2.2.1.2 Conditional knockout mice

For the genetic validation experiments, Cre-expressing mice were bred with “floxed” mouse strains containing paired loxP sites under the control of Math1 promoter, thus generating the genotype of interest.

In order to investigate *Dnmt1* ablation during cerebellar development, *Dnmt1*$^{Fl/Fl}$ mice with loxP sites flanking exons 4 and 5 were bred with *Math1-cre* mice resulting in an out-of-frame splice from exon 3 to exon 6 of *Dnmt1*, leading to a truncated mRNA encoding the first 67 amino acids of the protein in GCNPs (Jackson-Grusby et al., 2001). These offspring, *Math1-cre::Dnmt1*$^{Fl/+}$ mice, were mated with *Dnmt1*$^{Fl/Fl}$ mice, in order to generate animals of genetic background *Math1-cre::Dnmt1*$^{Fl/+}$ and *Math1-cre::Dnmt1*$^{Fl/Fl}$. Animals were sacrificed at P5 and P21 and their brains were analysed histologically. *Math1-cre* mice were used as a control group. For the genetic validation experiments during SHH-MB development, *Math1-cre::Dnmt1*$^{Fl/+}$ mice were instead bred with *Smo*$^{Fl/Fl}$ mice, resulting *in Math1-cre::Dnmt1*$^{Fl/+}$*::SmoM2*$^{Fl/+}$ and *Math1-cre::Dnmt1*$^{Fl/Fl}$*::SmoM2*$^{Fl/+}$ mice. These animals were either sacrificed at P5 or closely monitored for clinical symptoms according to a stringent scoring sheet (**Supplementary Table 1**) and sacrificed when exhibiting neurological symptoms. *Math1-cre::SmoM2*$^{Fl/+}$ mice were used as a tumor control group.

To investigate the role of *Smarca5* knockout in GCNPs, *Math1-cre* mice were mated with *Smarca5*$^{Fl/Fl}$ mice, resulting in excision of exon 5, which encodes the ATP-binding domain critical for remodelling activity (Corona et al., 1999), as previously described (Alvarez-Saavedra et al., 2014). These mice of genetic background *Math1-cre::Smarca5*$^{Fl/+}$ were mated with *Smarca5*$^{Fl/Fl}$ mice, generating *Math1-cre::Smarca5*$^{Fl/+}$ and *Math1-cre::Smarca5*$^{Fl/Fl}$ mice. Animals were sacrificed at P5 and P21 and their brains examined. *Math1-cre* mice were used as a control group. To investigate *Smarca5* ablation during SHH-MB development, *Math1-cre::Smarca5*$^{Fl/+}$ mice were mated with *Smo*$^{Fl/Fl}$ mice, resulting *in Math1-cre::Smarca5*$^{Fl/+}$*::SmoM2*$^{Fl/+}$ and *Math1-cre::Smarca5*$^{Fl/Fl}$*::SmoM2*$^{Fl/+}$ mice. These animals were either sacrificed at P5 or monitored for neurological symptoms according to a scoring sheet (**Supplementary Table 1**) and sacrificed when manifesting symptoms. *Math1-cre::SmoM2*$^{Fl/+}$ mice were used as a tumor control group.

2.2.1.3 Tamoxifen-inducible knockout mice

For the treatment study, we made use of a tamoxifen (TAM)-inducible *Math1-creER*^{T2} driver mouse line that allows spatio-temporal activation of Cre recombinase specifically in Math1-positive cerebellar GCNPs. This transgenic line expresses Cre-ER^{T}, a fusion protein between Cre recombinase and mutated human oestrogen receptor (ER) (Feil et al., 1997) under the control of *Math1* enhancer (Helms et al., 2000). In the presence of ER antagonist, TAM, Cre-ER^{T} recombinase activity is activated, resulting in the excision of STOP cassette flanked by loxP sites, enabling expression of transgenes (Machold and Fishell, 2005). Here, *Math1-creER*^{T2} mice were mated with *SmoM2*$^{Fl/Fl}$ mice, generating mice of genetic background *Math1-creER*^{T2}*::SmoM2*$^{Fl/+}$, thus representing an established model of SHH-MB (Merk et al., 2018). At P5, these pups received intraperitoneal injections (i.p.) with 30µl of 1mg TAM (T5648-1G, Sigma) dissolved in corn oil (Sigma-Aldrich, Burlington, Massachusetts, USA), in order to induce Cre activity.

2.2.1.4 Treatment study

Starting at P50, *Math1-creER*^{T2}*::SmoM2*$^{Fl/+}$ mice were randomized into vehicle control and drug treatment groups. Drug treatment groups included 2.5mg/kg 5-AzaC monotherapy, 20mg/kg LDE-225 monotherapy or combination of both inhibitors. Mice were treated 5 days a week for 3 weeks consecutively with a 2-day break between weeks. Both drugs were dissolved according to manufacturer´s instructions (Selleck Chemicals GmbH, Cologne, Germany). 5-AzaC was dissolved in 5% DMSO and 30% PEG300 and administered by means of i.p., while LDE-225 was dissolved in 2% DMSO and 98% corn oil and administered via oral gavage (o.g.). The vehicle

control group was treated with 5% DMSO and 30% PEG300 via i.p. Each drug (or vehicle control) was administered in a total volume of 50µl. Mice were sacrificed, when they exhibited neurological symptoms according to a scoring sheet (**Supplementary Table 1**).

2.2.2 Histological analysis

In order to isolate brain tissue for subsequent analyses, adult mice (≥ P21) were sacrificed by transcardiac perfusion, while pups at P5 were sacrificed by decapitation. To remove the brain, the cranial bone was opened by cutting from the occipital towards the frontal bone along the satura sagittalis using a straight scissor. Scull was removed until the entire brain surface was evident from the olfactory bulb to the hindbrain and gently, using a hippocampal spatula, the brain was lifted out of the scull after cutting remaining meningeal attachments and the optic and trigeminal nerves. Dissected brains were cut in the midline of brain surface, dividing them two halves, which were snap-frozen in liquid nitrogen. Finally, brains were embedded in cryomolds and fixed in Tissue-Tek® medium (O.C.T. Compound, Sakura Finetek, Tokyo, Japan). All brains were sectioned sagittally at 8µm thickness using a cryotome (LEICA CM 3060 S) and brain sections were stored at -20°C until stained.

For protein analysis of tumor tissue of *Math1-creER^{T2}::SmoM2$^{Fl/+}$* mice at P68, after cutting each brain in the midline, the cerebellum was carefully separated from the rest of the brain and entirely extracted. Using a scalpel, tumor tissue was cut from the outer surface of the cerebellum, transferred into 1.5ml Eppendorf tubes and snap-frozen in liquid nitrogen. Samples were stored at -80°C until protein extraction and detection, as described above (**Section 2.1.7**).

2.2.2.1 Haematoxylin & Eosing staining

After thawing cryosections for 10 minutes in RT, they were first fixed in acetone (neoFroxx, Einhausen, Germany) at -20°C and methanol at 4°C for 10 minutes each. Following two 5-minute washes with PBS, slides were stained with 0.1% Haematoxylin (Sigma-Aldrich, Burlington, Massachusetts, USA) for 10 minutes and washed with running tab water for another 5 minutes. Next, slides were counterstaining with 1% Eosin (Carl Roth GmbH + Co. KG, Karlsruhe, Germany) and washed with tab water, until streaking stopped. Afterwards, slides were passed through a graded series of ethanol, starting with two 5-minute incubations in 70% ethanol, followed by 1 minute in 95% ethanol and finally, 1 minute in 100% ethanol. Lastly, slides were incubated in xylene (AppliChem GmbH, Darmstadt, Germany) for 5 minutes, covered with Roti Histokit

mounting medium (Carl Roth GmbH + Co. KG, Karlsruhe, Germany) and a cover slip and air dried under the hood.

2.2.2.2 Immunohistochemistry

First, brain sections were thawed for 10 minutes in RT and then fixed either in acetone at -20ºC and methanol (AppliChem GmbH, Darmstadt, Germany) at 4ºC for 10 minutes each or 4% PFA (Sigma-Aldrich, Burlington, Massachusetts, USA) for 15 minutes in RT, depending on the primary antibody used. After washing the slides two times with PBS, tissue was marked using a lipophilic marker (Merck). To inactivate endogenous peroxidase, slides were incubated with BLOXALL solution (SP-6000-100, Vector Laboratories) for 10 minutes, then washed with PBS for 5 minutes and blocked with 10% bovine serum albumin (BSA) (Sigma-Aldrich, Burlington, Massachusetts, USA) in PBS-Tween 0.3% (Merck Millipore, Burlington, Massachusetts, USA) for 1 hour at RT. Finally, brain sections were incubated overnight with primary antibody of interest, diluted in 2% BSA in PBS-Tween 0.06% at 4ºC. A summary of all primary antibodies used and their usage information are listed on **Table 6**.

The next day, slides were first rinsed three times with PBS and then, incubated with horse anti-rabbit IgG secondary biotinylated antibody (H+L, BA-1100, Vector Laboratories Inc., Newark, California, USA) diluted at 1:400 in 2% BSA in PBS-Tween 0.06% for 1 hour at RT, followed by washes with PBS four times. Next, avidin/biotin-based peroxidase solution (VECTASTAIN ABC HRP Kit, PK-4000, Vector Laboratories Inc., Newark, California, USA) diluted in PBS-0.05% Tween was added on the slides for 30 minutes, followed by one wash with PBS. Slides were then stained with NovaRed-Peroxidase Solution (NovaRED Substrate Kit, HRP, SK-4800, Vector Laboratories Inc., Newark, California, USA) dissolved in distilled water for 1-5 minutes and rinsed with distilled water for 2 minutes to stop the reaction. Following counterstaining with 0.1% Haematoxylin for 45 seconds, slides were dehydrated with a series of ethanol dilutions. These included 2 minutes in 70% ethanol, 2 minutes in 90% ethanol and two times in 100% ethanol for 2 minutes. Finally, sections were incubated three times in xylene for 5 minutes each and mounted using Roti Histokit mounting medium.

Antibody	Species	Dilution	Fixation method	Catalog number	Company

Cleaved Caspase	Rabbit	1:100	Acetone/Methanol	#9664	Cell Signaling
Dnmt1-N	Rabbit	1:200	Acetone/Methanol	ab19905	Abcam Limited
Dnmt1-M	Rabbit	1;100	4% PFA	#5032	Cell Signaling Technology
Dnmt1-C	Rabbit	1:200	4% PFA	MA5-32547	Thermo Fisher Scientific
Dnmt3a	Rabbit	1:100	Acetone/Methanol	#3598	Cell Signaling Technology
Dnmt3b	Rabbit	1:200	Acetone/Methanol	ab2851	Abcam Limited
Ki67	Rabbit	1:100	Acetone/Methanol	ab16667	Abcam Limited
NeuN	Rabbit	1:400	4% PFA	#24307	Cell Signaling Technology
Pax6	Rabbit	1:400	4% PFA	ab19045	Abcam Limited
Smarca5	Rabbit	1:200	4% PFA	ab72499	Abcam Limited

Table 6. List of primary antibodies used for immunohistochemistry.

2.2.2.3 Microscopy and image processing

All (immune)histological images were acquired using bright-field microscopy (Axioplan 2, Carl Zeiss AG, Oberkochen, Germany). Overview pictures of H&E-stained cerebella were taken at 4x magnification using MosaiX tool on the Axio Vision 4.0 software. Images were processed on Adobe Photoshop CS5.1 (Adobe, San Jose, California, USA) or GNU Image Manipulation Program (Gimp, v 2.10.34).

For all quantifications of immunohistochemistry, the percentage of antibody-positive cells was calculated by dividing the number of cells stained positive for the marker of interest to the total number of cells in the region of interest. All cell quantifications were performed in ImageJ.

To estimate relative tumor area in *Math1-creER^{T2}::SmoM2$^{Fl/+}$* mice from vehicle control or drug treatment groups, overview images of 10 H&E-stained sections per animal per treatment group were acquired. Using freehand selection tool in ImageJ, the entire cerebellar surface and evident tumor area were manually outlined and the percentage of tumor area/entire cerebellar size was calculated in square micrometer (μm^2).

2.3 Statistical analysis

All statistical analyses were performed in GraphPad Prism 9 (GraphPad Software Inc., Insite Partners, New York City, USA) or R studio (v4.0.5, Posit PBC, Boston, Massachusetts, USA). Differences were considered statistically significant at $P < 0.05$, unless otherwise specified. For the analysis of both dependency screens, two statistical methods were employed, MAGeCK-RRA and BAGEL2 algorithms. Cell-specific essential genes were defined as the overlap of genes that were considered essential according to both algorithms at FDR < 5%. For the chemogenetic screen, a maximum likelihood estimation approach (MAGeCK-MLE) was used. Differential methylated probes from methylation profiling analysis were defined at thresholds of |β value| ≥ 0.1 and $p_{adj.} < 0.05$, while a cutoff of |LFC| ≥ 0.58 and $p_{adj} < 0.05$ were determined for the differential gene expression analysis from RNA-seq data. To identify significantly enriched gene sets from GSEA analysis, a cutoff of FDR < 25% was used. One-way or two-way ANOVA with Tukey´s or Bonferroni´s test for multiple comparisons were used, based on the number of groups and independent variables being compared. Fisher´s exact test was used for all immunohistochemical cell quantifications in mouse experiments. For PDOX experiments, the Shapiro-Wilk test was used to validate the assumption of normality. Statistical significance was then determined using Kruskal-Wallis test with Dunn's post hoc test for data with non-normal distribution. All Kaplan-Meier curves were analyzed based on Log-rank (Mantel-Cox) test. Statistics of intersections of all Venn diagrams were computed with *SuperExactTest* package on R studio.

3 Results

3.1 Characterization of two sonic hedgehog-medulloblastoma cell models using functional genomics

SMB21 and DAOY cells were screened with genome-wide CRISPR-Cas9 knockout libraries, murine Brie and human Brunello, respectively (Doench et al., 2016), in order to identify cell-specific genetic vulnerabilities (**Figure 5**). As expected, sgRNA distribution revealed a robust depletion of a subset of sgRNAs in both SMB21- and DAOY-screened cells as compared to their corresponding reference plasmids (**Figure 7A**). For the comparative analysis of both screens, we first used the *CRISPRcleanR* package to correct for gene-independent effects to CRISPR-Cas9 editing and to compute a dependency score per gene, and scaled corrected gene-level LFCs based on known pan-species non- and pan-essential control genes (https://github.com/hart-lab/bagel). Screen quality was assessed by analyzing the distribution of pan-species control genes. In both screened cell lines, pan-essentials were predominantly depleted, while the distribution of non-essentials remained unaffected (**Figure 7B**).

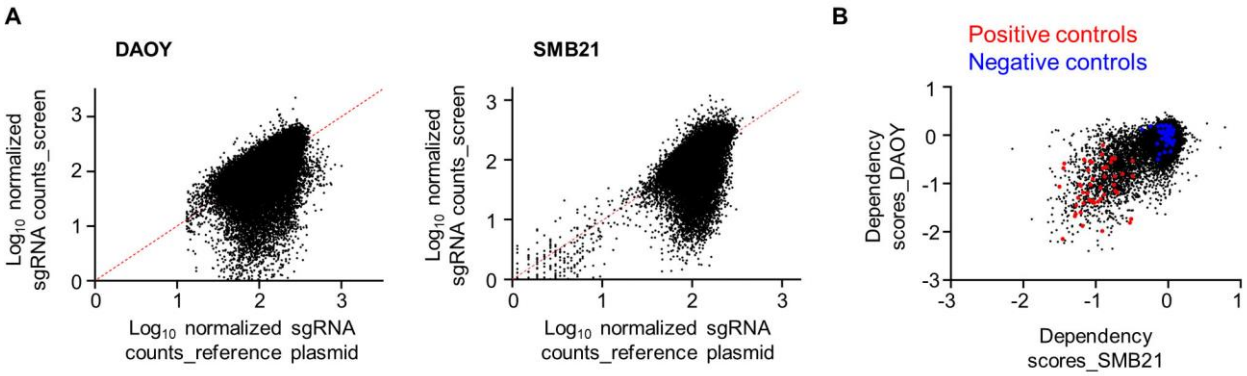

Figure 7. Negative selection screening in SMB21 and DAOY cells. (**A**) Scatterplot demonstrating distribution of sgRNAs in DAOY (left panel) and SMB21 (right panel) cells, as compared to their corresponding reference plasmid. (**B**) Scatter plot of dependency scores of DAOY (y axis) and SMB21 (x axis) cells. Red data points depict pan-species positive controls, while blue data points illustrate negative controls (Tsiami et al., 2024).

To derive genes uniquely depleted in either of the cell lines, a 9-square scatter plot of all dependency scores from both screens was generated using *MAGeCKFlute* R package (Wang et al., 2019a). We identified 345 SMB21-specific and 511 DAOY-specific depleted genes, for which comparative gene ontology analysis was performed (**Figure 8A-C**). By using biological processes

terms, we observed a significant enrichment of smoothened signaling pathway and cilia-related functions in genes exclusively depleted in SMB21 cells, while none of these terms were enriched in DAOY cells. Likewise, by interrogating cellular component terms, ciliary-associated structures were exclusively enriched in SMB21 cells.

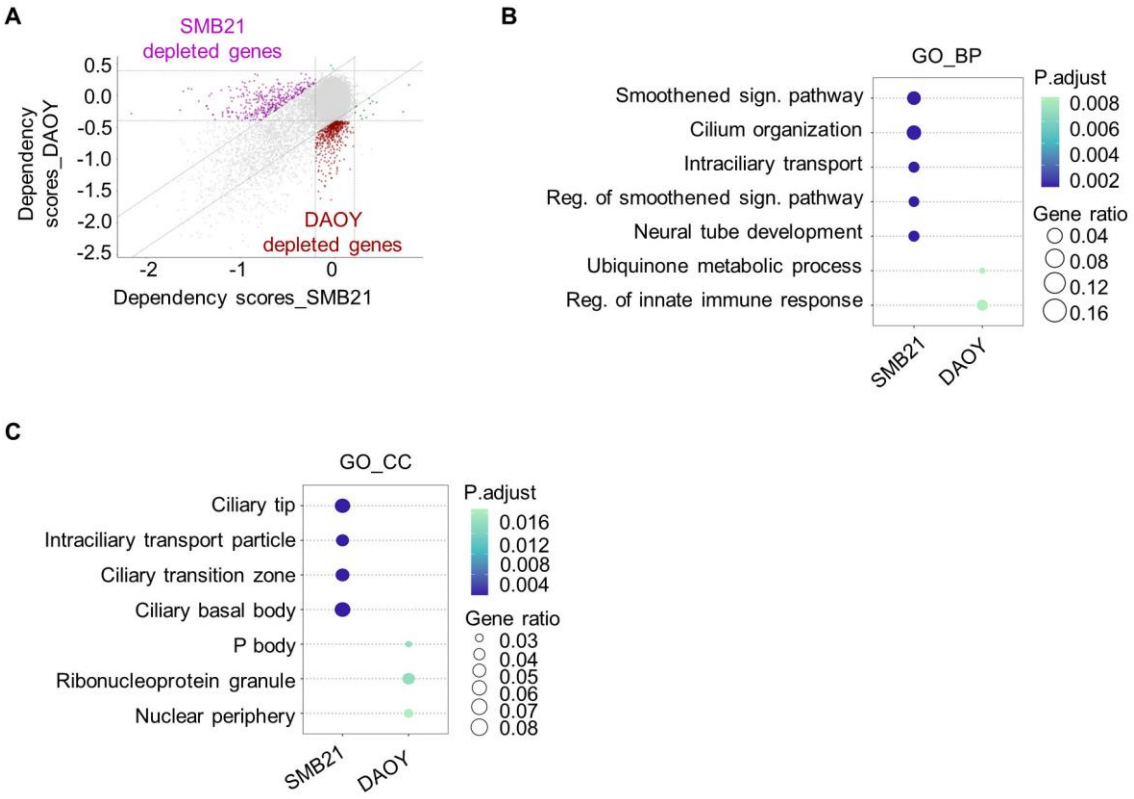

Figure 8. Comparative analysis of SMB21- and DAOY- depleted genes. (**A**) 9-square scatter plot demonstrating dependency scores of DAOY and SMB21 cells. Purple data points indicate depleted genes exclusively in SMB21 cells, while dark red data points depleted genes exclusively in DAOY cells. Diagonal dotted lines represent standard deviation of 2. Dotplots representing gene ontology analysis of cell-specific depleted genes, using biological process (GO_BP) (**B**) and cellular component (GO_CC) (**C**) terms. *P* adjusted values are color-coded and gene ratio size-coded, as indicated on the side bars (Tsiami et al., 2024).

Next, we aimed to unravel cell-specific essential genes, by combining MAGeCK-RRA (Li et al., 2014) and BAGEL2 (Kim and Hart, 2021) algorithms and identified 2,188 and 1,574 essential genes at FDR < 5% for SMB21 and DAOY cells, respectively. Out of these genes, 1,070 were significantly shared by both cell lines and were essentially associated with fundamental cellular

processes such as ribosome biogenesis, as deduced from gene ontology analysis (**Figure 9A, B**). Among the SMB21-specific dependencies we observed a strong depletion of positive regulators of the SHH pathway including *Smo* (LFC_{MAGeCK}= -3.49), *Gli1* (LFC_{MAGeCK} = -1.4) and *Gli2* (LFC_{MAGeCK}= -2.05) (**Figure 9C**). In contrast, the distribution of these genes remained unaffected in DAOY cells (LFC_{MAGeCK_SMO} = 0.57, LFC_{MAGeCK_GLI1} = 0.3, LFC_{MAGeCK_GLI2} = 0.66). As a matter of fact, comparative functional analysis of cell-specific essential genes demonstrated that top gene sets associated with active SHH signaling in GCNP cells were significantly enriched only in SMB21 cells (**Figure 9D**), providing further evidence that unlike DAOY, SMB21 cells represent a SHH-dependent MB model.

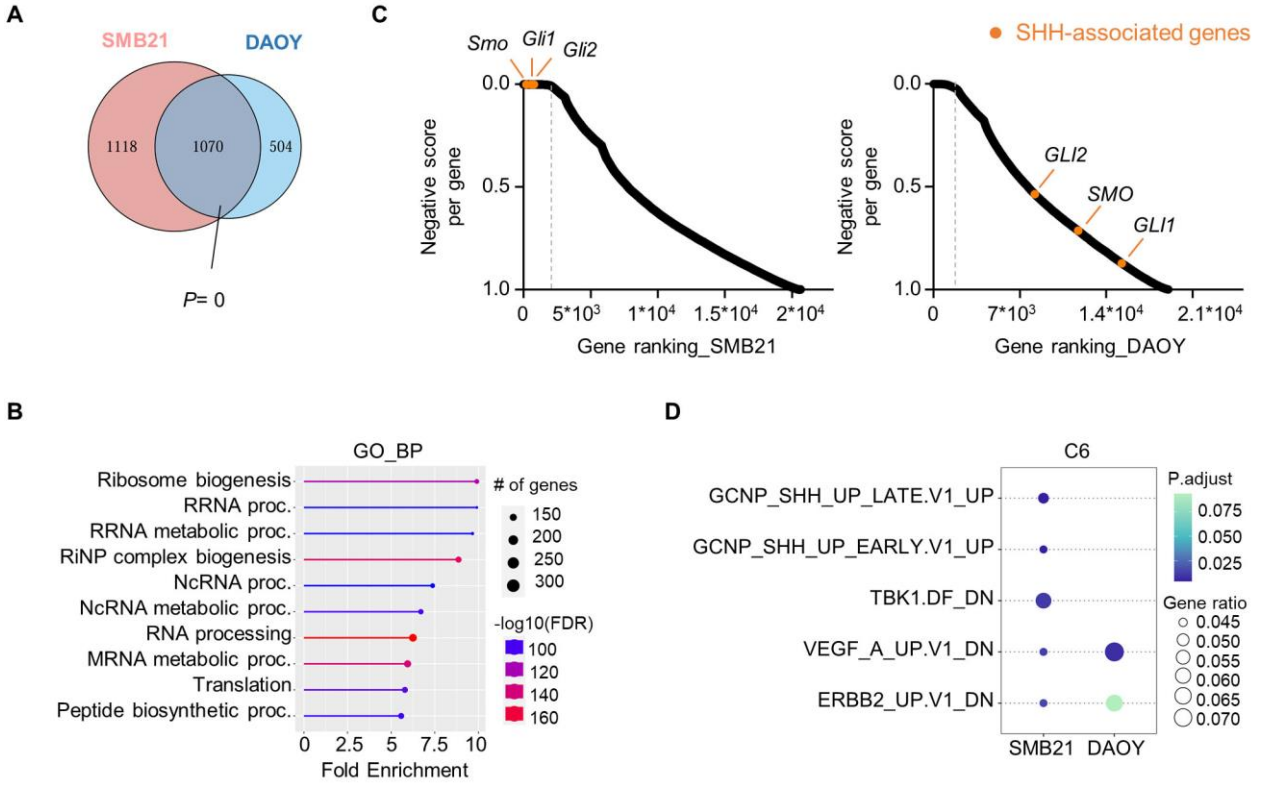

Figure 9. Comparative analysis of SMB21- and DAOY- essentialities using MAGeCK-RRA and BAGEL2 algorithms. (**A**) Venn diagram of essential genes shared by SMB21 and DAOY cells at FDR < 5%. Statistical analysis is derived from *SuperExactTest* R package. (**B**) Lollipop plot illustrating top 10 biological processes of overlapping essentialities between SMB21 and DAOY cells. Number of genes enriched are size-coded and FDR values color-coded, as indicated on the side bars. (**C**) Ranking plots depicting negative scores per gene in SMB21 (left) and DAOY (right) cells. Orange data points represent SHH positive regulators. Dotted line indicates 5% FDR cutoff. (**D**) Dotplot of top 5 C6 oncogenic gene sets enriched in DAOY and SMB21 context-specific dependencies (Tsiami et al., 2024).

To further investigate the differential dependency of SMB21 and DAOY cells on SHH signaling pathway, we evaluated the response of both cell models to two clinically available SMO inhibitors by performing dose-response assays (**Figure 10A, B**). Growth rate inhibition curves demonstrated that both drugs reduced SMB21 cell viability in a dose-dependent manner, exerting cytostatic effects, as inferred from their corresponding GR_{max} values. In contrast, DAOY cells did not respond to SMO inhibition at nanomolar and low micromolar concentrations.

A

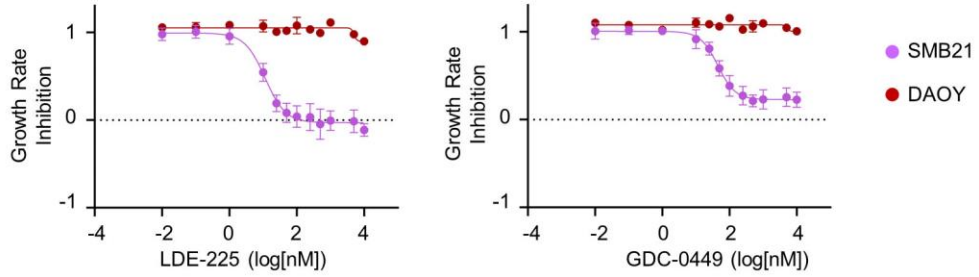

B

Cell line	LDE-225		GDC-0449	
	GR_{50} (µM)	GR_{max}	GR_{50} (µM)	GR_{max}
SMB21	0.010	-0.113	0.064	0.225
DAOY	Inf	0.897	Inf	1.004

Figure 10. SMO inhibition in SMB21 and DAOY cells. (**A**) Dose-dependent growth rate inhibition of SMB21 (purple data points) and DAOY (dark red points) cells treated with LDE-225 (left) and GDC-0449 (right) for 72 hours. Graphs display mean ± SD values. (**B**) Table summarizing average GR_{50} and GR_{max} values per cell line, as calculated using *GRmetrics* R package (n=4) (Tsiami et al., 2024).

In summary, our screening findings together with the pharmacological inhibition results provide strong evidence that SMB21 cells, as opposed to DAOY cells, rely on SHH signaling pathway for their proliferation and survival, thereby representing a reliable model system of SHH-driven MB, as previously shown (Zhao et al., 2015). Therefore, we proceeded with SMB21 screening data only in order to decipher genetic vulnerabilities for SHH-MB.

3.2 DNMT1 inhibition in sonic hedgehog subgroup of medulloblastoma

3.2.1 DNMT1 as a druggable dependency in SMB21 cells

By combining MAGeCK-RRA and BAGEL2 methods and subtracting a list of core constitutive essentials (Hart et al., 2015), we derived a total of 2,003 SMB21-associated essential genes (**Figure 11**). In order to unravel potential druggable targets, we interrogated these genes using the Drug-Gene interaction database (Cotto et al., 2018). 281 genes with predicted drug interactions were identified, out of which 213 proteins were targeted by FDA-approved drugs, including 81 proteins targeted exclusively by inhibitors or antagonists. Furthermore, we investigated potential functional protein association networks of these druggable dependencies using the Search Tool for the Retrieval of Interacting Genes/Proteins (STRING) database (Szklarczyk et al., 2015). Protein-protein interaction network revealed that many of these druggable genes are related to essential cellular processes such as DNA replication and mitochondria-related functions. Of note, a smaller subcluster emerged, consisting of CCND1, DNMT1, HDAC3, mTOR and SMO, associating SHH signaling with members of the epigenetic machinery.

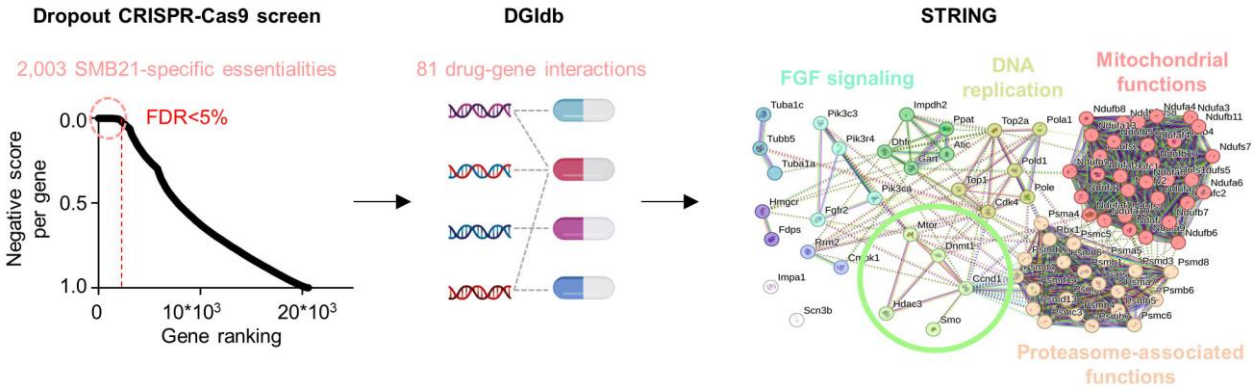

Figure 11. Unraveling druggable dependencies in SMB21 cells. SMB21-specific dependencies were determined at FDR < 5%, for which FDA-approved inhibitors were identified using the Drug-Gene Interaction Database (illustration generated with Biorender.com). Interaction network of 81 identified druggable proteins was generated using STRING database, depicting their physical and functional associations. Colored nodes indicate different interaction clusters, while white nodes represent genes without any interaction, as determined by MCL clustering. Dashed lines represent inner-cluster edges, while solid lines the type of interaction evidence (STRING database, version 12.0) (Tsiami et al., 2024).

As our screening findings suggested that these 5 druggable genes are essential for SMB21 survival, we therefore interrogated their expression profiles in relation to patient survival outcome, by analyzing publicly available microarray data from MB patients (GEO platform: GSE85218, GSE50161, GSE68015) (Cavalli et al., 2017, Gump et al., 2015, Griesinger et al., 2013). These data demonstrated that among these 5 genes only DNMT1 served as a prognostic factor for SHH subgroup of MB, with high *DNMT1* expression correlating with a significantly worse survival outcome (**Supplementary figure 3**). Within different SHH subtypes, *DNMT1* expression was lower in δ (SHH-4) subtype, which carries a more favorable prognosis, while its expression was significantly higher in MB-derived tissue than other CNS malignancies or healthy brain tissue (**Supplementary figure 4**). Taking into consideration previous studies, which have demonstrated that class I HDAC inhibitors effectively suppress SHH-MB growth of tumors both sensitive and resistant to SMO treatment by inhibiting SHH signaling (Pak et al., 2019, Coni et al., 2017), we further proceeded to investigate whether targeting epigenetic regulator DNMT1 could serve as an alternative targeted therapy approach for SHH-MB.

3.2.2 Pharmacological and genetic validation of DNMT1 in SMB cells

In order to evaluate DNMT1 inhibition in SHH-MB, we employed SMB cell lines deriving from *Ptch*$^{+/-}$ tumor mice, as well as derivative cell lines harboring mutations within SHH pathway rendering them resistant to SMO inhibition (Zhao et al., 2017, Zhao et al., 2015). These cell lines were first treated with two distinct hypomethylating agents. We used 5-AzaC, a nucleoside analogue of DNMT inhibitors, which incorporates into DNA and covalently binds to DNMTs, leading to enzyme degradation, as well as the small molecule inhibitor, SGI-1027, which binds to DNMT1 (Valente et al., 2014, Gros et al., 2015, Santi et al., 1984). While targeting SMO using LDE-225 and GDC-0449 inhibitors was not efficacious in blocking tumor proliferation in SMB21 cells with genetic alterations of the SHH pathway downstream of SMO (SMB21 *Sufu* KO and SMB21 GLI2ΔN cells), both DNMT1 inhibitors exerted highly cytotoxic effects on both SMO inhibitor-sensitive, as well as resistant SMB cells (**Figure 12**, **Table 7**).

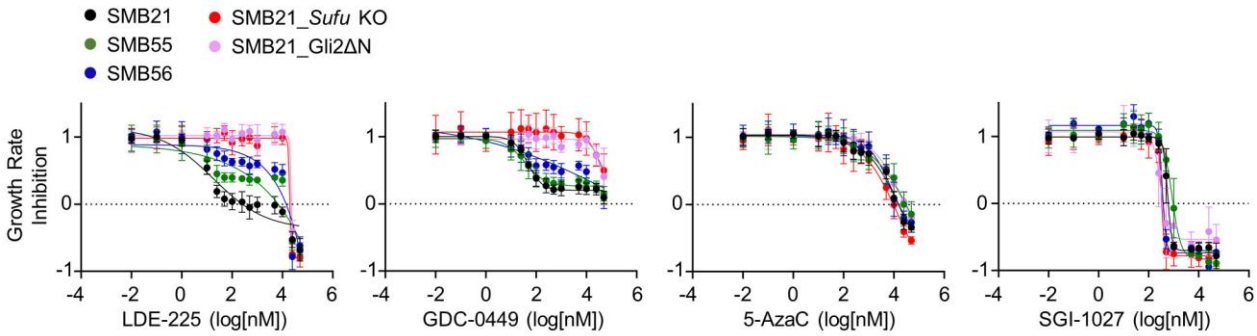

Figure 12. Pharmacological inhibition of SMO and DNMT1 in SMB cells. Dose-dependent growth rate inhibition of SMB parental and SMB21-derived cell lines treated with LDE-225, GDC-0449, 5-Azacytidine (5-AzaC) and SGI-1027 for 72 hours. Graphs display mean ± SD values.

	LDE-225		GDC-0449		5-Azacytidine		SGI-1027	
Cell line	GR_{50} (μM)	GR_{max}	GR_{50} (μM)	GR_{max}	GR_{50} (μM)	GR_{max}	GR_{50} (μM)	GR_{max}
SMB21	0.009	-0.677	0.066	0.096	3.181	-0.338	0.473	-0.782
SMB55	0.108	-0.699	0.069	0.150	3.588	-0.160	0.613	-0.893
SMB56	1.184	-0.236	1.208	-0.171	6.426	-0.208	0.309	-0.945
SMB21 *Sufu* KO	13.615	-0.236	45.832	0.484	1.209	-0.560	0.278	-0.808
SMB21 Gli2ΔN	16.374	-0.457	Inf	0.948	5.936	-0.196	0.241	-0.543

Table 7. Summary of growth rate inhibition features of all SMB cells treated with indicated inhibitors. GR_{50}=Inf represents GR_{50} values which could not be defined (asymptotic drug efficiency). All dose-response curves were analyzed using *GRmetrics* R package (Tsiami et al., 2024).

In addition to pharmacological inhibition, we also investigated loss of *Dnmt1* via genetic ablation experiments. For that purpose, we generated SMB cells with either *Smo* or *Dnmt1* knockdowns using the CRISPR-Cas9 system. We observed that loss of *Dnmt1* significantly reduced tumor survival of SMB21 cells similar to *Smo* knockdown, as compared to parental cells, well in line with the screening findings showing that *Dnmt1* is essential for SHH-MB proliferation (**Figure 13A**). Moreover, we explored whether *Dnmt1* knockdown affects SHH pathway output by evaluating expression of a positive regulator of the pathway, GLI1. Western blotting analysis showed that *Dnmt1* knockdown reduced GLI1 protein levels in all SMB-transduced cell lines similar to *Smo*

knockdown, used as positive control (**Figure 13B**), suggesting that targeting *Dnmt1* reduces SMB proliferation by suppressing SHH signaling.

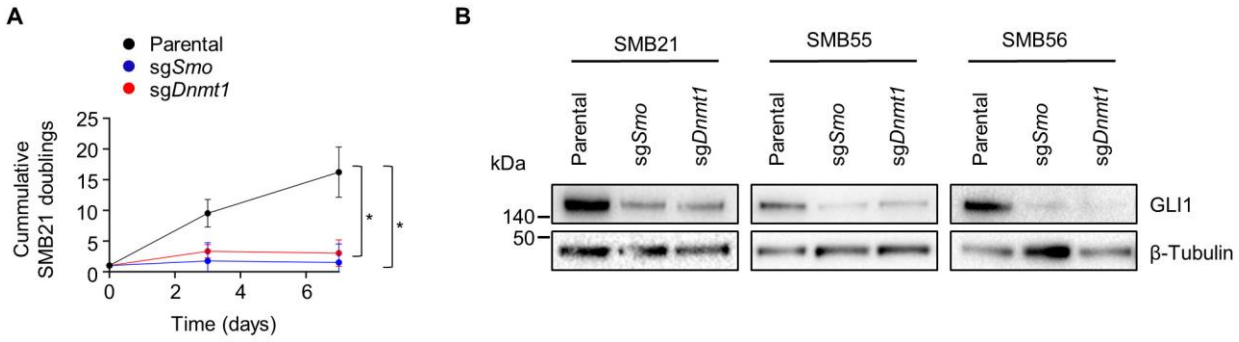

Figure 13. Genetic ablation of *Dnmt1* in SMB cells. (**A**) Analyses of cell population doublings for SMB21 cells transduced with the indicated sgRNA constructs over 7 days, as compared to SMB21 parental cells. Two-way ANOVA, Tukey´s multiple comparisons test (n = 3). (**B**) Western blotting illustrating GLI1 protein levels in SMB21, SMB55 and SMB56 parental and knockout conditions for *Smo* and *Dnmt1*. Graph displays mean ± SD values. *$p \leq 0.05$ (Tsiami et al., 2024).

In summary, our *in vitro* validation experiments provide evidence that targeting DNMT1 effectively mitigates SHH-MB proliferation regardless of the genetic alterations within the SHH pathway. Taking into consideration that 5-AzaC is an FDA-approved drug clinically applied for the treatment of acute myeloid leukemia and myelodysplastic syndromes (Diesch et al., 2016), we further proceeded with this inhibitor for all downstream analyses both *in vitro* and *in vivo*.

3.2.3 Methylation and gene expression alterations induced by DNMT1 inhibition

Having validated that targeting DNMT1 suppresses SHH-MB proliferation *in vitro*, we next aimed to gain insight into potential epigenetic and gene expression alterations induced in SHH-MB cells under pharmacological inhibition of DNMT1.

To address this, we first carried out DNA methylation profiling of SMB21 and SMB55 cells treated with 5-AzaC for 24 hours and performed differential methylation analysis compared to DMSO control. Variance visualization of 12 principal dimensions resulting from principal component analysis (PCA) of top 5,000 differential CpGs revealed highest variance in component PC1, thus capturing the differences between the two cell lines (**Figure 14A-D**). By analyzing an increasing fraction of differentially methylated probes (from 5,000 to 200,000), higher variance of component

PC2 was also observed, indicating sample clustering based on the drug treatment applied (**Supplementary figure 5A-D, Supplementary figure 6A-D**). Differential methylation analysis consistently displayed robust hypomethylation effects on both cell models upon exposure to 5-AzaC for 24 hours (**Figure 14D, E**).

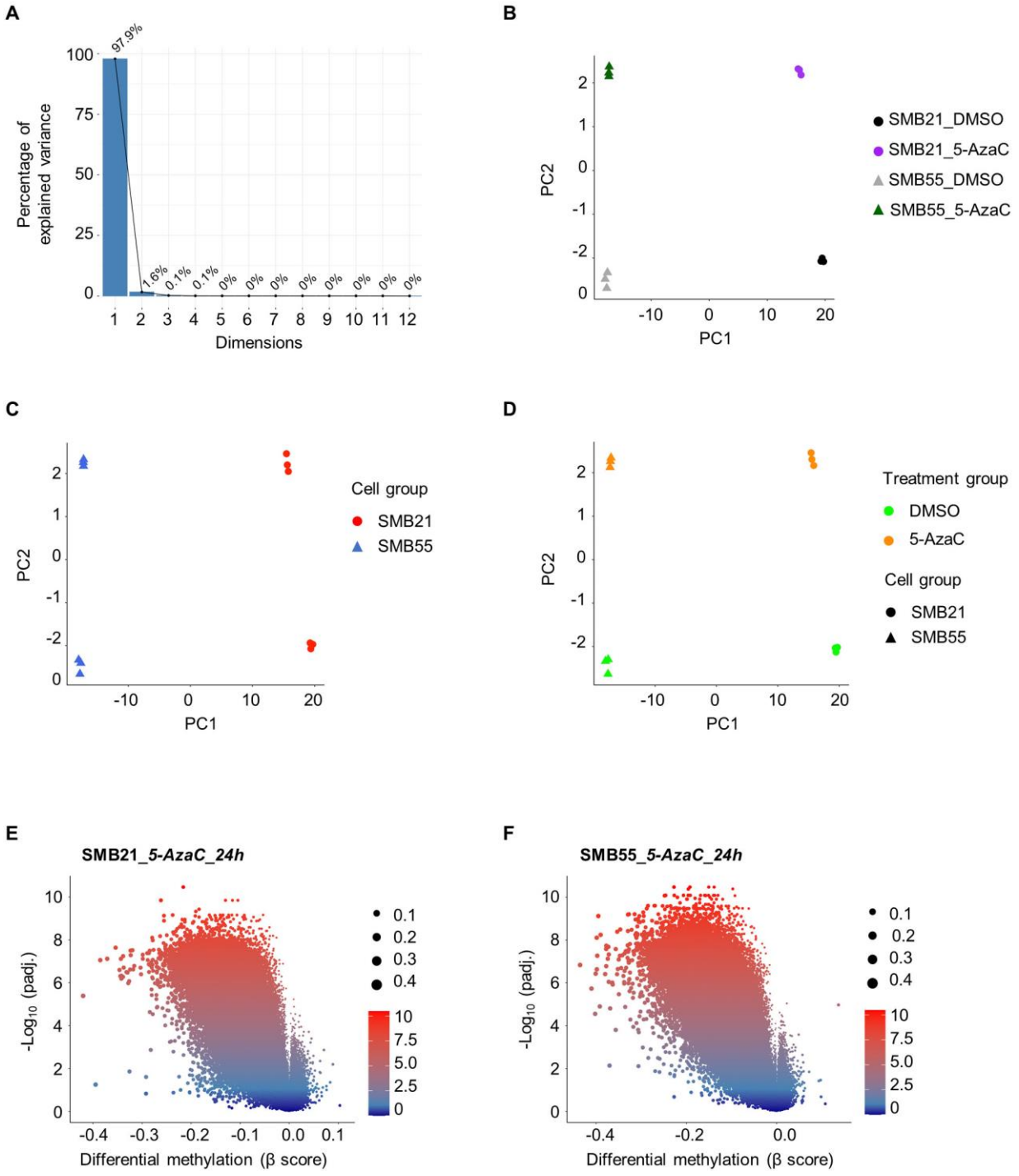

Figure 14. DNA methylation analysis of SMB cells treated with 5-Azacytidine. (**A**) Scree plot depicting variances among 12 principal dimensions, deriving from PCA of 5,000 differentially methylated probes in SMB21- and SMB55-treated cells. Percentages of variance are indicated per dimension. PCA plots of the top 5,000 differentially methylated CpGs based on (**B**) all four different conditions, (**C**) cell groups and (**D**) drug-treatment groups. Comparison of PC1 vs PC2 components is indicated in all plots. Specific groups are color- and shape-coded. Volcano plots of all differentially methylated probes in SMB21 (**E**) and SMB55 cells (**F**) treated with 5-AzaC for 24 hours as compared to DMSO control-treated cells. Adjusted *P*-values are color-coded, and β scores are size-coded (Tsiami et al., 2024).

By defining a threshold of |β value| ≥ 0.1 and $p_{adj.}$ < 0.05, we identified a total of 73,594 and 98,794 significantly hypomethylated probes in SMB21 and SMB55 cells, which were significantly enriched for 630 and 607 genes, respectively, displaying significant overlap (**Figure 15A**). Functional analysis of hypomethylated genes of both cell lines revealed their association in fundamental CNS processes including neuron projection development and differentiation, further explaining the observed phenotype induced in SMB cells under DNMT1 inhibition (**Figure 15B-D**).

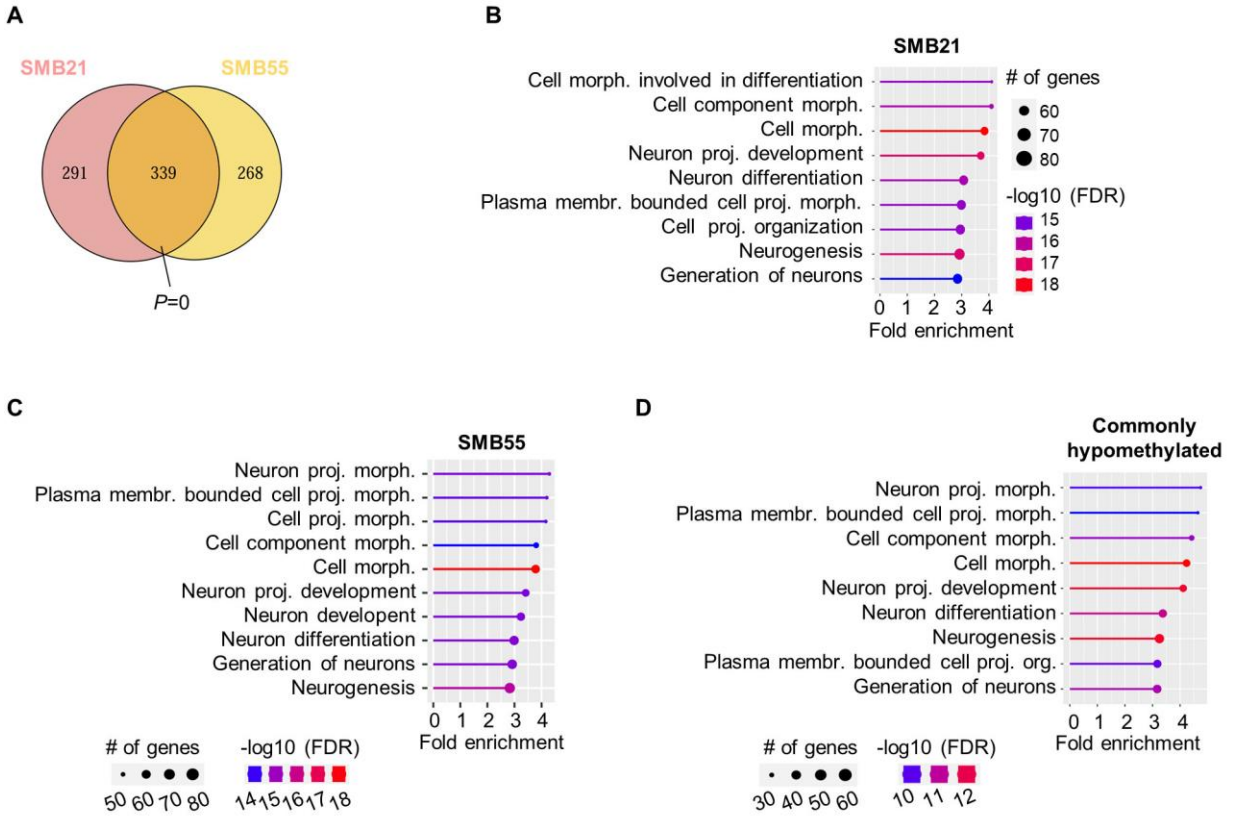

Figure 15. Functional annotation of differentially methylated genes in SMB cells. (**A**) Venn diagram of significantly hypomethylated genes shared by SMB21 and SMB55 cells at 24 hours treatment with 5-Azacyitidine. Statistical analysis was conducted using *SuperExactTest*. Lollipop plots of top biological processes of hypomethylated genes in SMB21 (**B**) and SMB55 cells (**C**) treated with 5-Azacytidine for 24 hours. (**D**) Lollipop plot of the top biological processes of commonly hypomethylated genes between SMB21 and SMB55 cells after 24h treatment of 5-Azacytidine (Tsiami et al., 2024).

Next, we aimed to explore potential global gene expression alterations in SMB cells attributed to DNMT1 inhibition. Therefore, we conducted RNA sequencing of SMB21 cells treated with 5-AzaC for 2 and 48 hours. Principal component analysis showed that different treatment groups formed distinct clusters, with the highest variance observed in PC1 between DMSO control and 48 hours treatment with 5-AzaC (**Figure 16A**). While methylation profiling demonstrated exclusively hypomethylating alterations under 24 hours treatment, our transcriptomics analysis uncovered both up- and down-regulated genes under DNMT1 inhibition at both time points (**Figure 16B**). We also observed differences in differential deregulated genes at 2 and 48 hours treatment, indicating a time-dependent longitudinal response to DNMT1 inhibition (**Figure 16C**).

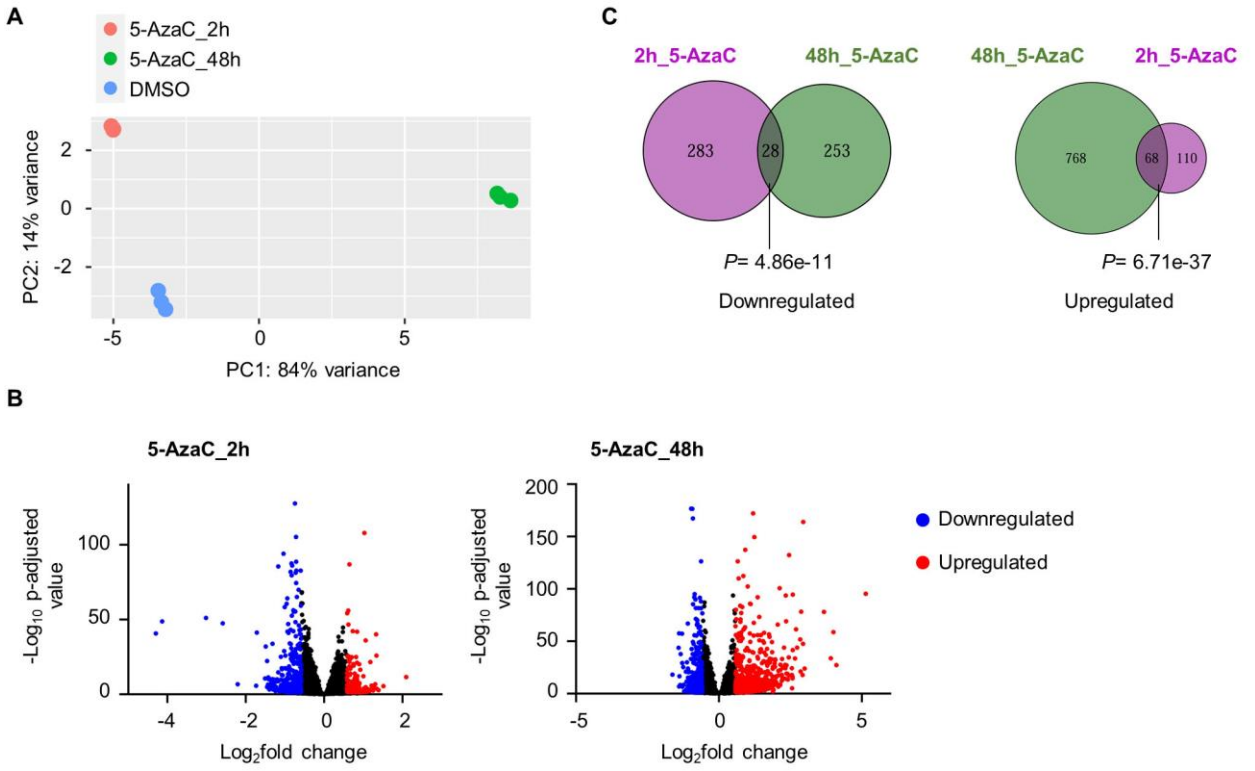

Figure 16. RNA sequencing of SMB21 cells. (**A**) Principal component analysis of global gene expression profiles from 5-Azacytidine (5-AzaC)-treated SMB21 cells at 2 and 48 hours and corresponding DMSO control. (**B**) Venn diagrams of overlapping downregulated (left) and upregulated genes (right) between 2h- and 48h-5-AzaC- treated SMB21 cells. Statistics are derived from *SuperExactTest.* (**C**) Volcano plots illustrating log_2fold change of all differentially expressed genes in SMB21 cells after 2 (left) and 48 hours (right) treatment with 5-AzaC. Blue data points depict significantly downregulated genes and red significantly upregulated, as defined at |log 2fold change| ≥ 0.58 threshold (Tsiami et al., 2024).

Moreover, to better understand the functional relevance of gene expression changes, we performed gene set enrichment analysis. Among the top Hallmark gene sets identified, “Hallmark_Hedgehog_Signaling” gene set was significantly downregulated after 2 hours treatment with 5-AzaC (**Figure 17A**), suggesting an early inhibitory effect of DNMT1 inhibition on positive regulators of the SHH pathway. In parallel, GSEA analysis for 48-hour treatment group using C6 oncogenic sets revealed a significant upregulation of “GCNP_SHH_UP_EARLY.V1_DN” and “GCNP_SHH_UP_LATE.V1_DN” gene sets, which refer to genes down-regulated upon SHH activation in GCNPs, the proposed cell origin of SHH-MB. To further corroborate our RNA-seq findings, we assessed the expression of GLI1, positive regulator of SHH pathway, on a protein level via western-blotting. Thus, we treated several SMB cell lines with their corresponding GR_{50} values of 5-AzaC for 48 hours and quantified their GLI1 protein levels (**Figure 17B, C**). Our data showed that 5-AzaC significantly decreased GLI1 protein expression levels in all cell lines tested, providing supporting evidence that DNMT1 inhibition reduces SHH-MB viability by attenuating SHH pathway output. Interestingly enough, we observed a significant reduction in GLI1 levels in LDE-225-resistant cells, SMB21 *Sufu* KO, suggesting that DNMT1 inhibition blocks SHH pathway activation in SMB tumors regardless of their sensitivity to SMO inhibition.

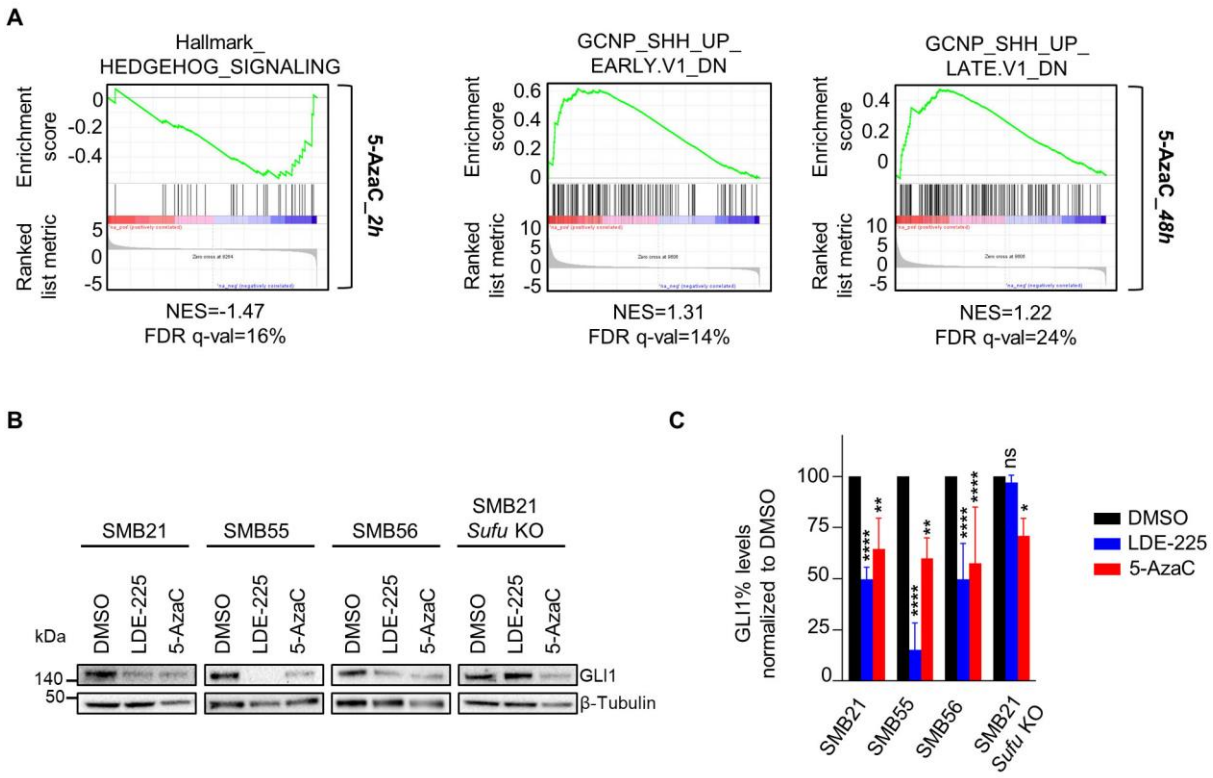

Figure 17. 5-Azacytidine suppresses SHH pathway activation. (**A**) Gene set enrichment plot illustrating significant downregulation of a gene set associated with active SHH signaling under 5-AzaC treatment for 2 hours (left panel). Gene set enrichment plots for two C6 oncogenic signature gene sets after 48 hours treatment with 5-AzaC depicting significant upregulation of genes known to be inhibited by active SHH signaling in granule cerebellar neuron precursors (middle and right panels). Normalized enrichment scores and corresponding FDR values are indicated below the plots. (**B**) Exemplary western blot analyses of GLI1 protein in SMB21, SMB55, SMB56 and SMB21 *Sufu* KO cells treated with DMSO ctr, LDE-225 or 5-AzaC for 48 hours. (**C**) Quantification of GLI1 protein levels shown in (**B**). Two-way ANOVA, Tukey´s multiple comparison test (n = 3). Graph displays mean ± SD values. * $p \leq 0.05$, ** $p \leq 0.01$, **** $p \leq 0.0001$ (Tsiami et al., 2024).

Moreover, the top Hallmark gene set significantly downregulated under 48-hour treatment with 5-AzaC included “HALLMARK_G2M_CHECKPOINT”, which refers to genes being involved in the G2/M checkpoint (**Figure 18A**). To gain more insight into cell cycle effects induced by DNMT1 inhibition in SHH-MB, SMB21 and SMB55 cells were treated with 5-AzaC for 48 hours and subjected to cell cycle analysis by flow cytometry (**Supplementary figure 7A, B**). Well in line with the RNA-seq findings, flow cytometry revealed a significant increase in the fraction of cells in G2-M transition phase under DNMT1 inhibition in both cell models (**Figure 18B, C**). This effect was accompanied by a concomitant reduction in percentage of SMB21 cells in G1 phase, all together

providing supporting evidence that 5-AzaC treatment affects cell cycle progression. In summary, our *omics* data demonstrate that DNMT1 inhibition induces global changes on a methylation and transcriptomic level in SHH-MB by suppressing SHH signaling cascade.

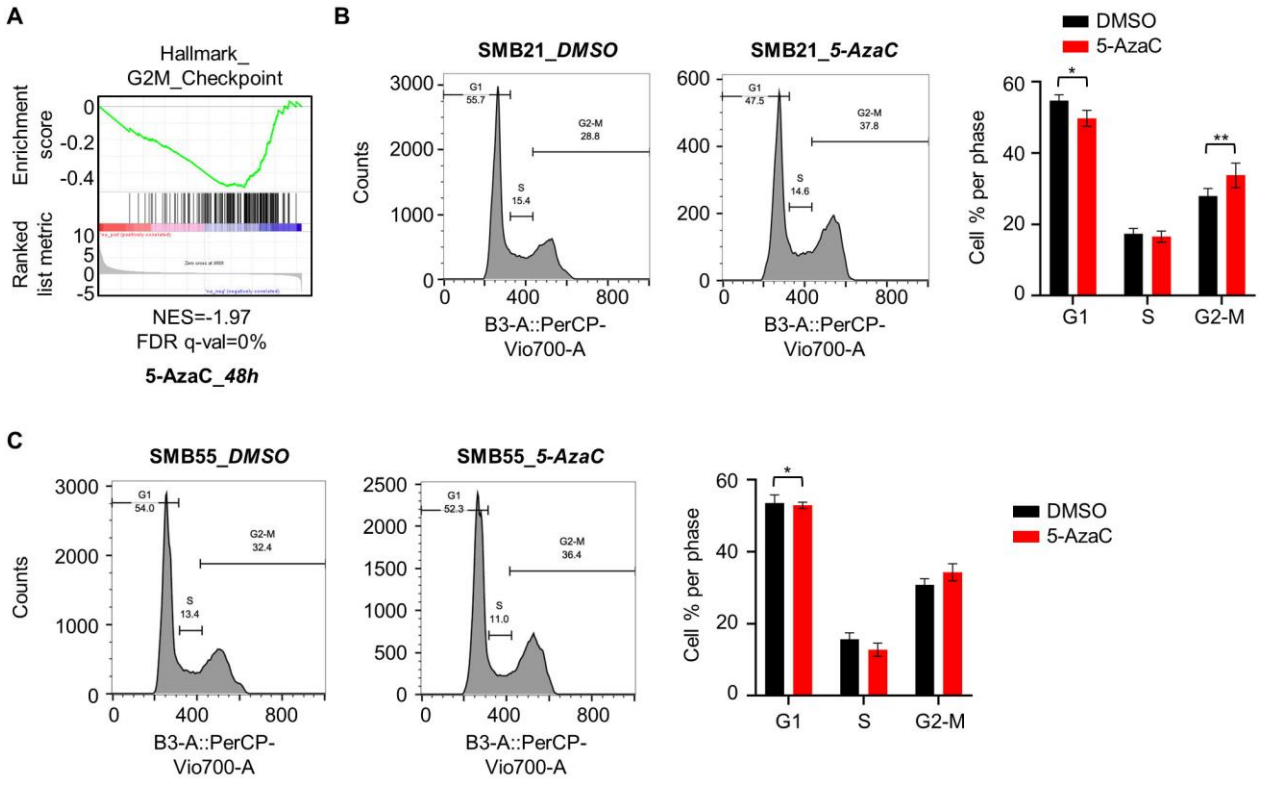

Figure 18. 5-Azacytidine alters cell division cycle in SMB cells. (**A**) Gene set enrichment plot illustrating significant downregulation of a gene set associated with cell cycle progression in SMB21 cells 48 hours post treatment with 5-AzaC. Normalized enriched score and corresponding FDR value are indicated below the plot. Representative cell cycle phase distribution in SMB21 (**B**) and SMB55 (**C**) cells treated with DMSO control or 5-AzaC for 48 hours. Corresponding graphs of cell % in each phase are shown. Two-way ANOVA, Bonferroni´s multiple comparison test (n = 3). Graph displays mean ± SD values. * $p \leq 0.05$, ** $p \leq 0.01$.

3.2.4 Role of DNMT1 in normal cerebellar and SHH-MB development *in vivo*

Having validated that genetic and pharmacological inhibition of DNMT1 efficaciously suppresses SHH-MB proliferation *in vitro*, we next aimed to explore the role of DNMT1 *in vivo*.

Mammalian DNMT1 is described as a maintenance methyltransferase, as it maintains DNA methylation state during chromosome replication and repair (Lucidi et al., 2019). This is achieved

by catalyzing the transfer of a methyl group from S-adenyl methionine to the fifth carbon of cytosine nucleotides to form 5-methylcytosine. Its indispensable role in murine embryogenesis has been described long ago, as conditional knockout of *Dnmt1* in embryonal stem cells results in developmental abnormalities and embryonic lethality (Li et al., 1992). Regarding its protein structure, mammalian DNMT1 consists of a large multi-domain *N*-terminal part and a *C*-terminal catalytic part (Jurkowska et al., 2011) (**Figure 19A**). While the *N*-terminal motif regulates enzyme interactions with other proteins, DNA and chromatin, and guides nuclear localization of enzymes, the *C*-terminal catalytic motif is involved in DNA binding and transferring of the methyl unit (Jurkowska et al., 2011, Lucidi et al., 2019). DNMT1 exists in three isoforms DNMT1s, DNMT1o and DNMT1p which have been identified in somatic cells, oocytes and embryos, respectively (Mertineit et al., 1998, Giraldo et al., 2013).

Here, we first assessed DNMT1 protein expression patterns in murine cerebellum by using three DNMT1 antibodies that recognize different protein domains (**Figure 19B**). These include DNMT1-N that binds to 100-200 amino acids of N-terminal, DNMT1-M which binds to the bromo adjacent homology N-domain and DNMT1-C which recognizes the catalytic *C*-terminal catalytic part. Immunohistochemical analysis of *Math1-cre* mice at P5 showed that DNMT1-N expression was primarily evident in mature migrated granule neurons of the internal granule layer. Unlike DNMT1-N, both DNMT1-M and DNMT1-C antibodies displayed similar expression patterns, as their signal was the strongest in proliferating GCNPs of the external granule layer. All three antibodies were detected at low expression levels in differentiated neurons of the internal granule layer at P21. Furthermore, we investigated the expression of two DNMT3 family members, DNMT3A and DNMT3B. Both enzymes are known as *de novo* DNMTs, as they establish basic CpG methylation level to unmodified DNA (Lucidi et al., 2019). They are essential for mammalian development with overlapping functions during early embryogenesis, with DNMT3A playing a more critical role at later developmental stages (Okano et al., 1999). Immunohistochemistry for both enzymes showed that DNMT3A is moderately expressed in proliferating GCNPs of the external granule layer in *Math1-cre* mice at P5, while DNMT3B expression was virtually absent in the cerebellum (**Figure 19C**). These results were well in agreement with previous reports of differential expression patterns of both enzymes in the CNS (Watanabe et al., 2002, Feng et al., 2005).

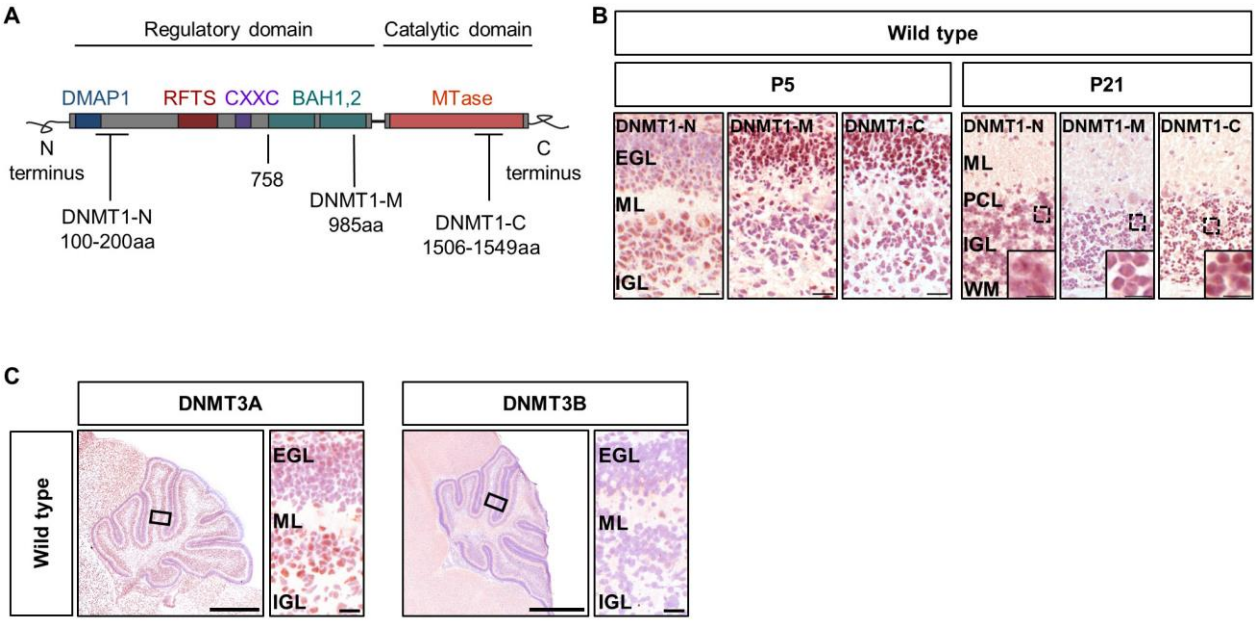

Figure 19. Expression of DNA methyltransferases in murine granule cell neuron precursors. (**A**) Schematic representation of the protein structure of mammalian DNMT1 (1620 aa). Regulatory and catalytic domains are indicated, along with the binding sites of three distinct DNMT1 antibodies (DNMT1-N, -M, and -C). DMAP1, DNMT1 associated protein 1; RFTS, replication foci targeting sequence; CXXC, zinc finger; BAH1/2, bromo adjacent homology domains; MTase, C-5 methyltransferase. (B) Representative images of wild type murine cerebella stained with DNMT1-N, DNMT1-M and DNMT1-C antibodies at P5 and P21. (C) Representative cerebella from wild type mice at P5 stained with DNMT3A (left panel) and DNMT3B (right panel) at indicated magnified regions. 4x magnification, scale bar, 500μm; 20x magnification, scale bar, 50μm; 40x magnification, scale bar, 20μm. EGL, external granular layer; ML, molecular layer; PCL, Purkinje cell layer; IGL, internal granular layer; WM, white matter (Tsiami et al., 2024).

To explore the role of *Dnmt1* in murine cerebellar development, we used the Cre/loxP system to genetically ablate *Dnmt1* in GCNPs, leading to an out-of-frame splice from exon 3 to exon 6 (Jackson-Grusby et al., 2001). Brains from mice with heterozygous or homozygous loss of *Dnmt1* were extensively examined via histology at P5 and P21. We first validated the loss of DNMT1 in proliferating GCNPs at P5 in the cerebella of *Math1-cre::Dnmt1*$^{Fl/Fl}$ mice via immunostaining using the DNMT1-C antibody (**Figure 20**). Through histological analysis of these brains at P5 we observed a thinner external granule cell layer formed in the cerebellum of *Math1-cre::Dnmt1*$^{Fl/Fl}$ mice as compared to the control group.

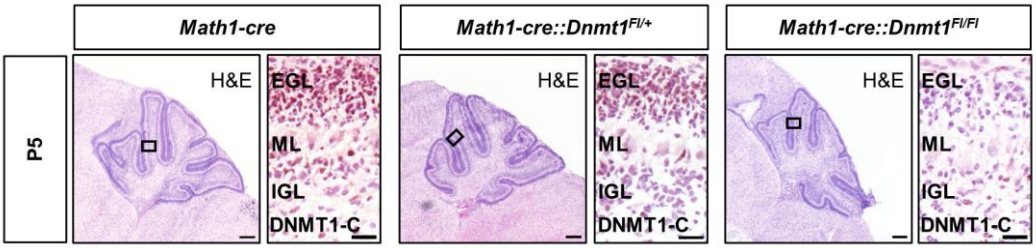

Figure 20. *Dnmt1* genetic depletion in granule cell neuron precursors at P5. Representative H&E stainings of whole cerebella from *Math1-cre, Math1-cre::Dnmt1*$^{Fl/+}$ and *Math1-cre::Dnmt1*$^{Fl/Fl}$ mice at P5, as well as immunostaining for DNMT1-C at indicated magnified regions. 4x magnification, scale bar, 500µm; 20x magnification, scale bar, 50µm. EGL, external granular layer; ML, molecular layer; IGL, internal granular layer (Tsiami et al., 2024).

Indeed, immunohistochemistry for Ki67 and cleaved caspase 3 markers revealed a significant reduction in proliferating GCNP cells and a significant fold increase in apoptotic cells, respectively, in the EGL of *Math1-cre::Dnmt1*$^{Fl/Fl}$ mice at P5 (**Figure 21A, B**).

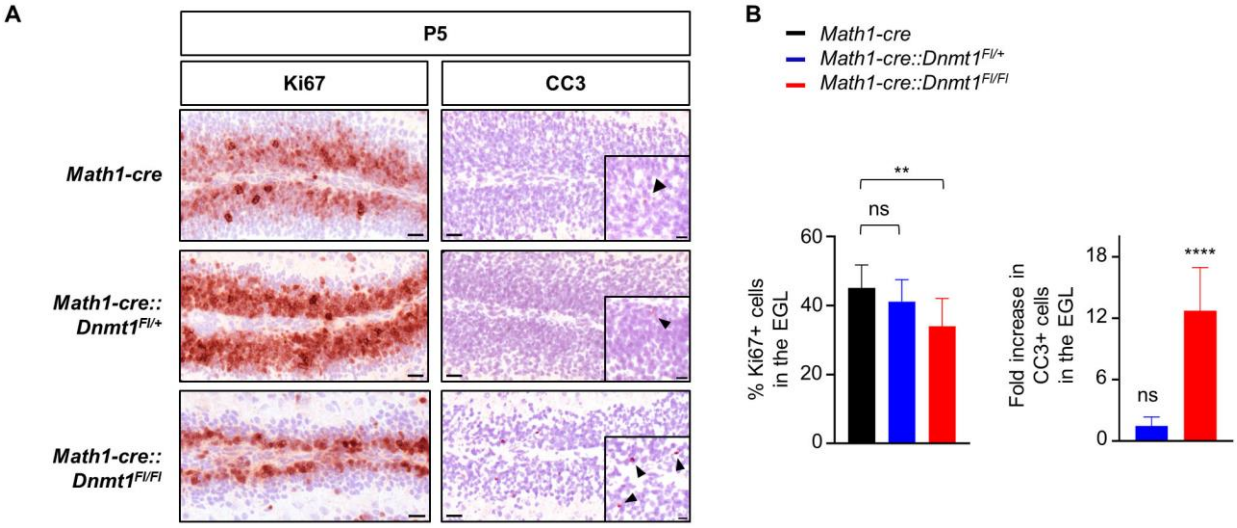

Figure 21. Loss of *Dnmt1* affects granule cell neuron precursor survival. (**A**) Representative images of EGL from *Math1-cre, Math1-cre::Dnmt1*$^{Fl/+}$ and *Math1-cre::Dnmt1*$^{Fl/Fl}$ mice stained with Ki67 (left panel) and cleaved caspase 3 (right panel) immunomarkers at P5. (**B**) Quantification of Ki67- (left panel) and cleaved caspase 3-positive (right panel) cells in the EGL of mice shown in (**A**) (n = 3, Fisher´s exact test). 20x magnification, scale bar, 50µm; 40x magnification, scale bar, 20µm. EGL, external granular layer; ML, molecular layer; IGL, internal granular layer. All graphs display mean ± SD values. ** $p \leq 0.01$, **** $p \leq 0.0001$ (Tsiami et al., 2024).

Notably, at P21 mice with *Dnmt1* knockout displayed a remarkably smaller cerebellum, a phenotype referred to as cerebellar hypoplasia, as determined via H&E staining (**Figure 22**). This developmental deficit was not detected in *Dnmt1* heterozygously depleted mice.

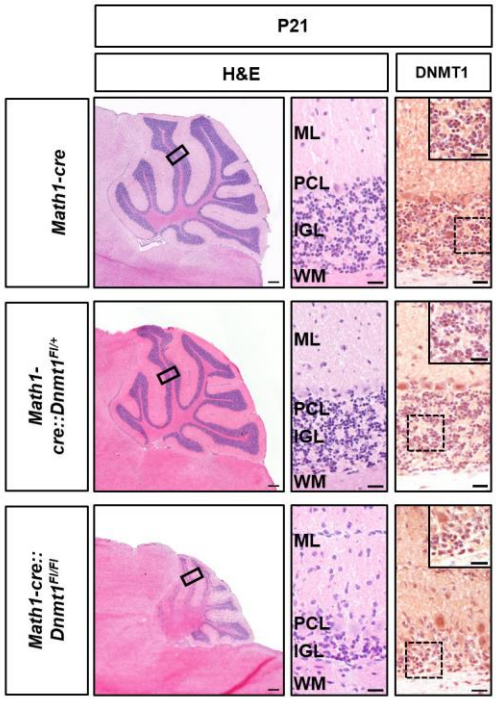

Figure 22. *Dnmt1* depletion in granule cell neuron precursors induces cerebellar hypoplasia. Exemplary H&E stainings of whole cerebella from *Math1-cre, Math1-cre::Dnmt1*$^{Fl/+}$ and *Math1-cre::Dnmt1*$^{Fl/Fl}$ mice at P21, as well as immohistochemistry for DNMT1-C antibody. 4x magnification, scale bar, 500μm; 20x magnification, scale bar, 50μm; 40x magnification, scale bar, 20μm. ML, molecular layer; PCL, Purkinje cell layer; IGL, internal granular layer; WM, white matter (Tsiami et al., 2024).

To gain further insight into the observed phenotype, we stained these brains with several immunomarkers. We identified a significant increase of NeuN- and Pax6-positive cells in the molecular layer of the cerebella of *Math1-cre::Dnmt1*$^{Fl/Fl}$ mice (**Figure 23A, B**). These data suggested that migration of GCNPs was impeded and that these cells prematurely differentiated within the molecular layer. In contrast, neither proliferating nor apoptotic cells were identified in any of these genotypes at P21. Taken together, our histological data suggest that loss of *Dnmt1* affects normal murine cerebellar development by interfering with GCNP proliferation and migration.

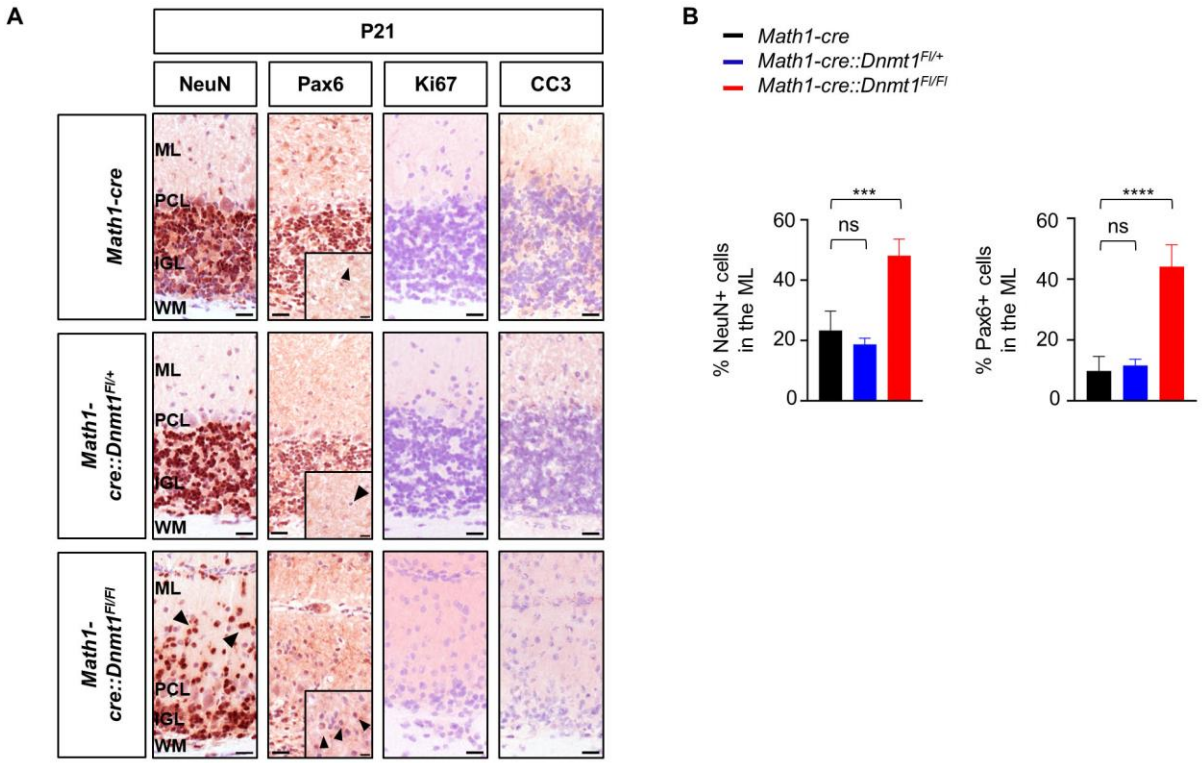

Figure 23. *Dnmt1* knockout affects migratory capacity of granule cell neuron precursors. (**A**) Exemplary cerebellar layers from *Math1-cre, Math1-cre::Dnmt1*$^{Fl/+}$ and *Math1-cre::Dnmt1*$^{Fl/Fl}$ mice at P21 stained with NeuN, Pax6, Ki67 and cleaved caspase 3. (**B**) Quantification of NeuN- (left panel) and Pax6-positive (right panel) cells, as shown in (**A**) (n = 3, Fisher´s exact test). 20x magnification, scale bar, 50µm. 40x magnification, scale bar, 20µm. ML, molecular layer; PCL, Purkinje cell layer; IGL, internal granular layer; WM, white matter. All graphs display mean ± SD values. *** $p \leq 0.001$, **** $p \leq 0.0001$ (Tsiami et al., 2024).

Next, we asked whether loss of *Dnmt1* has an impact on SHH-MB growth *in vivo*. For that, we employed an established mouse model of SHH-MB, *Math1-cre::SmoM2*$^{Fl/+}$, which constitutively expresses a mutated form of *Smo* in GCNPs (Mao et al., 2006, Matei et al., 2005). We generated tumor mice of genetic background *Math1-cre::Dnmt1*$^{Fl/+}$*::SmoM2*$^{Fl/+}$ and *Math1-cre::Dnmt1*$^{Fl/Fl}$*::SmoM2*$^{Fl/+}$, as validated via immunohistochemistry and histologically examined their brains at P5 (**Figure 24**). All three genotypes displayed cerebellar tumors, while a smaller tumor formation was observed in the anterior part of the cerebellum in mice with homozygous loss of *Dnmt1*.

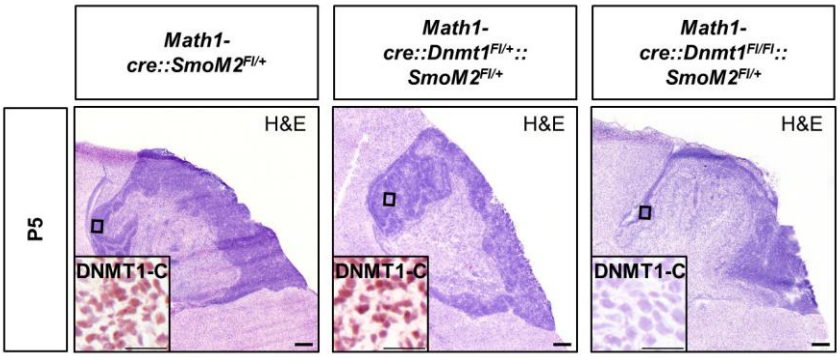

Figure 24. Genetic loss of *Dnmt1* in SHH-MB mice. Whole cerebellar tumors from *Math1-cre::SmoM2*$^{Fl/+}$, *Math1-cre::Dnmt1*$^{Fl/+}$*::SmoM2*$^{Fl/+}$ and *Math1-cre::Dnmt1*$^{Fl/Fl}$*::SmoM2*$^{Fl/+}$ mice stained with H&E at P5. Magnified regions indicate immunostaining for DNMT1-C marker. 4x magnification, scale bar, 500μm; 20x magnification, scale bar, 50μm (Tsiami et al., 2024).

Immunostaining of cerebellar tumors revealed a significant reduction of tumor proliferating cells in *Math1-cre::SmoM2*$^{Fl/+}$ mice with both heterozygous and homozygous *Dnmt1* knockout, when compared to tumor control group (**Figure 25A, B**). We also detected a significant increase in apoptotic cells only in tumors of *Math1-cre::Dnmt1*$^{Fl/Fl}$*::SmoM2*$^{Fl/+}$ mice.

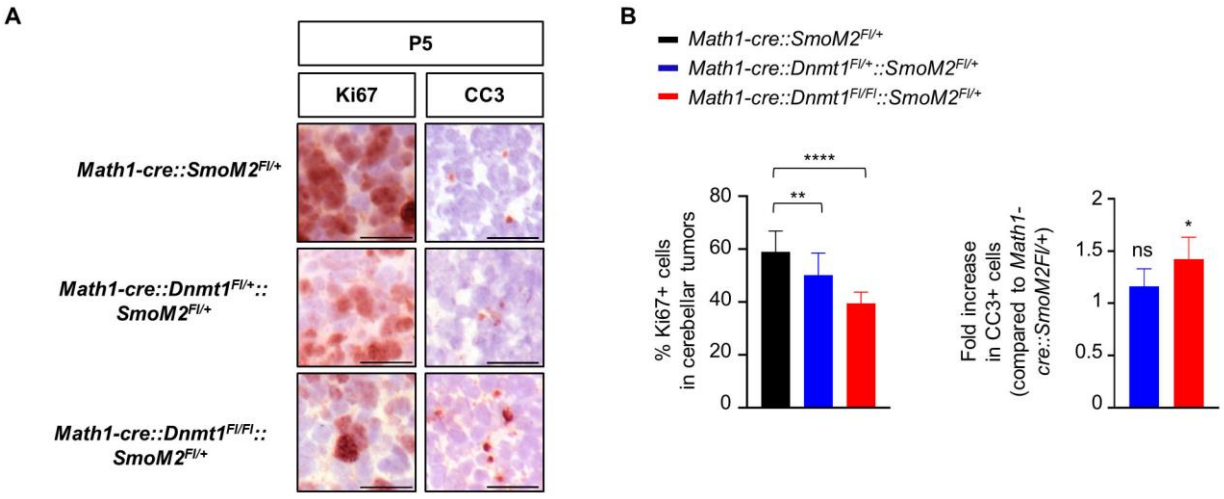

Figure 25. Loss of *Dnmt1* reduces SHH-MB growth. (**A**) Representative cerebellar tumors from *Math1-cre::SmoM2*$^{Fl/+}$, *Math1-cre::Dnmt1*$^{Fl/+}$*::SmoM2*$^{Fl/+}$ and *Math1-cre::Dnmt1*$^{Fl/Fl}$*::SmoM2*$^{Fl/+}$ mice stained with Ki67 (left panel) and cleaved caspase 3 (right panel) at P5. (**B**) Quantification of Ki67- (left panel) and cleaved caspase 3-positive cells (right panel) from brain tumors shown in (**A**) (n = 3, Fisher´s exact test).

20 × magnification, scale bar, 50μm. All graphs display mean ± SD. * $p \leq 0.05$, ** $p \leq 0.01$, **** $p \leq 0.0001$ (Tsiami et al., 2024).

Additionally, we monitored these mice for neurological symptoms and analyzed their survival outcome. *Math1-cre::Dnmt1*$^{Fl/Fl}$*::SmoM2*$^{Fl/+}$ mice exhibited a significantly prolonged survival when compared to *Math1-cre::SmoM2*$^{Fl/+}$ mice (*P*= 0.0324) (**Figure 26**). Histological analysis of these brains revealed differences on overall tumor appearance, as smaller cerebellar tumor formation was observed in the cerebella of *Math1-cre::Dnmt1*$^{Fl/Fl}$*::SmoM2*$^{Fl/+}$ mice with favorable survival outcome (**Figure 27**). Overall, our *in vivo* data highlight that *Dnmt1* plays a critical role in GCNP-derived SHH-MB progression in mice.

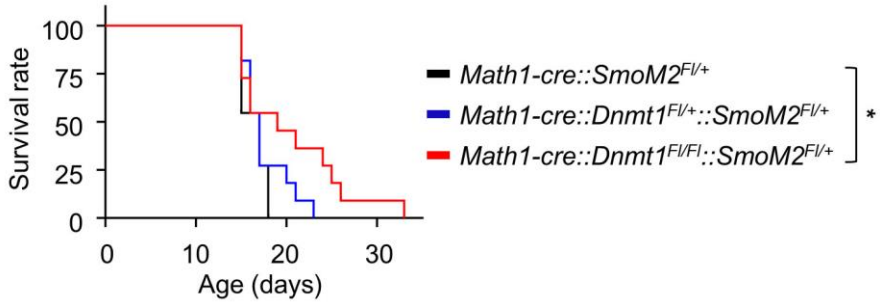

Figure 26. *Dnmt1* knockout prolongs survival of SHH-MB mice. Kaplan-Meier curve of *Math1-cre::SmoM2*$^{Fl/+}$ (n = 11), *Math1-cre::Dnmt1*$^{Fl/+}$*::SmoM2*$^{Fl/+}$ (n = 11) and *Math1-cre::Dnmt1*$^{Fl/Fl}$*::SmoM2*$^{Fl/+}$ mice (n=11). Significance in survival was determined using the log rank (Mantel-Cox) test (* $p \leq 0.05$) (Tsiami et al., 2024).

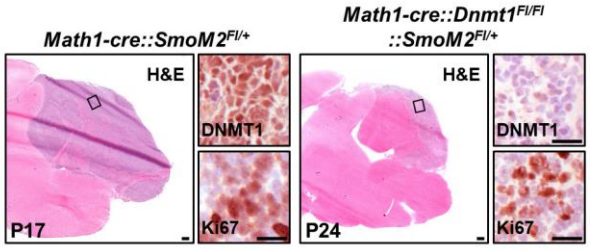

Figure 27. Genetic loss of *Dnmt1 in vivo*. H&E-stained cerebellar tumors from *Math1-cre::SmoM2*$^{Fl/+}$ (left) and *Math1-cre::Dnmt1*$^{Fl/Fl}$*::SmoM2*$^{Fl/+}$ (right) mice at different endpoints. Immunohistochemistry for DNMT1-

C (upper panel) and Ki67 (lower panel) in tumors from these mice are indicated. 4x magnification, scale bar, 500µm; 20x magnification, scale bar, 50µm.

3.2.5 Synergistic action of SMO and DNMT1 inhibition in suppressing SHH-MB proliferation

Having explored the promising anti-tumor effects of DNMT1 inhibition in SHH-MB, our next goal was to unravel potential synergistic partners of 5-AzaC that could serve as combinatorial treatments for this tumor entity.

To achieve this, we carried out an additional CRISPR-Cas9 knockout screen in SMB21 cells on a genome-scale under 5-AzaC treatment, in order to identify depleted genes, which synergize with 5-AzaC in suppressing cancer cell viability. Similar to the dependency screen, Cas9-expressing SMB21 cells were transduced with lentiviral murine library Brie and following puromycin selection, cells were split into DMSO control and 5-AzaC arms. First, analysis of the distribution of pan- and non-essential genes in the DMSO arm showed depletion of pan-essentials and LFC close to zero for all non-essentials, indicating good screen performance (**Figure 28A**). To identify potential drug modifiers, we first compared both drug and DMSO arms to the reference plasmid. *Smo* was highly depleted in the DMSO arm vs reference plasmid comparison (β score = -1.98), further corroborating our previous dependency screen findings, while it displayed an even more robust depletion in the 5-AzaC versus reference plasmid comparison (β score = -3.48) (**Figure 28B**). Moreover, when comparing the drug arm to DMSO control, we deciphered *Smo* as the top depleted hit in 5-AzaC-treated cells with the highest negative β score at FDR=0 (**Figure 28C**). On the sgRNA level, all four different sgRNAs targeting *Smo* had lower counts in the 5-AzaC-treated cells, as compared to DMSO arm (**Figure 28D**). All together our screening data indicate that loss of *Smo* sensitizes SMB21 cells to 5-AzaC treatment.

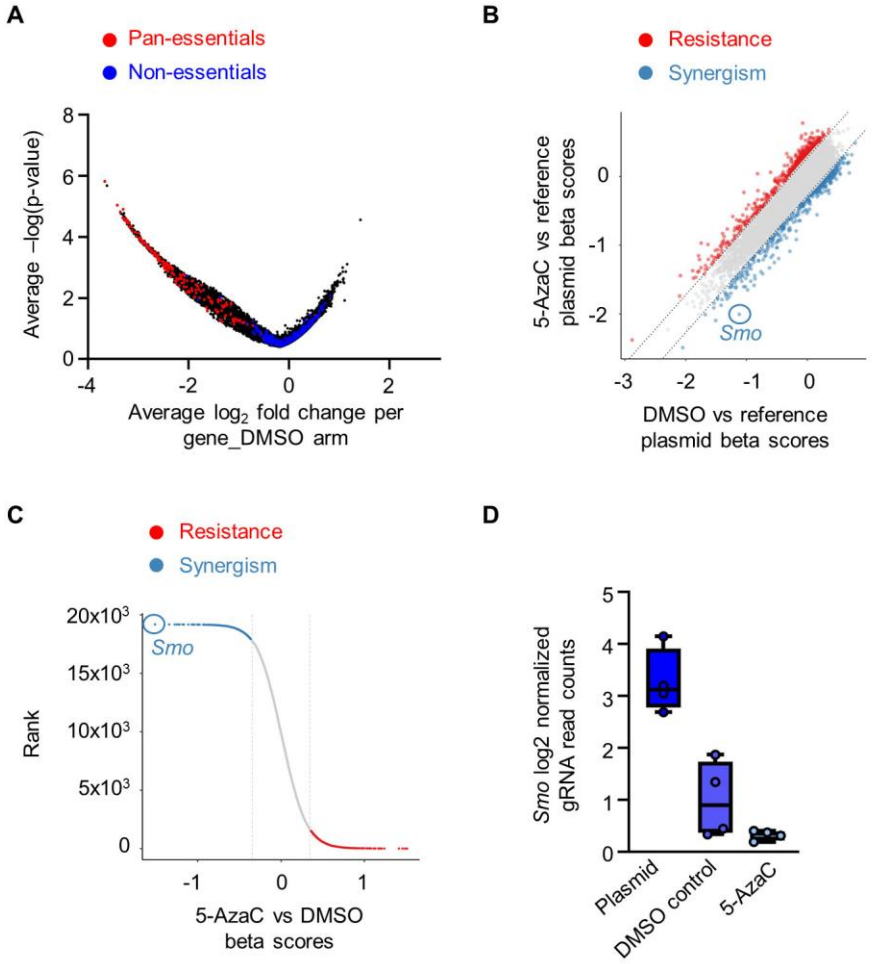

Figure 28. CRISPR-Cas9 drug screen identifies *Smo* knockout as a synergistic partner for 5-Azacytidine. (**A**) Volcano plot illustrating log_2fold change and associated p values per gene in DMSO ctr-treated SMB21 cells, when compared to the reference plasmid, using the hypergeometric distribution method. Red data points indicate pan-essential genes and blue ones depict non-essential genes. (**B**) Scatter plot illustrating correlation of beta scores of 5-AzaC-treated cells (y axis) and DMSO control-treated cells (x axis) compared to the reference plasmid. Red data points indicate potential resistance hits against 5-AzaC and blue data points depict potential synergistic hits for 5-AzaC. Dotted lines represent 1.5-fold standard deviation. (**C**) Rank plot of genes in the 5-AzaC arm ranked by their beta score, as compared to DMSO control´s beta scores. Red data points indicated positively selected genes and blue data points negatively selected. Dotted lines represent 1.5-fold standard deviation. (**D**) Box plots depicting the log_2 normalized read counts per single guide RNA targeting *Smo* in the reference plasmid, DMSO control and 5-AzaC arms. Data are shown as box plots with whiskers representing minimum and maximum data point per group (Tsiami et al., 2024).

We next aimed to pharmacologically validate the drug screen findings *in vitro*, by evaluating combination treatment of 5-AzaC and LDE-225 in SMB cells. Acute cytotoxicity assays

demonstrated that both inhibitors acted synergistically in inhibiting SMB21 and SMB55 proliferation, as deduced from their positive mean synergy scores, 11.7 and 10.46, respectively (**Figure 29, Supplementary figure 8A**).

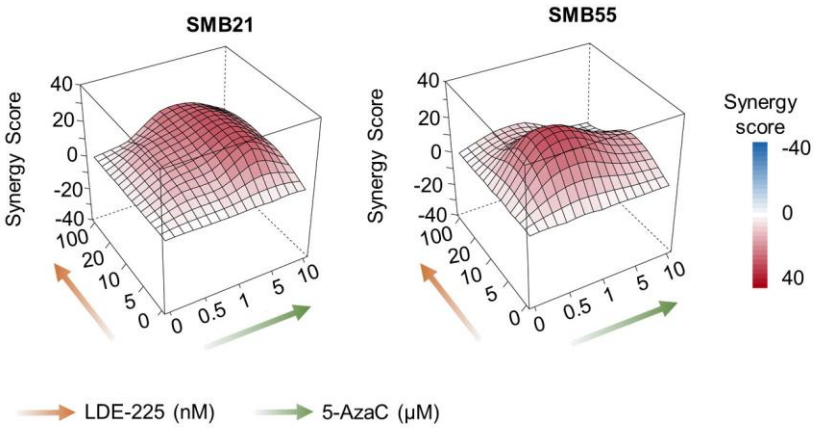

Figure 29. Synergistic effects of LDE-225 and 5-Azacytidine combination treatment. Three-dimensional (3D) interaction landscapes evaluating drug combination of LDE-225 and 5-AzaC in SMB21 (left) and SMB55 (right) cells (n=5). Gradient arrows represent concentration range of LDE-225 (orange) and 5-AzaC (green) applied to the cells. Synergism was calculated based on the ZIP model using *synergyfiner* R package (Tsiami et al., 2024).

When it comes to combination treatments in cancer research, often drugs are administered simultaneously in order to optimize their anti-tumor efficacy (Miles et al., 2002, Zhang et al., 2014, Alcon et al., 2020). For this reason, we evaluated whether the synergistic effect of 5-AzaC and LDE-225 is increased when applied simultaneously or sequentially (**Figure 30**). Drug proliferation assays of SMB21 cells showed that both sequential treatments did not differ from their corresponding monotherapies, while simultaneous combination treatment was significantly more cytotoxic than both sequential treatments, suggesting that DNMT1 and SMO inhibition enhance their cytotoxic effects on SMB cells, when combined simultaneously.

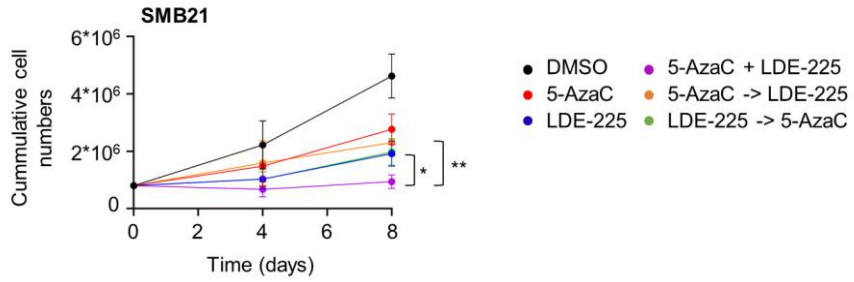

Figure 30. Simultaneous vs sequential combination treatment of LDE-225 and 5-Azacytidine. (A) 8-day proliferation assay evaluating 5-AzaC monotherapy, LDE-225 monotherapy, as well as simultaneous and sequential combinatorial treatment of both drugs in SMB21 cells. Two-way ANOVA, Tukey´s multiple comparisons test (n = 5). Graphs display mean ± SD values. * $p \leq 0.05$, ** $p \leq 0.01$ (Tsiami et al., 2024).

Additionally, we investigated whether combination therapy affects SHH pathway activation. Following treatment with 5-AzaC monotherapy, LDE-225 monotherapy or combination of both inhibitors for 48 hours, we evaluated GLI1 protein levels in SMB21 cells via western blotting (**Figure 31A, B**). We found that combination treatment reduced GLI1 expression at levels that differed significantly from the effect of both monotherapies, providing evidence on their synergistic interaction in blocking SHH pathway activation.

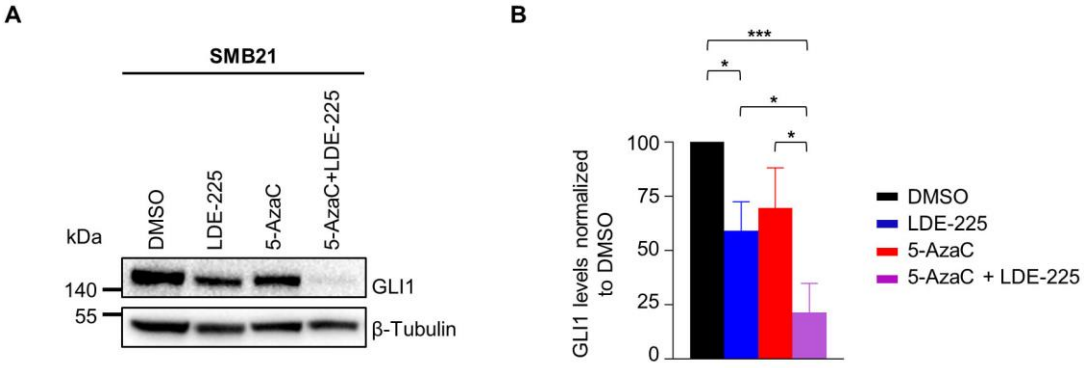

Figure 31. Combination treatment of LDE-225 and 5-Azacytidine inhibits SHH pathway output. (**A**) Representative western blotting analyses of GLI1 protein in SMB21 cells treated with indicated drugs for 48 hours. (**B**) Quantification of GLI1 levels shown in (**A**). Two-way ANOVA, Tukey´s multiple comparisons test (n = 3). Graphs display mean ± SD values. * $p \leq 0.05$, ** $p \leq 0.01$, *** $p \leq 0.001$ (Tsiami et al., 2024).

Furthermore, we assessed combination treatment of both drugs in SMO inhibitor-resistant cells. Notably, no synergism was observed in SMB21 *Sufu* KO cells (synergy score= 2.7) (**Figure 32A,**

Supplementary figure 8B). Combination treatment reduced cell viability and GLI1 expression to similar levels as 5-AzaC monotherapy, indicating that this inhibitory effect is driven by 5-AzaC alone (**Figure 32B-D**). Thus, we demonstrate that the synergistic effect of combination treatment is only efficacious in SMO inhibition-sensitive SHH-MB models.

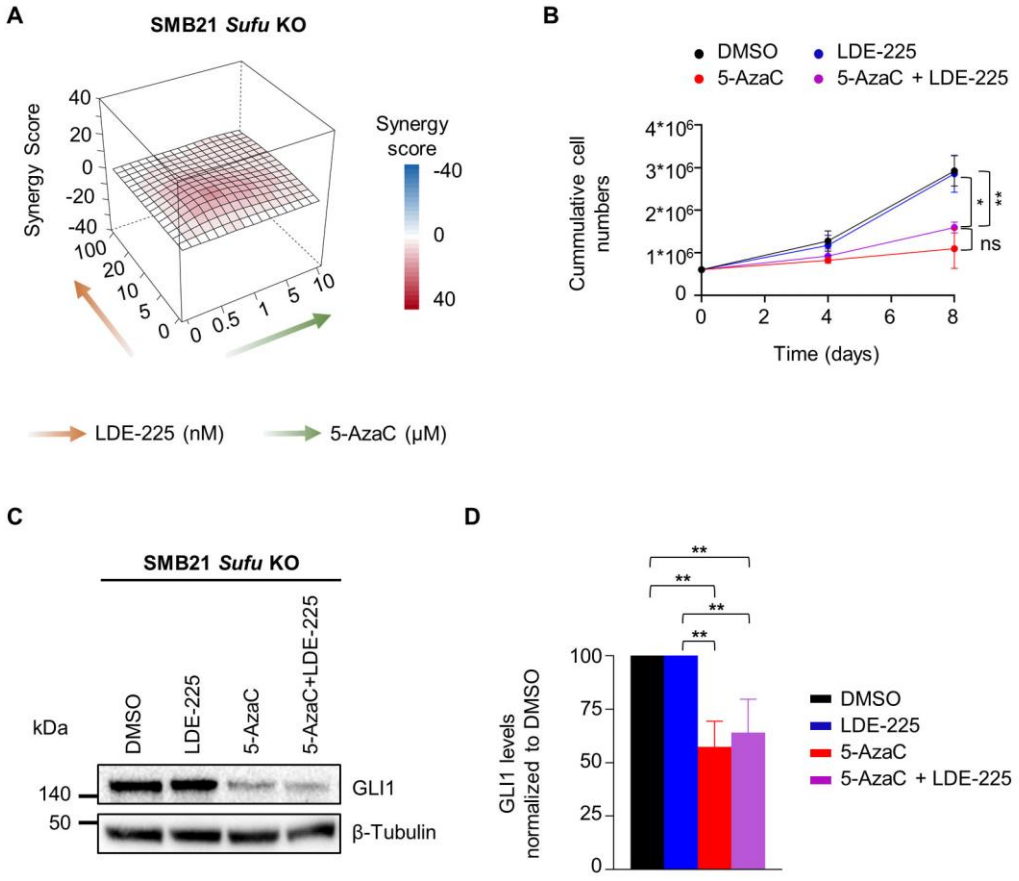

Figure 32. LDE-225 and 5-Azacytidine combination treatment is not efficacious in SMO inhibition-resistant SMB cells. (**A**) 3D interaction landscape evaluating LDE-225 and 5-Azacytidine combination treatment in SMB21 *Sufu* KO cells (n=5) based on ZIP model. Gradient arrows represent concentration range of LDE-225 (orange) and 5-AzaC (green) applied to the cells. (**B**) Proliferation assay assessing LDE-225 monotherapy, 5-AzaC monotherapy, as well as drug combination treatment in SMB21 *Sufu* KO cells for 8 days. Two-way ANOVA, Tukey´s multiple comparisons test (n = 4). (**C**) Representative western blots depicting GLI1 protein in SMB21 *Sufu* KO cells treated with indicated drugs for 48 hours. (**D**) Quantification of GLI1 levels shown in (**C**). Two-way ANOVA, Tukey´s multiple comparisons test (n = 3). Graphs display mean ± SD values. * $p \leq 0.05$, ** $p \leq 0.01$ (Tsiami et al., 2024).

To further substantiate the translational potential of our findings, we evaluated both monotherapies and combination treatment in a patient-derived xenograft organoid (PDXO) model, which recapitulates hallmark features of SHH subgroup of MB (Lago et al., 2023). Immunohistochemical analysis for Ki67 marker at the end of the 1-week treatment revealed reduced tumor proliferation under 5-AzaC and LDE-225 monotherapies, while simultaneous combination treatment of both drugs was more potent in suppressing tumor proliferation than both monotherapies (**Figure 33A, B**).

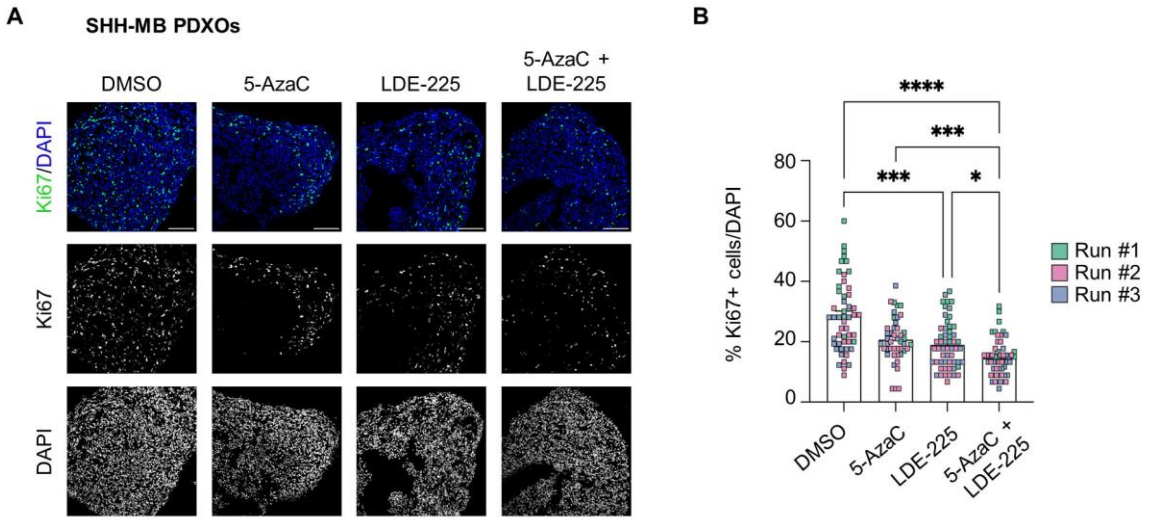

Figure 33. Synergistic effects of LDE-225 and 5-Azacytidine combination treatment in patient-derived xenograft organoids representing SHH-MB. (**A**) Exemplary confocal images of SHH-MB PDXOs treated with 5-AzaC monotherapy, LDE-225 monotherapy, simultaneous combinatorial treatment of both drugs or DMSO control. Organoids were stained for DAPI and Ki67 7 days post drug treatment. (**B**) Quantification of the fraction of Ki67-positive cells in SHH-MB PDXOs shown in (**A**). Different replicates are color-coded (n = 3, Kruskal–Wallis test). Graphs display mean ± sem. * $p \leq 0.05$, *** $p \leq 0.001$, **** $p \leq 0.0001$ (Tsiami et al., 2024).

Having shown that combination therapy of LDE-225 and 5-AzaC exerts synergistic effects in both murine and human SHH-MB cell models, we next aimed to investigate this treatment approach in a human non-SHH MB cell model. To this end, we made use of a previously described Group 3-driven MB PDXO model (Lago et al., 2023). As expected, unlike SHH-MB cells, Group 3-MB cells were not sensitive to SMO inhibition (**Figure 34A, B**). DNMT1 inhibition alone significantly blocked tumor proliferation, while no difference in suppressed tumor proliferation was observed between

combination therapy and 5-AzaC monotherapy, suggesting that synergistic effects of SMO and DNMT1 inhibition are only efficacious in tumor cells with active SHH signaling.

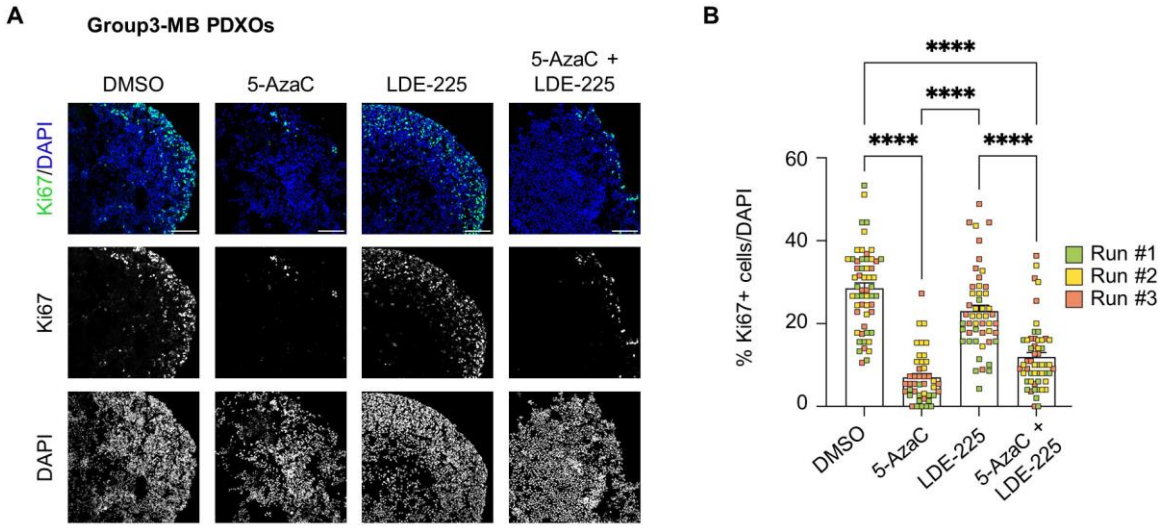

Figure 34. Evaluation of combined therapy of LDE-225 and 5-Azacytidine in patient-derived xenograft organoids representing Group 3-MB. (**A**) Representative confocal images of Group 3-MB PDXOs treated with 5-AzaC monotherapy, LDE-225 monotherapy, simultaneous combinatorial treatment of both drugs or DMSO control. Organoids were stained for DAPI and Ki67 7 days post drug treatment. (**B**) Quantification of the fraction of Ki67-positive cells in Group 3-MB PDXOs shown in (**A**). Different replicates are color-coded (n = 3, Kruskal-Wallis test). Graphs display mean ± sem. **** $p \leq 0.0001$ (Tsiami et al., 2024).

Finally, we investigated DNMT1 inhibition alone or in combination with SMO inhibition as a potential treatment option for SHH-MB *in vivo*. To ensure an efficient therapeutic time window in adult mice, we used a TAM-inducible *Math1-creER*^{T2} mouse line (Machold and Fishell, 2005) to generate a previously established mouse model of SHH-MB (Merk et al., 2018). After inducing Cre activity at P5, *Math1-creER*^{T2}*::SmoM2*$^{Fl/+}$ mice were randomized into vehicle control group, 5-AzaC monotherapy, LDE-225 monotherapy or simultaneous combination treatment, as determined earlier, and treated for 3 weeks consecutively starting from P50 (**Figure 35A**). Survival analysis revealed a significant survival benefit of mice treated with either 5-AzaC or LDE-225 ($P_{5\text{-}AzaC}$= 0.0073 and $P_{LDE\text{-}225}$= 0.0014, respectively), when compared to vehicle control group, while no difference was observed between the monotherapies (P= 0.0729) (**Figure 35B**). Combination-treated mice also exhibited a significantly prolonged survival outcome compared to both the control (P= 0.0001) and 5-AzaC groups (P= 0.0134), however, their survival did not differ significantly from the LDE-225-treated group (P= 0.9099).

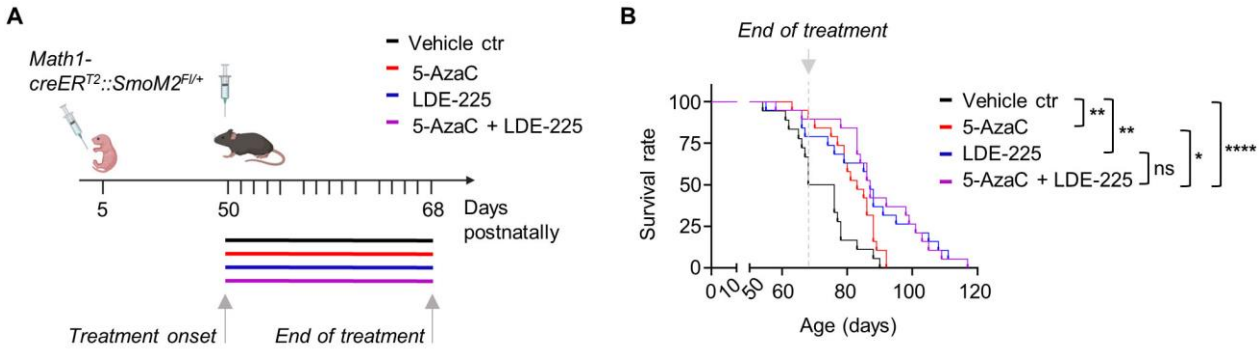

Figure 35. Evaluating DNMT1 inhibition alone or in combination with SMO inhibition in a SHH-MB mouse model. (**A**) Schematic representation of tumor induction and drug treatment timeline in *Math1-creER^{T2}::SmoM2$^{Fl/+}$* mice. (**B**) Kaplan-Meier curve of *Math1-creER^{T2}::SmoM2$^{Fl/+}$* mice treated with 5-Azacytidine monotherapy (n = 19), LDE225 monotherapy (n = 19), drug combination treatment (n = 19), and vehicle control (n = 18). Vertical dashed line indiacates the last day of treatment. Significance in survival as compared to vehicle-treated mice was determined using the log rank (Mantel-Cox) test. * $p \leq 0.05$, ** $p \leq 0.01$, **** $p \leq 0.0001$ (Tsiami et al., 2024).

To gain further insight into the treatment effects on tumor growth, we histologically analyzed murine brains at P68, the last day of the treatment schedule (**Figure 36A**). First, we evaluated relative tumor to total cerebellar area and show that mice treated with combination of both inhibitors displayed a remarkable reduction in tumor size at the last day of the treatment, differing significantly from either monotherapies or vehicle control groups (**Figure 36B**).

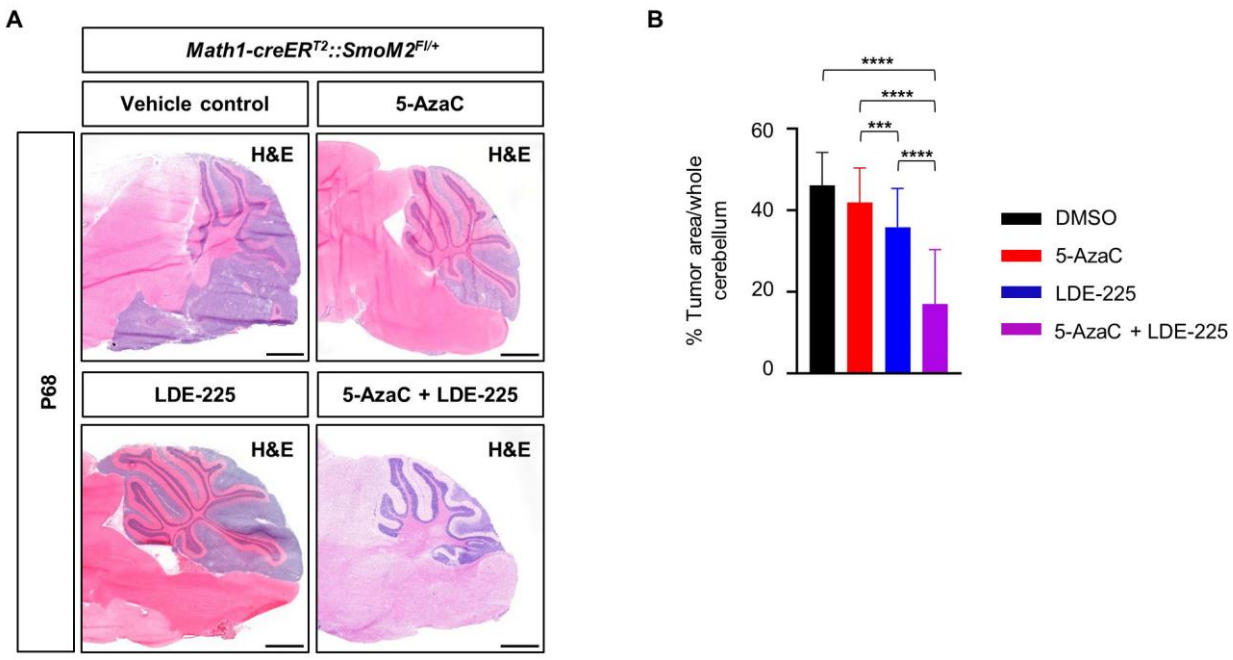

Figure 36. LDE-225 and 5-Azacytidine combination treatment reduce SHH-MB growth *in vivo*. (**A**) Representative H&E stainings of whole cerebellar tumors from *Math1-creER^{T2}::SmoM2$^{Fl/+}$* mice at P68. 4x magnification, scale bar, 500μm. (**B**) Percentage of relative tumor area to whole cerebellum in *Math1-creER^{T2}::SmoM2$^{Fl/+}$* mice from indicated groups at P68 (n=3, one-way ANOVA with Tukey´s multiple comparisons). Graph displays mean ± SD values. *** p ≤ 0.001, **** p ≤ 0.0001 (Tsiami et al., 2024).

Moreover, these brains were further evaluated in regard to tumor proliferation via immunostaining for Ki67 marker (**Figure 37A, B**). Both 5-AzaC and LDE-225 monotherapy groups exhibited a significant decrease in tumor proliferating cells in the cerebella of these mice, when compared to the control group, without statistically differing from each other. A significant reduction in the fraction of tumor proliferating cells was also detected in mice treated with combination of DNMT1 and SMO inhibition, as compared to all treatment groups.

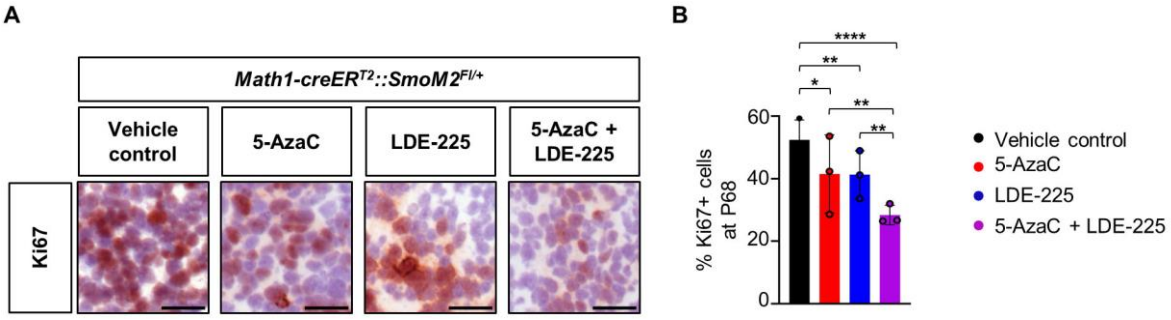

Figure 37. LDE-225 and 5-Azacytidine combination treatment mitigates SHH-MB proliferation *in vivo*. (**A**) Representative cerebellar tumors from *Math1-creER^{T2}::SmoM2$^{Fl/+}$* mice stained with Ki67 marker at P68. 20x magnification, scale bar, 50µm. (**B**) Graph illustrating percentage of Ki67-positive cells in tumors shown in (**A**), (n = 3, Fisher´s exact test). Graph displays mean ± SD values. * $p \leq 0.05$, ** $p \leq 0.01$, **** $p \leq 0.0001$ (Tsiami et al., 2024).

No significance was detected in the percentage of apoptotic cells in any of the four groups, as determined via immunostaining for cleaved caspase 3 (**Figure 38A, B**).

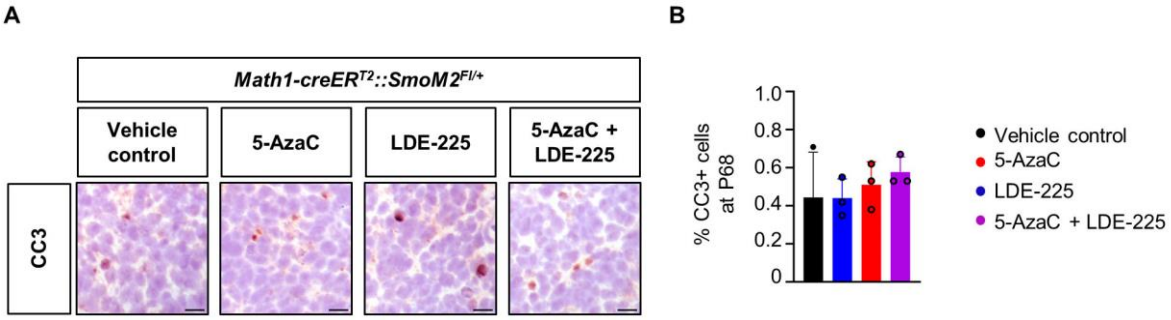

Figure 38. LDE-225 and 5-Azacytidine combination treatment does not induce apoptosis in SHH-MB tumors *in vivo*. (**A**) Representative cerebellar tumors from *Math1-creER^{T2}::SmoM2$^{Fl/+}$* mice stained with cleaved caspase marker at P68. 20x magnification, scale bar, 50µm. (**B**) Graph illustrating percentage of cleaved caspase 3-positive cells in tumors shown in (**A**), (n = 3, Fisher´s exact test). Graph displays mean ± SD values.

Last, tumor tissue was collected from *Math1-creER^{T2}::SmoM2$^{Fl/+}$* mice of all treatment groups at P68 for further analysis (**Figure 39**). Western blotting demonstrated the most prominent reduction of GLI1 protein levels in mice treated with combination of 5-AzaC and LDE-225, as compared to vehicle control group, further indicating that combination therapy inhibits SHH pathway activation.

Similarly, protein levels of proliferating marker, PCNA, also displayed a strong decrease in the combination treatment group, corroborating the immunohistochemical results.

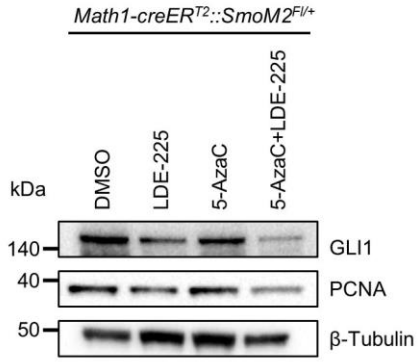

Figure 39. Protein analysis of harvested cerebellar tumors from *Math1-creER^{T2}::SmoM2$^{Fl/+}$* mice at P68. Western blots depicting GLI1 and PCNA protein levels in cerebellar tumors harvested from *Math1-creER^{T2}::SmoM2$^{Fl/+}$* mice treated with indicated drugs (Tsiami et al., 2024).

To summarize, we present that treatment modalities involving DNMT1 inhibition efficaciously inhibit tumor growth in a preclinical mouse model of SHH-MB. These anti-tumor effects are further enhanced upon combination of DNMT1 inhibition with SMO inhibition, thereby resulting in SHH signalling blockade.

3.3 *Smarca5* as a genetic vulnerability for SHH-MB

3.3.1 *Smarca5* is required for SHH-MB survival *in vitro*

In addition to epigenetic regulator DNMT1 emerging as a SHH-MB-genetic vulnerability, remarkably six members of the SNF2-family of ATP-dependent chromatin remodelers also scored highly in the dropout screen performed in SMB21 cells, including *Smarca4* ($LFC_{MAGeCK\text{-}RRA}$ = -1.76), *Smarca5* ($LFC_{MAGeCK\text{-}RRA}$ = -1.82) and *Smarca6* ($LFC_{MAGeCK\text{-}RRA}$ = -0.54) (**Figure 40A-C**).

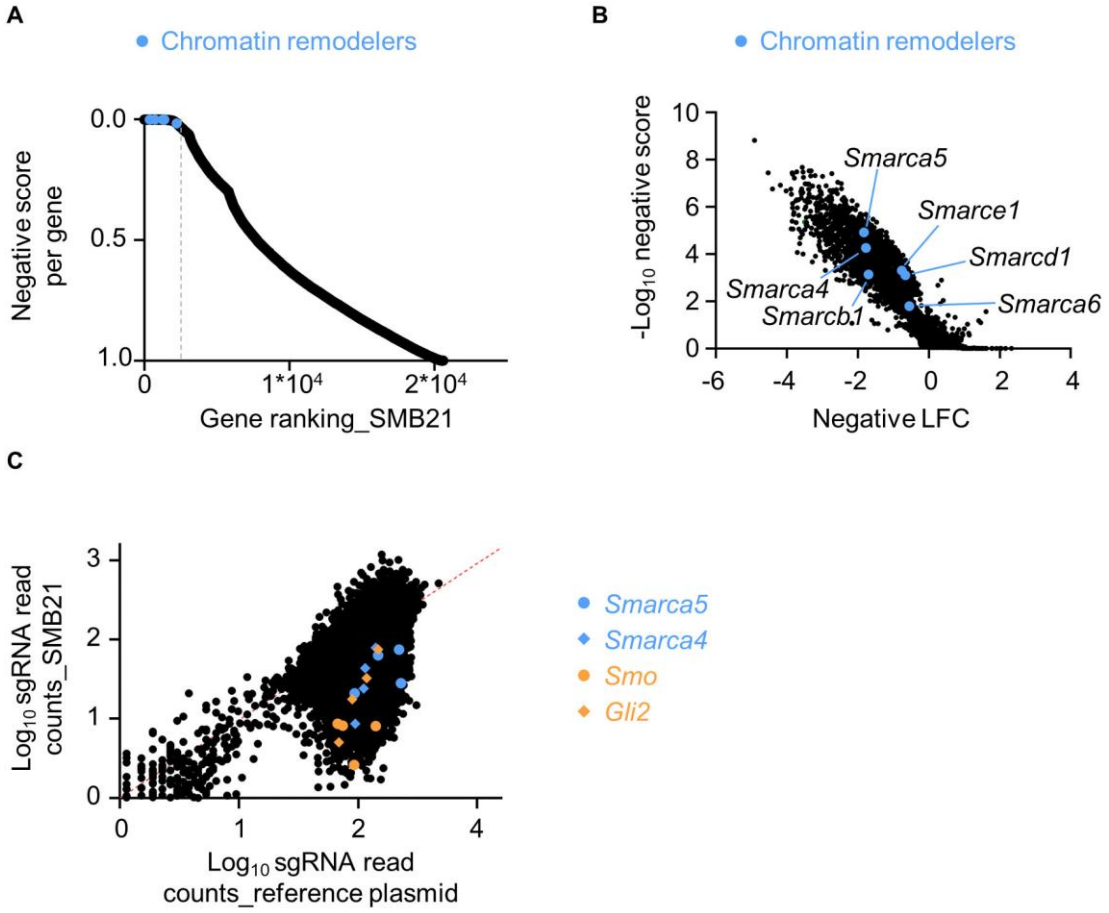

Figure 40. ATP-dependent chromatin remodelers emerge as SMB21 genetic dependencies. (**A**) Ranking plot depicting 6 chromatin remodelers (light blue data points) scoring among the most depleted genes below 5% FDR in SMB21-screened cells. (**B**) Volcano plot illustrating negative scores and corresponding negative log2fold change of chromatin remodelers, as determined by MAGeCK-RRA. (**C**). Scatterplot demonstrating uniform depletion of different sgRNAs targeting chromatin remodelers (light blue data points) and SHH-positive regulators (orange data points).

Analysis of a publicly available microarray dataset revealed that among these genes, *SMARCA5* expression was significantly higher in patient-derived tissue belonging to SHH subgroup (Cavalli et al., 2017), as compared to the rest consensus MB subgroups (**Supplementary figure 9**). Similarly, *SMARCA6* also displayed a significantly higher expression in SHH subgroup, as previously shown (Robinson et al., 2019). Interrogation of additional microarray datasets (Griesinger et al., 2013, Gump et al., 2015) revealed higher *SMARCA5* expression in primary human MB tissue than other CNS tumor-derived and healthy brain tissue, while within four SHH-MB subtypes, lower expression was observed in SHH-γ (SHH-2) tumors (**Supplementary figure 10**), which have a better prognosis than α and β subtypes. No survival benefit was detected in MB

patients assigned to low and high *SMARCA5* expression in any of the four subgroups (**Supplementary figure 11**). These data along with a previous study demonstrating that loss of *Smarca5* leads to cerebellar hypoplasia (Alvarez-Saavedra et al., 2014) prompted us to further elucidate the role of *Smarca5* in SHH-MB progression.

To validate the screening findings, we generated SMB21 cells with loss of *Smarca5* using the CRISPR-Cas9 system. We first evaluated their proliferative capacity and show that *Smarca5* knockdown significantly inhibits SMB viability, as compared to parental SMB21 cells (**Figure 41A**). Reduction of cell viability did not differ from the effect of *Smo* knockdown, overall suggesting that *Smarca5* is essential for SMB survival. Furthermore, we sought to answer whether loss of *Smarca5* affects SHH pathway, by assessing GLI1 expression via western blotting. We show that loss of *Smarca5* and *Smo* reduced GLI1 protein expression at similar levels, differing significantly from parental cells (**Figure 41B, C**). Taken together, our screening data in combination with our genetic validation experiments portray that *Smarca5* is required for SHH-MB proliferation *in vitro*, by regulating SHH signaling.

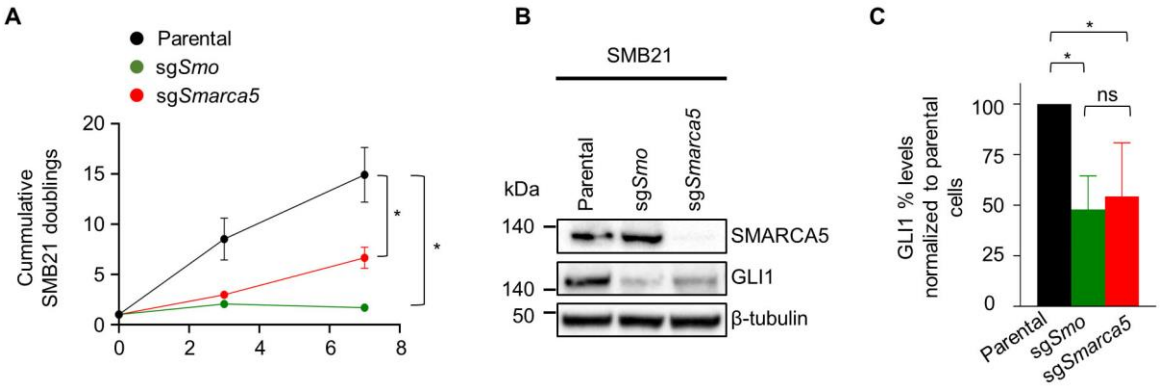

Figure 41. Genetic ablation of *Smarca5* in SMB cells. (**A**) Analyses of cell population doublings for SMB21 cells transduced with the indicated sgRNA constructs over 7 days, as compared to SMB21 parental cells. (**B**) Western blotting illustrating SMARCA5 and GLI1 protein levels in SMB21 parental and sgRNA-transduced cells. (**C**) GLI1 protein quantification shown in (**B**). Two-way ANOVA, Tukey´s multiple comparisons tests (n = 3). Graphs display mean ± SD values. *$p \leq 0.05$.

3.3.2 Loss of *Smarca5* in GCNPs impairs murine cerebellar development

While our *in vitro* data provided us with strong evidence that SMB cells depend on chromatin remodeler *Smarca5* for their proliferation and survival, we further explored its function in regard to murine cerebellar development. For that, we generated *Math1-cre::Smarca5*$^{Fl/+}$ and *Math1-*

cre::Smarca5$^{Fl/Fl}$ mice using Math1 promoter, in order to ensure *Smarca5* depletion in GCNPs, as described before (Machold and Fishell, 2005, Alvarez-Saavedra et al., 2014). We first validated the expression of SMARCA5 in proliferating GCNPs of the EGL, as well as neurons of the IGL in the cerebella of *Math1-cre* and *Math1-cre::Smarca5*$^{Fl/+}$ mice at P5, while its expression was absent in *Math1-cre::Smarca5*$^{Fl/Fl}$ mice (**Figure 42**).

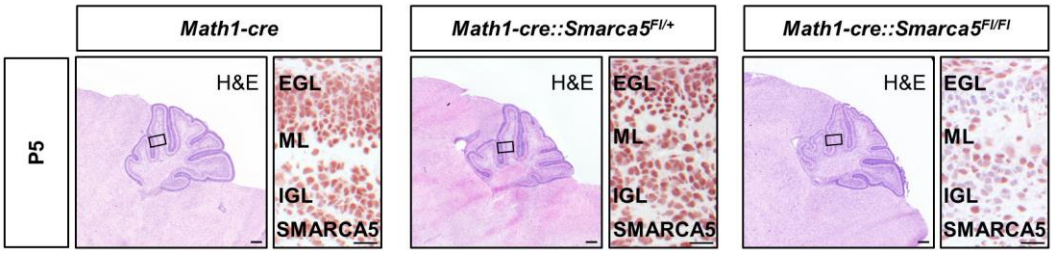

Figure 42. Genetic loss of *Smarca5* in granule cell neuron precursors at P5. Representative overview cerebella from *Math1-cre, Math1-cre::Smarca5*$^{Fl/+}$ and *Math1-cre::Smarca5*$^{Fl/Fl}$ mice stained with H&E, as well as SMARCA5 immunomarker at indicated magnified regions. 4x magnification, scale bar, 500µm; 20x magnification, scale bar, 50µm. EGL, external granular layer; ML, molecular layer; IGL, internal granular layer.

At P5, examination of H&E-stained cerebella revealed a thinner external granule cell layer in the anterior part of the cerebellum of *Math1-cre::Smarca5*$^{Fl/+}$ mice (**Figure 42**), as confirmed by a significant reduction in GCNP proliferating cells in the EGL of these mice (**Figure 43A**). In addition to deficits in proliferation, we also observed a significant increase in granule cell apoptosis in the EGL of *Smarca5*-homozygously depleted mice (**Figure 43B**)

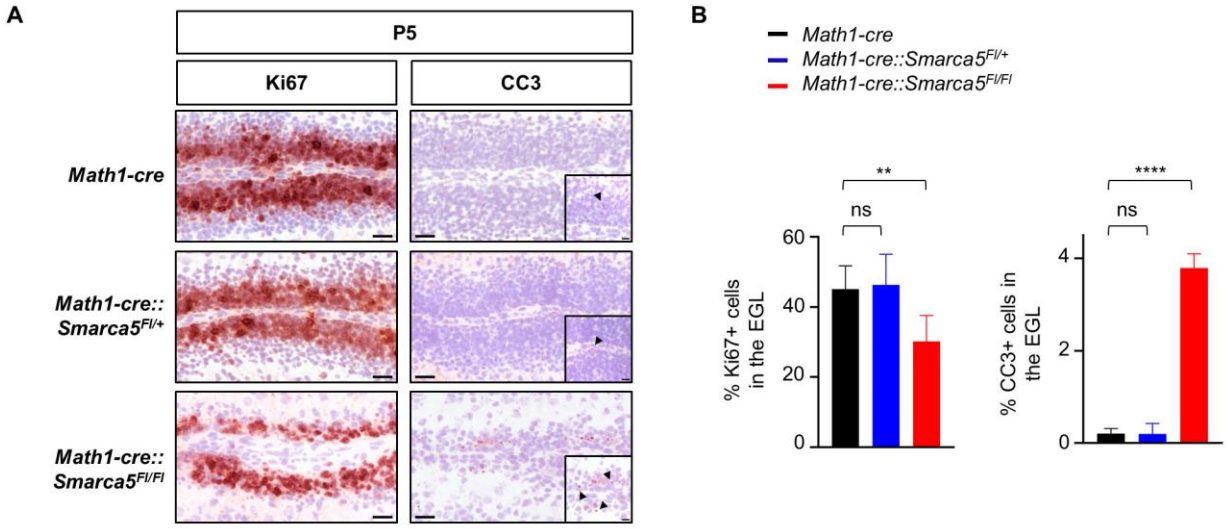

Figure 43. *Smarca5* knockout reduces viability of granule cell neuron precursors. (**A**) Representative images of EGL from *Math1-cre, Math1-cre::Smarca5*$^{Fl/+}$ and *Math1-cre::Smarca5*$^{Fl/Fl}$ mice stained with Ki67 (left panel) and cleaved caspase 3 (right panel) immunomarkers at P5. (**B**) Quantification of Ki67- (left panel) and cleaved caspase 3-positive (right panel) cells in the EGL of mice shown in (**A**). 20x magnification, scale bar, 50µm; 40x magnification, scale bar, 20µm. EGL, external granular layer; ML, molecular layer; IGL, internal granular layer. All graphs display mean ± SD values. ** $p \leq 0.01$, **** $p \leq 0.0001$.

Besides P5, we also histologically analysed these mouse groups at a later time point, P21. *Math1-cre::Smarca5*$^{Fl/Fl}$ mice, similar to adult *Math1-cre::Dnmt1*$^{Fl/Fl}$ mice suffered from severe cerebellar hypoplasia, a malformation not observed in *Math1-cre::Smarca5*$^{Fl/+}$ mice (**Figure 44**).

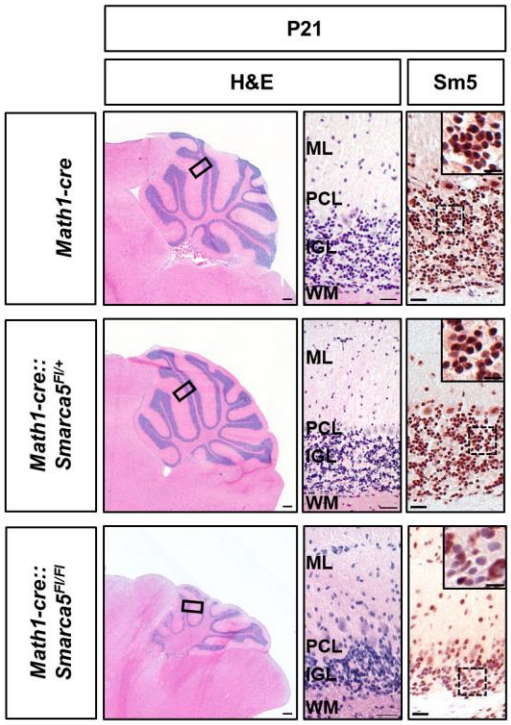

Figure 44. *Smarca5* depletion in granule cell neuron precursors results in cerebellar hypoplasia. Representative H&E stainings of whole cerebella from *Math1-cre, Math1-cre::Smarca5*$^{Fl/+}$ and *Math1-cre::Smarca5*$^{Fl/Fl}$ mice at P21, as well as immunostaining for SMARCA5. 4x magnification, scale bar, 500µm; 20x magnification, scale bar, 50µm; 40x magnification, scale bar, 20µm. ML, molecular layer; PCL, Purkinje cell layer; IGL, internal granular layer; WM, white matter.

Immunostaining analyses revealed a significant increase in NeuN- and Pax6-positive cells in the molecular layer of cerebella of *Math1-cre::Smarca5*$^{Fl/Fl}$ mice, suggesting that *Smarca5* ablation disrupted migration of mature granule neurons towards the IGL (**Figure 45A, B**). No proliferating cells were detected in any of these mouse groups. Well in line with a previous study (Alvarez-Saavedra et al., 2014), our *in* vivo findings demonstrate that *Smarca5* plays an essential role in proliferation and migration of GCNPs during early postnatal cerebellar development.

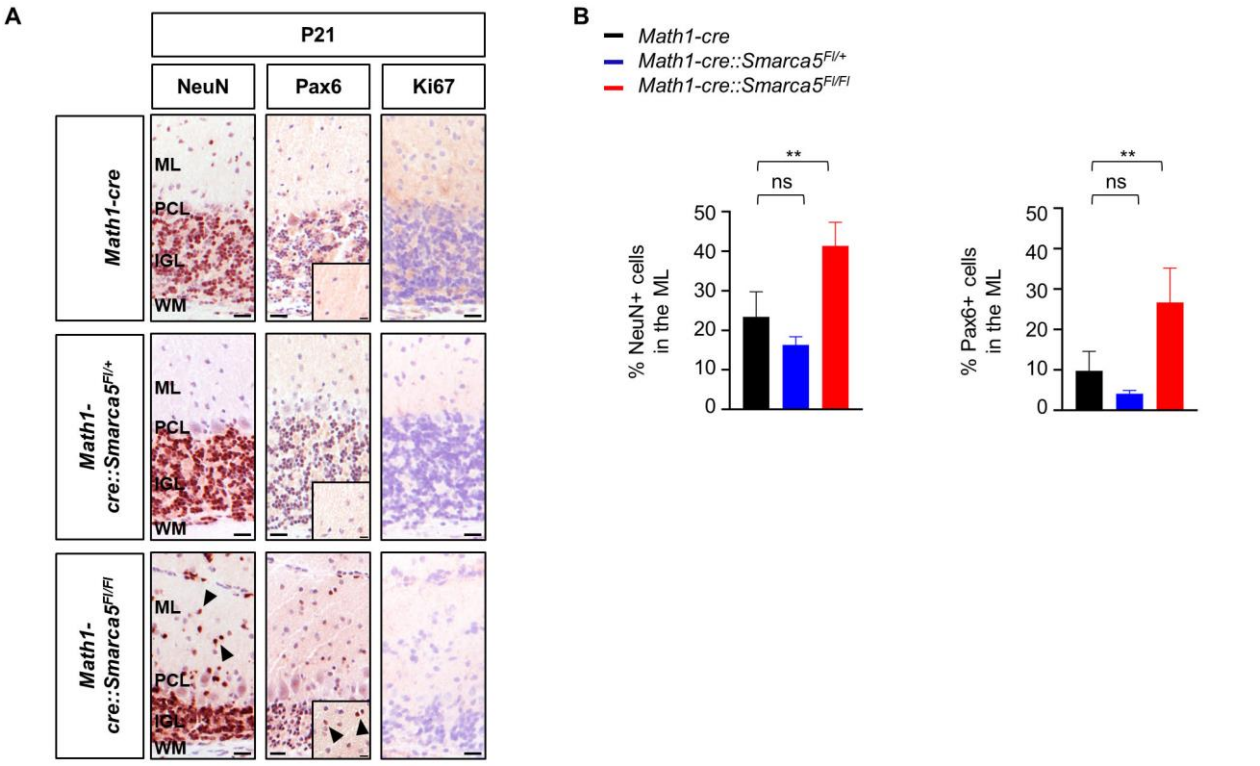

Figure 45. Genetic loss of *Smarca5* impairs migration of granule cell neuron precursors. (**A**) Exemplary cerebella from *Math1-cre, Math1-cre::Smarca5*$^{Fl/+}$ and *Math1-cre::Smarca5*$^{Fl/Fl}$ mice at P21 stained with NeuN, Pax6 and Ki67. (**B**) Quantification of NeuN- (left panel) and Pax6-positive (right panel) cells, as shown in (**A**). 20x magnification, scale bar, 50µm. 40x magnification, scale bar, 20µm. ML, molecular layer; PCL, Purkinje cell layer; IGL, internal granular layer; WM, white matter. All graphs display mean ± SD values (** $p \leq 0.01$).

3.3.3 *Smarca5* knockout reduces SHH-MB proliferation *in vivo*

Having validated that *Smarca5* has an impact on murine cerebellar formation, we proceeded to determine its role in SHH-MB growth *in vivo*. Likewise, using the Math1 promoter, we specifically ablated *Smarca5* in GCNPs in *Math1-cre::SmoM2*$^{Fl/+}$ mice, an established model of SHH-MB (Mao et al., 2006), thus generating *Math1-cre::Smarca5*$^{Fl/+}$*::SmoM2*$^{Fl/+}$ and *Math1-cre::Smarca5*$^{Fl/Fl}$*::SmoM2*$^{Fl/+}$ mice with evident tumor morphology (**Figure 46**).

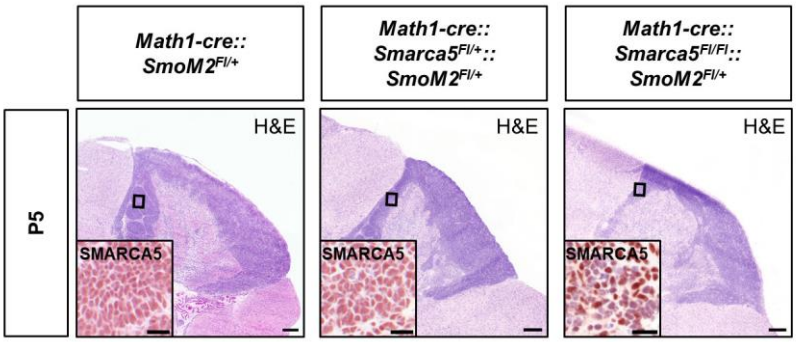

Figure 46. *Smarca5* depletion in SHH-MB mice. Whole cerebellar tumors from *Math1-cre::SmoM2*$^{Fl/+}$, *Math1-cre::Smarca5*$^{Fl/+}$*::SmoM2*$^{Fl/+}$ and *Math1-cre::Smarca5*$^{Fl/Fl}$*::SmoM2*$^{Fl/+}$ mice stained H&E at P5. Maginified regions indicate immunostaining for SMARCA5 marker. 4x magnification, scale bar, 500μm; 20x magnification, scale bar, 50μm.

Cerebellar tumors of these mice were examined via immunohistology at P5 (**Figure 47A, B**). *Math1-cre::Smarca5*$^{Fl/Fl}$*::SmoM2*$^{Fl/+}$ mice exhibited a significant decrease in tumor proliferating cells in their cerebella when compared to tumor control group, as determined using Ki67 marker. In parallel, a significant increase in apoptotic cells was observed in tumors from both *Math1-cre::Smarca5*$^{Fl/+}$*::SmoM2*$^{Fl/+}$ and *Math1-cre::Smarca5*$^{Fl/Fl}$*::SmoM2*$^{Fl/+}$ mice.

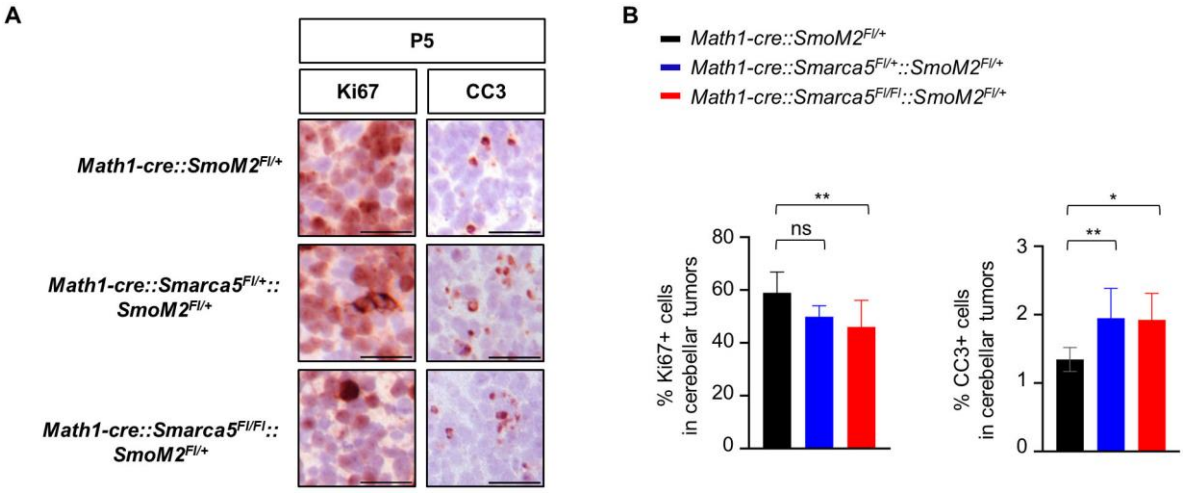

Figure 47. Genetic depletion of *Smarca5* mitigates SHH-MB growth. (**A**) Representative cerebellar tumors from *Math1-cre::SmoM2*$^{Fl/+}$, *Math1-cre::Smarca5*$^{Fl/+}$*::SmoM2*$^{Fl/+}$ and *Math1-cre::smarca5*$^{Fl/Fl}$*::SmoM2*$^{Fl/+}$ mice at P5 stained with Ki67 (left panel) and cleaved caspase 3 (right panel). (**B**) Quantification of Ki67- (left panel) and cleaved caspase 3-positive cells (right panel) from brain tumors shown in (**A**). 20x magnification, scale bar, 50μm. All graphs display mean ± SD values. * $p \leq 0.05$, ** $p \leq 0.01$.

Finally, mice were monitored for neurological symptoms and their survival outcome was analyzed using Kaplan-Meier method (**Figure 48**). *Math1-cre::Smarca5*$^{Fl/Fl}$*::SmoM2*$^{Fl/+}$ mice displayed a significant increase in their survival time, as compared to *Math1-cre::SmoM2*$^{Fl/+}$ mice. No survival benefit was observed in *Smarca5*-heterozygously mice.

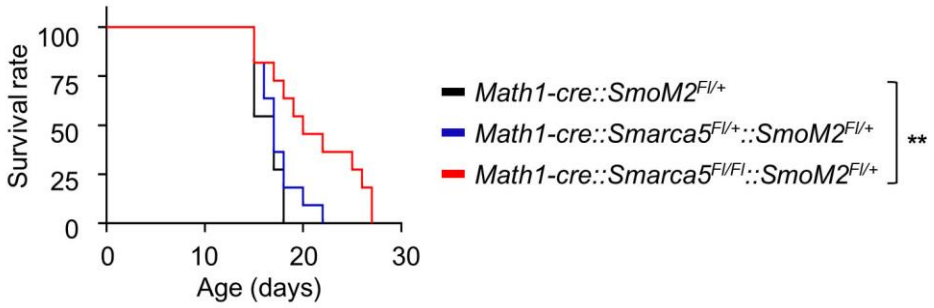

Figure 48. *Smarca5* loss extends survival of SHH-MB mice. Kaplan-Meier curve of *Math1-cre::SmoM2*$^{Fl/+}$ (n = 11), *Math1-cre::Smarca5*$^{Fl/+}$*::SmoM2*$^{Fl/+}$ (n = 11) and *Math1-cre::Smarca5*$^{Fl/Fl}$*::SmoM2*$^{Fl/+}$ mice (n=11). Significance in survival was determined using the log rank (Mantel-Cox) test (** $p \leq 0.01$).

Surprisingly, histological examination of cerebellar tumors revealed no apparent differences in histomorphology between *Math1-cre::Smarca5*$^{Fl/Fl}$*::SmoM2*$^{Fl/+}$ mice that reached their endpoint at P27 and *Math1-cre::SmoM2*$^{Fl/+}$ mice at P15 (**Figure 49A**). Thus, we evaluated the efficacy of Cre recombination by quantifying the fraction of SMARCA5-negative cells in tumors from *Math1-cre::Smarca5*$^{Fl/Fl}$*::SmoM2*$^{Fl/+}$ mice at different time points (**Figure 49B**, **C**). We show that with increasing age, the percentage of SMARCA5-depleted cells decreases in cerebellar tumors, suggesting that SMARCA5- depleted cells are negatively selected during tumor development. Therefore, remaining cells are primarily SMARCA5-positive, potentially explaining the phenotypes observed. To summarize, we demonstrate that loss of *Smarca5* prolongs survival of SHH-MB mice, thus proposing a new role for chromatin remodelers in SHH-MB development.

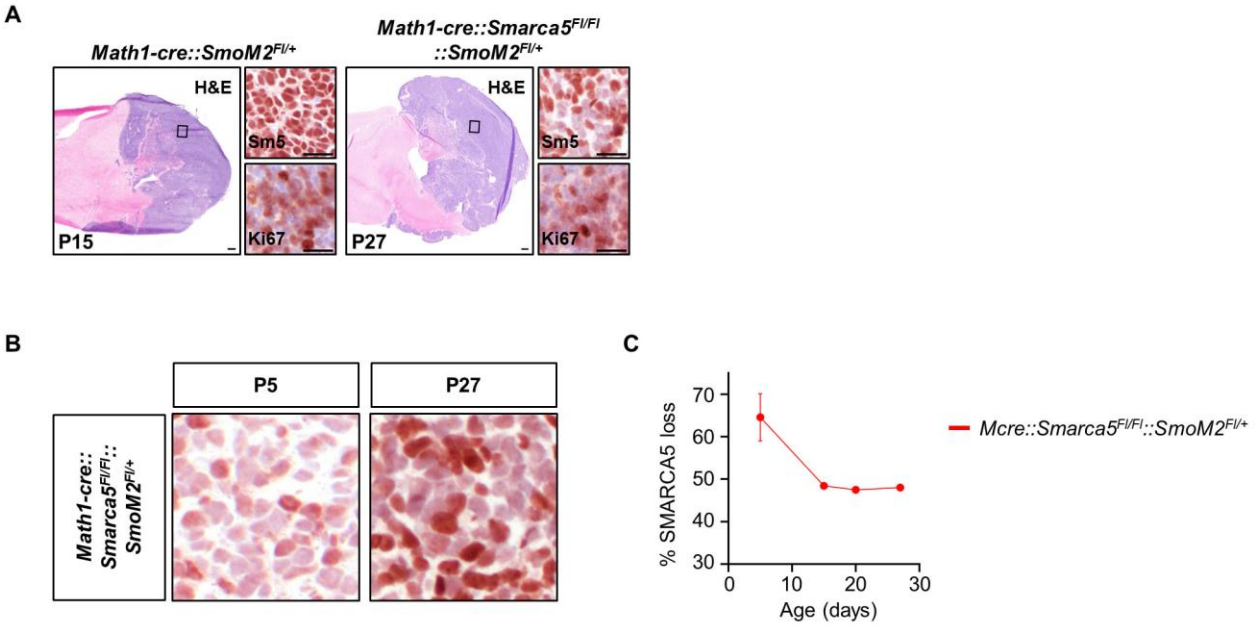

Figure 49. *Smarca5* recombination efficiency *in vivo*. (**A**) H&E-stained cerebellar tumors from *Math1-cre::SmoM2*$^{Fl/+}$ (left) and *Math1-cre::Smarca5*$^{Fl/Fl}$*::SmoM2*$^{Fl/+}$ (right) mice at different endpoints. Immunohistochemistry for SMARCA5 (Sm5) (upper panel) and Ki67 (lower panel) in tumors from these mice are indicated. (**B**) Immunohistochemistry for SMARCA5 cerebellar tumors from *Math1-cre::Smarca5*$^{Fl/Fl}$*::SmoM2*$^{Fl/+}$ mice at different time points. (**C**) Fraction of SMARCA5-negative cells in cerebellar tumors from mice shown in (**B**). 4x magnification, scale bar, 500μm; 20x magnification, scale bar, 50μm; 40x magnification, scale bar, 20μm. Graph displays mean ±SD values.

4 Discussion

Medulloblastoma is the most common malignant embryonal brain tumor that arises either in the cerebellum or brainstem (Gibson et al., 2010), affecting children and adolescents aged 0-19 years old (Ostrom et al., 2023). While current therapy regimens including maximal surgical resection, craniospinal irradiation in non-infants, and chemotherapy may cure up to 70-80% of MB patients (Packer et al., 2006, Gajjar et al., 2006, von Bueren et al., 2016, Michalski et al., 2021), survivors often suffer from long-term sequelae due to intensive treatment. Thus, new and less toxic treatment modalities are urgently needed.

Several molecular studies leveraging transcriptomics, epigenomics and proteomics have highlighted the clinical and genetic heterogeneity of MB (Cavalli et al., 2017, Archer et al., 2018, Hovestadt et al., 2014, Northcott et al., 2017, Schwalbe et al., 2017), thereby resulting in tumor classification in four consensus molecular subgroups: WNT, SHH, Group 3 and Group 4 (Taylor et al., 2012). SHH subgroup of MB, which is the focus of this study, is associated with aberrant activation of SHH signaling cascade and is proposed to originate from granule neuron progenitors of the cerebellum (Schüller et al., 2008, Kim et al., 2003, Yang et al., 2008). With respect to tumor classification, SHH-MB is divided on the basis of *TP53* mutations into *TP53*-mutant and *TP53*-wildtype tumors (Louis et al., 2016), therefore underlining its clinicopathological diversity. Recent advances deriving from large-scale cohort studies have further revealed intertumoral molecular heterogeneity within SHH-MB (Cavalli et al., 2017, Schwalbe et al., 2017, Robinson et al., 2018), leading to delineation of four SHH subtypes designated as SHH-1, 2, 3 and 4, as recognized by the latest *WHO Classification of CNS Tumors* (Louis et al., 2021). Inhibiting SHH signaling pathway at the level of SMO is a promising targeted therapy approach for SHH-driven malignancies including BCC and MB (Sekulic et al., 2015, Migden et al., 2015, Li et al., 2019, Lou et al., 2016, Robinson et al., 2015). However, primary resistance of patients harboring mutations in SHH-associated genes downstream of *PTCH1* (Kool et al., 2014), or acquired resistance to drug treatment (Rudin et al., 2009) have limited its clinical efficacy. Therefore, it is imperative that novel therapeutic targets potentially beyond the SHH pathway are identified, that will be efficacious irrespective of the mutational burden of SHH-MB patients.

With the advent of CRISPR-Cas9 technology, functional genomics provide a “phenotype-to-genotype” approach to systemically perturbate gene function and associate it with phenotypic changes in cancer cells (Shalem et al., 2015). In particular, genome-wide CRISPR-Cas9 loss-of-function screens are a powerful tool to unravel cell-specific genetic dependencies, thereby effectively nominating novel therapeutic targets for cancer treatments (Behan et al., 2019). In that regard, we made use of genome-wide CRISPR-Cas9 knockout libraries, in order to describe the

suitability of two MB cell lines, human DAOY (Jacobsen et al., 1985) and murine SMB21 (Zhao et al., 2015), as SHH-representative models. Our screening data demonstrated a robust depletion of key positive regulators of the SHH pathway such as *Smo* and *Gli2* in SMB21 cells, while none of these genes scored as hits in DAOY cells (**Figure 8**, **Figure 9**). Functional annotation of cell-specific dependencies showed a significant enrichment of smoothened signaling and cilia-related functions and components known to be required for active SHH signal transduction (Corbit et al., 2005, Haycraft et al., 2005, Huangfu et al., 2003), exclusively in SMB21 cells, providing further evidence that SMB21 cells depend on SHH pathway for their proliferation, in contrast to DAOY cells. In line with the screening results, we show that SMB21 cells are sensitive to SMO inhibition in a dose-dependent manner, as demonstrated before (Zhao et al., 2015), while DAOY cells did not respond to treatment (**Figure 10**), further corroborating a previous study characterizing them as a SMO inhibition-resistant, yet SHH-assigned, model (Pambid et al., 2014). An additional study investigating subgroup-specific gene expression which has previously presented that DAOY cells proved difficult to be classified as SHH-representative (Othman et al., 2014), was later contradicted by another study indicating expression of key components of SHH signaling in DAOY (Higdon et al., 2017). Despite DAOY being the most cited human MB cell line (Ivanov et al., 2016), its suitability for high-throughput studies for drug discovery as a SHH-representative model is still controversial due to the lack of consistent data. In that regard, it has been previously suggested that cultured tumor models do not stably maintain SHH pathway activity (Sasai et al., 2006), raising concerns about existing tumor cell models, all together highlighting the necessity for novel, stable *in vitro* models that faithfully recapitulate tumor heterogeneity, as well as the molecular and physiological characteristics of SHH-MB. Of note, 3D culture technologies including organoid-based tumor models constitute a revolutionary tool that is warranted to improve preclinical research, while limiting the use of animal testing in drug discovery (Takahashi, 2019). A few studies so far have recently generated patient-derived or human induced pluripotent stem cells-derived tumor organoids that mimic hallmark features of MB tumorigenesis *in vitro* (Lago et al., 2023, Ballabio et al., 2020, van Essen et al., 2024). Here, we made use of two MB PDXO models, previously described to maintain the genomic signature of the parental tumors (Lago et al., 2023), in order to evaluate therapeutic response to various drug treatments. As expected, we observed heterogeneous sensitivity of SHH- and Group 3- MB PDXOs to SMO inhibition, reflecting their differential tumor origin (**Figure 33, Figure 34**), therefore indicating that PDXOs can efficiently be used for testing drug responses. However, limitations in regard to genome-wide CRISPR-based screens in organoids are still encountered. Technical hurdles primarily involve the high number of cells that need to be transduced, in order to achieve an efficient MOI, often compromised by low library coverage (Ringel et al., 2020, Ungricht et al., 2022). Optimizing screening conditions will

allow high-quality CRISPR-Cas9 genetic screening applications in 3D tumor model systems on a whole genome scale, thus enabling identification of genetic dependencies and chemogenetic interactors.

Having validated that SMB21 cells represent a faithful SHH-dependent MB model, we next aimed to decipher SMB21-specific dependencies beyond the SHH pathway. First, we sought to unravel potential druggable genetic vulnerabilities using the Drug-Gene Interaction database (Cotto et al., 2018), thereby unraveling a functional protein-protein interaction (Szklarczyk et al., 2015) of SHH pathway (SMO) with regulators of epigenome (DNMT1 and HDAC3), cell cycle (CCND1) and metabolism (mTOR) (**Figure 11**). Previous studies have described the anti-tumor effects of HDAC inhibition alone (Pak et al., 2019, Coni et al., 2017) or in combination with DNMT1 inhibition (Ecke et al., 2009) in *in vitro* and *in vivo* models of SHH-MB. Analysis of microarray data showed that among these interactors only *DNMT1* expression served as a prognostic marker for survival outcome, as high gene expression is associated with significantly worse survival outcome in SHH-MB patients (**Supplementary figure 3**). The targetability of DNMT enzymes by different drug classes render them promising targets, thus prompting us to investigate the therapeutic potential of DNMT1 inhibition in SHH-MB. Through pharmacological validation using nucleoside analogue, 5-AzaC, and non-nucleoside small molecule inhibitor, SGI-1027, we proved that DNMT1 inhibition efficaciously suppresses tumor survival of several SHH-MB cell lines, both sensitive and resistant to SMO inhibition (**Figure 12**). It is worth mentioning that all SMB cell lines used here represent dysregulated p53 signaling (Zhao et al., 2015), indicating that DNMT1 inhibition might serve as a promising therapeutic approach for SHH-activated and *TP53*-mutant MBs which are highly enriched in SHH-3 subtype, thus comprising a very high-risk group with worse outcome (Zhukova et al., 2013, Ramaswamy et al., 2016, Cavalli et al., 2017). While both DNMT inhibitors tested were highly potent in all SMB cell lines, we selectively proceeded with FDA-approved 5-AzaC for further validations, given its clinical application in other malignancies.

To gain a mechanistic insight into the anti-tumor effects of hypomethylating agent, 5-AzaC, we performed *omics* analyses. As expected, we observed robust hypomethylation in both SMB21 and SMB55 cells induced by DNMT1 inhibition, which was predominantly associated with neuron-related essential processes such as neurogenesis and differentiation (**Figure 15**). In this context, we show via immunohistology that GCNPs, the proposed origin of SHH-MB (Kim et al., 2003, Yang et al., 2008, Schüller et al., 2008), robustly express DNMT1 during early and late postnatal cerebellar development (**Figure 19**). This did not apply neither for DNMT3A nor for DNMT3B enzymes, whose expression was either weak or absent in GCNPs, further corroborating our screening findings that they do not represent SHH-MB dependencies ($LFC_{MAGeCK\text{-}RRA\_Dnmt3a}$= 0.26 and $LFC_{MAGeCK\text{-}RRA\_Dnmt3b}$= -0.17, respectively). Thus, we hypothesize that the observed epigenetic alterations in GCNP-derived SHH-MB cells are a direct effect of targeting DNMT1. Additionally,

RNA sequencing of SMB21 cells revealed global gene expression alterations as early as 2 hours post 5-AzaC treatment, which were mutually exclusive from 48-hour treatment (

Figure 16). Interestingly, already at 2-hour treatment with 5-AzaC a well-curated set of positive SHH regulators emerged as one of the top downregulated gene sets, while late treatment significantly upregulated genes known to be down-regulated upon SHH activation in GCNPs (**Figure 17**). All together these data underline the early and late regulatory effects of DNMT1 inhibition on SHH signaling output. Our findings are in agreement with a previous siRNA screen identifying DNMT1 as a positive regulator of GLI signaling and demonstrating that DNMT1 inhibition attenuates SHH-MB growth both *in vitro* and *in vivo* by inhibiting SHH signaling (Yang et al., 2022). Of note, reduction of GLI1 expression was also observed in SMB21 *Sufu* KO cells, suggesting that DNMT1 inhibition mitigates SHH-MB survival despite the presence of SHH-associated genetic alterations downstream of *Smo*. Moreover, transcriptomics analysis together with flow cytometry revealed that 5-AzaC treatment resulted in SMB cell accumulation in G2/M transition phase (**Figure 18**), as similarly observed in previous studies reporting that 5-AzaC induces cell cycle arrest at G2/M phase in several cancer cell lines (Miari et al., 2021, Tonon et al., 2022, Wang et al., 2015b). While according to the Cancer Dependency Map (https://depmap.org/portal/) *DNMT1* is by now considered a common essential gene in the vast majority of human cancer cell lines, including CNS tumor entities, we provide strong evidence that DNMT1 regulates SHH signaling and serves as a promising druggable target for SHH-MB, irrespective of the genetic alterations within the SHH pathway. In that regard, many drugs assessed in clinical trials target pan-essential genes including CDK4/6 and MEK1/2 inhibitors, yet, it is important that developing such therapeutics requires careful target prioritization and pharmacodynamics optimization, in order to ensure an increased therapeutic index (Chang et al., 2021).

To further validate our *in vitro* findings, we next addressed the function of *Dnmt1* in cerebellar granule neuron development *in vivo*. First, we demonstrate that DNMT1 is expressed in proliferating GCNPs in the developing murine cerebellum (**Figure 19**), well in line with previous studies showing DNMT1 expression in the murine cerebellum during early postnatal development, which is maintained in postmitotic differentiated neurons (Fan et al., 2001, Goto et al., 1994, Inano et al., 2000). To evaluate the role of *Dnmt1* during murine normal cerebellar and tumor development, we genetically ablated it in Math1-expressing GCNPs, the putative cell origin of SHH-MB (Kim et al., 2003, Yang et al., 2008, Schüller et al., 2008). We observed impaired proliferative and migratory activity of GCNPs in *Math1-cre::Dnmt1*$^{Fl/Fl}$ mice (**Figure 21**), while at P21 these mice displayed cerebellar hypoplasia (**Figure 22**), overall indicating that *Dnmt1*

expression is indispensable for proper cerebellar formation during early postnatal murine development. However, taking into consideration that *Dnmt1* is expressed in the murine brain during embryogenesis (Goto et al., 1994), any potential effects on cerebellar formation deriving from its conditional ablation during early embryonal development should still be addressed. Finally, the impact of *Dnmt1* loss was assessed in SHH-MB-bearing mice (Mao et al., 2006), which resulted in significant decrease in tumor proliferating cells in their cerebella (**Figure 25**), as well as a favorable survival outcome (**Figure 26**), further strengthening our screening findings that *Dnmt1* is required for GCNP-derived MB survival.

Combinatorial therapies involving drugs targeting different pathways can yield anti-cancer effects in a synergistic or additive manner, therefore constituting an attractive therapeutic strategy for several malignancies (Bayat Mokhtari et al., 2017). In light of the therapeutic potency that two combined drugs can have on tumor growth, we aimed to decipher potential synergistic partners of DNMT1 inhibition for the treatment of SHH-MB. To this end, we employed a genome-wide CRISPR-Cas9 knockout drug screen in SMB21 cells, in order to unravel chemogenetic interactors for 5-AzaC. Our downstream bioinformatic analysis revealed *Smo* as a strong hit of the drug screen in the 5-AzaC-treated arm (**Figure 28**), indicating that *Smo* knockout potentially synergizes with DNMT1 inhibition to suppress SHH-MB cell proliferation. In that regard, protein-protein interaction network analysis of SMB21-specific essentialities also revealed a functional association between SMO and DNMT1 (**Figure 11**). Interestingly, a previous RNAi silencing screen in acute myeloid leukemia cells identified *SMO* as a 5-AzaC sensitizing hit, showing synergistic effects of concurrent combination of SMO and DNMT1 inhibition (Tibes et al., 2015). In a similar context, a more recent study demonstrated synergistic effects of combination treatment of GLI and DNMT1 inhibitors in leiomyosarcoma cells, which however were not observed upon combination of SMO and DNMT1 inhibition (Garcia et al., 2020). Yet, these results indicate the potential of targeting the SHH pathway together with DNMT1 to suppress tumor growth.

When it comes to their clinical applications, SMO inhibitor, LDE-225, and 5-AzaC, are both FDA-approved drugs used for treatment of different tumor entities. In particular, clinical data regarding efficacy and safety of LDE-225 have reported that it is well-tolerated in adult patients with locally advanced or metastatic BCC, as well as in pediatric patients with relapsed SHH-activated MB, with safety profiles in children being consistent with the ones established for adult patients (Dummer et al., 2020, Kieran et al., 2017, Li et al., 2019). While most adverse effects are manageable and reversible with dose interruptions, growth plate changes are the only significant toxicities often observed in prepubertal pediatric patients that further need to be evaluated (Kieran et al., 2017, Li et al., 2019). Similar to LDE-225, 5-AzaC is well-tolerated in patients with

myelodysplastic syndrome and acute myeloid leukemia. Although myelosuppression can be the most common adverse effect observed, when transient, it can be managed with dosage modifications (García-Delgado et al., 2014, Jen et al., 2022, Vigil et al., 2010).

Based on all aforementioned observations, we proceeded to investigate the therapeutic potential of combining SMO and DNMT1 inhibition in SHH-MB. Indeed, we show that SMO inhibition using LDE-225 combined with 5-AzaC exerts synergistic effects in reducing SHH-MB viability *in vitro*. We demonstrate that strongest synergism was achieved when the drugs were applied simultaneously rather sequentially (**Figure 29**, **Figure 30**), while this inhibitory effect was mediated by blocking SHH signaling (**Figure 31**). Furthermore, no synergism was observed in SMB21 cells with loss of *Sufu*, which renders them resistant to SMO inhibition, suggesting that combined therapy of SMO and DNMT1 inhibition is only efficacious in SHH tumors that do not harbor genetic alterations downstream of *SMO* (**Figure 32**). Moreover, we made use of the potential therapeutic applications of MB patient-derived xenograft organoids (Lago et al., 2023) and demonstrate that combinatorial treatment of LDE-225 and 5-AzaC synergistically suppresses viability of SHH-driven MB PDXOs, which were sensitive to both monotherapies (**Figure 33**). DNMT1 inhibition alone also blocked cell proliferation in Group3-MB PDXOs, corroborating findings from the Cancer Dependency Map that *DNMT1* is a genetic dependency in 1,086 out of 1,150 human cancer cell lines (https://depmap.org/portal/), while no synergistic effects of LDE-225 and 5-AzaC were observed (**Figure 34**). All together, our data propose the synergistic potential of combining SMO and DNMT1 inhibition in tumor cells with activated SHH signaling.

Having shown that pharmacological inhibition of DNMT1 efficaciously inhibits SHH-MB proliferation *in vitro*, we aimed to explore its therapeutic potential alone or in combination with SMO inhibition *in vivo*. Taking into account that *Math1-cre::SmoM2*$^{Fl/+}$ mice displayed a median survival of only 17 days in our study, we used a TAM-inducible *Math1-creER*^{T2} mouse line (Machold and Fishell, 2005), aiming to generate a previously established mouse model of SHH-MB (Merk et al., 2018). This way, we ensured an appropriate therapeutic window in adult mice, thus avoiding potential developmental deficits induced in young pups due to intensive treatment. Survival analysis showed that combined treatment of 5-AzaC and LDE-225 significantly prolonged the survival of *Math1-creER*^{T2}*::SmoM2*$^{Fl/+}$ mice, as compared to 5-AzaC- and control-treated mice, however, their outcome did not differ from LDE-225-treated mice (**Figure 35**). Interestingly, we observed histomorphological differences between the combination- and the monotherapies-treated mice in regard to tumor size and tumor proliferative activity in brains harvested at the last day of the 3-week treatment schedule (**Figure 36, Figure 37**). While advanced imaging techniques such as bioluminescence would have been a more precise approach to monitor tumor growth,

given that these tumors are highly infiltrative within the normal cerebellar tissue, however, due to lack of such equipment in our facility, we exclusively examined these brains histologically. Furthermore, we observed a strong reduction of GLI1 protein levels in the combination therapy group (**Figure 39**), further enhancing our *in vitro* findings that combination of DNMT1 and SMO inhibition regulate SHH signaling output. Since no drug-related toxic effects were observed in any of the treatment groups, continuous treatment schedules of 5-AzaC and LDE-225 combination could have exhibited even more potent anti-tumor effects in mice. Additionally, different concentrations of drug combinations could be evaluated in the future to identify the drug dosages that exert highest synergistic effects, potentially resulting in improved survival outcome. In summary, we provide strong evidence that DNMT1 and SMO inhibition act synergistically to suppress tumor growth in both *in vitro* and *in vivo* SHH-driven MB models, therefore proposing a novel combination treatment modality for this tumor entity.

Moreover, the dropout screen in SMB21 cells revealed several epigenetic modulators, besides *Dnmt1*, as SMB21-specific vulnerabilities at FDR < 5%, including six members of the SNF2-family of ATP-dependent chromatin remodelers: *Smarca4*, *Smarca5*, *Smarca6*, *Smarcb1*, *Smarcd1* and *Smarce1* (**Figure 40**). Previous studies have provided evidence that chromatin remodelers play a crucial role in MB pathogenesis. Among these, mutations affecting the SWI/SNF complex including *SMARCB1*, *SMARCD1*, *SMARCE1* may be seen in SHH-MBs (Kool et al., 2014). While *SMARCB1* mutations primarily affect embryonal rhabdoid tumors (AT/RT) (Hasselblatt et al., 2011), it has been described as a key mediator of SHH signaling (Jagani et al., 2010), in addition to being essential for GCNP proliferation (Moreno et al., 2014). Mutations in *SMARCA4* often occur in WNT- and Group 3 subgroups of MB, while SHH-MBs are essentially free of such mutations (Pugh et al., 2012, Parsons et al., 2011, Yi and Wu, 2018). Similar to *Smarcb1*, *Smarca4* has been previously shown to have pro-proliferative roles in cerebellar granule neurons precursors (Moreno et al., 2014) and it has been described to be important in SHH-MB formation and progression by regulating the expression of SHH-associated targets has been described (Shi et al., 2016). What is more, *Smarca6* displays high expression levels in murine cerebellum and SHH-MB, and acts as a downstream effector of SHH pathway (Robinson et al., 2019). When it comes to *Smarca5*, its loss reduces GCNP proliferation, resulting in cerebellar hypoplasia, thereby proposing a critical role in cerebellar formation (Alvarez-Saavedra et al., 2014). Additionally, analysis of patient dataset (Griesinger et al., 2013, Cavalli et al., 2017) revealed higher *SMARCA5* gene expression in primary MB tissue and specifically in SHH subgroup, as compared to other CNS tumor-derived and healthy cerebral tissues (**Supplementary figure 10**). Despite *SMARCA5* being considered a dependency in 697/1,150 cancer cell lines (https://depmap.org/portal/), based

on the mounting evidence describing the role of chromatin remodelers in MB, we sought to address *Smarca5* involvement in the development of SHH-MB.

While no available inhibitor exists targeting specifically SMARCA5, downstream validation of this screening hit was exclusively performed via genetic ablation experiments. Knockout of *Smarca5* in SMB21 cells resulted in a significant decrease in cell viability, supporting our screening results that *Smarca5* is a genetic dependency for SMB21 cells. In particular, this inhibitory effect was mediated via downregulation of GLI1 protein expression, indicating that *Smarca5* regulates SHH signaling output (**Figure 41**). To further substantiate our *in vitro* findings, we evaluated the role of *Smarca5* during normal cerebellar and SHH-MB development in mouse models. First, through immunohistochemistry we observed high expression of SMARCA5 in proliferating GCNPs in the EGL of *Math1-cre* mice at P5 (**Figure 42**), in accordance with previous studies portraying SMARCA5 expression predominantly in proliferating cells during early brain development (Lazzaro and Picketts, 2001), that marks the peak proliferative period of GCNPS (up to P7) (Alvarez-Saavedra et al., 2014). *Smarca5* knockout in Math1-expressing GCNPs, the putative cell origin of SHH-MB (Kim et al., 2003, Yang et al., 2008, Schüller et al., 2008), affected GCNP survival in the external granule cell layer (**Figure 43**) and caused morphological changes in cerebellar formation at P21 (**Figure 44**). While the importance of *Smarca5* during murine development had been previously investigated (Alvarez-Saavedra et al., 2014), its role in SHH-MB growth was addressed for the first time in this study. We demonstrate that loss of *Smarca5* in Math1-expressing GCNPs significantly reduced the fraction of tumor proliferating cells in the cerebella of SHH-MB mice (Mao et al., 2006) (**Figure 47**), while also significantly prolonged their survival outcome (**Figure 48**). Notably, we observed that the fraction of SMARCA5-negative cells reduces over time in *Math1-cre::Smarca5*$^{Fl/Fl}$*::SmoM2*$^{Fl/+}$ mice, suggesting that SMARCA5-depleted cells are negatively selected, resulting in cell death over time (**Figure 49**). Thus, the observed tumor phenotype is likely attributed to inefficiently recombined cells, suggesting that if *Smarca5* knockout penetrance was higher, differences in survival would be more prominent. This hypothesis should be further tested by performing double immunostaining for cleaved caspase 3 and SMARCA5 markers to ensure that SMARCA5-negative cells are undergoing apoptosis. Overall, our data indicate that loss of *Smarca5* mitigates SHH-MB progression *in vivo*, thus suggesting its critical role in SHH-MB development.

Taken together, by conducting a genome-scale CRISPR-Cas9 knockout screen in a previously characterized murine cell model of SHH-MB, SMB21 (Zhao et al., 2015), we deciphered several epigenetic regulators involving DNA methylatransferase *Dnmt1* and chromatin remodeler *Smarca5* as strong dependency hits. Microarray expression data of both genes revealed high

expression of both genes in SHH-α (SHH-3) tumors (**Supplementary figure 4, Supplementary figure 10**), which are enriched in *TP53* mutations and thus constitute a high-risk group with worse prognosis (Zhukova et al., 2013, Ramaswamy et al., 2016, Cavalli et al., 2017). Hence, given that SMB21 cells carry a *TP53* mutation, our data proposing the involvement of the epigenetic machinery in SHH-MB pathogenesis could be of relevance for *TP53*-mutant SHH-MBs. In general, epigenetic regulators are known to govern the expression and silencing of certain genes, therefore producing a cellular homeostatic environment (Bayat Mokhtari et al., 2017). The epigenome can be modified via processes involving DNA methylation, chromatin remodeling and histone modification, while it plays a critical role in tumorigenesis, often resulting in activation of oncogenes or silencing of tumor suppressor genes (Roussel and Stripay, 2018). Distinct methylation patterns that are subgroup-specific have been identified (Schwalbe et al., 2013), while epigenetic discrepancies have also been observed across different age groups within SHH-MB subtype, with children exhibiting predominantly global hypermethylation (Schwalbe et al., 2017). Additional large-scale *omics* studies have shed light on the mutational events in chromatin modifying genes across all MB molecular subgroups, underlining subgroup-specificity (Kool et al., 2014, Northcott et al., 2017, Pugh et al., 2012, Parsons et al., 2011). Pan-cancer genome analyses across diverse human tumor entities including MB have revealed that tumor mutational burden is higher in adults than in the pediatric population (Chalmers et al., 2017, Gröbner et al., 2018), implying that other than genetic mutations, mechanisms involving the epigenome are also important for MB formation (Shiraishi and Kawauchi, 2021). In regard to SHH-MB, chromatin organization is affected across different age groups, with recurrent mutations in chromatin modifiers accounting for 44% of all SHH-MB patients (Skowron et al., 2021). Such alterations include chromatin regulator *BCOR* and histone methyltransferase *MLL2* which appear in both pediatric and adult SHH-MBs (Kool et al., 2014). Yet, some alterations in chromatin modifiers and transcriptional regulators appear to be age-specific (Kool et al., 2014, Skowron et al., 2021). Such events include deactivating mutations in transcriptional co-activator *CREBBP* and chromatin reader *BRPF1* which predominantly affect SHH-4 subtype, namely adult SHH-MB patients (Kool et al., 2014, Skowron et al., 2021). Based on these studies suggesting that the epigenome is involved in the pathogenesis of SHH-MB, this thesis addresses the role of *Dnmt1* and *Smarca5* in *in vivo* mouse models. Conditional ablation of these genes in GCNPs resulted in similar severe phenotypic changes in mice, demonstrating that their expression is required for GCNP survival and migration during early postnatal cerebellar development. Nonetheless, their role during murine embryogenesis still needs to be elucidated. Moreover, knocking out these genes led to a prolonged survival time of SHH-MB mice, further proposing a role of the epigenetic machinery in SHH-MB progression. In that regard, previous studies have shown that mutated BRPF1 enhances tumorigenesis together with SmoM2 (Aiello et

al., 2019), while loss of *Bcor* or *Kmtd2* result in increased tumor penetrance in SHH-MB mice (Kutscher et al., 2020, Sanghrajka et al., 2023). Another study has demonstrated that loss of *Crebbp* impairs cerebellar development and reduces viability of GCNP-derived tumors (Merk et al., 2018). All together, these experimental findings underline the important function of epigenetic regulators in proper cerebellar development, as well as provide evidence that the epigenome is substantially involved in GCNP-derived pathogenesis of SHH-MB. A better understanding of chromatin biology in cancer research will enable the establishment of novel treatment modalities targeting epigenetic regulators in SHH-driven MB.

To conclude, this study leverages forward genetic screens, aiming to unravel genetic dependencies for SHH-driven MB that could potentially represent therapeutic targets for this tumor entity. By conducting genome-wide CRISPR-Cas9 knockout screens (Doench et al., 2016) in two previously described in *vitro* MB models (Jacobsen et al., 1985, Zhao et al., 2015), we provided supporting evidence that murine SMB21 cells represent a reliable system model that recapitulates hallmark features of SHH-MB, unlike human DAOY cells which prove not to be SHH-dependent. Additionally, functional genomics revealed several SMB21 essentialities beyond the SHH pathway representing members of the epigenetic machinery such as *Dnmt1* and *Smarca5*. We demonstrate that their expression in GCNPs, the putative cell origin of SHH-MB (Kim et al., 2003, Yang et al., 2008, Schüller et al., 2008), is critical for proper cerebellar development, as we as progression of GCNP-derived MB. Furthermore, we prove that pharmacological inhibition of DNMT1 using FDA-approved drug, 5-AzaC, efficaciously suppresses survival of several SHH-MB cell lines irrespective of their mutational burden via blockade of SHH signaling pathway. Finally, via a chemogenetic CRISPR-based knockout screen in SMB21 cells, we provide a list of genes that could serve as synergistic partners for 5-AzaC treatment, with *Smo* being the top hit modulating drug response. Our data indicate that combination treatment of 5-AzaC and LDE-225 exerts synergistic effects in inhibiting tumor proliferation in *in vitro* and *in vivo* murine MB models, as well as patient-derived xenograft organoids, an effect exclusively observed in tumors with active SHH signaling. A more profound understanding of the epigenetic machinery in SHH-MB using advanced technological tools that enable epigenomic and chromatin profiling (Skene et al., 2018, Kaya-Okur et al., 2020) could facilitate the identification of further therapeutic vulnerabilities in MB. Summarizing, this thesis presents inhibition of epigenetic regulator DNMT1 alone or in combination with SMO inhibition as a novel targeted therapy approach for SHH subgroup of medulloblastoma.

5 References

Abrahám, H., Tornóczky, T., Kosztolányi, G. and Seress, L. (2001) 'Cell formation in the cortical layers of the developing human cerebellum', *Int J Dev Neurosci,* 19(1), pp. 53-62. DOI: 10.1016/s0736-5748(00)00065-4.

Aiello, G., Ballabio, C., Ruggeri, R., Fagnocchi, L., Anderle, M., Morassut, I., Caron, D., Garilli, F., Gianno, F., Giangaspero, F., Piazza, S., Romanel, A., Zippo, A. and Tiberi, L. (2019) 'Truncated BRPF1 Cooperates with Smoothened to Promote Adult Shh Medulloblastoma', *Cell Rep,* 29(12), pp. 4036-4052.e10. DOI: 10.1016/j.celrep.2019.11.046.

Alcon, C., Manzano-Muñoz, A., Prada, E., Mora, J., Soriano, A., Guillén, G., Gallego, S., Roma, J., Samitier, J., Villanueva, A. and Montero, J. (2020) 'Sequential combinations of chemotherapeutic agents with BH3 mimetics to treat rhabdomyosarcoma and avoid resistance', *Cell Death Dis,* 11(8), pp. 634. DOI: 10.1038/s41419-020-02887-y.

Aldinger, K. A., Thomson, Z., Phelps, I. G., Haldipur, P., Deng, M., Timms, A. E., Hirano, M., Santpere, G., Roco, C., Rosenberg, A. B., Lorente-Galdos, B., Gulden, F. O., O'Day, D., Overman, L. M., Lisgo, S. N., Alexandre, P., Sestan, N., Doherty, D., Dobyns, W. B., Seelig, G., Glass, I. A. and Millen, K. J. (2021) 'Spatial and cell type transcriptional landscape of human cerebellar development', *Nat Neurosci,* 24(8), pp. 1163-1175. DOI: 10.1038/s41593-021-00872-y.

Alvarez-Saavedra, M., De Repentigny, Y., Lagali, P. S., Raghu Ram, E. V., Yan, K., Hashem, E., Ivanochko, D., Huh, M. S., Yang, D., Mears, A. J., Todd, M. A., Corcoran, C. P., Bassett, E. A., Tokarew, N. J., Kokavec, J., Majumder, R., Ioshikhes, I., Wallace, V. A., Kothary, R., Meshorer, E., Stopka, T., Skoultchi, A. I. and Picketts, D. J. (2014) 'Snf2h-mediated chromatin organization and histone H1 dynamics govern cerebellar morphogenesis and neural maturation', *Nat Commun,* 5, pp. 4181. DOI: 10.1038/ncomms5181.

Archer, T. C., Ehrenberger, T., Mundt, F., Gold, M. P., Krug, K., Mah, C. K., Mahoney, E. L., Daniel, C. J., LeNail, A., Ramamoorthy, D., Mertins, P., Mani, D. R., Zhang, H., Gillette, M. A., Clauser, K., Noble, M., Tang, L. C., Pierre-François, J., Silterra, J., Jensen, J., Tamayo, P., Korshunov, A., Pfister, S. M., Kool, M., Northcott, P. A., Sears, R. C., Lipton, J. O., Carr, S. A., Mesirov, J. P., Pomeroy, S. L. and Fraenkel, E. (2018) 'Proteomics, Post-translational Modifications, and Integrative Analyses Reveal Molecular Heterogeneity within Medulloblastoma Subgroups', *Cancer Cell,* 34(3), pp. 396-410.e8. DOI: 10.1016/j.ccell.2018.08.004.

Bajaj, J., Hamilton, M., Shima, Y., Chambers, K., Spinler, K., Van Nostrand, E. L., Yee, B. A., Blue, S. M., Chen, M., Rizzeri, D., Chuah, C., Oehler, V. G., Broome, H. E., Sasik, R., Scott-Browne, J., Rao, A., Yeo, G. W. and Reya, T. (2020) 'An in vivo genome-wide CRISPR screen identifies the RNA-binding protein Staufen2 as a key regulator of myeloid leukemia', *Nat Cancer,* 1(4), pp. 410-422. DOI: 10.1038/s43018-020-0054-2.

Ballabio, C., Anderle, M., Gianesello, M., Lago, C., Miele, E., Cardano, M., Aiello, G., Piazza, S., Caron, D., Gianno, F., Ciolfi, A., Pedace, L., Mastronuzzi, A., Tartaglia, M., Locatelli, F., Ferretti, E., Giangaspero, F. and Tiberi, L. (2020) 'Modeling medulloblastoma in vivo and with human cerebellar organoids', *Nature Communications,* 11(1), pp. 583. DOI: 10.1038/s41467-019-13989-3.

Bayat Mokhtari, R., Homayouni, T. S., Baluch, N., Morgatskaya, E., Kumar, S., Das, B. and Yeger, H. (2017) 'Combination therapy in combating cancer', *Oncotarget,* 8(23), pp. 38022-38043. DOI: 10.18632/oncotarget.16723.

Behan, F. M., Iorio, F., Picco, G., Gonçalves, E., Beaver, C. M., Migliardi, G., Santos, R., Rao, Y., Sassi, F., Pinnelli, M., Ansari, R., Harper, S., Jackson, D. A., McRae, R., Pooley, R., Wilkinson, P., van der Meer, D., Dow, D., Buser-Doepner, C., Bertotti, A., Trusolino, L., Stronach, E. A., Saez-Rodriguez, J., Yusa,

K. and Garnett, M. J. (2019) 'Prioritization of cancer therapeutic targets using CRISPR-Cas9 screens', *Nature,* 568(7753), pp. 511-516. DOI: 10.1038/s41586-019-1103-9.

Berns, K., Hijmans, E. M., Mullenders, J., Brummelkamp, T. R., Velds, A., Heimerikx, M., Kerkhoven, R. M., Madiredjo, M., Nijkamp, W., Weigelt, B., Agami, R., Ge, W., Cavet, G., Linsley, P. S., Beijersbergen, R. L. and Bernards, R. (2004) 'A large-scale RNAi screen in human cells identifies new components of the p53 pathway', *Nature,* 428(6981), pp. 431-7. DOI: 10.1038/nature02371.

Borghesani, P. R., Peyrin, J. M., Klein, R., Rubin, J., Carter, A. R., Schwartz, P. M., Luster, A., Corfas, G. and Segal, R. A. (2002) 'BDNF stimulates migration of cerebellar granule cells', *Development,* 129(6), pp. 1435-42. DOI: 10.1242/dev.129.6.1435.

Brugières, L., Remenieras, A., Pierron, G., Varlet, P., Forget, S., Byrde, V., Bombled, J., Puget, S., Caron, O., Dufour, C., Delattre, O., Bressac-de Paillerets, B. and Grill, J. (2012) 'High frequency of germline SUFU mutations in children with desmoplastic/nodular medulloblastoma younger than 3 years of age', *J Clin Oncol,* 30(17), pp. 2087-93. DOI: 10.1200/jco.2011.38.7258.

Cai, E. P., Ishikawa, Y., Zhang, W., Leite, N. C., Li, J., Hou, S., Kiaf, B., Hollister-Lock, J., Yilmaz, N. K., Schiffer, C. A., Melton, D. A., Kissler, S. and Yi, P. (2020) 'Genome-scale in vivo CRISPR screen identifies RNLS as a target for beta cell protection in type 1 diabetes', *Nat Metab,* 2(9), pp. 934-945. DOI: 10.1038/s42255-020-0254-1.

Carter, R. A., Bihannic, L., Rosencrance, C., Hadley, J. L., Tong, Y., Phoenix, T. N., Natarajan, S., Easton, J., Northcott, P. A. and Gawad, C. (2018) 'A Single-Cell Transcriptional Atlas of the Developing Murine Cerebellum', *Curr Biol,* 28(18), pp. 2910-2920.e2. DOI: 10.1016/j.cub.2018.07.062.

Cavalli, F. M. G., Remke, M., Rampasek, L., Peacock, J., Shih, D. J. H., Luu, B., Garzia, L., Torchia, J., Nor, C., Morrissy, A. S., Agnihotri, S., Thompson, Y. Y., Kuzan-Fischer, C. M., Farooq, H., Isaev, K., Daniels, C., Cho, B. K., Kim, S. K., Wang, K. C., Lee, J. Y., Grajkowska, W. A., Perek-Polnik, M., Vasiljevic, A., Faure-Conter, C., Jouvet, A., Giannini, C., Nageswara Rao, A. A., Li, K. K. W., Ng, H. K., Eberhart, C. G., Pollack, I. F., Hamilton, R. L., Gillespie, G. Y., Olson, J. M., Leary, S., Weiss, W. A., Lach, B., Chambless, L. B., Thompson, R. C., Cooper, M. K., Vibhakar, R., Hauser, P., van Veelen, M. C., Kros, J. M., French, P. J., Ra, Y. S., Kumabe, T., López-Aguilar, E., Zitterbart, K., Sterba, J., Finocchiaro, G., Massimino, M., Van Meir, E. G., Osuka, S., Shofuda, T., Klekner, A., Zollo, M., Leonard, J. R., Rubin, J. B., Jabado, N., Albrecht, S., Mora, J., Van Meter, T. E., Jung, S., Moore, A. S., Hallahan, A. R., Chan, J. A., Tirapelli, D. P. C., Carlotti, C. G., Fouladi, M., Pimentel, J., Faria, C. C., Saad, A. G., Massimi, L., Liau, L. M., Wheeler, H., Nakamura, H., Elbabaa, S. K., Perezpeña-Diazconti, M., Chico Ponce de León, F., Robinson, S., Zapotocky, M., Lassaletta, A., Huang, A., Hawkins, C. E., Tabori, U., Bouffet, E., Bartels, U., Dirks, P. B., Rutka, J. T., Bader, G. D., Reimand, J., Goldenberg, A., Ramaswamy, V. and Taylor, M. D. (2017) 'Intertumoral Heterogeneity within Medulloblastoma Subgroups', *Cancer Cell,* 31(6), pp. 737-754.e6. DOI: 10.1016/j.ccell.2017.05.005.

Chalmers, Z. R., Connelly, C. F., Fabrizio, D., Gay, L., Ali, S. M., Ennis, R., Schrock, A., Campbell, B., Shlien, A., Chmielecki, J., Huang, F., He, Y., Sun, J., Tabori, U., Kennedy, M., Lieber, D. S., Roels, S., White, J., Otto, G. A., Ross, J. S., Garraway, L., Miller, V. A., Stephens, P. J. and Frampton, G. M. (2017) 'Analysis of 100,000 human cancer genomes reveals the landscape of tumor mutational burden', *Genome Med,* 9(1), pp. 34. DOI: 10.1186/s13073-017-0424-2.

Chang, C. H., Zanini, M., Shirvani, H., Cheng, J. S., Yu, H., Feng, C. H., Mercier, A. L., Hung, S. Y., Forget, A., Wang, C. H., Cigna, S. M., Lu, I. L., Chen, W. Y., Leboucher, S., Wang, W. J., Ruat, M., Spassky, N., Tsai, J. W. and Ayrault, O. (2019) 'Atoh1 Controls Primary Cilia Formation to Allow for SHH-Triggered Granule Neuron Progenitor Proliferation', *Dev Cell,* 48(2), pp. 184-199.e5. DOI: 10.1016/j.devcel.2018.12.017.

Chang, L., Ruiz, P., Ito, T. and Sellers, W. R. (2021) 'Targeting pan-essential genes in cancer: Challenges and opportunities', *Cancer Cell,* 39(4), pp. 466-479. DOI: 10.1016/j.ccell.2020.12.008.

Chen, A., Wen, S., Liu, F., Zhang, Z., Liu, M., Wu, Y., He, B., Yan, M., Kang, T., Lam, E. W., Wang, Z. and Liu, Q. (2021) 'CRISPR/Cas9 screening identifies a kinetochore-microtubule dependent mechanism for

Aurora-A inhibitor resistance in breast cancer', *Cancer Commun (Lond),* 41(2), pp. 121-139. DOI: 10.1002/cac2.12125.

Chen, H. and Boutros, P. C. (2011) 'VennDiagram: a package for the generation of highly-customizable Venn and Euler diagrams in R', *BMC Bioinformatics,* 12, pp. 35. DOI: 10.1186/1471-2105-12-35.

Chen, S., Sanjana, N. E., Zheng, K., Shalem, O., Lee, K., Shi, X., Scott, D. A., Song, J., Pan, J. Q., Weissleder, R., Lee, H., Zhang, F. and Sharp, P. A. (2015) 'Genome-wide CRISPR screen in a mouse model of tumor growth and metastasis', *Cell,* 160(6), pp. 1246-60. DOI: 10.1016/j.cell.2015.02.038.

Cheung, H. W., Cowley, G. S., Weir, B. A., Boehm, J. S., Rusin, S., Scott, J. A., East, A., Ali, L. D., Lizotte, P. H., Wong, T. C., Jiang, G., Hsiao, J., Mermel, C. H., Getz, G., Barretina, J., Gopal, S., Tamayo, P., Gould, J., Tsherniak, A., Stransky, N., Luo, B., Ren, Y., Drapkin, R., Bhatia, S. N., Mesirov, J. P., Garraway, L. A., Meyerson, M., Lander, E. S., Root, D. E. and Hahn, W. C. (2011) 'Systematic investigation of genetic vulnerabilities across cancer cell lines reveals lineage-specific dependencies in ovarian cancer', *Proc Natl Acad Sci U S A,* 108(30), pp. 12372-7. DOI: 10.1073/pnas.1109363108.

Chow, R. D., Guzman, C. D., Wang, G., Schmidt, F., Youngblood, M. W., Ye, L., Errami, Y., Dong, M. B., Martinez, M. A., Zhang, S., Renauer, P., Bilguvar, K., Gunel, M., Sharp, P. A., Zhang, F., Platt, R. J. and Chen, S. (2017) 'AAV-mediated direct in vivo CRISPR screen identifies functional suppressors in glioblastoma', *Nat Neurosci,* 20(10), pp. 1329-1341. DOI: 10.1038/nn.4620.

Collier, N. J., Ali, F. R. and Lear, J. T. (2016) 'The safety and efficacy of sonidegib for the treatment of locally advanced basal cell carcinoma', *Expert Rev Anticancer Ther,* 16(10), pp. 1011-8. DOI: 10.1080/14737140.2016.1230020.

Coni, S., Mancuso, A. B., Di Magno, L., Sdruscia, G., Manni, S., Serrao, S. M., Rotili, D., Spiombi, E., Bufalieri, F., Petroni, M., Kusio-Kobialka, M., De Smaele, E., Ferretti, E., Capalbo, C., Mai, A., Niewiadomski, P., Screpanti, I., Di Marcotullio, L. and Canettieri, G. (2017) 'Corrigendum: Selective targeting of HDAC1/2 elicits anticancer effects through Gli1 acetylation in preclinical models of SHH Medulloblastoma', *Sci Rep,* 7, pp. 46645. DOI: 10.1038/srep46645.

Corbit, K. C., Aanstad, P., Singla, V., Norman, A. R., Stainier, D. Y. and Reiter, J. F. (2005) 'Vertebrate Smoothened functions at the primary cilium', *Nature,* 437(7061), pp. 1018-21. DOI: 10.1038/nature04117.

Corona, D. F., Längst, G., Clapier, C. R., Bonte, E. J., Ferrari, S., Tamkun, J. W. and Becker, P. B. (1999) 'ISWI is an ATP-dependent nucleosome remodeling factor', *Mol Cell,* 3(2), pp. 239-45. DOI: 10.1016/s1097-2765(00)80314-7.

Cotto, K. C., Wagner, A. H., Feng, Y. Y., Kiwala, S., Coffman, A. C., Spies, G., Wollam, A., Spies, N. C., Griffith, O. L. and Griffith, M. (2018) 'DGIdb 3.0: a redesign and expansion of the drug-gene interaction database', *Nucleic Acids Res,* 46(D1), pp. D1068-d1073. DOI: 10.1093/nar/gkx1143.

Diesch, J., Zwick, A., Garz, A. K., Palau, A., Buschbeck, M. and Götze, K. S. (2016) 'A clinical-molecular update on azanucleoside-based therapy for the treatment of hematologic cancers', *Clin Epigenetics,* 8, pp. 71. DOI: 10.1186/s13148-016-0237-y.

Dijkgraaf, G. J., Alicke, B., Weinmann, L., Januario, T., West, K., Modrusan, Z., Burdick, D., Goldsmith, R., Robarge, K., Sutherlin, D., Scales, S. J., Gould, S. E., Yauch, R. L. and de Sauvage, F. J. (2011) 'Small molecule inhibition of GDC-0449 refractory smoothened mutants and downstream mechanisms of drug resistance', *Cancer Res,* 71(2), pp. 435-44. DOI: 10.1158/0008-5472.Can-10-2876.

Doench, J. G. (2018) 'Am I ready for CRISPR? A user's guide to genetic screens', *Nat Rev Genet,* 19(2), pp. 67-80. DOI: 10.1038/nrg.2017.97.

Doench, J. G., Fusi, N., Sullender, M., Hegde, M., Vaimberg, E. W., Donovan, K. F., Smith, I., Tothova, Z., Wilen, C., Orchard, R., Virgin, H. W., Listgarten, J. and Root, D. E. (2016) 'Optimized sgRNA design to maximize activity and minimize off-target effects of CRISPR-Cas9', *Nature Biotechnology,* 34(2), pp. 184-191. DOI: 10.1038/nbt.3437.

Dong, M. B., Wang, G., Chow, R. D., Ye, L., Zhu, L., Dai, X., Park, J. J., Kim, H. R., Errami, Y., Guzman, C. D., Zhou, X., Chen, K. Y., Renauer, P. A., Du, Y., Shen, J., Lam, S. Z., Zhou, J. J., Lannin, D. R., Herbst, R. S. and Chen, S. (2019) 'Systematic Immunotherapy Target Discovery Using Genome-Scale In Vivo CRISPR Screens in CD8 T Cells', *Cell,* 178(5), pp. 1189-1204.e23. DOI: 10.1016/j.cell.2019.07.044.

Dummer, R., Guminksi, A., Gutzmer, R., Lear, J. T., Lewis, K. D., Chang, A. L. S., Combemale, P., Dirix, L., Kaatz, M., Kudchadkar, R., Loquai, C., Plummer, R., Schulze, H. J., Stratigos, A. J., Trefzer, U., Squittieri, N. and Migden, M. R. (2020) 'Long-term efficacy and safety of sonidegib in patients with advanced basal cell carcinoma: 42-month analysis of the phase II randomized, double-blind BOLT study', *Br J Dermatol,* 182(6), pp. 1369-1378. DOI: 10.1111/bjd.18552.

Ecke, I., Petry, F., Rosenberger, A., Tauber, S., Mönkemeyer, S., Hess, I., Dullin, C., Kimmina, S., Pirngruber, J., Johnsen, S. A., Uhmann, A., Nitzki, F., Wojnowski, L., Schulz-Schaeffer, W., Witt, O. and Hahn, H. (2009) 'Antitumor effects of a combined 5-aza-2'deoxycytidine and valproic acid treatment on rhabdomyosarcoma and medulloblastoma in Ptch mutant mice', *Cancer Res,* 69(3), pp. 887-95. DOI: 10.1158/0008-5472.Can-08-0946.

Estoppey, D., Hewett, J. W., Guy, C. T., Harrington, E., Thomas, J. R., Schirle, M., Cuttat, R., Waldt, A., Gerrits, B., Yang, Z., Schuierer, S., Pan, X., Xie, K., Carbone, W., Knehr, J., Lindeman, A., Russ, C., Frias, E., Hoffman, G. R., Varadarajan, M., Ramadan, N., Reece-Hoyes, J. S., Wang, Q., Chen, X., McAllister, G., Roma, G., Bouwmeester, T. and Hoepfner, D. (2017) 'Identification of a novel NAMPT inhibitor by CRISPR/Cas9 chemogenomic profiling in mammalian cells', *Sci Rep,* 7, pp. 42728. DOI: 10.1038/srep42728.

Evers, B., Jastrzebski, K., Heijmans, J. P., Grernrum, W., Beijersbergen, R. L. and Bernards, R. (2016) 'CRISPR knockout screening outperforms shRNA and CRISPRi in identifying essential genes', *Nat Biotechnol,* 34(6), pp. 631-3. DOI: 10.1038/nbt.3536.

Fan, G., Beard, C., Chen, R. Z., Csankovszki, G., Sun, Y., Siniaia, M., Biniszkiewicz, D., Bates, B., Lee, P. P., Kuhn, R., Trumpp, A., Poon, C., Wilson, C. B. and Jaenisch, R. (2001) 'DNA hypomethylation perturbs the function and survival of CNS neurons in postnatal animals', *J Neurosci,* 21(3), pp. 788-97. DOI: 10.1523/jneurosci.21-03-00788.2001.

Feil, R., Wagner, J., Metzger, D. and Chambon, P. (1997) 'Regulation of Cre recombinase activity by mutated estrogen receptor ligand-binding domains', *Biochem Biophys Res Commun,* 237(3), pp. 752-7. DOI: 10.1006/bbrc.1997.7124.

Feng, J., Chang, H., Li, E. and Fan, G. (2005) 'Dynamic expression of de novo DNA methyltransferases Dnmt3a and Dnmt3b in the central nervous system', *J Neurosci Res,* 79(6), pp. 734-46. DOI: 10.1002/jnr.20404.

Gajjar, A., Chintagumpala, M., Ashley, D., Kellie, S., Kun, L. E., Merchant, T. E., Woo, S., Wheeler, G., Ahern, V., Krasin, M. J., Fouladi, M., Broniscer, A., Krance, R., Hale, G. A., Stewart, C. F., Dauser, R., Sanford, R. A., Fuller, C., Lau, C., Boyett, J. M., Wallace, D. and Gilbertson, R. J. (2006) 'Risk-adapted craniospinal radiotherapy followed by high-dose chemotherapy and stem-cell rescue in children with newly diagnosed medulloblastoma (St Jude Medulloblastoma-96): long-term results from a prospective, multicentre trial', *Lancet Oncol,* 7(10), pp. 813-20. DOI: 10.1016/s1470-2045(06)70867-1.

García-Delgado, R., de Miguel, D., Bailén, A., González, J. R., Bargay, J., Falantes, J. F., Andreu, R., Ramos, F., Tormo, M., Brunet, S., Figueredo, A., Casaño, J., Medina, A., Badiella, L., Jurado, A. F. and Sanz, G. (2014) 'Effectiveness and safety of different azacitidine dosage regimens in patients with myelodysplastic syndromes or acute myeloid leukemia', *Leuk Res,* 38(7), pp. 744-50. DOI: 10.1016/j.leukres.2014.03.004.

Garcia-Lopez, J., Kumar, R., Smith, K. S. and Northcott, P. A. (2021) 'Deconstructing Sonic Hedgehog Medulloblastoma: Molecular Subtypes, Drivers, and Beyond', *Trends Genet,* 37(3), pp. 235-250. DOI: 10.1016/j.tig.2020.11.001.

Garcia, N., Al-Hendy, A., Baracat, E. C., Carvalho, K. C. and Yang, Q. (2020) 'Targeting Hedgehog Pathway and DNA Methyltransferases in Uterine Leiomyosarcoma Cells', *Cells,* 10(1). DOI: 10.3390/cells10010053.

Gibson, P., Tong, Y., Robinson, G., Thompson, M. C., Currle, D. S., Eden, C., Kranenburg, T. A., Hogg, T., Poppleton, H., Martin, J., Finkelstein, D., Pounds, S., Weiss, A., Patay, Z., Scoggins, M., Ogg, R., Pei, Y., Yang, Z. J., Brun, S., Lee, Y., Zindy, F., Lindsey, J. C., Taketo, M. M., Boop, F. A., Sanford, R. A., Gajjar, A., Clifford, S. C., Roussel, M. F., McKinnon, P. J., Gutmann, D. H., Ellison, D. W., Wechsler-Reya, R. and Gilbertson, R. J. (2010) 'Subtypes of medulloblastoma have distinct developmental origins', *Nature,* 468(7327), pp. 1095-9. DOI: 10.1038/nature09587.

Gilbert, L. A., Horlbeck, M. A., Adamson, B., Villalta, J. E., Chen, Y., Whitehead, E. H., Guimaraes, C., Panning, B., Ploegh, H. L., Bassik, M. C., Qi, L. S., Kampmann, M. and Weissman, J. S. (2014) 'Genome-Scale CRISPR-Mediated Control of Gene Repression and Activation', *Cell,* 159(3), pp. 647-61. DOI: 10.1016/j.cell.2014.09.029.

Giraldo, A. M., DeCourcy, K., Ball, S. F., Hylan, D. and Ayares, D. L. (2013) 'Gene expression of Dnmt1 isoforms in porcine oocytes, embryos, and somatic cells', *Cell Reprogram,* 15(4), pp. 309-21. DOI: 10.1089/cell.2012.0088.

Goodrich, L. V., Milenković, L., Higgins, K. M. and Scott, M. P. (1997) 'Altered neural cell fates and medulloblastoma in mouse patched mutants', *Science,* 277(5329), pp. 1109-13. DOI: 10.1126/science.277.5329.1109.

Goto, K., Numata, M., Komura, J. I., Ono, T., Bestor, T. H. and Kondo, H. (1994) 'Expression of DNA methyltransferase gene in mature and immature neurons as well as proliferating cells in mice', *Differentiation,* 56(1-2), pp. 39-44. DOI: 10.1046/j.1432-0436.1994.56120039.x.

Grammel, D., Warmuth-Metz, M., von Bueren, A. O., Kool, M., Pietsch, T., Kretzschmar, H. A., Rowitch, D. H., Rutkowski, S., Pfister, S. M. and Schüller, U. (2012) 'Sonic hedgehog-associated medulloblastoma arising from the cochlear nuclei of the brainstem', *Acta Neuropathol,* 123(4), pp. 601-14. DOI: 10.1007/s00401-012-0961-0.

Griesinger, A. M., Birks, D. K., Donson, A. M., Amani, V., Hoffman, L. M., Waziri, A., Wang, M., Handler, M. H. and Foreman, N. K. (2013) 'Characterization of distinct immunophenotypes across pediatric brain tumor types', *J Immunol,* 191(9), pp. 4880-8. DOI: 10.4049/jimmunol.1301966.

Gröbner, S. N., Worst, B. C., Weischenfeldt, J., Buchhalter, I., Kleinheinz, K., Rudneva, V. A., Johann, P. D., Balasubramanian, G. P., Segura-Wang, M., Brabetz, S., Bender, S., Hutter, B., Sturm, D., Pfaff, E., Hübschmann, D., Zipprich, G., Heinold, M., Eils, J., Lawerenz, C., Erkek, S., Lambo, S., Waszak, S., Blattmann, C., Borkhardt, A., Kuhlen, M., Eggert, A., Fulda, S., Gessler, M., Wegert, J., Kappler, R., Baumhoer, D., Burdach, S., Kirschner-Schwabe, R., Kontny, U., Kulozik, A. E., Lohmann, D., Hettmer, S., Eckert, C., Bielack, S., Nathrath, M., Niemeyer, C., Richter, G. H., Schulte, J., Siebert, R., Westermann, F., Molenaar, J. J., Vassal, G., Witt, H., Burkhardt, B., Kratz, C. P., Witt, O., van Tilburg, C. M., Kramm, C. M., Fleischhack, G., Dirksen, U., Rutkowski, S., Frühwald, M., von Hoff, K., Wolf, S., Klingebiel, T., Koscielniak, E., Landgraf, P., Koster, J., Resnick, A. C., Zhang, J., Liu, Y., Zhou, X., Waanders, A. J., Zwijnenburg, D. A., Raman, P., Brors, B., Weber, U. D., Northcott, P. A., Pajtler, K. W., Kool, M., Piro, R. M., Korbel, J. O., Schlesner, M., Eils, R., Jones, D. T. W., Lichter, P., Chavez, L., Zapatka, M. and Pfister, S. M. (2018) 'Author Correction: The landscape of genomic alterations across childhood cancers', *Nature,* 559(7714), pp. E10. DOI: 10.1038/s41586-018-0167-2.

Gros, C., Fleury, L., Nahoum, V., Faux, C., Valente, S., Labella, D., Cantagrel, F., Rilova, E., Bouhlel, M. A., David-Cordonnier, M. H., Dufau, I., Ausseil, F., Mai, A., Mourey, L., Lacroix, L. and Arimondo, P. B. (2015) 'New insights on the mechanism of quinoline-based DNA Methyltransferase inhibitors', *J Biol Chem,* 290(10), pp. 6293-302. DOI: 10.1074/jbc.M114.594671.

Gump, J. M., Donson, A. M., Birks, D. K., Amani, V. M., Rao, K. K., Griesinger, A. M., Kleinschmidt-DeMasters, B. K., Johnston, J. M., Anderson, R. C., Rosenfeld, A., Handler, M., Gore, L., Foreman,

N. and Hankinson, T. C. (2015) 'Identification of targets for rational pharmacological therapy in childhood craniopharyngioma', *Acta Neuropathol Commun,* 3, pp. 30. DOI: 10.1186/s40478-015-0211-5.

Hafner, M., Niepel, M., Chung, M. and Sorger, P. K. (2016) 'Growth rate inhibition metrics correct for confounders in measuring sensitivity to cancer drugs', *Nat Methods,* 13(6), pp. 521-7. DOI: 10.1038/nmeth.3853.

Hahn, H., Wojnowski, L., Specht, K., Kappler, R., Calzada-Wack, J., Potter, D., Zimmer, A., Müller, U., Samson, E., Quintanilla-Martinez, L. and Zimmer, A. (2000) 'Patched target Igf2 is indispensable for the formation of medulloblastoma and rhabdomyosarcoma', *J Biol Chem,* 275(37), pp. 28341-4. DOI: 10.1074/jbc.C000352200.

Hallahan, A. R., Pritchard, J. I., Hansen, S., Benson, M., Stoeck, J., Hatton, B. A., Russell, T. L., Ellenbogen, R. G., Bernstein, I. D., Beachy, P. A. and Olson, J. M. (2004) 'The SmoA1 mouse model reveals that notch signaling is critical for the growth and survival of sonic hedgehog-induced medulloblastomas', *Cancer Res,* 64(21), pp. 7794-800. DOI: 10.1158/0008-5472.Can-04-1813.

Hart, T., Brown, K. R., Sircoulomb, F., Rottapel, R. and Moffat, J. (2014) 'Measuring error rates in genomic perturbation screens: gold standards for human functional genomics', *Mol Syst Biol,* 10(7), pp. 733. DOI: 10.15252/msb.20145216.

Hart, T., Chandrashekhar, M., Aregger, M., Steinhart, Z., Brown, K. R., MacLeod, G., Mis, M., Zimmermann, M., Fradet-Turcotte, A., Sun, S., Mero, P., Dirks, P., Sidhu, S., Roth, F. P., Rissland, O. S., Durocher, D., Angers, S. and Moffat, J. (2015) 'High-Resolution CRISPR Screens Reveal Fitness Genes and Genotype-Specific Cancer Liabilities', *Cell,* 163(6), pp. 1515-26. DOI: 10.1016/j.cell.2015.11.015.

Hasselblatt, M., Gesk, S., Oyen, F., Rossi, S., Viscardi, E., Giangaspero, F., Giannini, C., Judkins, A. R., Frühwald, M. C., Obser, T., Schneppenheim, R., Siebert, R. and Paulus, W. (2011) 'Nonsense mutation and inactivation of SMARCA4 (BRG1) in an atypical teratoid/rhabdoid tumor showing retained SMARCB1 (INI1) expression', *Am J Surg Pathol,* 35(6), pp. 933-5. DOI: 10.1097/PAS.0b013e3182196a39.

Hatton, B. A., Villavicencio, E. H., Tsuchiya, K. D., Pritchard, J. I., Ditzler, S., Pullar, B., Hansen, S., Knoblaugh, S. E., Lee, D., Eberhart, C. G., Hallahan, A. R. and Olson, J. M. (2008) 'The Smo/Smo model: hedgehog-induced medulloblastoma with 90% incidence and leptomeningeal spread', *Cancer Res,* 68(6), pp. 1768-76. DOI: 10.1158/0008-5472.Can-07-5092.

Haycraft, C. J., Banizs, B., Aydin-Son, Y., Zhang, Q., Michaud, E. J. and Yoder, B. K. (2005) 'Gli2 and Gli3 localize to cilia and require the intraflagellar transport protein polaris for processing and function', *PLoS Genet,* 1(4), pp. e53. DOI: 10.1371/journal.pgen.0010053.

Helms, A. W., Abney, A. L., Ben-Arie, N., Zoghbi, H. Y. and Johnson, J. E. (2000) 'Autoregulation and multiple enhancers control Math1 expression in the developing nervous system', *Development,* 127(6), pp. 1185-96. DOI: 10.1242/dev.127.6.1185.

Higdon, R., Kala, J., Wilkins, D., Yan, J. F., Sethi, M. K., Lin, L., Liu, S., Montague, E., Janko, I., Choiniere, J., Kolker, N., Hancock, W. S., Kolker, E. and Fanayan, S. (2017) 'Integrated Proteomic and Transcriptomic-Based Approaches to Identifying Signature Biomarkers and Pathways for Elucidation of Daoy and UW228 Subtypes', *Proteomes,* 5(1). DOI: 10.3390/proteomes5010005.

Hou, P., Wu, C., Wang, Y., Qi, R., Bhavanasi, D., Zuo, Z., Dos Santos, C., Chen, S., Chen, Y., Zheng, H., Wang, H., Perl, A., Guo, D. and Huang, J. (2017) 'A Genome-Wide CRISPR Screen Identifies Genes Critical for Resistance to FLT3 Inhibitor AC220', *Cancer Res,* 77(16), pp. 4402-4413. DOI: 10.1158/0008-5472.Can-16-1627.

Hovestadt, V., Jones, D. T., Picelli, S., Wang, W., Kool, M., Northcott, P. A., Sultan, M., Stachurski, K., Ryzhova, M., Warnatz, H. J., Ralser, M., Brun, S., Bunt, J., Jäger, N., Kleinheinz, K., Erkek, S., Weber, U. D., Bartholomae, C. C., von Kalle, C., Lawerenz, C., Eils, J., Koster, J., Versteeg, R., Milde, T., Witt, O., Schmidt, S., Wolf, S., Pietsch, T., Rutkowski, S., Scheurlen, W., Taylor, M. D., Brors, B., Felsberg, J., Reifenberger, G., Borkhardt, A., Lehrach, H., Wechsler-Reya, R. J., Eils, R., Yaspo, M. L., Landgraf,

P., Korshunov, A., Zapatka, M., Radlwimmer, B., Pfister, S. M. and Lichter, P. (2014) 'Decoding the regulatory landscape of medulloblastoma using DNA methylation sequencing', *Nature,* 510(7506), pp. 537-41. DOI: 10.1038/nature13268.

Hsu, P. D., Lander, E. S. and Zhang, F. (2014) 'Development and applications of CRISPR-Cas9 for genome engineering', *Cell,* 157(6), pp. 1262-1278. DOI: 10.1016/j.cell.2014.05.010.

Hsu, P. D., Scott, D. A., Weinstein, J. A., Ran, F. A., Konermann, S., Agarwala, V., Li, Y., Fine, E. J., Wu, X., Shalem, O., Cradick, T. J., Marraffini, L. A., Bao, G. and Zhang, F. (2013) 'DNA targeting specificity of RNA-guided Cas9 nucleases', *Nat Biotechnol,* 31(9), pp. 827-32. DOI: 10.1038/nbt.2647.

Huang, A., Garraway, L. A., Ashworth, A. and Weber, B. (2020) 'Synthetic lethality as an engine for cancer drug target discovery', *Nat Rev Drug Discov,* 19(1), pp. 23-38. DOI: 10.1038/s41573-019-0046-z.

Huang, G. H., Xu, Q. F., Cui, Y. H., Li, N., Bian, X. W. and Lv, S. Q. (2016) 'Medulloblastoma stem cells: Promising targets in medulloblastoma therapy', *Cancer Sci,* 107(5), pp. 583-9. DOI: 10.1111/cas.12925.

Huangfu, D., Liu, A., Rakeman, A. S., Murcia, N. S., Niswander, L. and Anderson, K. V. (2003) 'Hedgehog signalling in the mouse requires intraflagellar transport proteins', *Nature,* 426(6962), pp. 83-7. DOI: 10.1038/nature02061.

Inano, K., Suetake, I., Ueda, T., Miyake, Y., Nakamura, M., Okada, M. and Tajima, S. (2000) 'Maintenance-type DNA methyltransferase is highly expressed in post-mitotic neurons and localized in the cytoplasmic compartment', *J Biochem,* 128(2), pp. 315-21. DOI: 10.1093/oxfordjournals.jbchem.a022755.

Iorio, F., Behan, F. M., Gonçalves, E., Bhosle, S. G., Chen, E., Shepherd, R., Beaver, C., Ansari, R., Pooley, R., Wilkinson, P., Harper, S., Butler, A. P., Stronach, E. A., Saez-Rodriguez, J., Yusa, K. and Garnett, M. J. (2018) 'Unsupervised correction of gene-independent cell responses to CRISPR-Cas9 targeting', *BMC Genomics,* 19(1), pp. 604. DOI: 10.1186/s12864-018-4989-y.

Ivanov, D. P., Coyle, B., Walker, D. A. and Grabowska, A. M. (2016) 'In vitro models of medulloblastoma: Choosing the right tool for the job', *J Biotechnol,* 236, pp. 10-25. DOI: 10.1016/j.jbiotec.2016.07.028.

Jackson-Grusby, L., Beard, C., Possemato, R., Tudor, M., Fambrough, D., Csankovszki, G., Dausman, J., Lee, P., Wilson, C., Lander, E. and Jaenisch, R. (2001) 'Loss of genomic methylation causes p53-dependent apoptosis and epigenetic deregulation', *Nat Genet,* 27(1), pp. 31-9. DOI: 10.1038/83730.

Jackson, A. L., Bartz, S. R., Schelter, J., Kobayashi, S. V., Burchard, J., Mao, M., Li, B., Cavet, G. and Linsley, P. S. (2003) 'Expression profiling reveals off-target gene regulation by RNAi', *Nat Biotechnol,* 21(6), pp. 635-7. DOI: 10.1038/nbt831.

Jackson, A. L. and Linsley, P. S. (2010) 'Recognizing and avoiding siRNA off-target effects for target identification and therapeutic application', *Nat Rev Drug Discov,* 9(1), pp. 57-67. DOI: 10.1038/nrd3010.

Jacobsen, P. F., Jenkyn, D. J. and Papadimitriou, J. M. (1985) 'Establishment of a human medulloblastoma cell line and its heterotransplantation into nude mice', *J Neuropathol Exp Neurol,* 44(5), pp. 472-85. DOI: 10.1097/00005072-198509000-00003.

Jagani, Z., Mora-Blanco, E. L., Sansam, C. G., McKenna, E. S., Wilson, B., Chen, D., Klekota, J., Tamayo, P., Nguyen, P. T., Tolstorukov, M., Park, P. J., Cho, Y. J., Hsiao, K., Buonamici, S., Pomeroy, S. L., Mesirov, J. P., Ruffner, H., Bouwmeester, T., Luchansky, S. J., Murtie, J., Kelleher, J. F., Warmuth, M., Sellers, W. R., Roberts, C. W. and Dorsch, M. (2010) 'Loss of the tumor suppressor Snf5 leads to aberrant activation of the Hedgehog-Gli pathway', *Nat Med,* 16(12), pp. 1429-33. DOI: 10.1038/nm.2251.

Jen, E. Y., Wang, X., Li, M., Li, H., Lee, S. L., Ni, N., Przepiorka, D., Vallejo, J., Leong, R., Ma, L., Gehrke, B. J., McLamore, S., Theoret, M. R. and de Claro, R. A. (2022) 'FDA Approval Summary: Oral Azacitidine

for Continued Treatment of Adults with Acute Myeloid Leukemia Unable to Complete Intensive Curative Therapy', *Clin Cancer Res,* 28(14), pp. 2989-2993. DOI: 10.1158/1078-0432.Ccr-21-4525.

Joung, J., Konermann, S., Gootenberg, J. S., Abudayyeh, O. O., Platt, R. J., Brigham, M. D., Sanjana, N. E. and Zhang, F. (2017) 'Genome-scale CRISPR-Cas9 knockout and transcriptional activation screening', *Nat Protoc,* 12(4), pp. 828-863. DOI: 10.1038/nprot.2017.016.

Juraschka, K. and Taylor, M. D. (2019) 'Medulloblastoma in the age of molecular subgroups: a review', *J Neurosurg Pediatr,* 24(4), pp. 353-363. DOI: 10.3171/2019.5.Peds18381.

Jurkowska, R. Z., Jurkowski, T. P. and Jeltsch, A. (2011) 'Structure and function of mammalian DNA methyltransferases', *Chembiochem,* 12(2), pp. 206-22. DOI: 10.1002/cbic.201000195.

Kawauchi, D., Robinson, G., Uziel, T., Gibson, P., Rehg, J., Gao, C., Finkelstein, D., Qu, C., Pounds, S., Ellison, D. W., Gilbertson, R. J. and Roussel, M. F. (2012) 'A mouse model of the most aggressive subgroup of human medulloblastoma', *Cancer Cell,* 21(2), pp. 168-80. DOI: 10.1016/j.ccr.2011.12.023.

Kaya-Okur, H. S., Janssens, D. H., Henikoff, J. G., Ahmad, K. and Henikoff, S. (2020) 'Efficient low-cost chromatin profiling with CUT&Tag', *Nat Protoc,* 15(10), pp. 3264-3283. DOI: 10.1038/s41596-020-0373-x.

Kieran, M. W., Chisholm, J., Casanova, M., Brandes, A. A., Aerts, I., Bouffet, E., Bailey, S., Leary, S., MacDonald, T. J., Mechinaud, F., Cohen, K. J., Riccardi, R., Mason, W., Hargrave, D., Kalambakas, S., Deshpande, P., Tai, F., Hurh, E. and Geoerger, B. (2017) 'Phase I study of oral sonidegib (LDE225) in pediatric brain and solid tumors and a phase II study in children and adults with relapsed medulloblastoma', *Neuro Oncol,* 19(11), pp. 1542-1552. DOI: 10.1093/neuonc/nox109.

Kim, E. and Hart, T. (2021) 'Improved analysis of CRISPR fitness screens and reduced off-target effects with the BAGEL2 gene essentiality classifier', *Genome Med,* 13(1), pp. 2. DOI: 10.1186/s13073-020-00809-3.

Kim, J. Y., Nelson, A. L., Algon, S. A., Graves, O., Sturla, L. M., Goumnerova, L. C., Rowitch, D. H., Segal, R. A. and Pomeroy, S. L. (2003) 'Medulloblastoma tumorigenesis diverges from cerebellar granule cell differentiation in patched heterozygous mice', *Dev Biol,* 263(1), pp. 50-66. DOI: 10.1016/s0012-1606(03)00434-2.

King, A. A., Seidel, K., Di, C., Leisenring, W. M., Perkins, S. M., Krull, K. R., Sklar, C. A., Green, D. M., Armstrong, G. T., Zeltzer, L. K., Wells, E., Stovall, M., Ullrich, N. J., Oeffinger, K. C., Robison, L. L. and Packer, R. J. (2017) 'Long-term neurologic health and psychosocial function of adult survivors of childhood medulloblastoma/PNET: a report from the Childhood Cancer Survivor Study', *Neuro Oncol,* 19(5), pp. 689-698. DOI: 10.1093/neuonc/now242.

Klisch, T. J., Xi, Y., Flora, A., Wang, L., Li, W. and Zoghbi, H. Y. (2011) 'In vivo Atoh1 targetome reveals how a proneural transcription factor regulates cerebellar development', *Proc Natl Acad Sci U S A,* 108(8), pp. 3288-93. DOI: 10.1073/pnas.1100230108.

Komuro, H. and Rakic, P. (1998) 'Distinct modes of neuronal migration in different domains of developing cerebellar cortex', *J Neurosci,* 18(4), pp. 1478-90. DOI: 10.1523/jneurosci.18-04-01478.1998.

Komuro, H., Yacubova, E., Yacubova, E. and Rakic, P. (2001) 'Mode and tempo of tangential cell migration in the cerebellar external granular layer', *J Neurosci,* 21(2), pp. 527-40. DOI: 10.1523/jneurosci.21-02-00527.2001.

Konermann, S., Brigham, M. D., Trevino, A. E., Joung, J., Abudayyeh, O. O., Barcena, C., Hsu, P. D., Habib, N., Gootenberg, J. S., Nishimasu, H., Nureki, O. and Zhang, F. (2015) 'Genome-scale transcriptional activation by an engineered CRISPR-Cas9 complex', *Nature,* 517(7536), pp. 583-8. DOI: 10.1038/nature14136.

Kool, M., Jones, D. T., Jäger, N., Northcott, P. A., Pugh, T. J., Hovestadt, V., Piro, R. M., Esparza, L. A., Markant, S. L., Remke, M., Milde, T., Bourdeaut, F., Ryzhova, M., Sturm, D., Pfaff, E., Stark, S., Hutter, S., Seker-Cin, H., Johann, P., Bender, S., Schmidt, C., Rausch, T., Shih, D., Reimand, J., Sieber, L., Wittmann, A., Linke, L., Witt, H., Weber, U. D., Zapatka, M., König, R., Beroukhim, R., Bergthold, G., van Sluis, P., Volckmann, R., Koster, J., Versteeg, R., Schmidt, S., Wolf, S., Lawerenz, C.,

Bartholomae, C. C., von Kalle, C., Unterberg, A., Herold-Mende, C., Hofer, S., Kulozik, A. E., von Deimling, A., Scheurlen, W., Felsberg, J., Reifenberger, G., Hasselblatt, M., Crawford, J. R., Grant, G. A., Jabado, N., Perry, A., Cowdrey, C., Croul, S., Zadeh, G., Korbel, J. O., Doz, F., Delattre, O., Bader, G. D., McCabe, M. G., Collins, V. P., Kieran, M. W., Cho, Y. J., Pomeroy, S. L., Witt, O., Brors, B., Taylor, M. D., Schüller, U., Korshunov, A., Eils, R., Wechsler-Reya, R. J., Lichter, P. and Pfister, S. M. (2014) 'Genome sequencing of SHH medulloblastoma predicts genotype-related response to smoothened inhibition', *Cancer Cell,* 25(3), pp. 393-405. DOI: 10.1016/j.ccr.2014.02.004.

Kool, M., Korshunov, A., Remke, M., Jones, D. T., Schlanstein, M., Northcott, P. A., Cho, Y. J., Koster, J., Schouten-van Meeteren, A., van Vuurden, D., Clifford, S. C., Pietsch, T., von Bueren, A. O., Rutkowski, S., McCabe, M., Collins, V. P., Bäcklund, M. L., Haberler, C., Bourdeaut, F., Delattre, O., Doz, F., Ellison, D. W., Gilbertson, R. J., Pomeroy, S. L., Taylor, M. D., Lichter, P. and Pfister, S. M. (2012) 'Molecular subgroups of medulloblastoma: an international meta-analysis of transcriptome, genetic aberrations, and clinical data of WNT, SHH, Group 3, and Group 4 medulloblastomas', *Acta Neuropathol,* 123(4), pp. 473-84. DOI: 10.1007/s00401-012-0958-8.

Kuhn, M., Santinha, A. J. and Platt, R. J. (2021) 'Moving from in vitro to in vivo CRISPR screens', *Gene and Genome Editing,* 2, pp. 100008. DOI: https://doi.org/10.1016/j.ggedit.2021.100008.

Kutscher, L. M., Okonechnikov, K., Batora, N. V., Clark, J., Silva, P. B. G., Vouri, M., van Rijn, S., Sieber, L., Statz, B., Gearhart, M. D., Shiraishi, R., Mack, N., Orr, B. A., Korshunov, A., Gudenas, B. L., Smith, K. S., Mercier, A. L., Ayrault, O., Hoshino, M., Kool, M., von Hoff, K., Graf, N., Fleischhack, G., Bardwell, V. J., Pfister, S. M., Northcott, P. A. and Kawauchi, D. (2020) 'Functional loss of a noncanonical BCOR-PRC1.1 complex accelerates SHH-driven medulloblastoma formation', *Genes Dev,* 34(17-18), pp. 1161-1176. DOI: 10.1101/gad.337584.120.

Lago, C., Federico, A., Leva, G., Mack, N. L., Schwalm, B., Ballabio, C., Gianesello, M., Abballe, L., Giovannoni, I., Reddel, S., Rossi, S., Leone, N., Carai, A., Mastronuzzi, A., Bisio, A., Soldano, A., Quintarelli, C., Locatelli, F., Kool, M., Miele, E. and Tiberi, L. (2023) 'Patient- and xenograft-derived organoids recapitulate pediatric brain tumor features and patient treatments', *EMBO Mol Med,* 15(12), pp. e18199. DOI: 10.15252/emmm.202318199.

Langford, D. J., Bailey, A. L., Chanda, M. L., Clarke, S. E., Drummond, T. E., Echols, S., Glick, S., Ingrao, J., Klassen-Ross, T., Lacroix-Fralish, M. L., Matsumiya, L., Sorge, R. E., Sotocinal, S. G., Tabaka, J. M., Wong, D., van den Maagdenberg, A. M., Ferrari, M. D., Craig, K. D. and Mogil, J. S. (2010) 'Coding of facial expressions of pain in the laboratory mouse', *Nat Methods,* 7(6), pp. 447-9. DOI: 10.1038/nmeth.1455.

Lau, J., Schmidt, C., Markant, S. L., Taylor, M. D., Wechsler-Reya, R. J. and Weiss, W. A. (2012) 'Matching mice to malignancy: molecular subgroups and models of medulloblastoma', *Childs Nerv Syst,* 28(4), pp. 521-32. DOI: 10.1007/s00381-012-1704-1.

Lazzaro, M. A. and Picketts, D. J. (2001) 'Cloning and characterization of the murine Imitation Switch (ISWI) genes: differential expression patterns suggest distinct developmental roles for Snf2h and Snf2l', *J Neurochem,* 77(4), pp. 1145-56. DOI: 10.1046/j.1471-4159.2001.00324.x.

Lee, Y., Kawagoe, R., Sasai, K., Li, Y., Russell, H. R., Curran, T. and McKinnon, P. J. (2007) 'Loss of suppressor-of-fused function promotes tumorigenesis', *Oncogene,* 26(44), pp. 6442-7. DOI: 10.1038/sj.onc.1210467.

Li, E., Bestor, T. H. and Jaenisch, R. (1992) 'Targeted mutation of the DNA methyltransferase gene results in embryonic lethality', *Cell,* 69(6), pp. 915-26. DOI: 10.1016/0092-8674(92)90611-f.

Li, F. P. and Fraumeni, J. F., Jr. (1969) 'Rhabdomyosarcoma in children: epidemiologic study and identification of a familial cancer syndrome', *J Natl Cancer Inst,* 43(6), pp. 1365-73.

Li, W., Köster, J., Xu, H., Chen, C. H., Xiao, T., Liu, J. S., Brown, M. and Liu, X. S. (2015) 'Quality control, modeling, and visualization of CRISPR screens with MAGeCK-VISPR', *Genome Biol,* 16, pp. 281. DOI: 10.1186/s13059-015-0843-6.

Li, W., Xu, H., Xiao, T., Cong, L., Love, M. I., Zhang, F., Irizarry, R. A., Liu, J. S., Brown, M. and Liu, X. S. (2014) 'MAGeCK enables robust identification of essential genes from genome-scale CRISPR/Cas9 knockout screens', *Genome Biol,* 15(12), pp. 554. DOI: 10.1186/s13059-014-0554-4.

Li, Y., Song, Q. and Day, B. W. (2019) 'Phase I and phase II sonidegib and vismodegib clinical trials for the treatment of paediatric and adult MB patients: a systemic review and meta-analysis', *Acta Neuropathol Commun,* 7(1), pp. 123. DOI: 10.1186/s40478-019-0773-8.

Lou, E., Schomaker, M., Wilson, J. D., Ahrens, M., Dolan, M. and Nelson, A. C. (2016) 'Complete and sustained response of adult medulloblastoma to first-line sonic hedgehog inhibition with vismodegib', *Cancer Biol Ther,* 17(10), pp. 1010-1016. DOI: 10.1080/15384047.2016.1220453.

Louis, D. N., Ohgaki, H., Wiestler, O. D., Cavenee, W. K., Burger, P. C., Jouvet, A., Scheithauer, B. W. and Kleihues, P. (2007) 'The 2007 WHO classification of tumours of the central nervous system', *Acta Neuropathol,* 114(2), pp. 97-109. DOI: 10.1007/s00401-007-0243-4.

Louis, D. N., Perry, A., Reifenberger, G., von Deimling, A., Figarella-Branger, D., Cavenee, W. K., Ohgaki, H., Wiestler, O. D., Kleihues, P. and Ellison, D. W. (2016) 'The 2016 World Health Organization Classification of Tumors of the Central Nervous System: a summary', *Acta Neuropathol,* 131(6), pp. 803-20. DOI: 10.1007/s00401-016-1545-1.

Louis, D. N., Perry, A., Wesseling, P., Brat, D. J., Cree, I. A., Figarella-Branger, D., Hawkins, C., Ng, H. K., Pfister, S. M., Reifenberger, G., Soffietti, R., von Deimling, A. and Ellison, D. W. (2021) 'The 2021 WHO Classification of Tumors of the Central Nervous System: a summary', *Neuro Oncol,* 23(8), pp. 1231-1251. DOI: 10.1093/neuonc/noab106.

Love, M. I., Huber, W. and Anders, S. (2014) 'Moderated estimation of fold change and dispersion for RNA-seq data with DESeq2', *Genome Biol,* 15(12), pp. 550. DOI: 10.1186/s13059-014-0550-8.

Lucidi, A., Tomaselli, D., Rotili, D. and Mai, A. (2019) 'DNA Methylation: Biological Implications and Modulation of Its Aberrant Dysregulation', *DNA, Rna, and Histone Methylomes*, pp. 295-331. DOI: 10.1007/978-3-030-14792-1_12.

Machold, R. and Fishell, G. (2005) 'Math1 is expressed in temporally discrete pools of cerebellar rhombic-lip neural progenitors', *Neuron,* 48(1), pp. 17-24. DOI: 10.1016/j.neuron.2005.08.028.

Mali, P., Aach, J., Stranges, P. B., Esvelt, K. M., Moosburner, M., Kosuri, S., Yang, L. and Church, G. M. (2013) 'CAS9 transcriptional activators for target specificity screening and paired nickases for cooperative genome engineering', *Nat Biotechnol,* 31(9), pp. 833-8. DOI: 10.1038/nbt.2675.

Mao, J., Ligon, K. L., Rakhlin, E. Y., Thayer, S. P., Bronson, R. T., Rowitch, D. and McMahon, A. P. (2006) 'A novel somatic mouse model to survey tumorigenic potential applied to the Hedgehog pathway', *Cancer Res,* 66(20), pp. 10171-8. DOI: 10.1158/0008-5472.Can-06-0657.

Matei, V., Pauley, S., Kaing, S., Rowitch, D., Beisel, K. W., Morris, K., Feng, F., Jones, K., Lee, J. and Fritzsch, B. (2005) 'Smaller inner ear sensory epithelia in Neurog 1 null mice are related to earlier hair cell cycle exit', *Dev Dyn,* 234(3), pp. 633-50. DOI: 10.1002/dvdy.20551.

McDade, J. R., Waxmonsky, N. C., Swanson, L. E. and Fan, M. (2016) 'Practical Considerations for Using Pooled Lentiviral CRISPR Libraries', *Curr Protoc Mol Biol,* 115, pp. 31.5.1-31.5.13. DOI: 10.1002/cpmb.8.

Merk, D. J., Ohli, J., Merk, N. D., Thatikonda, V., Morrissy, S., Schoof, M., Schmid, S. N., Harrison, L., Filser, S., Ahlfeld, J., Erkek, S., Raithatha, K., Andreska, T., Weißhaar, M., Launspach, M., Neumann, J. E., Shakarami, M., Plenker, D., Marra, M. A., Li, Y., Mungall, A. J., Moore, R. A., Ma, Y., Jones, S. J. M., Lutz, B., Ertl-Wagner, B., Rossi, A., Wagener, R., Siebert, R., Jung, A., Eberhart, C. G., Lach, B., Sendtner, M., Pfister, S. M., Taylor, M. D., Chavez, L., Kool, M. and Schüller, U. (2018) 'Opposing Effects of CREBBP Mutations Govern the Phenotype of Rubinstein-Taybi Syndrome and Adult SHH Medulloblastoma', *Dev Cell,* 44(6), pp. 709-724.e6. DOI: 10.1016/j.devcel.2018.02.012.

Mertineit, C., Yoder, J. A., Taketo, T., Laird, D. W., Trasler, J. M. and Bestor, T. H. (1998) 'Sex-specific exons control DNA methyltransferase in mammalian germ cells', *Development,* 125(5), pp. 889-97. DOI: 10.1242/dev.125.5.889.

Miari, R., Azzam, N., Bar-Shalom, R. and Fares, F. (2021) '5-aza-2'-deoxycytidine induces apoptosis and inhibits tumour growth in vivo of FaDu cells, a specific HPVnegative HNSCC cell line', *PLoS One,* 16(9), pp. e0253756. DOI: 10.1371/journal.pone.0253756.

Michalski, J. M., Janss, A. J., Vezina, L. G., Smith, K. S., Billups, C. A., Burger, P. C., Embry, L. M., Cullen, P. L., Hardy, K. K., Pomeroy, S. L., Bass, J. K., Perkins, S. M., Merchant, T. E., Colte, P. D., Fitzgerald, T. J., Booth, T. N., Cherlow, J. M., Muraszko, K. M., Hadley, J., Kumar, R., Han, Y., Tarbell, N. J., Fouladi, M., Pollack, I. F., Packer, R. J., Li, Y., Gajjar, A. and Northcott, P. A. (2021) 'Children's Oncology Group Phase III Trial of Reduced-Dose and Reduced-Volume Radiotherapy With Chemotherapy for Newly Diagnosed Average-Risk Medulloblastoma', *J Clin Oncol,* 39(24), pp. 2685-2697. DOI: 10.1200/jco.20.02730.

Migden, M. R., Guminski, A., Gutzmer, R., Dirix, L., Lewis, K. D., Combemale, P., Herd, R. M., Kudchadkar, R., Trefzer, U., Gogov, S., Pallaud, C., Yi, T., Mone, M., Kaatz, M., Loquai, C., Stratigos, A. J., Schulze, H. J., Plummer, R., Chang, A. L., Cornélis, F., Lear, J. T., Sellami, D. and Dummer, R. (2015) 'Treatment with two different doses of sonidegib in patients with locally advanced or metastatic basal cell carcinoma (BOLT): a multicentre, randomised, double-blind phase 2 trial', *Lancet Oncol,* 16(6), pp. 716-28. DOI: 10.1016/s1470-2045(15)70100-2.

Miles, D., von Minckwitz, G. and Seidman, A. D. (2002) 'Combination versus sequential single-agent therapy in metastatic breast cancer', *Oncologist,* 7 Suppl 6, pp. 13-9.

Moreno, N., Schmidt, C., Ahlfeld, J., Pöschl, J., Dittmar, S., Pfister, S. M., Kool, M., Kerl, K. and Schüller, U. (2014) 'Loss of Smarc proteins impairs cerebellar development', *J Neurosci,* 34(40), pp. 13486-91. DOI: 10.1523/jneurosci.2560-14.2014.

Mulhern, R. K., Palmer, S. L., Merchant, T. E., Wallace, D., Kocak, M., Brouwers, P., Krull, K., Chintagumpala, M., Stargatt, R., Ashley, D. M., Tyc, V. L., Kun, L., Boyett, J. and Gajjar, A. (2005) 'Neurocognitive consequences of risk-adapted therapy for childhood medulloblastoma', *J Clin Oncol,* 23(24), pp. 5511-9. DOI: 10.1200/jco.2005.00.703.

Munoz, D. M., Cassiani, P. J., Li, L., Billy, E., Korn, J. M., Jones, M. D., Golji, J., Ruddy, D. A., Yu, K., McAllister, G., DeWeck, A., Abramowski, D., Wan, J., Shirley, M. D., Neshat, S. Y., Rakiec, D., de Beaumont, R., Weber, O., Kauffmann, A., McDonald, E. R., 3rd, Keen, N., Hofmann, F., Sellers, W. R., Schmelzle, T., Stegmeier, F. and Schlabach, M. R. (2016) 'CRISPR Screens Provide a Comprehensive Assessment of Cancer Vulnerabilities but Generate False-Positive Hits for Highly Amplified Genomic Regions', *Cancer Discov,* 6(8), pp. 900-13. DOI: 10.1158/2159-8290.Cd-16-0178.

Northcott, P. A., Buchhalter, I., Morrissy, A. S., Hovestadt, V., Weischenfeldt, J., Ehrenberger, T., Gröbner, S., Segura-Wang, M., Zichner, T., Rudneva, V. A., Warnatz, H. J., Sidiropoulos, N., Phillips, A. H., Schumacher, S., Kleinheinz, K., Waszak, S. M., Erkek, S., Jones, D. T. W., Worst, B. C., Kool, M., Zapatka, M., Jäger, N., Chavez, L., Hutter, B., Bieg, M., Paramasivam, N., Heinold, M., Gu, Z., Ishaque, N., Jäger-Schmidt, C., Imbusch, C. D., Jugold, A., Hübschmann, D., Risch, T., Amstislavskiy, V., Gonzalez, F. G. R., Weber, U. D., Wolf, S., Robinson, G. W., Zhou, X., Wu, G., Finkelstein, D., Liu, Y., Cavalli, F. M. G., Luu, B., Ramaswamy, V., Wu, X., Koster, J., Ryzhova, M., Cho, Y. J., Pomeroy, S. L., Herold-Mende, C., Schuhmann, M., Ebinger, M., Liau, L. M., Mora, J., McLendon, R. E., Jabado, N., Kumabe, T., Chuah, E., Ma, Y., Moore, R. A., Mungall, A. J., Mungall, K. L., Thiessen, N., Tse, K., Wong, T., Jones, S. J. M., Witt, O., Milde, T., Von Deimling, A., Capper, D., Korshunov, A., Yaspo, M. L., Kriwacki, R., Gajjar, A., Zhang, J., Beroukhim, R., Fraenkel, E., Korbel, J. O., Brors, B., Schlesner, M., Eils, R., Marra, M. A., Pfister, S. M., Taylor, M. D. and Lichter, P. (2017) 'The whole-genome landscape of medulloblastoma subtypes', *Nature,* 547(7663), pp. 311-317. DOI: 10.1038/nature22973.

Northcott, P. A., Hielscher, T., Dubuc, A., Mack, S., Shih, D., Remke, M., Al-Halabi, H., Albrecht, S., Jabado, N., Eberhart, C. G., Grajkowska, W., Weiss, W. A., Clifford, S. C., Bouffet, E., Rutka, J. T., Korshunov, A., Pfister, S. and Taylor, M. D. (2011a) 'Pediatric and adult sonic hedgehog medulloblastomas are

clinically and molecularly distinct', *Acta Neuropathol,* 122(2), pp. 231-40. DOI: 10.1007/s00401-011-0846-7.

Northcott, P. A., Korshunov, A., Witt, H., Hielscher, T., Eberhart, C. G., Mack, S., Bouffet, E., Clifford, S. C., Hawkins, C. E., French, P., Rutka, J. T., Pfister, S. and Taylor, M. D. (2011b) 'Medulloblastoma comprises four distinct molecular variants', *J Clin Oncol,* 29(11), pp. 1408-14. DOI: 10.1200/jco.2009.27.4324.

Northcott, P. A., Robinson, G. W., Kratz, C. P., Mabbott, D. J., Pomeroy, S. L., Clifford, S. C., Rutkowski, S., Ellison, D. W., Malkin, D., Taylor, M. D., Gajjar, A. and Pfister, S. M. (2019) 'Medulloblastoma', *Nat Rev Dis Primers,* 5(1), pp. 11. DOI: 10.1038/s41572-019-0063-6.

Ocasio, J. K., Babcock, B., Malawsky, D., Weir, S. J., Loo, L., Simon, J. M., Zylka, M. J., Hwang, D., Dismuke, T., Sokolsky, M., Rosen, E. P., Vibhakar, R., Zhang, J., Saulnier, O., Vladoiu, M., El-Hamamy, I., Stein, L. D., Taylor, M. D., Smith, K. S., Northcott, P. A., Colaneri, A., Wilhelmsen, K. and Gershon, T. R. (2019) 'scRNA-seq in medulloblastoma shows cellular heterogeneity and lineage expansion support resistance to SHH inhibitor therapy', *Nat Commun,* 10(1), pp. 5829. DOI: 10.1038/s41467-019-13657-6.

Okano, M., Bell, D. W., Haber, D. A. and Li, E. (1999) 'DNA methyltransferases Dnmt3a and Dnmt3b are essential for de novo methylation and mammalian development', *Cell,* 99(3), pp. 247-57. DOI: 10.1016/s0092-8674(00)81656-6.

Oliver, T. G., Read, T. A., Kessler, J. D., Mehmeti, A., Wells, J. F., Huynh, T. T., Lin, S. M. and Wechsler-Reya, R. J. (2005) 'Loss of patched and disruption of granule cell development in a pre-neoplastic stage of medulloblastoma', *Development,* 132(10), pp. 2425-39. DOI: 10.1242/dev.01793.

Ostrom, Q. T., Price, M., Neff, C., Cioffi, G., Waite, K. A., Kruchko, C. and Barnholtz-Sloan, J. S. (2023) 'CBTRUS Statistical Report: Primary Brain and Other Central Nervous System Tumors Diagnosed in the United States in 2016-2020', *Neuro Oncol,* 25(Supplement_4), pp. iv1-iv99. DOI: 10.1093/neuonc/noad149.

Othman, R. T., Kimishi, I., Bradshaw, T. D., Storer, L. C., Korshunov, A., Pfister, S. M., Grundy, R. G., Kerr, I. D. and Coyle, B. (2014) 'Overcoming multiple drug resistance mechanisms in medulloblastoma', *Acta Neuropathol Commun,* 2, pp. 57. DOI: 10.1186/2051-5960-2-57.

Owa, T., Taya, S., Miyashita, S., Yamashita, M., Adachi, T., Yamada, K., Yokoyama, M., Aida, S., Nishioka, T., Inoue, Y. U., Goitsuka, R., Nakamura, T., Inoue, T., Kaibuchi, K. and Hoshino, M. (2018) 'Meis1 Coordinates Cerebellar Granule Cell Development by Regulating Pax6 Transcription, BMP Signaling and Atoh1 Degradation', *J Neurosci,* 38(5), pp. 1277-1294. DOI: 10.1523/jneurosci.1545-17.2017.

Packer, R. J., Gajjar, A., Vezina, G., Rorke-Adams, L., Burger, P. C., Robertson, P. L., Bayer, L., LaFond, D., Donahue, B. R., Marymont, M. H., Muraszko, K., Langston, J. and Sposto, R. (2006) 'Phase III study of craniospinal radiation therapy followed by adjuvant chemotherapy for newly diagnosed average-risk medulloblastoma', *J Clin Oncol,* 24(25), pp. 4202-8. DOI: 10.1200/jco.2006.06.4980.

Pak, E., MacKenzie, E. L., Zhao, X., Pazyra-Murphy, M. F., Park, P. M. C., Wu, L., Shaw, D. L., Addleson, E. C., Cayer, S. S., Lopez, B. G., Agar, N. Y. R., Rubin, L. L., Qi, J., Merk, D. J. and Segal, R. A. (2019) 'A large-scale drug screen identifies selective inhibitors of class I HDACs as a potential therapeutic option for SHH medulloblastoma', *Neuro Oncol,* 21(9), pp. 1150-1163. DOI: 10.1093/neuonc/noz089.

Pambid, M. R., Berns, R., Adomat, H. H., Hu, K., Triscott, J., Maurer, N., Zisman, N., Ramaswamy, V., Hawkins, C. E., Taylor, M. D., Dunham, C., Guns, E. and Dunn, S. E. (2014) 'Overcoming resistance to Sonic Hedgehog inhibition by targeting p90 ribosomal S6 kinase in pediatric medulloblastoma', *Pediatr Blood Cancer,* 61(1), pp. 107-15. DOI: 10.1002/pbc.24675.

Parsons, D. W., Li, M., Zhang, X., Jones, S., Leary, R. J., Lin, J. C., Boca, S. M., Carter, H., Samayoa, J., Bettegowda, C., Gallia, G. L., Jallo, G. I., Binder, Z. A., Nikolsky, Y., Hartigan, J., Smith, D. R., Gerhard, D. S., Fults, D. W., VandenBerg, S., Berger, M. S., Marie, S. K., Shinjo, S. M., Clara, C., Phillips, P. C., Minturn, J. E., Biegel, J. A., Judkins, A. R., Resnick, A. C., Storm, P. B., Curran, T., He, Y., Rasheed, B. A., Friedman, H. S., Keir, S. T., McLendon, R., Northcott, P. A., Taylor, M. D., Burger, P. C., Riggins,

G. J., Karchin, R., Parmigiani, G., Bigner, D. D., Yan, H., Papadopoulos, N., Vogelstein, B., Kinzler, K. W. and Velculescu, V. E. (2011) 'The genetic landscape of the childhood cancer medulloblastoma', *Science,* 331(6016), pp. 435-9. DOI: 10.1126/science.1198056.

Pei, Y., Moore, C. E., Wang, J., Tewari, A. K., Eroshkin, A., Cho, Y. J., Witt, H., Korshunov, A., Read, T. A., Sun, J. L., Schmitt, E. M., Miller, C. R., Buckley, A. F., McLendon, R. E., Westbrook, T. F., Northcott, P. A., Taylor, M. D., Pfister, S. M., Febbo, P. G. and Wechsler-Reya, R. J. (2012) 'An animal model of MYC-driven medulloblastoma', *Cancer Cell,* 21(2), pp. 155-67. DOI: 10.1016/j.ccr.2011.12.021.

Pöschl, J., Stark, S., Neumann, P., Gröbner, S., Kawauchi, D., Jones, D. T., Northcott, P. A., Lichter, P., Pfister, S. M., Kool, M. and Schüller, U. (2014) 'Genomic and transcriptomic analyses match medulloblastoma mouse models to their human counterparts', *Acta Neuropathol,* 128(1), pp. 123-36. DOI: 10.1007/s00401-014-1297-8.

Pugh, T. J., Weeraratne, S. D., Archer, T. C., Pomeranz Krummel, D. A., Auclair, D., Bochicchio, J., Carneiro, M. O., Carter, S. L., Cibulskis, K., Erlich, R. L., Greulich, H., Lawrence, M. S., Lennon, N. J., McKenna, A., Meldrim, J., Ramos, A. H., Ross, M. G., Russ, C., Shefler, E., Sivachenko, A., Sogoloff, B., Stojanov, P., Tamayo, P., Mesirov, J. P., Amani, V., Teider, N., Sengupta, S., Francois, J. P., Northcott, P. A., Taylor, M. D., Yu, F., Crabtree, G. R., Kautzman, A. G., Gabriel, S. B., Getz, G., Jäger, N., Jones, D. T., Lichter, P., Pfister, S. M., Roberts, T. M., Meyerson, M., Pomeroy, S. L. and Cho, Y. J. (2012) 'Medulloblastoma exome sequencing uncovers subtype-specific somatic mutations', *Nature,* 488(7409), pp. 106-10. DOI: 10.1038/nature11329.

Ramaswamy, V., Remke, M., Bouffet, E., Bailey, S., Clifford, S. C., Doz, F., Kool, M., Dufour, C., Vassal, G., Milde, T., Witt, O., von Hoff, K., Pietsch, T., Northcott, P. A., Gajjar, A., Robinson, G. W., Padovani, L., André, N., Massimino, M., Pizer, B., Packer, R., Rutkowski, S., Pfister, S. M., Taylor, M. D. and Pomeroy, S. L. (2016) 'Risk stratification of childhood medulloblastoma in the molecular era: the current consensus', *Acta Neuropathol,* 131(6), pp. 821-31. DOI: 10.1007/s00401-016-1569-6.

Rausch, T., Jones, D. T., Zapatka, M., Stütz, A. M., Zichner, T., Weischenfeldt, J., Jäger, N., Remke, M., Shih, D., Northcott, P. A., Pfaff, E., Tica, J., Wang, Q., Massimi, L., Witt, H., Bender, S., Pleier, S., Cin, H., Hawkins, C., Beck, C., von Deimling, A., Hans, V., Brors, B., Eils, R., Scheurlen, W., Blake, J., Benes, V., Kulozik, A. E., Witt, O., Martin, D., Zhang, C., Porat, R., Merino, D. M., Wasserman, J., Jabado, N., Fontebasso, A., Bullinger, L., Rücker, F. G., Döhner, K., Döhner, H., Koster, J., Molenaar, J. J., Versteeg, R., Kool, M., Tabori, U., Malkin, D., Korshunov, A., Taylor, M. D., Lichter, P., Pfister, S. M. and Korbel, J. O. (2012) 'Genome sequencing of pediatric medulloblastoma links catastrophic DNA rearrangements with TP53 mutations', *Cell,* 148(1-2), pp. 59-71. DOI: 10.1016/j.cell.2011.12.013.

Ribi, K., Relly, C., Landolt, M. A., Alber, F. D., Boltshauser, E. and Grotzer, M. A. (2005) 'Outcome of medulloblastoma in children: long-term complications and quality of life', *Neuropediatrics,* 36(6), pp. 357-65. DOI: 10.1055/s-2005-872880.

Ringel, T., Frey, N., Ringnalda, F., Janjuha, S., Cherkaoui, S., Butz, S., Srivatsa, S., Pirkl, M., Russo, G., Villiger, L., Rogler, G., Clevers, H., Beerenwinkel, N., Zamboni, N., Baubec, T. and Schwank, G. (2020) 'Genome-Scale CRISPR Screening in Human Intestinal Organoids Identifies Drivers of TGF-β Resistance', *Cell Stem Cell,* 26(3), pp. 431-440.e8. DOI: 10.1016/j.stem.2020.02.007.

Robinson, G. W., Orr, B. A., Wu, G., Gururangan, S., Lin, T., Qaddoumi, I., Packer, R. J., Goldman, S., Prados, M. D., Desjardins, A., Chintagumpala, M., Takebe, N., Kaste, S. C., Rusch, M., Allen, S. J., Onar-Thomas, A., Stewart, C. F., Fouladi, M., Boyett, J. M., Gilbertson, R. J., Curran, T., Ellison, D. W. and Gajjar, A. (2015) 'Vismodegib Exerts Targeted Efficacy Against Recurrent Sonic Hedgehog-Subgroup Medulloblastoma: Results From Phase II Pediatric Brain Tumor Consortium Studies PBTC-025B and PBTC-032', *J Clin Oncol,* 33(24), pp. 2646-54. DOI: 10.1200/jco.2014.60.1591.

Robinson, G. W., Rudneva, V. A., Buchhalter, I., Billups, C. A., Waszak, S. M., Smith, K. S., Bowers, D. C., Bendel, A., Fisher, P. G., Partap, S., Crawford, J. R., Hassall, T., Indelicato, D. J., Boop, F., Klimo, P., Sabin, N. D., Patay, Z., Merchant, T. E., Stewart, C. F., Orr, B. A., Korbel, J. O., Jones, D. T. W., Sharma, T., Lichter, P., Kool, M., Korshunov, A., Pfister, S. M., Gilbertson, R. J., Sanders, R. P., Onar-

Thomas, A., Ellison, D. W., Gajjar, A. and Northcott, P. A. (2018) 'Risk-adapted therapy for young children with medulloblastoma (SJYC07): therapeutic and molecular outcomes from a multicentre, phase 2 trial', *Lancet Oncol,* 19(6), pp. 768-784. DOI: 10.1016/s1470-2045(18)30204-3.

Robinson, M. H., Maximov, V., Lallani, S., Farooq, H., Taylor, M. D., Read, R. D. and Kenney, A. M. (2019) 'Upregulation of the chromatin remodeler HELLS is mediated by YAP1 in Sonic Hedgehog Medulloblastoma', *Sci Rep,* 9(1), pp. 13611. DOI: 10.1038/s41598-019-50088-1.

Root, D. E., Hacohen, N., Hahn, W. C., Lander, E. S. and Sabatini, D. M. (2006) 'Genome-scale loss-of-function screening with a lentiviral RNAi library', *Nat Methods,* 3(9), pp. 715-9. DOI: 10.1038/nmeth924.

Rouet, P., Smih, F. and Jasin, M. (1994) 'Introduction of double-strand breaks into the genome of mouse cells by expression of a rare-cutting endonuclease', *Mol Cell Biol,* 14(12), pp. 8096-106. DOI: 10.1128/mcb.14.12.8096-8106.1994.

Roussel, M. F. and Stripay, J. L. (2018) 'Epigenetic Drivers in Pediatric Medulloblastoma', *Cerebellum,* 17(1), pp. 28-36. DOI: 10.1007/s12311-017-0899-9.

Rudin, C. M., Hann, C. L., Laterra, J., Yauch, R. L., Callahan, C. A., Fu, L., Holcomb, T., Stinson, J., Gould, S. E., Coleman, B., LoRusso, P. M., Von Hoff, D. D., de Sauvage, F. J. and Low, J. A. (2009) 'Treatment of medulloblastoma with hedgehog pathway inhibitor GDC-0449', *N Engl J Med,* 361(12), pp. 1173-8. DOI: 10.1056/NEJMoa0902903.

Sanghrajka, R. M., Koche, R., Medrano, H., El Nagar, S., Stephen, D. N., Lao, Z., Bayin, N. S., Ge, K. and Joyner, A. L. (2023) 'KMT2D suppresses Sonic hedgehog-driven medulloblastoma progression and metastasis', *iScience,* 26(10), pp. 107831. DOI: 10.1016/j.isci.2023.107831.

Sanson, K. R., Hanna, R. E., Hegde, M., Donovan, K. F., Strand, C., Sullender, M. E., Vaimberg, E. W., Goodale, A., Root, D. E., Piccioni, F. and Doench, J. G. (2018) 'Optimized libraries for CRISPR-Cas9 genetic screens with multiple modalities', *Nat Commun,* 9(1), pp. 5416. DOI: 10.1038/s41467-018-07901-8.

Santi, D. V., Norment, A. and Garrett, C. E. (1984) 'Covalent bond formation between a DNA-cytosine methyltransferase and DNA containing 5-azacytosine', *Proc Natl Acad Sci U S A,* 81(22), pp. 6993-7. DOI: 10.1073/pnas.81.22.6993.

Sasai, K., Romer, J. T., Lee, Y., Finkelstein, D., Fuller, C., McKinnon, P. J. and Curran, T. (2006) 'Shh pathway activity is down-regulated in cultured medulloblastoma cells: implications for preclinical studies', *Cancer Res,* 66(8), pp. 4215-22. DOI: 10.1158/0008-5472.Can-05-4505.

Schüller, U., Heine, V. M., Mao, J., Kho, A. T., Dillon, A. K., Han, Y. G., Huillard, E., Sun, T., Ligon, A. H., Qian, Y., Ma, Q., Alvarez-Buylla, A., McMahon, A. P., Rowitch, D. H. and Ligon, K. L. (2008) 'Acquisition of granule neuron precursor identity is a critical determinant of progenitor cell competence to form Shh-induced medulloblastoma', *Cancer Cell,* 14(2), pp. 123-34. DOI: 10.1016/j.ccr.2008.07.005.

Schwalbe, E. C., Lindsey, J. C., Nakjang, S., Crosier, S., Smith, A. J., Hicks, D., Rafiee, G., Hill, R. M., Iliasova, A., Stone, T., Pizer, B., Michalski, A., Joshi, A., Wharton, S. B., Jacques, T. S., Bailey, S., Williamson, D. and Clifford, S. C. (2017) 'Novel molecular subgroups for clinical classification and outcome prediction in childhood medulloblastoma: a cohort study', *Lancet Oncol,* 18(7), pp. 958-971. DOI: 10.1016/s1470-2045(17)30243-7.

Schwalbe, E. C., Williamson, D., Lindsey, J. C., Hamilton, D., Ryan, S. L., Megahed, H., Garami, M., Hauser, P., Dembowska-Baginska, B., Perek, D., Northcott, P. A., Taylor, M. D., Taylor, R. E., Ellison, D. W., Bailey, S. and Clifford, S. C. (2013) 'DNA methylation profiling of medulloblastoma allows robust subclassification and improved outcome prediction using formalin-fixed biopsies', *Acta Neuropathol,* 125(3), pp. 359-71. DOI: 10.1007/s00401-012-1077-2.

Sekulic, A., Migden, M. R., Lewis, K., Hainsworth, J. D., Solomon, J. A., Yoo, S., Arron, S. T., Friedlander, P. A., Marmur, E., Rudin, C. M., Chang, A. L., Dirix, L., Hou, J., Yue, H. and Hauschild, A. (2015) 'Pivotal

ERIVANCE basal cell carcinoma (BCC) study: 12-month update of efficacy and safety of vismodegib in advanced BCC', *J Am Acad Dermatol,* 72(6), pp. 1021-6.e8. DOI: 10.1016/j.jaad.2015.03.021.

Shalem, O., Sanjana, N. E., Hartenian, E., Shi, X., Scott, D. A., Mikkelson, T., Heckl, D., Ebert, B. L., Root, D. E., Doench, J. G. and Zhang, F. (2014) 'Genome-scale CRISPR-Cas9 knockout screening in human cells', *Science,* 343(6166), pp. 84-87. DOI: 10.1126/science.1247005.

Shalem, O., Sanjana, N. E. and Zhang, F. (2015) 'High-throughput functional genomics using CRISPR-Cas9', *Nat Rev Genet,* 16(5), pp. 299-311. DOI: 10.1038/nrg3899.

Shi, X., Wang, Q., Gu, J., Xuan, Z. and Wu, J. I. (2016) 'SMARCA4/Brg1 coordinates genetic and epigenetic networks underlying Shh-type medulloblastoma development', *Oncogene,* 35(44), pp. 5746-5758. DOI: 10.1038/onc.2016.108.

Shiraishi, R. and Kawauchi, D. (2021) 'Epigenetic regulation in medulloblastoma pathogenesis revealed by genetically engineered mouse models', *Cancer Sci,* 112(8), pp. 2948-2957. DOI: 10.1111/cas.14990.

Silva, J. M., Li, M. Z., Chang, K., Ge, W., Golding, M. C., Rickles, R. J., Siolas, D., Hu, G., Paddison, P. J., Schlabach, M. R., Sheth, N., Bradshaw, J., Burchard, J., Kulkarni, A., Cavet, G., Sachidanandam, R., McCombie, W. R., Cleary, M. A., Elledge, S. J. and Hannon, G. J. (2005) 'Second-generation shRNA libraries covering the mouse and human genomes', *Nat Genet,* 37(11), pp. 1281-8. DOI: 10.1038/ng1650.

Skene, P. J., Henikoff, J. G. and Henikoff, S. (2018) 'Targeted in situ genome-wide profiling with high efficiency for low cell numbers', *Nat Protoc,* 13(5), pp. 1006-1019. DOI: 10.1038/nprot.2018.015.

Skowron, P., Farooq, H., Cavalli, F. M. G., Morrissy, A. S., Ly, M., Hendrikse, L. D., Wang, E. Y., Djambazian, H., Zhu, H., Mungall, K. L., Trinh, Q. M., Zheng, T., Dai, S., Stucklin, A. S. G., Vladoiu, M. C., Fong, V., Holgado, B. L., Nor, C., Wu, X., Abd-Rabbo, D., Bérubé, P., Wang, Y. C., Luu, B., Suarez, R. A., Rastan, A., Gillmor, A. H., Lee, J. J. Y., Zhang, X. Y., Daniels, C., Dirks, P., Malkin, D., Bouffet, E., Tabori, U., Loukides, J., Doz, F. P., Bourdeaut, F., Delattre, O. O., Masliah-Planchon, J., Ayrault, O., Kim, S. K., Meyronet, D., Grajkowska, W. A., Carlotti, C. G., de Torres, C., Mora, J., Eberhart, C. G., Van Meir, E. G., Kumabe, T., French, P. J., Kros, J. M., Jabado, N., Lach, B., Pollack, I. F., Hamilton, R. L., Rao, A. A. N., Giannini, C., Olson, J. M., Bognár, L., Klekner, A., Zitterbart, K., Phillips, J. J., Thompson, R. C., Cooper, M. K., Rubin, J. B., Liau, L. M., Garami, M., Hauser, P., Li, K. K. W., Ng, H. K., Poon, W. S., Yancey Gillespie, G., Chan, J. A., Jung, S., McLendon, R. E., Thompson, E. M., Zagzag, D., Vibhakar, R., Ra, Y. S., Garre, M. L., Schüller, U., Shofuda, T., Faria, C. C., López-Aguilar, E., Zadeh, G., Hui, C. C., Ramaswamy, V., Bailey, S. D., Jones, S. J., Mungall, A. J., Moore, R. A., Calarco, J. A., Stein, L. D., Bader, G. D., Reimand, J., Ragoussis, J., Weiss, W. A., Marra, M. A., Suzuki, H. and Taylor, M. D. (2021) 'The transcriptional landscape of Shh medulloblastoma', *Nat Commun,* 12(1), pp. 1749. DOI: 10.1038/s41467-021-21883-0.

Smith, M. J., Beetz, C., Williams, S. G., Bhaskar, S. S., O'Sullivan, J., Anderson, B., Daly, S. B., Urquhart, J. E., Bholah, Z., Oudit, D., Cheesman, E., Kelsey, A., McCabe, M. G., Newman, W. G. and Evans, D. G. (2014) 'Germline mutations in SUFU cause Gorlin syndrome-associated childhood medulloblastoma and redefine the risk associated with PTCH1 mutations', *J Clin Oncol,* 32(36), pp. 4155-61. DOI: 10.1200/jco.2014.58.2569.

Steliarova-Foucher, E., Colombet, M., Ries, L. A. G., Moreno, F., Dolya, A., Bray, F., Hesseling, P., Shin, H. Y. and Stiller, C. A. (2017) 'International incidence of childhood cancer, 2001-10: a population-based registry study', *Lancet Oncol,* 18(6), pp. 719-731. DOI: 10.1016/s1470-2045(17)30186-9.

Sulahian, R., Kwon, J. J., Walsh, K. H., Pailler, E., Bosse, T. L., Thaker, M., Almanza, D., Dempster, J. M., Pan, J., Piccioni, F., Dumont, N., Gonzalez, A., Rennhack, J., Nabet, B., Bachman, J. A., Goodale, A., Lee, Y., Bagul, M., Liao, R., Navarro, A., Yuan, T. L., Ng, R. W. S., Raghavan, S., Gray, N. S., Tsherniak, A., Vazquez, F., Root, D. E., Firestone, A. J., Settleman, J., Hahn, W. C. and Aguirre, A. J. (2019) 'Synthetic Lethal Interaction of SHOC2 Depletion with MEK Inhibition in RAS-Driven Cancers', *Cell Rep,* 29(1), pp. 118-134.e8. DOI: 10.1016/j.celrep.2019.08.090.

Swanson, D. J. and Goldowitz, D. (2011) 'Experimental Sey mouse chimeras reveal the developmental deficiencies of Pax6-null granule cells in the postnatal cerebellum', *Dev Biol,* 351(1), pp. 1-12. DOI: 10.1016/j.ydbio.2010.11.018.

Szklarczyk, D., Franceschini, A., Wyder, S., Forslund, K., Heller, D., Huerta-Cepas, J., Simonovic, M., Roth, A., Santos, A., Tsafou, K. P., Kuhn, M., Bork, P., Jensen, L. J. and von Mering, C. (2015) 'STRING v10: protein-protein interaction networks, integrated over the tree of life', *Nucleic Acids Res,* 43(Database issue), pp. D447-52. DOI: 10.1093/nar/gku1003.

Takahashi, T. (2019) 'Organoids for Drug Discovery and Personalized Medicine', *Annu Rev Pharmacol Toxicol,* 59, pp. 447-462. DOI: 10.1146/annurev-pharmtox-010818-021108.

Taylor, M. D., Liu, L., Raffel, C., Hui, C. C., Mainprize, T. G., Zhang, X., Agatep, R., Chiappa, S., Gao, L., Lowrance, A., Hao, A., Goldstein, A. M., Stavrou, T., Scherer, S. W., Dura, W. T., Wainwright, B., Squire, J. A., Rutka, J. T. and Hogg, D. (2002) 'Mutations in SUFU predispose to medulloblastoma', *Nat Genet,* 31(3), pp. 306-10. DOI: 10.1038/ng916.

Taylor, M. D., Northcott, P. A., Korshunov, A., Remke, M., Cho, Y. J., Clifford, S. C., Eberhart, C. G., Parsons, D. W., Rutkowski, S., Gajjar, A., Ellison, D. W., Lichter, P., Gilbertson, R. J., Pomeroy, S. L., Kool, M. and Pfister, S. M. (2012) 'Molecular subgroups of medulloblastoma: the current consensus', *Acta Neuropathol,* 123(4), pp. 465-72. DOI: 10.1007/s00401-011-0922-z.

Tibes, R., Al-Kali, A., Oliver, G. R., Delman, D. H., Hansen, N., Bhagavatula, K., Mohan, J., Rakhshan, F., Wood, T., Foran, J. M., Mesa, R. A. and Bogenberger, J. M. (2015) 'The Hedgehog pathway as targetable vulnerability with 5-azacytidine in myelodysplastic syndrome and acute myeloid leukemia', *J Hematol Oncol,* 8, pp. 114. DOI: 10.1186/s13045-015-0211-8.

Tonon, F., Cemazar, M., Kamensek, U., Zennaro, C., Pozzato, G., Caserta, S., Ascione, F., Grassi, M., Guido, S., Ferrari, C., Cansolino, L., Trotta, F., Kuzmanov, B. G., Forte, G., Martino, F., Perrone, F., Bomben, R., Gattei, V., Elvassore, N., Murano, E., Truong, N. H., Olson, M., Farra, R., Grassi, G. and Dapas, B. (2022) '5-Azacytidine Downregulates the Proliferation and Migration of Hepatocellular Carcinoma Cells In Vitro and In Vivo by Targeting miR-139-5p/ROCK2 Pathway', *Cancers (Basel),* 14(7). DOI: 10.3390/cancers14071630.

Tsiami, F., Drwesh, L., Surender, S., Fitzgerald, J., Schittenhelm, J., Picketts, D. J., Segal, R. A., Tabatabai, G. and Merk, D. J. (2025) 'SMARCA5 is required for the development of granule cell neuron precursors and Sonic Hedgehog Medulloblastoma growth', *Scientific Reports,* 15(1), pp. 26091. DOI: 10.1038/s41598-025-11857-3.

Tsiami, F., Lago, C., Pozza, N., Piccioni, F., Zhao, X., Lülsberg, F., Root, D. E., Tiberi, L., Kool, M., Schittenhelm, J., Bandopadhayay, P., Segal, R. A., Tabatabai, G. and Merk, D. J. (2024) 'Genome-wide CRISPR-Cas9 knockout screens identify DNMT1 as a druggable dependency in sonic hedgehog medulloblastoma', *Acta Neuropathol Commun,* 12(1), pp. 125. DOI: 10.1186/s40478-024-01831-x.

Tzelepis, K., Koike-Yusa, H., De Braekeleer, E., Li, Y., Metzakopian, E., Dovey, O. M., Mupo, A., Grinkevich, V., Li, M., Mazan, M., Gozdecka, M., Ohnishi, S., Cooper, J., Patel, M., McKerrell, T., Chen, B., Domingues, A. F., Gallipoli, P., Teichmann, S., Ponstingl, H., McDermott, U., Saez-Rodriguez, J., Huntly, B. J. P., Iorio, F., Pina, C., Vassiliou, G. S. and Yusa, K. (2016) 'A CRISPR Dropout Screen Identifies Genetic Vulnerabilities and Therapeutic Targets in Acute Myeloid Leukemia', *Cell Rep,* 17(4), pp. 1193-1205. DOI: 10.1016/j.celrep.2016.09.079.

Ungricht, R., Guibbal, L., Lasbennes, M. C., Orsini, V., Beibel, M., Waldt, A., Cuttat, R., Carbone, W., Basler, A., Roma, G., Nigsch, F., Tchorz, J. S., Hoepfner, D. and Hoppe, P. S. (2022) 'Genome-wide screening in human kidney organoids identifies developmental and disease-related aspects of nephrogenesis', *Cell Stem Cell,* 29(1), pp. 160-175.e7. DOI: 10.1016/j.stem.2021.11.001.

Valente, S., Liu, Y., Schnekenburger, M., Zwergel, C., Cosconati, S., Gros, C., Tardugno, M., Labella, D., Florean, C., Minden, S., Hashimoto, H., Chang, Y., Zhang, X., Kirsch, G., Novellino, E., Arimondo, P. B., Miele, E., Ferretti, E., Gulino, A., Diederich, M., Cheng, X. and Mai, A. (2014) 'Selective non-

nucleoside inhibitors of human DNA methyltransferases active in cancer including in cancer stem cells', *J Med Chem,* 57(3), pp. 701-13. DOI: 10.1021/jm4012627.

van Essen, M. J., Apsley, E. J., Riepsaame, J., Xu, R., Northcott, P. A., Cowley, S. A., Jacob, J. and Becker, E. B. E. (2024) 'PTCH1-mutant human cerebellar organoids exhibit altered neural development and recapitulate early medulloblastoma tumorigenesis', *Dis Model Mech,* 17(2). DOI: 10.1242/dmm.050323.

Vigil, C. E., Martin-Santos, T. and Garcia-Manero, G. (2010) 'Safety and efficacy of azacitidine in myelodysplastic syndromes', *Drug Des Devel Ther,* 4, pp. 221-9. DOI: 10.2147/dddt.s3143.

Vladoiu, M. C., El-Hamamy, I., Donovan, L. K., Farooq, H., Holgado, B. L., Sundaravadanam, Y., Ramaswamy, V., Hendrikse, L. D., Kumar, S., Mack, S. C., Lee, J. J. Y., Fong, V., Juraschka, K., Przelicki, D., Michealraj, A., Skowron, P., Luu, B., Suzuki, H., Morrissy, A. S., Cavalli, F. M. G., Garzia, L., Daniels, C., Wu, X., Qazi, M. A., Singh, S. K., Chan, J. A., Marra, M. A., Malkin, D., Dirks, P., Heisler, L., Pugh, T., Ng, K., Notta, F., Thompson, E. M., Kleinman, C. L., Joyner, A. L., Jabado, N., Stein, L. and Taylor, M. D. (2019) 'Childhood cerebellar tumours mirror conserved fetal transcriptional programs', *Nature,* 572(7767), pp. 67-73. DOI: 10.1038/s41586-019-1158-7.

von Bueren, A. O., Kortmann, R. D., von Hoff, K., Friedrich, C., Mynarek, M., Müller, K., Goschzik, T., Zur Mühlen, A., Gerber, N., Warmuth-Metz, M., Soerensen, N., Deinlein, F., Benesch, M., Zwiener, I., Kwiecien, R., Faldum, A., Bode, U., Fleischhack, G., Hovestadt, V., Kool, M., Jones, D., Northcott, P., Kuehl, J., Pfister, S., Pietsch, T. and Rutkowski, S. (2016) 'Treatment of Children and Adolescents With Metastatic Medulloblastoma and Prognostic Relevance of Clinical and Biologic Parameters', *J Clin Oncol,* 34(34), pp. 4151-4160. DOI: 10.1200/jco.2016.67.2428.

Wallace, V. A. (1999) 'Purkinje-cell-derived Sonic hedgehog regulates granule neuron precursor cell proliferation in the developing mouse cerebellum', *Curr Biol,* 9(8), pp. 445-8. DOI: 10.1016/s0960-9822(99)80195-x.

Walter, B., Hirsch, S., Kuhlburger, L., Stahl, A., Schnabel, L., Wisser, S., Haeusser, L. A., Tsiami, F., Plöger, S., Aghaallaei, N., Dick, A. M., Skokowa, J., Schmees, C., Templin, M., Schenke-Layland, K., Tatagiba, M., Nahnsen, S., Merk, D. J. and Tabatabai, G. (2024) 'Functionally-instructed modifiers of response to ATR inhibition in experimental glioma', *J Exp Clin Cancer Res,* 43(1), pp. 77. DOI: 10.1186/s13046-024-02995-z.

Wang, B., Wang, M., Zhang, W., Xiao, T., Chen, C. H., Wu, A., Wu, F., Traugh, N., Wang, X., Li, Z., Mei, S., Cui, Y., Shi, S., Lipp, J. J., Hinterndorfer, M., Zuber, J., Brown, M., Li, W. and Liu, X. S. (2019a) 'Integrative analysis of pooled CRISPR genetic screens using MAGeCKFlute', *Nat Protoc,* 14(3), pp. 756-780. DOI: 10.1038/s41596-018-0113-7.

Wang, C., Wang, G., Feng, X., Shepherd, P., Zhang, J., Tang, M., Chen, Z., Srivastava, M., McLaughlin, M. E., Navone, N. M., Hart, G. T. and Chen, J. (2019b) 'Genome-wide CRISPR screens reveal synthetic lethality of RNASEH2 deficiency and ATR inhibition', *Oncogene,* 38(14), pp. 2451-2463. DOI: 10.1038/s41388-018-0606-4.

Wang, T., Birsoy, K., Hughes, N. W., Krupczak, K. M., Post, Y., Wei, J. J., Lander, E. S. and Sabatini, D. M. (2015a) 'Identification and characterization of essential genes in the human genome', *Science,* 350(6264), pp. 1096-101. DOI: 10.1126/science.aac7041.

Wang, T., Wei, J. J., Sabatini, D. M. and Lander, E. S. (2014) 'Genetic screens in human cells using the CRISPR-Cas9 system', *Science,* 343(6166), pp. 80-4. DOI: 10.1126/science.1246981.

Wang, T., Yu, H., Hughes, N. W., Liu, B., Kendirli, A., Klein, K., Chen, W. W., Lander, E. S. and Sabatini, D. M. (2017) 'Gene Essentiality Profiling Reveals Gene Networks and Synthetic Lethal Interactions with Oncogenic Ras', *Cell,* 168(5), pp. 890-903.e15. DOI: 10.1016/j.cell.2017.01.013.

Wang, W., Wang, J., Chen, M., Liang, Y., Li, Z., Zhang, Z. and Jing, H. (2015b) '5-Azacitidine Remolds the Methylation Status and Inhibits Growth in Multiple Myeloma', *Blood,* 126(23), pp. 4817. DOI: https://doi.org/10.1182/blood.V126.23.4817.4817.

Waszak, S. M., Northcott, P. A., Buchhalter, I., Robinson, G. W., Sutter, C., Groebner, S., Grund, K. B., Brugières, L., Jones, D. T. W., Pajtler, K. W., Morrissy, A. S., Kool, M., Sturm, D., Chavez, L., Ernst, A., Brabetz, S., Hain, M., Zichner, T., Segura-Wang, M., Weischenfeldt, J., Rausch, T., Mardin, B. R., Zhou, X., Baciu, C., Lawerenz, C., Chan, J. A., Varlet, P., Guerrini-Rousseau, L., Fults, D. W., Grajkowska, W., Hauser, P., Jabado, N., Ra, Y. S., Zitterbart, K., Shringarpure, S. S., De La Vega, F. M., Bustamante, C. D., Ng, H. K., Perry, A., MacDonald, T. J., Hernáiz Driever, P., Bendel, A. E., Bowers, D. C., McCowage, G., Chintagumpala, M. M., Cohn, R., Hassall, T., Fleischhack, G., Eggen, T., Wesenberg, F., Feychting, M., Lannering, B., Schüz, J., Johansen, C., Andersen, T. V., Röösli, M., Kuehni, C. E., Grotzer, M., Kjaerheim, K., Monoranu, C. M., Archer, T. C., Duke, E., Pomeroy, S. L., Shelagh, R., Frank, S., Sumerauer, D., Scheurlen, W., Ryzhova, M. V., Milde, T., Kratz, C. P., Samuel, D., Zhang, J., Solomon, D. A., Marra, M., Eils, R., Bartram, C. R., von Hoff, K., Rutkowski, S., Ramaswamy, V., Gilbertson, R. J., Korshunov, A., Taylor, M. D., Lichter, P., Malkin, D., Gajjar, A., Korbel, J. O. and Pfister, S. M. (2018) 'Spectrum and prevalence of genetic predisposition in medulloblastoma: a retrospective genetic study and prospective validation in a clinical trial cohort', *Lancet Oncol,* 19(6), pp. 785-798. DOI: 10.1016/s1470-2045(18)30242-0.

Watanabe, D., Suetake, I., Tada, T. and Tajima, S. (2002) 'Stage- and cell-specific expression of Dnmt3a and Dnmt3b during embryogenesis', *Mech Dev,* 118(1-2), pp. 187-90. DOI: 10.1016/s0925-4773(02)00242-3.

Wechsler-Reya, R. J. and Scott, M. P. (1999) 'Control of neuronal precursor proliferation in the cerebellum by Sonic Hedgehog', *Neuron,* 22(1), pp. 103-14. DOI: 10.1016/s0896-6273(00)80682-0.

Wetmore, C., Eberhart, D. E. and Curran, T. (2001) 'Loss of p53 but not ARF accelerates medulloblastoma in mice heterozygous for patched', *Cancer Res,* 61(2), pp. 513-6.

Wolter, M., Reifenberger, J., Sommer, C., Ruzicka, T. and Reifenberger, G. (1997) 'Mutations in the human homologue of the Drosophila segment polarity gene patched (PTCH) in sporadic basal cell carcinomas of the skin and primitive neuroectodermal tumors of the central nervous system', *Cancer Res,* 57(13), pp. 2581-5.

Yang, F., Rodriguez-Blanco, J., Long, J., Swiderska-Syn, M., Wynn, D. T., Li, B., Shen, C., Nayak, A., Ban, Y., Sun, X., Suter, R. K., McCrea, H. J., Capobianco, A. J., Ayad, N. G. and Robbins, D. J. (2022) 'A Druggable UHRF1/DNMT1/GLI Complex Regulates Sonic Hedgehog-Dependent Tumor Growth', *Mol Cancer Res,* 20(11), pp. 1598-1610. DOI: 10.1158/1541-7786.Mcr-22-0182.

Yang, Z. J., Ellis, T., Markant, S. L., Read, T. A., Kessler, J. D., Bourboulas, M., Schüller, U., Machold, R., Fishell, G., Rowitch, D. H., Wainwright, B. J. and Wechsler-Reya, R. J. (2008) 'Medulloblastoma can be initiated by deletion of Patched in lineage-restricted progenitors or stem cells', *Cancer Cell,* 14(2), pp. 135-45. DOI: 10.1016/j.ccr.2008.07.003.

Yau, E. H., Kummetha, I. R., Lichinchi, G., Tang, R., Zhang, Y. and Rana, T. M. (2017) 'Genome-Wide CRISPR Screen for Essential Cell Growth Mediators in Mutant KRAS Colorectal Cancers', *Cancer Res,* 77(22), pp. 6330-6339. DOI: 10.1158/0008-5472.Can-17-2043.

Yauch, R. L., Dijkgraaf, G. J., Alicke, B., Januario, T., Ahn, C. P., Holcomb, T., Pujara, K., Stinson, J., Callahan, C. A., Tang, T., Bazan, J. F., Kan, Z., Seshagiri, S., Hann, C. L., Gould, S. E., Low, J. A., Rudin, C. M. and de Sauvage, F. J. (2009) 'Smoothened mutation confers resistance to a Hedgehog pathway inhibitor in medulloblastoma', *Science,* 326(5952), pp. 572-4. DOI: 10.1126/science.1179386.

Yi, J. and Wu, J. (2018) 'Epigenetic regulation in medulloblastoma', *Mol Cell Neurosci,* 87, pp. 65-76. DOI: 10.1016/j.mcn.2017.09.003.

Yu, G., Wang, L. G., Han, Y. and He, Q. Y. (2012) 'clusterProfiler: an R package for comparing biological themes among gene clusters', *Omics,* 16(5), pp. 284-7. DOI: 10.1089/omi.2011.0118.

Zhang, R., Yang, J., Sima, M., Zhou, Y. and Kopeček, J. (2014) 'Sequential combination therapy of ovarian cancer with degradable N-(2-hydroxypropyl)methacrylamide copolymer paclitaxel and gemcitabine conjugates', *Proc Natl Acad Sci U S A,* 111(33), pp. 12181-6. DOI: 10.1073/pnas.1406233111.

Zhao, X., Pak, E., Ornell, K. J., Pazyra-Murphy, M. F., MacKenzie, E. L., Chadwick, E. J., Ponomaryov, T., Kelleher, J. F. and Segal, R. A. (2017) 'A Transposon Screen Identifies Loss of Primary Cilia as a Mechanism of Resistance to SMO Inhibitors', *Cancer Discov,* 7(12), pp. 1436-1449. DOI: 10.1158/2159-8290.Cd-17-0281.

Zhao, X., Ponomaryov, T., Ornell, K. J., Zhou, P., Dabral, S. K., Pak, E., Li, W., Atwood, S. X., Whitson, R. J., Chang, A. L., Li, J., Oro, A. E., Chan, J. A., Kelleher, J. F. and Segal, R. A. (2015) 'RAS/MAPK Activation Drives Resistance to Smo Inhibition, Metastasis, and Tumor Evolution in Shh Pathway-Dependent Tumors', *Cancer Res,* 75(17), pp. 3623-35. DOI: 10.1158/0008-5472.Can-14-2999-t.

Zheng, S., Wang, W., Aldahdooh, J., Malyutina, A., Shadbahr, T., Tanoli, Z., Pessia, A. and Tang, J. (2022) 'SynergyFinder Plus: Toward Better Interpretation and Annotation of Drug Combination Screening Datasets', *Genomics Proteomics Bioinformatics,* 20(3), pp. 587-596. DOI: 10.1016/j.gpb.2022.01.004.

Zhou, W., Triche, T. J., Jr., Laird, P. W. and Shen, H. (2018) 'SeSAMe: reducing artifactual detection of DNA methylation by Infinium BeadChips in genomic deletions', *Nucleic Acids Res,* 46(20), pp. e123. DOI: 10.1093/nar/gky691.

Zhukova, N., Ramaswamy, V., Remke, M., Pfaff, E., Shih, D. J., Martin, D. C., Castelo-Branco, P., Baskin, B., Ray, P. N., Bouffet, E., von Bueren, A. O., Jones, D. T., Northcott, P. A., Kool, M., Sturm, D., Pugh, T. J., Pomeroy, S. L., Cho, Y. J., Pietsch, T., Gessi, M., Rutkowski, S., Bognar, L., Klekner, A., Cho, B. K., Kim, S. K., Wang, K. C., Eberhart, C. G., Fevre-Montange, M., Fouladi, M., French, P. J., Kros, M., Grajkowska, W. A., Gupta, N., Weiss, W. A., Hauser, P., Jabado, N., Jouvet, A., Jung, S., Kumabe, T., Lach, B., Leonard, J. R., Rubin, J. B., Liau, L. M., Massimi, L., Pollack, I. F., Shin Ra, Y., Van Meir, E. G., Zitterbart, K., Schüller, U., Hill, R. M., Lindsey, J. C., Schwalbe, E. C., Bailey, S., Ellison, D. W., Hawkins, C., Malkin, D., Clifford, S. C., Korshunov, A., Pfister, S., Taylor, M. D. and Tabori, U. (2013) 'Subgroup-specific prognostic implications of TP53 mutation in medulloblastoma', *J Clin Oncol,* 31(23), pp. 2927-35. DOI: 10.1200/jco.2012.48.5052.

Zurawel, R. H., Chiappa, S. A., Allen, C. and Raffel, C. (1998) 'Sporadic medulloblastomas contain oncogenic beta-catenin mutations', *Cancer Res,* 58(5), pp. 896-9.

6 Statement of contributions

This thesis was supervised by Dr. rer. nat. Daniel J. Merk and Prof. Dr. Dr. Ghazaleh Tabatabai.

All data from chapters 3.1, 3.2 and 3.3 involving both *in vitro* and *in vivo* experiments were collected, analyzed and visualized by the candidate. The dependency CRISPR-Cas9 knockout screen in SMB21 cells was performed by Dr. rer. nat. Daniel J. Merk during his postdoctoral training in Dr. Rosalind Segal´s laboratory (Dana-Farber Cancer Institute, Boston, Massachusetts, USA). The dependency CRISPR-Cas9 knockout screen in DAOY cells and the CRISPR-Cas9 drug screen in SMB21 cells were conducted by the candidate. Bioinformatic analysis and visualization of CRISPR-Cas9 screens, RNA sequencing and methylation dataset was performed by the candidate under close supervision of Dr. rer. nat. Daniel J. Merk.

All experiments presented on PDXOs were conducted by Dr. Chiara Lago and Noemi Pozza in Armenise-Harvard Laboratory of Brain Disorders and Cancer, CIBIO, in University of Trento in Italy in the group of Dr. Luca Tiberi. Data were analyzed and visualized in close collaboration.

7 Appendix

7.1 Supplementary figures

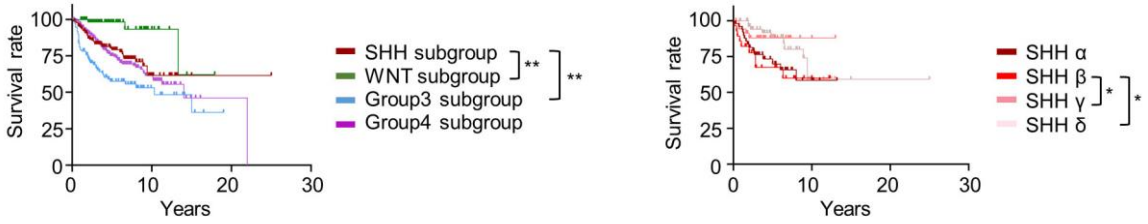

Supplementary figure 1. Analysis of survival outcome of medulloblastoma (MB) patients using Cavalli dataset. Kaplan-Meier curves of MB patients stratified to four different MB subgroups (left) and SHH-MB subtypes (right). Significance in survival is indicated using log rank (Mantel-Cox) test (*$p \leq 0.05$, ** $p \leq 0.01$) (Cavalli et al., 2017).

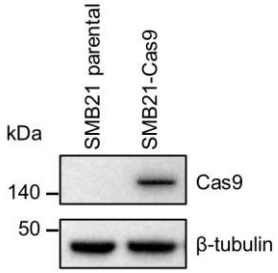

Supplementary figure 2. Western blotting depicting Cas9 protein expression in SMB21 parental and Cas9-transduced cells.

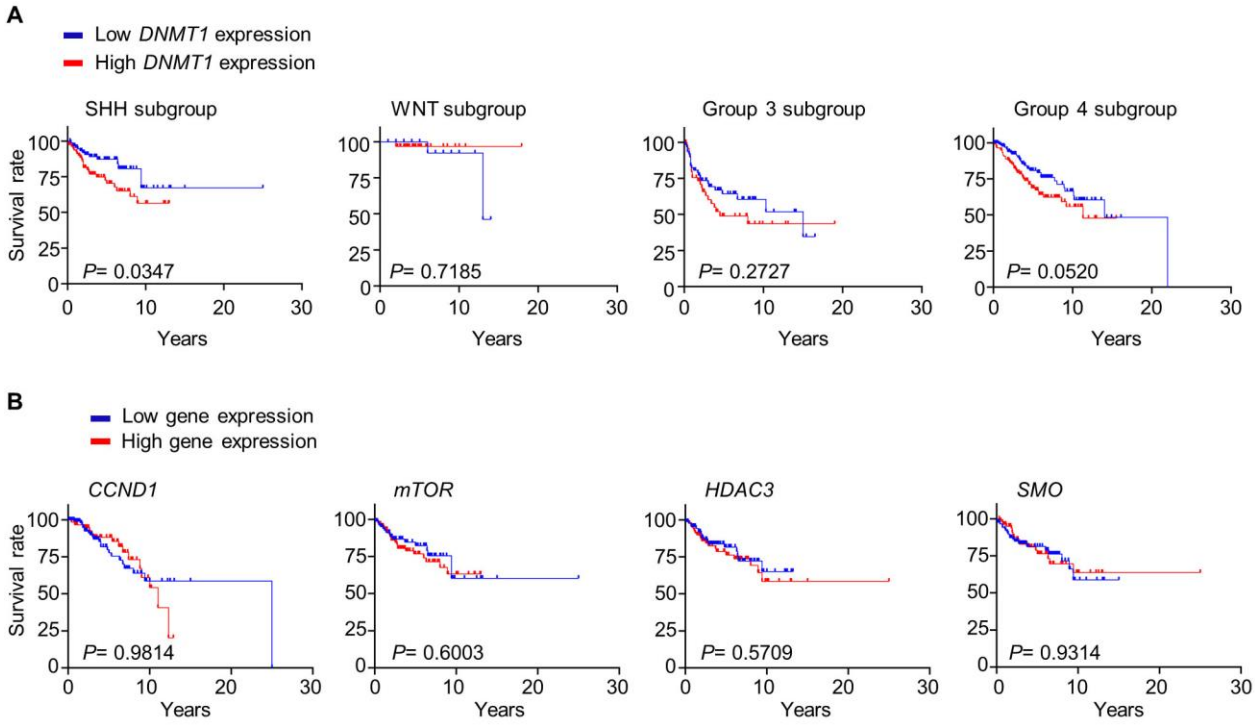

Supplementary figure 3. Survival curves of medulloblastoma patients in regard to specific gene expression using Cavalli dataset. (**A**) Kaplan-Meier curves of subgroup-specific MB patients assigned to low and high *DNMT1* expression. (**B**) Kaplan-Meier curves of SHH-MB patients stratified into low and high expression of *CCND1*, *mTOR*, *HDAC3* and *SMO*. Significance in survival is calculate based on the log rank (Mantel-Cox) test. *P* values are presented (Cavalli et al., 2017).

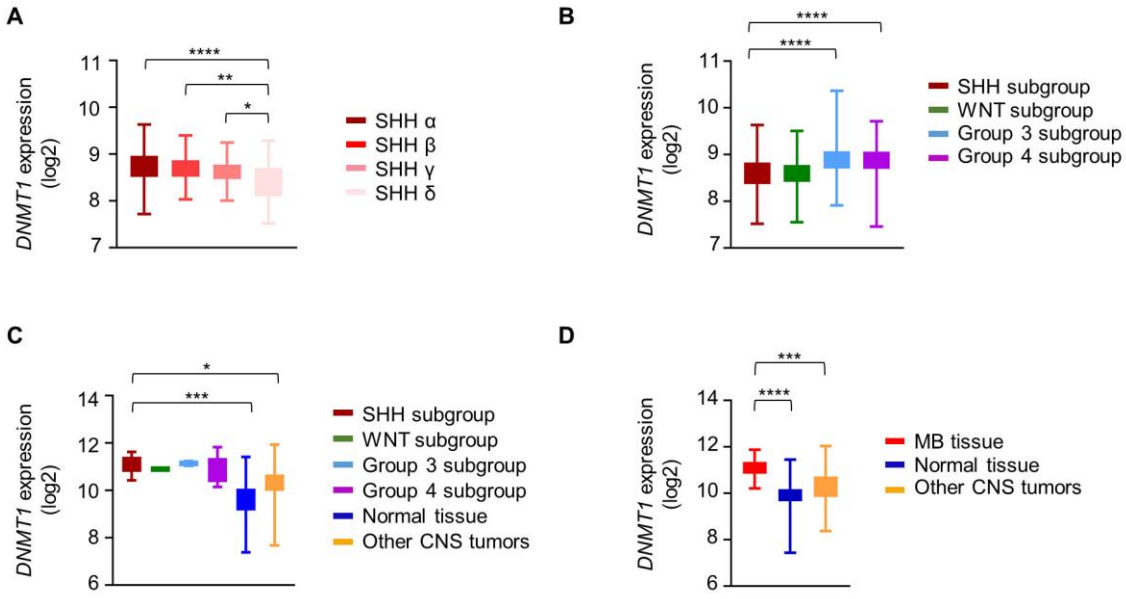

Supplementary figure 4. *DNMT1* expression in patient-derived medulloblastoma tissue according to publicly microarray data. Box plots illustrating gene expression patients within different SHH-MB subtypes (**A**), within subgroup-specific MBs (**B**), as compared to normal tissue and other CNS tumors (**C**, **D**). Whiskers in all box plots represent minimum and maximum data point per group and one-way ANOVA, Tukey´s multiple comparisons test was performed. All graphs display mean ± SD values. *$p \leq 0.05$, **$p \leq 0.01$, *** $p \leq 0.001$, ****$p \leq 0.0001$ (Cavalli et al., 2017, Griesinger et al., 2013, Gump et al., 2015).

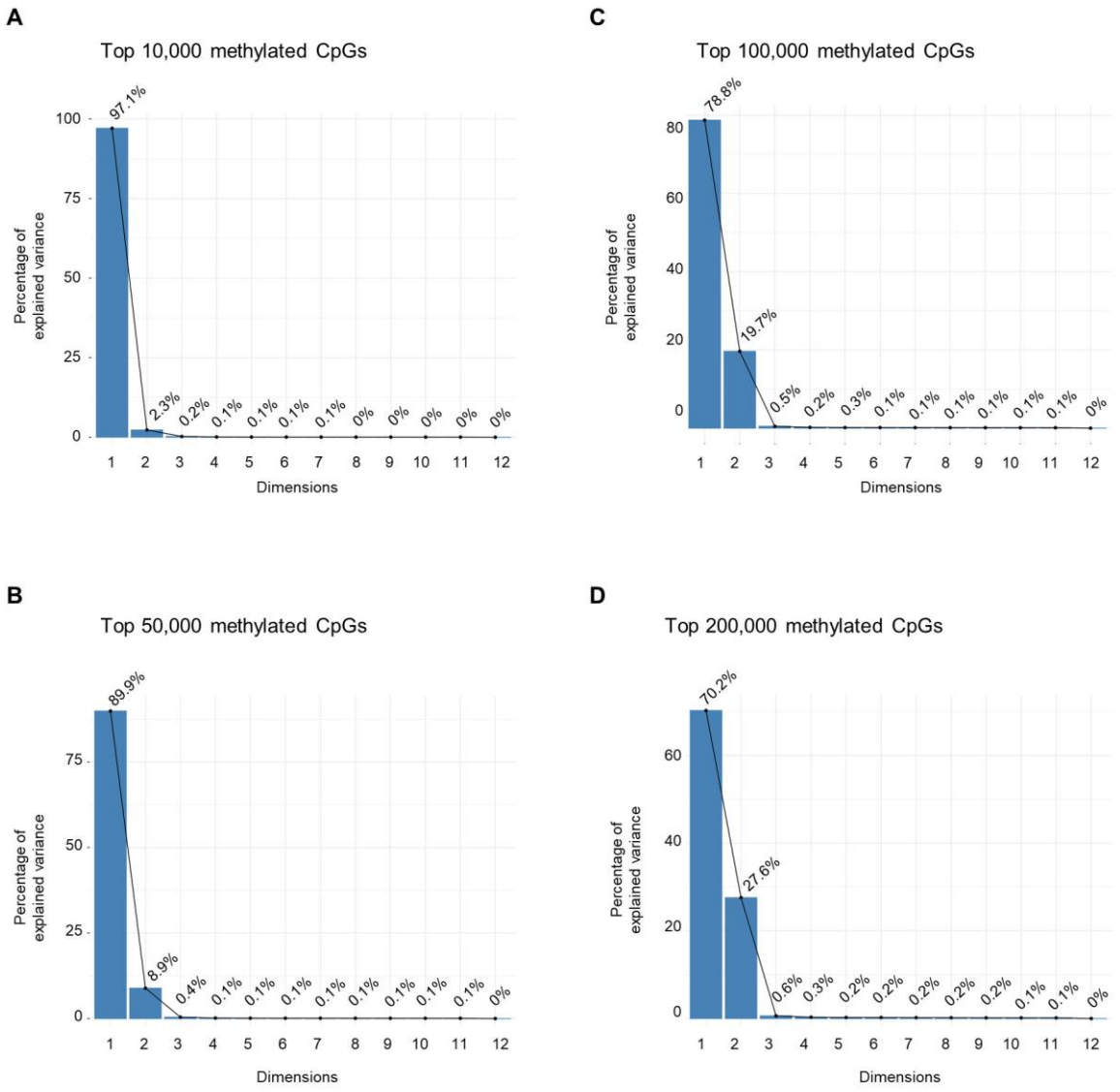

Supplementary figure 5. Scree plots illustrating variances of 12 dimensions deriving from PCA of (**A**) 10,000, (**B**) 50,000, (**C**) 100,000 and (**D**) 200,000 differentially methylated probes in SMB21- and SMB55-treated cells. Percentages of variance are indicated per dimension.

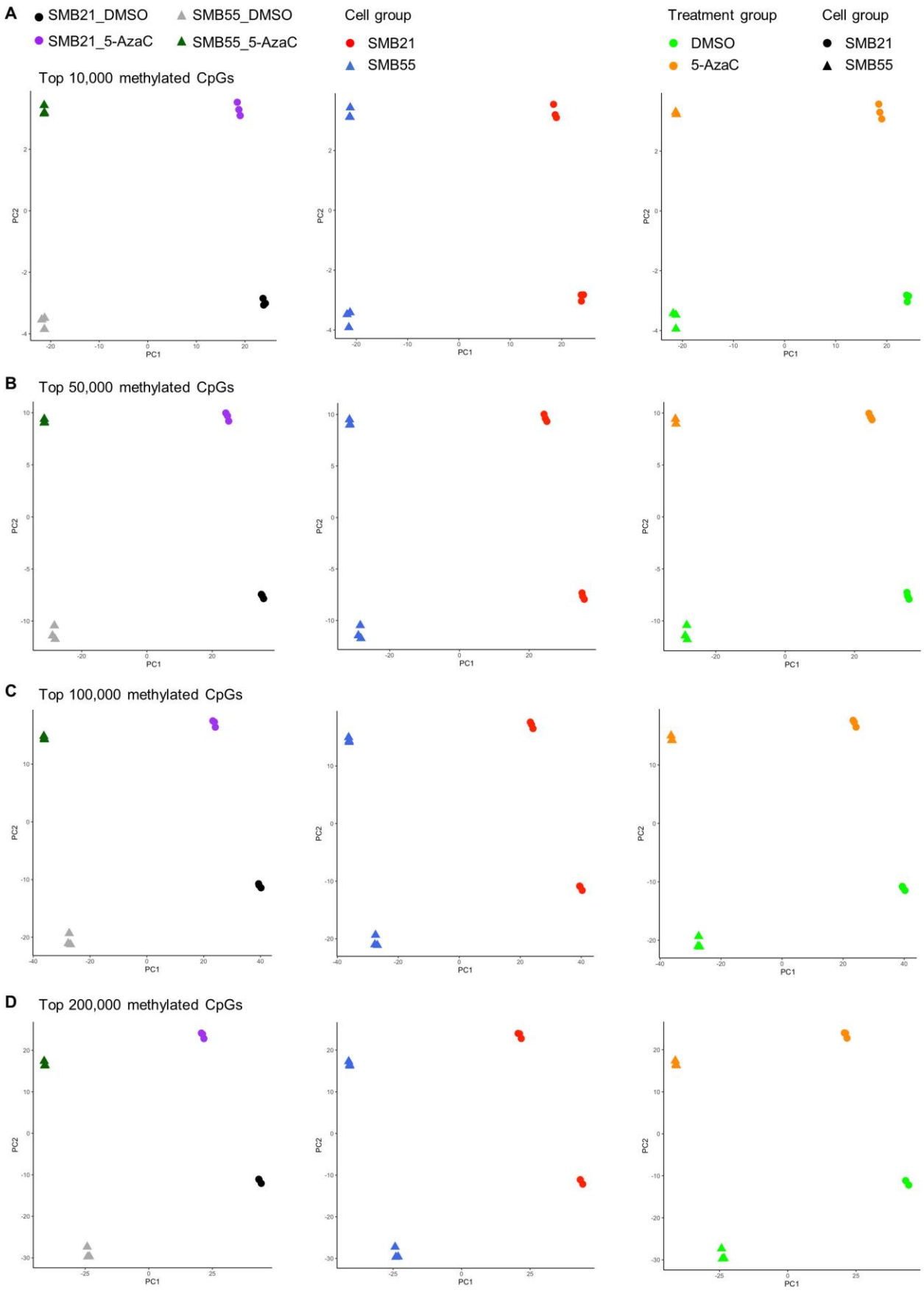
A
SMB21_DMSO
SMB55_DMSO
SMB21_5-AzaC
SMB55_5-AzaC
Cell group
SMB21
SMB55
Treatment group
DMSO
5-AzaC
Cell group
SMB21
SMB55
Top 10,000 methylated CpGs
B
Top 50,000 methylated CpGs
C
Top 100,000 methylated CpGs
D
Top 200,000 methylated CpGs
PC1
PC2

Supplementary figure 6. PCA plots of the top (**A**) 10,000, (**B**) 50,000, (**C**) 100,000 and (**D**) 200,000 differentially methylated CpGs in SMB21- and SMB55-treated cells based on all four different conditions (left), cell groups (middle) and drug-treatment groups (right). All plots indicate PC1 vs PC2 comparison. Specific groups are color- and shape-coded.

A

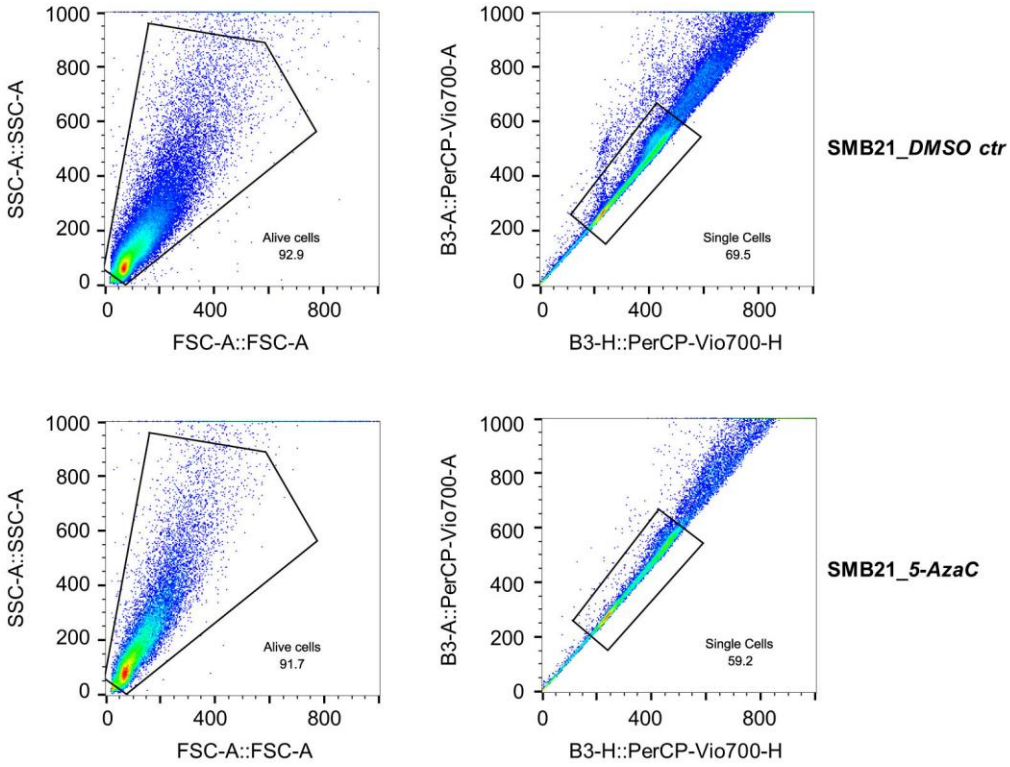
SSC-A::SSC-A
FSC-A::FSC-A
Alive cells
92.9
B3-A::PerCP-Vio700-A
B3-H::PerCP-Vio700-H
Single Cells
69.5
SMB21_DMSO ctr
Alive cells
91.7
Single Cells
59.2
SMB21_5-AzaC

B

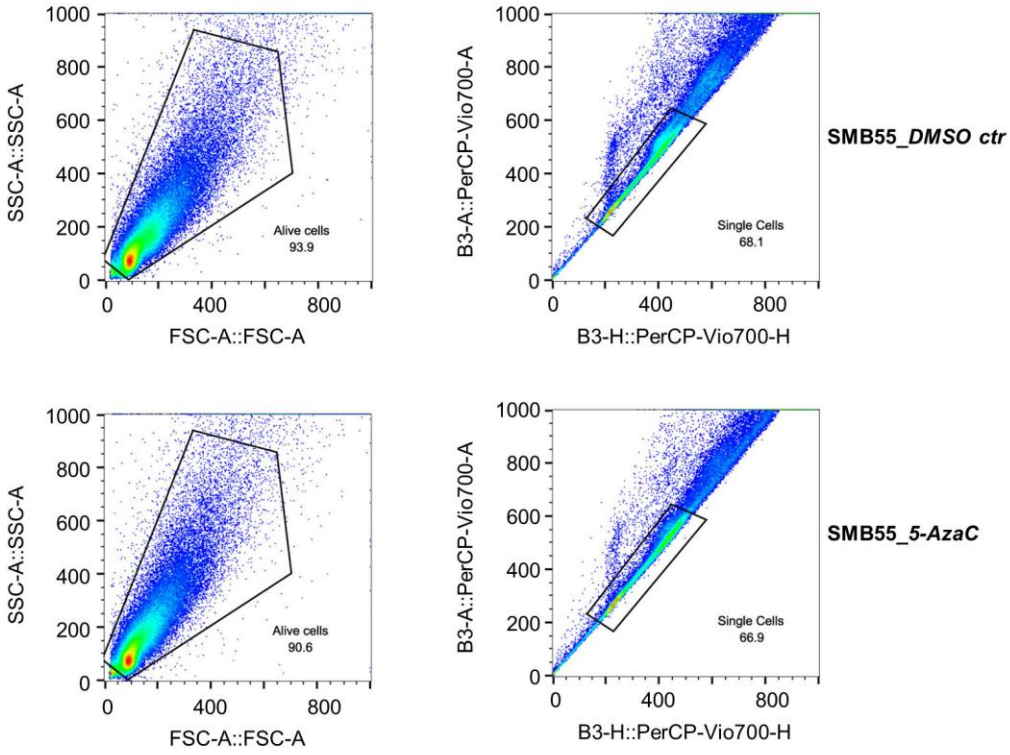
SSC-A::SSC-A
FSC-A::FSC-A
Alive cells
93.9
B3-A::PerCP-Vio700-A
B3-H::PerCP-Vio700-H
Single Cells
68.1
SMB55_DMSO ctr
Alive cells
90.6
Single Cells
66.9
SMB55_5-AzaC

Supplementary figure 7. Gating strategy for SMB cell cycle analysis by flow cytometry. Representative gating for SMB21 (**A**) and SMB55 cells (**B**) treated with DMSO control (upper panel) and 5-Azacytidine (lower panel). Forward (FSC) vs side (SSC) scatter gating is depicted (left panel), indicating the percentage of alive cells per condition. Density plot using B3-A (area) vs B3-H (height) channels (right panel). Doublets are excluded, thereby selecting only single cells for the analysis.

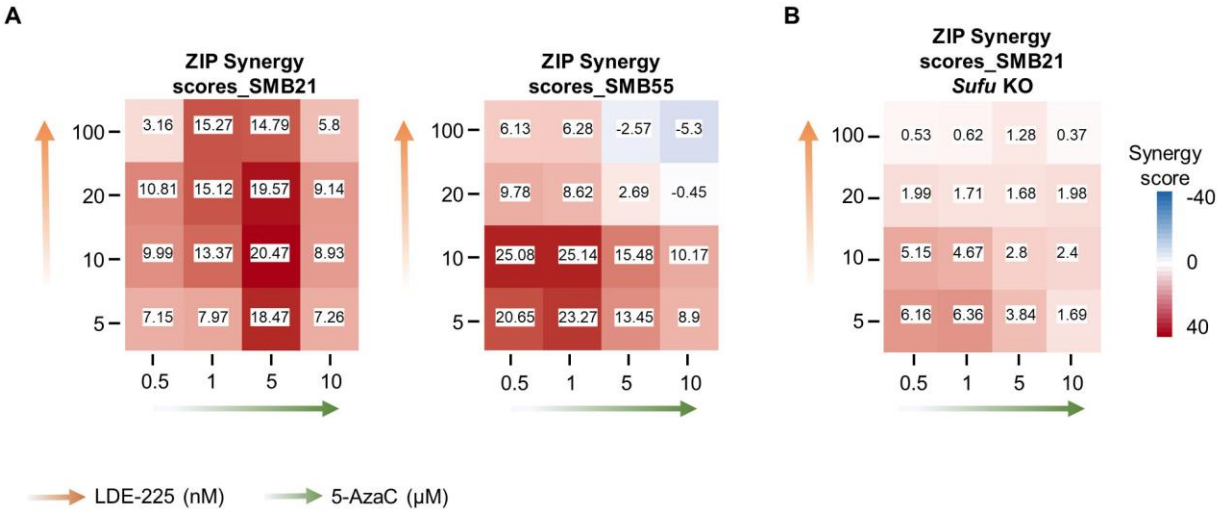

Supplementary figure 8. Heatmaps illustrating the degree of interaction across different concentration ranges of LDE-225 and 5-Azacytidine combination in SMB21 (left) and SMB55 (right) (**A**) and SMB21 *Sufu* KO (**B**) cells. Scores derive from the ZIP model, as calculated using *synergyfinder* R package. Gradient arrows represent concentration range of LDE-225 (orange) and 5-Azacytidine (green) applied to the cells. Synergism was calculated based on the ZIP model.

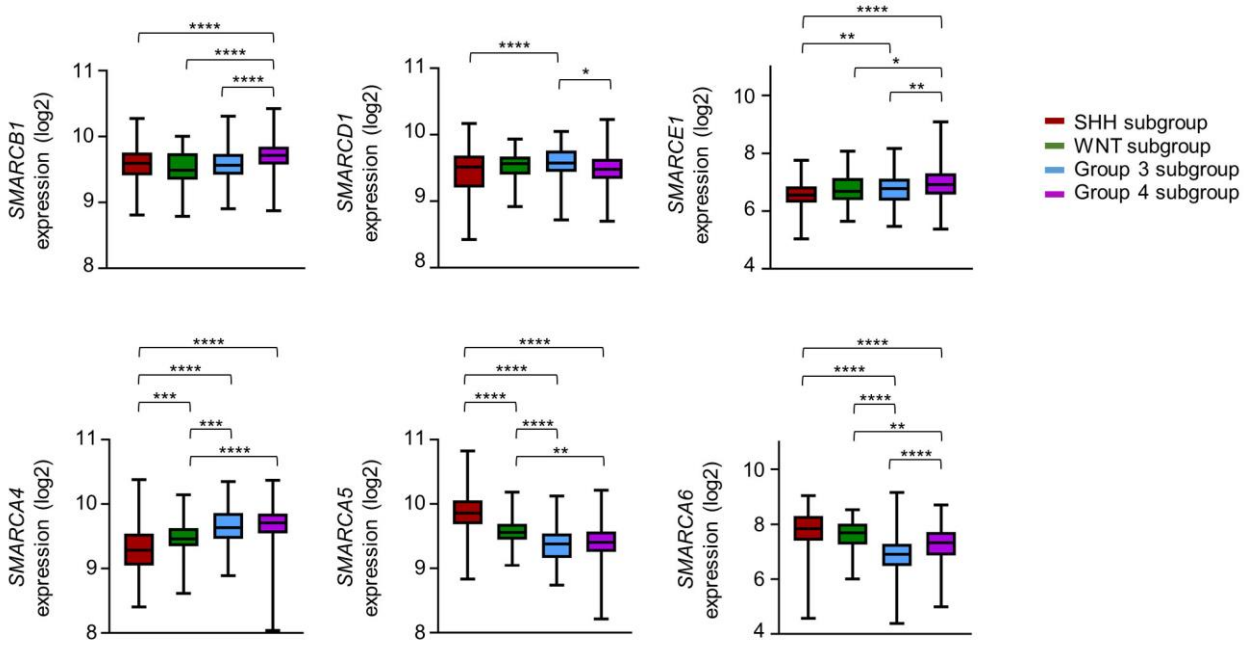

Supplementary figure 9. Microarray expression data of several chromatin remodelers in patient-derived medulloblastoma tissue. Box plots illustrating gene expression of *SMARCB1*, *SMARCD1*, *SMARCE1*, *SMARCA4*, *SMARCA5* and *SMARCA6* in MB patients assigned to different subgroups. Whiskers in all box plots represent minimum and maximum data point per group. One-way ANOVA, Tukey´s multiple comparisons test was performed. All graphs display mean ± SD values. *$p \leq 0.05$, **$p \leq 0.01$, ***$p \leq 0.001$, ****$p \leq 0.0001$ (Cavalli et al., 2017).

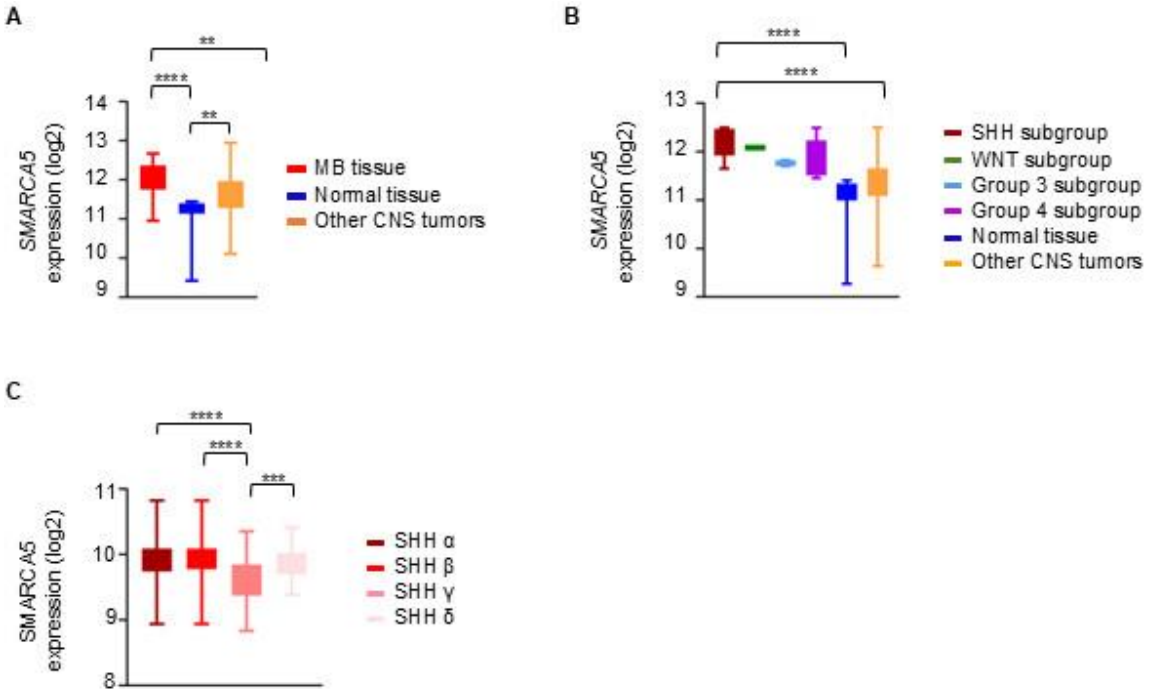

Supplementary figure 10. *SMARCA5* expression in patient-derived medulloblastoma tissue from publicly available microarray data. Box plots illustrating gene expression in MB (**A**) and subgroup-specific MB (**B**) patient-derived tissue, compared to normal tissue and other central nervous system tumors, as well as within different SHH-MB subtypes (**C**). Whiskers in all box plots represent minimum and maximum data point per group and one-way ANOVA, Tukey´s multiple comparisons test was performed. All graphs display mean ± SD values. ***p* ≤ 0.01, ****p* ≤ 0.001, *****p* ≤ 0.0001 0001 (Cavalli et al., 2017, Griesinger et al., 2013, Gump et al., 2015).

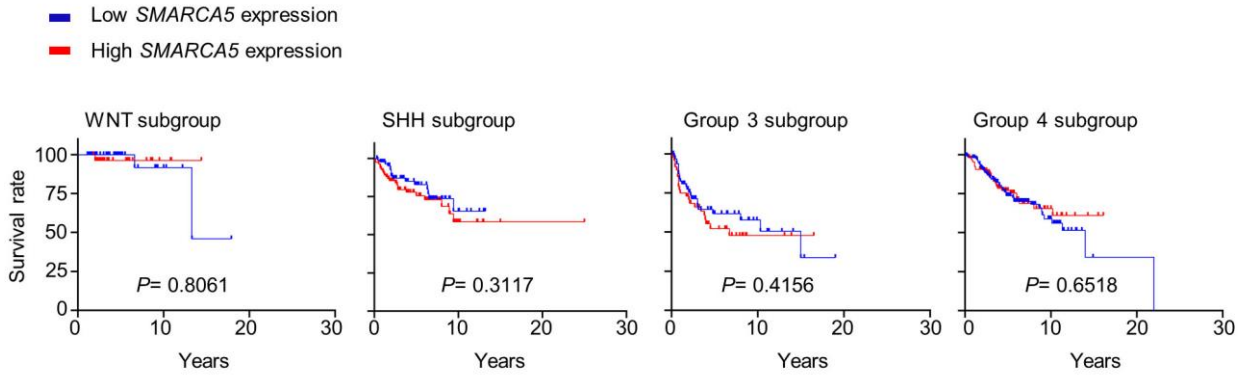

Supplementary figure 11. Survival curves of medulloblastoma patients assigned to low and high *SMARCA5* expression using Cavalli dataset. Kaplan-Meier curves of medulloblastoma patients stratified to SHH, WNT, Group 3 and Group 4 subgroups. Significance in survival is calculated based on the log rank (Mantel-Cox) test. *P* values are indicated (Cavalli et al., 2017).

7.2 Supplementary Table

Parameters	Evaluation	Score
General appearance		
State of care	Smooth, shiny fur	0
	No fur grooming, dull fur	1
	No fur grooming, dirty	3
	No fur grooming, dirty (Piloerection)	4 (Endpoint)
Eyes	Normal	0
	Subtly sunk in, swollen	1
	Closed lids	3
	Strongly sunken in, lids closed, sticky	4 (Endpoint)
Body posture	Normal	0
	Slightly bent	1
	Hunchback	3
	Strongly bent, paws under the belly	4 (Endpoint)
Breathing	Regular	0
	Regular, slightly enhanced	1
	Clearly enhanced	3
	Difficulty in breathing, pumping	4 (Endpoint)
Behavior/activity	Normal	0
	Slightly changed	1
	Reduced activity/movement, isolated	3
	Apathic, inactive	4 (Endpoint)
Nutritional status		
Body condition score	Vertebrae and pelvic bones only palpable when slightly pressed	0
	Vertebrae and pelvic bones easily palpable, abdominal reaction visible form the side	1
	Vertebrae visible, pelvic bones palpable	3
	Vertebrae, pelvic bones and ribs visible	4 (Endpoint)

Weight (related to original weight, corrected to expected weight gain of healthy mice)	Normal, continuous increase (fluctuations up to 5%)	0
	Weight loss (5-10%)	1
	Weight loss > 10% to < 20%	3
	Weight loss up to ≥20%	4 (Endpoint)
Experimental criteria: tumor growth		
Neurological symptoms	None	0
	Slight loss of balance, occasionally missed steps	1
	Moderate loss of balance, every third step missed, moderate ataxia	3
	Strong loss of balance, strong ataxia, complete inactivity	Endpoint
Evaluation of "Grimace scale"	Normal	0
	1 score in pain criteria (endpoint if not improved after 24 hours)	3
	More than 1 score in pain criteria	Endpoint
Additional evaluation on general appearance and nutritional status	Weight loss at ≥ 20%	Endpoint
	Neurological symptoms with strong loss of balance, complete inactivity, ataxia and severe paralysis	
	More than 1 point in pain criteria (Grimace scale)	
	1x score equal to 4	
	4 additional points by Tumor growth evaluation	
	Strong paralysis	

Supplementary Table 1. Scoring sheet for animal experiments. Assessment of pain using the "Grimace scale" was conducted according to (Langford et al., 2010).

7.3 Publication

Parts of this thesis have been published in the following research articles:

Tsiami, F., Lago, C., Pozza, N., Piccioni, F., Zhao, X., Lülsberg, F., Root, D. E., Tiber, L., Kool, M., Schittenhelm, J., Bandopadhayay, P., Segal, R. A., Tabatabai, G., & Merk, D. J. (2024). Genome-wide CRISPR-Cas9 knockout screens identify DNMT1 as a druggable dependency in sonic hedgehog medulloblastoma. *Acta Neuropathol Commun*, 12(1), 125. https://doi.org/10.1186/s40478-024-01831-x (Tsiami et al., 2024).

Tsiami, F., Drwesh, L., Surender, S., Fitzgerald, J., Schittenhelm, J., Picketts, D. J., Segal, R. A., Tabatabai, G., & Merk, D. J. (2025). SMARCA5 is required for the development of granule cell neuron progenitors and Sonic Hedgehog Medulloblastoma growth. *Scientific Reports*, 15(1), pp. 26091.https://www.nature.com/articles/s41598-025-11857-3 (Tsiami et al., 2025).

8 Acknowledgements

First and foremost, I would like to thank my supervisor, Dr. Daniel Merk, for the unwavering support and guidance throughout my studies. You have truly taught me a lot and you have been a great mentor to me. More importantly, you have helped me grow as a scientist. I would especially like to express my gratitude to Prof. Dr. Ghazaleh Tabatabai, for giving me the opportunity to engage in the field of Neuro-Oncology early in my academic journey. Your support and encouragement throughout the years have been invaluable to me and I have truly learned immensely from all these years working in your department.

I also want to thank all my colleagues in the laboratory for the pleasant working atmosphere and for the scientific input and sharing of knowledge over the years. Special thanks to Anke Jakob, Heike Pfrommer and Sarah Hendel who constantly supported me and helped me move forward with my projects, as well as my office mate, Surender Surender, with whom we shared both stressful and enjoyable moments in the lab.

Additionally, I would like to thank my advisory board members, Dr. Pratiti Bandopadhayay and Prof. Dr. Simone Mayer. Your scientific insights throughout the years have always been valuable to me and have significantly shaped my thesis.

I would also like to thank Dr. Mathias Jucker and Dr. Marc Welzer, for granting me access to their facility´s microscope and training me to use it. Additionally, I would like to thank Dr. Luca Tiberi and Dr. Chiara Lago for our great collaboration in the DNMT1 project.

Special thanks to my cousin, Dr. Kassandra Xanthopoulou, for her support while writing my thesis. I want to thank all my friends in Tübingen and Stuttgart; without them life in Germany would not have been the same. Lastly, I want to thank my family and friends who have always been by my side, even virtually, encouraged me and reminded me of my worth.